UNIVERSITY OF COPENHAGEN
FACULTY OF SCIENCE

Dark Cosmology Centre

Emission line imaging and spectroscopy of distant galaxies

Johannes Zabl

Dissertation
Submitted for the Degree

Philosophiæ Doctor

Principal Supervisor: Prof. Johan Peter Uldall Fynbo

Dark Cosmology Centre
The PhD School of Science
Faculty of Science
University of Copenhagen

This is a version with typos corrected after submission!

Submission: *20/04/2015*
Defence: *02/07/2015*
Revised version: *27/08/2015*

Opponents: *Prof. Steen Hansen*
Prof. Susanna Vergani
Prof. Erik Zackrisson

ACKNOWLEDGMENT

First and above all, I want to thank my supervisor, Johan, for having provided me with the opportunity to pursue a dream. He has been at all times most supportive and encouraging.

Among the people at DARK, I want to especially thank Bo, Peter, Sune, Lise, all my fellow PhD students, my PhD committee (Thomas, Marianne, Stefania), and all others for interesting collaboration, advice, discussions, and social time. Without the amazing support of Julie, Michelle, Corinne, Damon, and Brian all administrative and computational problems would have been orders of magnitude more complicated. Thanks! Certainly not to forget are also Kristian and Jens, whose grants made my PhD studies possible.

Then, I want to thank Sangeeta and James for taking me into their group during a great and inspiring stay at Arizona State University, and my former Diplom thesis supervisors, Wolfram and Palle, for continuing their collaboration with me.

Finally and above all, I want to thank my family for always supporting my dreams.

Johannes

ABSTRACT

One of the main quests of contemporary astrophysics is to understand how and when galaxies form and how they evolve over cosmic times. Until star formation in galaxies is quenched through a still debated processes, they form stars more or less steadily out of gas that has cooled down in their interiors. The necessary gas supply is either provided through accretion from the surrounding medium or through mergers. Feedback mechanisms, e.g. provided by active galactic nuclei (AGN) or supernovae, regulate the star-formation and create outflows, which enrich the surrounding medium with energy, momentum, and metals both on small and large scales.

While galaxies are star-forming, the telltale signature of their spectra are strong emission lines. Emission lines are an extremely valuable "tool". The strength and shape of and ratios between these lines allow to constrain physical properties like star-formation rate, dust-extinction, energetics of the ionizing source, gas-phase metallicity, and kinematics of the gas. Further, they provide a unique signature which allows to safely secure redshifts even for low mass galaxies, whose stellar continuum emission is out of reach of spectrographs on the current generation of telescopes. Finally, emission lines can also be used in the first place to select large samples of galaxies at well defined redshifts through narrowband (NB) surveys. The idea here is that an emission line in a NB filter raises the filter averaged flux density compared to that expected from the continuum. Different emission lines can cause such an excess, which are at the wavelength of the NB filter at different redshifts.

Contemporary NB surveys have a strong focus on searches for Ly α emitters at the highest redshifts. Ly α is so well suited for high redshift studies because it is the intrinsically brightest emission line and has a low rest-frame wavelength. However, as it is a resonant line, it can be diluted through scattering at neutral hydrogen, and has due to the resulting increased optical path length an enhanced probability of being destroyed by dust. As part of this thesis I will present XSHOOTER rest-frame far-UV spectroscopy for Himiko, a NB selected giant Ly α emitter at redshift $z = 6.6$. This redshift corresponds to a time when the universe was only 6 per cent of its present age. While this is not the most distant object known, it is due to its strong Ly α emission arguably one of the most remarkable ones.

Himiko's Ly α line is at an observed frame wavelength of about 923 nm. Searches for yet more distant Ly α emitters require NB filters in the near-infrared atmospheric transmission windows. A currently ongoing survey with such a filter is executed as part of the UltraVISTA survey. These UltraVISTA NB118 data provide an unprecedented combination of depth and width. Whereas the search for Ly α at $z = 8.8$ is the main goal of this survey, it also results in huge line flux limited samples at lower redshifts. The relevant emission lines are mainly [O II] at $z \sim 2.2$, Hβ+[O III] at $z \sim 1.4$, and H α at $z \sim 0.81$. In the conclusion of this thesis, I will give a sneak peak at a case study for follow-up spectroscopy of NB118 selected [O II] emitters.

In principle, a direct product from NB surveys are line fluxes for the selected objects. However, as the effective bandpasses of NB interference filters in the fast convergent beams of survey telescopes cannot be made with tophat bandpass shapes, flux measurements for individual objects have uncertainties. We applied a novel NB measurement method to a sample of UltraVISTA NB118 H α emitters, and demonstrate

that this technique allows to recover more accurate fluxes. Additionally, the method allows to determine more accurate redshifts.

The gas surrounding a galaxy can either be observed through absorption of background sources or by probing for extended Ly α emission. In this thesis, I present results based on the latter approach. Extended Ly α emission can be produced in place through ionization from a central or several distributed source, through resonant scattering of Ly α photons at the neutral hydrogen, shock ionization from outflows, or gravitational cooling radiation.

Around some objects the extended Ly α emission is so strong that it can be detected for individual objects. Himiko is one of these, even so effects of cosmological surface-brightness dimming make the detection of extended emission at high redshifts notoriously difficult. We constrained with our work, which of the possible mechanisms is most likely responsible for the majority of Himiko's Ly α emission. As ionization source we considered both young stellar populations, possibly in its primordial metal free form, and an AGN. We conclude that normal Pop II star formation is the most likely source for the detected Ly α emission.

Himiko is a rare object. However, recent observational studies, which are in line with theoretical works, have shown that extended Ly α emission is not a rare phenomenon at all, but probably a typical property around star-forming galaxies at high redshifts. While this more typical emission is to weak to be detected for individual objects, it has been found in stacking analysis of large samples; but a recent non-detection of such emission for a sample of Ly α emitter $z \sim 2$, corresponding to a time around the peak of cosmic star-formation activity, has raised the question whether the halo properties change with time. We performed a stacking analysis with an independent sample and find a halo consistent with measurements at higher redshifts.

CONTENTS

1

INTRODUCTION

Human behavior flows from three main sources: desire, emotion, and knowledge. - Plato

In this introduction I will present a brief overview about how galaxies form and evolve over cosmic times, and what can be observed. Naturally, I will focus here mainly on those concepts and observables, which are relevant for the projects presented in this thesis.

After starting with a short description of the cosmological context (sec. 1.1), I will discuss galaxy formation and evolution (sec. 1.2). A quick mentioning of galaxies in the local universe is followed by a summary of the evolution of properties and relations. The section is concluded by a discussion of the first galaxies.

Then, I will describe what can be measured for galaxies at high redshift (sec. 1.3). More concretely, the contributions to the observable spectrum are discussed. In the last part of the section I will describe how these observables are measured (sec. 1.3.7).

1.1 FROM BIG BANG TO THE FORMATION OF STRUCTURE

It was in a singularity, often referred to as Big Bang, that the history of our universe (Figure 1.1) apparently began. It has expanded since and today it has an age of 13.5 Gyr.[1] This age can be measured so precisely, as the stage of the universe is set by a fundamental framework, described by Einstein's general theory of relativity, a theory which unites space and time and connects them through 'Einstein's field equation' to the energy and matter density of the universe. Under the assumption of a homogeneous and isotropic universe on sufficiently large scales, a concept which is referred to as the cosmological principle, space can be described through a scale factor, a, and a curvature constant. The field equations can be solved, resulting in two differential equations (Friedmann, 1922) for the scale factor of the universe $a(t)$, which gives the ratio of the proper physical distances between two points in the homogeneous universe measured at cosmic time t and today.

The ingredients in the Friedman equations are the mass densities or equivalently energy densities of the different constituents of the universe. The two main constituents to the present energy density are non-relativistic matter particles ($\sim 30\%$) and dark energy ($\sim 70\%$). Photons contributed at very early times strongly to the energy budget, but are today almost negligible compared to the energy density of matter, a consequence of their density scaling and redshift. While it is not clear what exactly dark energy is, such an energy density with an equation of state very different from normal non-relativistic or relativistic matter

---

[1] Throughout this thesis, for reasons of comparability to other observational studies, a specific set of cosmological parameters ($H_0 = 70\ \mathrm{km\,s^{-1}\,Mpc}$, $\Omega_{\mathrm{m},0} = 0.3$, $\Omega_{\Lambda,0} = 0.7$) was used. More precise cosmological parameters ($H_0 = 67.8\ \mathrm{km\,s^{-1}\,Mpc}$, $\Omega_{\mathrm{m},0} = 0.308$, $\Omega_{\Lambda,0} = 0.692$; Planck+WP+highL+BAO), including the CMB data from the Planck Satellite, result with 13.8 Gyr in a slightly higher age (Planck Collaboration et al., 2014)

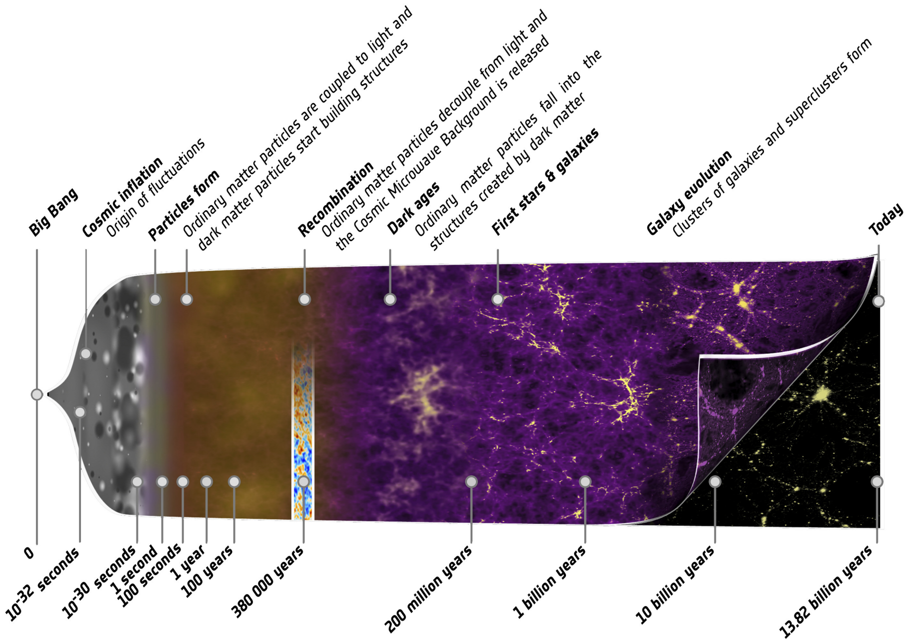

Figure 1.1 An illustration of the astrophysical history of the Universe. The currently observable Universe is part of something bigger that was blown up from a microscopical scale during an inflationary state that perhaps was the unset of the Big Bang. During inflation seeds for future structures were implanted in the distribution of matter via quantum fluctuations inflated to a macroscopic scale. After the universe became mater dominated and especially after the epoch of recombination structure formation accelerated. The first stars and galaxies probably formed after a few hundred million years and today, 13.8 billion years after the Big Bang, we can look back and study the full history of galaxy formation and evolution (Source ESA)

[2], is required to explain the findings of accelerated expansion based on the type Ia supernovae (Riess et al., 1998; Perlmutter et al., 1999). The curvature, the baryonic and DM density and other parameters can be inferred from the cosmic microwave background (CMB, Planck Collaboration 2014, the spatial distribution of galaxies (e.g. Percival et al., 2010), and the type Ia supernovae. The CMB radiation are the photons emitted about 400000 yrs after the Big Bang, the time when the universe became cool enough, so that electrons and photons combined to neutral hydrogen atoms and photons could afterwards freely travel through space without being scattered at the free electrons.

With the expansion of space, also the wavelength of electromagnetic waves is stretched out. This means that light emitted with wavelength λ_{rest} in the reference frame of a galaxy at some cosmic time t_{rest} has a longer wavelength when it reaches a telescope on earth at cosmic time t_{obs}. It is useful to define the redshift, z,

$$1 + z = \frac{\lambda_{\mathrm{obs}}}{\lambda_{\mathrm{rest}}} = \frac{a(t_{\mathrm{obs}})}{a(t_{\mathrm{rest}})} \, . \tag{1.1}$$

---

[2] relativistic ($v \sim c$) or non-relativistic ($v \ll c$) refers to the speed of the particles at the epoch of recombination

When relating intrinsic quantities of galaxies to measurable quantities, distance measures are required. Mainly, these are the luminosity distance, d_L, which relates the luminosity of an object, L, to a flux measurable on earth, f,

$$f = \frac{L}{4\pi d_\mathrm{L}^2} \, , \tag{1.2}$$

and the angular diameter distance, d_A, which relates an angle on the sky, θ, to an object's physical size, D.

$$\theta = \frac{D}{d_\mathrm{A}} \tag{1.3}$$

It is important to realize that d_A and d_L are in a cosmological context not identical (Hogg, 1999). In a flat universe without curvature, which our universe seems to be, d_A and d_L are related by $d_\mathrm{A} = \frac{d_\mathrm{L}}{(1+z)^2}$. An important consequence of this is that the surface brightness of an extend object, which is the ratio $\frac{f}{\theta^2} \propto \frac{d_\mathrm{A}^2}{d_\mathrm{L}^2}$, scales in the flat universe with $\frac{1}{(1+z)^4}$. This strong scaling of the surface brightness with redshift makes observation of low-surface brightness extended emission observationally difficult at high redshifts.

The CMB radiation, which is essentially a black-body radiation, has small temperature variations on the order of $\frac{\Delta T}{T} \sim 10^{-5}$. These are caused by density fluctuation, which are the seeds from which later the structure in the universe grows. From the angular distribution of the CMB fluctuations, it can be inferred that only a small fraction of about 15% (Planck Collaboration et al., 2014) of the matter is baryonic, where baryonic is basically all matter built up from protons and neutrons. The majority of the matter needs to be an unknown form, which does not interact with light other than via gravity, and is hence referred to as Dark Matter (DM). While theoretical particle physics suggests several candidates for DM, it has not been observed directly. As the properties of the DM are strongly impacting the structure formation in the early universe, currently the most favored candidates are cold dark matter (CDM) particles, meaning matter with a non-relativistic equation of state. Such a matter gives good agreement between calculations or simulations of the structure growth and observations of the large scale galaxy distribution (Blumenthal et al., 1984; Davis et al., 1985), especially when dark energy is included.

Over-densities of matter collapse under the impact of self gravity against the expanding background of the universe, until they reach a quasi equilibrium state, which is referred to as a virialized halo. In a ΛCDM universe, the formation of structure will be hierarchical, meaning that the smallest halos grow first, which than merge together to form larger halos.

1.2 Galaxies over cosmic times

> *That this in all Probability may be the real Case, is in some Degree made evident by the many cloudy Spots, just perceivable by us, as far without our starry Regions, in which tho' visibly luminous Spaces, no one Star or particular constituent Body can possibly be distinguished; those in all likelyhood may be external Creation, bordering upon the known one; too remote for even our Telescopes to reach* - Wright (1750)

1.2.1 Galaxies in the local universe

While speculated already in the middle of the 18th century (e.g. Wright, 1750; Kant, 1755), it was only about 100 yrs ago that it became observationally clear through the accessibility of an accurate distance indicator that some of the nebulae observed on the sky are indeed outside of our own galaxy. As the galaxies accessible to the photographic observations with the telescopes of the early 20th century showed a range of morphologies, necessarily a first step towards an understanding was a purely taxonomic approach.

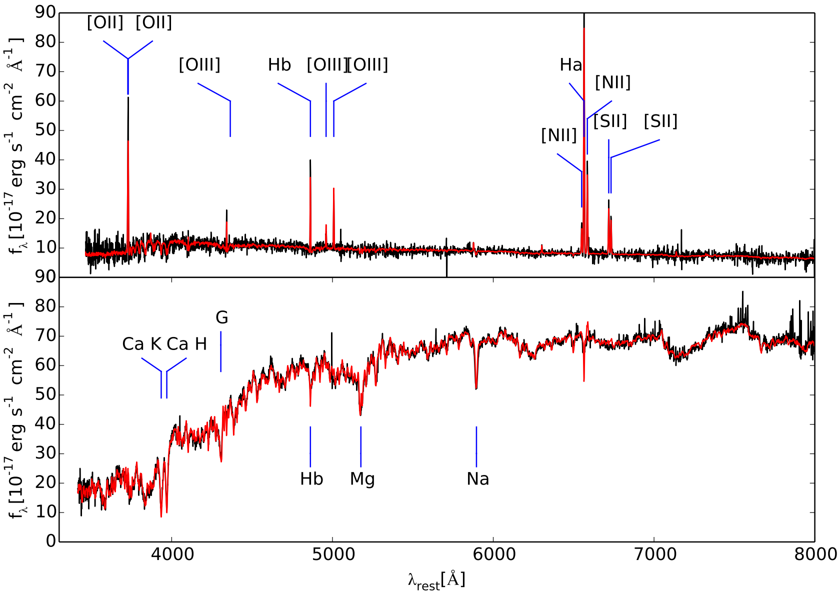

Figure 1.2 Two SDSS DR9 spectra of galaxies at redshift $z \sim 0.1$ (Ahn et al., 2012). In the upper panel a strongly star-forming galaxy is shown. It has prominent strong emission lines (cf. sec. 1.3.3) and only weak absorption features, consistent with a very young stellar population. In the lower panel the spectrum of an elliptical galaxy is shown, whose spectrum is dominated by strong absorption lines, consistent with an old stellar population. The black curve is the observed spectrum, while the red curve is a model fit used for the redshift determination, as provided in the SDSS data products (Bolton et al., 2012). Wavelengths are rest-frame vacuum wavelengths. Important spectral features are marked.

Edwin Hubble's classification scheme (Hubble, 1926, 1936), which is often referred to has 'tuning fork diagram', is still the basis for modern visual morphological classifications. It splits the galaxy population into ellipticals, which have mainly old stellar populations and whose kinetic energy required for fullfilling the essential virial theorem is in pseudo-random motion of the stars, while for the spiral galaxies, whose stellar light is dominated by young stars, and have strong emission lines, the majority of kinetic energy is in ordered circular motion in a disk. Spectra for a star-forming galaxy and an elliptical galaxy are shown in Figure 1.2.

The morphologies, physical properties, and spatial distribution of the galaxies closest to us both in space and in time are the ultimate anchor point, any successful theory of galaxy formation and evolution must be reaching at. Ideally, such a model would be from first principles only, but due to the complex physics involved, for many parts in theoretical picture of galaxy evolution a semi-empirical approach is required, which needs to be gauged by observation of the different populations through cosmic times.

Importantly, the finite speed of light provides a natural time machine, allowing to scan through the history with today's telescopes. While it is not possible to observe exactly the same objects at very different times, the study of the evolution of population properties allows to put the required constrains on the theories of galaxy evolution. Hence, careful observations both of statistical population properties and detailed studies of the physical properties in individual objects are required.

1.2.2 GALAXY EVOLUTION

While for the closest galaxies detailed resolved studies of the properties of galaxies are possible, in the more distance universe mainly integrated properties over the complete galaxies can be inferred. Nevertheless, it is possible to measure a large variety of quantities. Among others, these are star-formation rates (SFR), stellar population ages, stellar masses (M_*), gas-phase metallicities (Z), dynamical masses, and, if sufficient spatial resolution is available, surface brightness-profiles, and morphologies. Also important is the large-scale distribution of galaxies in general and subpopulations, which will confirm whether the prediction of the theoretical concepts to understand the formation of structure are correct.

A wealth of studies has traced the SFR density, meaning the SFR per volume over cosmic times. The well established result of these studies is that the cosmos had its hay-day around 10 Gyrs ago, at a redshift of $z \sim 2$ (e.g. Madau & Dickinson, 2014). Before that the cosmic SFR increased rapidly over a relatively short time-scale. The activity of active galactic nuclei (AGN) is strongly correlated with the star-formation activity (e.g. Shankar et al., 2009; Delvecchio et al., 2014). How quickly the first galaxies and AGNs formed is important, as they are gradually ionize the universe again.

Interestingly, the vast majority of typical star-forming galaxies are located on a relatively tight sequence in the SFR-M_* space (e.g Noeske et al., 2007; Daddi et al., 2007), which is referred to as the main sequence of star-forming galaxies. Its normalization changes with redshift, similar to the cosmic star-formation history. This means that at the peak of star-formation activity not only more galaxies are forming stars, but also individual galaxies of the same mass produce more stars. As cold gas is the fuel for star-formation, it needs to be available (e.g Finlator & Davé, 2008; Dayal et al., 2013).

Further important insight into the evolution of galaxies can be gained by analyzing how the chemical enrichment proceeded (e.g. Pei & Fall, 1995; Matteucci, 2012). This is particular important for gauging the role of outflows of enriched gas and infall of pristine gas. Importantly, several correlations between metallicity and other observables exist. As an example, metallicity on average increases over the population with mass (Tremonti et al. 2004) and metallicity correlates with environment (Cooper et al. 2008). Different studies show clearly an evolution of the mass-metallicity relation with redshift (e.g. Maiolino et al., 2008; Zahid et al., 2011; Yabe et al., 2012; Henry et al., 2013), in a sense that high redshift galaxies at a given mass are metal poorer, as is expected for gradual metal enrichment in galaxies by stellar yields combined with outflows and inflows. While the number of studies at higher redshifts with the advent of the current generation of NIR spectrographs is quickly increasing, the results are still limited and biased towards either high mass or strong star-formation rate or both. Probing galaxies over the complete range would be especially interesting with respect to the results of Mannucci et al. (2010), who have identified a possible fundamental relation between mass, metallicity and star formation rate (FMR). An interesting approach to extent the measurement to lower masses at relatively high redshifts is to select galaxies in absorption against bright background sources like Quasars or Gamma-Ray bursts (Fynbo et al., 2008; Rafelski et al., 2012; Møller et al., 2013; Christensen et al., 2014; Arabsalmani et al., 2015). Another way is to use very deep emission line selected surveys, a selection method used throughout this thesis.

An important aspect of galaxy evolution in an hierarchical ΛCDM universe are mergers between galaxies and the respective halos which are hosting them. While massive elliptical galaxies are assumed to be the end state of mergers between two spiral galaxies with similar masses (major mergers) (e.g. Toomre, 1977; Mihos & Hernquist, 1996), as more recently became clear, the reverse statement is not necessarily true. Mergers can also produce rotational supported systems (e.g. Springel & Hernquist, 2005; Ueda et al., 2014).

In any case, if the two merging galaxies have gas (wet-merger), the galaxies might for a short time very heavily form stars, in a so called star-burst, where the SFR can be above the main-sequence of star-forming galaxies expected for the given redshift (e.g. **?**). During this merger induced star-formation, the galaxies will have a very irregular morphology, especially in the blue light dominated by young stars.

The fact that many of the high redshift star-forming galaxies have irregular morphologies is consistent with the expectations of merger triggered events (e.g. Conselice, 2014). However, even if the galaxies have no sign merging, interesting conclusions can be drawn from measuring their sizes (e.g. Malhotra et al., 2012).

It is of fundamental importance to measure all these relations and their scatter as accurate as possible in order to constrain galaxy formation models (e.g. **?**).

1.2.3 THE FIRST GALAXIES

While the matter content in the favored ΛCDM scenario is dominated by DM, driving hence the large scale evolution, the 15% in baryonic matter is also of fundamental importance. This is the material out of which galaxies form and what can be directly observed due to the interaction with light, may it be in emission or in absorption. The presence of DM can only be inferred through the gravity which it is exerting on matter and light.

This also means that DM is dissipationless, meaning that it cannot get rid of its energy radiatively. By contrast, baryonic matter can do so through different processes, whose respective efficiencies depend on the temperature, but also on whether the gas is pre-enriched with metals, the density of the gas, and the background radiation field (e.g. Cox & Tucker, 1969; Sutherland & Dopita, 1993; Wiersma et al., 2009). As long as at least some sufficiently efficient cooling channel is available, the gas can collapse further than the DM halo, forming a galaxy at the peak of DM's gravitational potential. Sufficient means that the cooling time of the gas is shorter than the free fall time of the collapsing gas cloud, a requirement which can be understood as 'the' criterion for the formation of a galaxy (Rees & Ostriker, 1977).

There are two different approaches to understand the formation of the end state of galaxy formation and evolution, todays spirals and ellipticals. The first is a 'monolithic' collapse of the primordial gas, suggested by Eggen et al. (1962) to explain the metallicity dependence of the orbits of close-by main sequence stars. The outcome of the collapse is decided by how fast sub-clumps and consequently stars form in the collapsing gas compared to the cooling time scale of the complete halo (e.g. Larson, 1975; Gott & Thuan, 1976). If the latter is shorter, there is no time to redistribute angular momentum, as stars are essentially collisionless. Otherwise, assuming some initial angular momentum, the gas has the possibility to redistribute in the energetically favored configuration of a disk. While this scenario can explain several of the properties of galaxies, it does not hold up to scrutiny in many details.

Second, naturally arising from the structure growth in a ΛCDM universe is a hierarchical merging scenario, where statistically the smallest DM halos form first and a successive merging of different halos, their gas and their galaxies takes place over cosmic times (e.g. White & Rees, 1978; White & Frenk, 1991; Cole et al., 1994; Vogelsberger et al., 2014). As mentioned above the merging can transform the structural properties of the galaxies, e.g. rotational supported system to pressure supported systems, or increase their masses and sizes (Bezanson et al., 2009; Toft et al., 2014).

Even so the ΛCDM universe is most likely the correct model, the formation of the seeds in the merging and gas accretion process must have inevitably taken place in a small version of the Eggen et al. (1962) scenario. This results in the question, when and how the first galaxies formed.

The first population of stars is referred to as Pop III (e.g. Bond, 1981). These stars are formed out of the primordial gas having chemical abundances solely determined in the Big Bang nucleosynthesis (e.g. Alpher et al., 1948). Hence, it is composed mainly of H and He, mixed with a tiny amount of Li, tinier amount of Be and B, and almost no C,N,O (e.g. Wagoner et al., 1967; Coc et al., 2014). Later generations of stars, like the low metallicity but yet metal enriched halo stars of our Milky Way (Pop II) or the metal enriched population in the disk (Pop I), are produced from gas enriched by the yields from the nucleosynthesis in previous generation of stars (e.g. Burbidge et al., 1957; Nomoto et al., 2013).

After the universe became neutral in the recombination observed as CMB, a universe devoid of photons capable of ionizing hydrogen, the first significant number of stars could form in halos with masses of 10^6 $\mathrm{M}_\odot$ at redshifts of about $z = 30 - 15$ (Bromm 2013 and references therein), motivated by molecular hydrogen H_2 being the lowest temperature cooling channel for primordial gas.

More precisely, at the viral temperature of these halos the excitation of rotational levels of H_2 becomes possible, and despite the ineffectiveness of H_2 production, the produced amount is at the prevailing densities high enough to get the cooling time below the free-fall time. While in the ΛCDM universe halos as high as $z = 60$ can fulfill these criteria, the volume density of such halos is only at redshift $z \sim 30$ sufficiently abundant that one can refer to them as a population.

While it is not completely clear whether the primordial gas collapsing in the mini-halos forms finally a single very massive star with $O(100M_\odot)$ or whether some fragmentation of the gas can take place, the stars formed under these conditions are expected to be at least on average more massive than typical stars formed in a Pop II (e.g Tumlinson et al., 2004; Clark et al., 2011; Susa et al., 2014). After these massive stars explode in supernovae (SN), which can be depending on stellar mass through a core-collapse similar to that for massive Pop II stars or through the more exotic pair instability SNe, the surrounding medium gets quickly enriched with metals (e.g. Scannapieco et al., 2003; Pallottini et al., 2014). Further, with the presence of these first stars UV photons have their comeback in the universe, both above the threshold to re-ionize the neutral hydrogen (13.6 eV or 1216 Å) and somewhat below, where the range from 11.2 to 13.6 eV is relevant for the photo-dissociation of H_2 through absorption in the Lyman and Werner systems (e.g. Field et al., 1966; Black & Dalgarno, 1976).

The physics of the formation of the first generation of stars, starting from the cooling of the gas in the halo through the protostar to the onset of hydrogen burning, has been strongly impacted both by the absence or presence of metals or dust, and by ionized gas, which can be produced by ionizing photons or shocks. At what exact metallicity star-formation changes to a mode with the possibly universal mass distribution for Pop I+II star-formation (Bastian et al. 2010 and references therein), is as many of these theoretical predictions for the Pop III stars not entirely certain. Typically, the suggested values lie between 10^{-5} and 10^{-3} of the solar metallicity, referred to as the critical metallicity. The change in the fragmentation properties could be triggered by the available amount of metals for metal line cooling or a sufficient amount of dust produced in SN to allow for dust cooling (e.g. Bromm, 2013, and references therin).

Pop III stars produce a lot of UV photons in excess of the hydrogen ionization threshold and beyond. For once, this is because they are likely more massive than Pop II stars, but even if they would have the same mass, this would hold true, as Pop III stars have significantly hotter photospheres compared to Pop II stars of the same mass (Tumlinson & Shull, 2000; Schaerer, 2002). Resulting from these spectral properties, the H II regions surrounding the stars will have very strong H and He nebular emission.

There are several high redshift Ly α emitters with rest-frame Ly α equivalent widths around 300 Å and above (e.g. Malhotra & Rhoads, 2002; Kashikawa et al., 2012). For typical metal abundance in Pop II stars between 1/100 and 1/10 of the solar value combined with a typical IMF slope and without excessively massive stars, it is even for an extremely young population difficult to have a Ly α EW_0 beyond $\sim$ 400Å (e.g Raiter et al., 2010), and assuming ages distributed over a span of 1 Gyr assuming constant SFH, values beyond $\sim$ 200Å seem implausible.[3] However, for even lower metallicities such Ly α equivalent widths become possible. Therefore, Pop III stars are considered as one possible explanation for these objects.

Currently, direct observational evidence for a Pop III and hence direct constraints are still missing. However, this will be one of the exciting fields in the coming years. Searches for Pop III through spectral

---

[3] Malhotra & Rhoads (2002) have derived the often quoted value of 240Å as maximum value for a constant star-forming population. This was assuming already a very top-heavy IMF.

signatures might already be possible now, but certainly should be with the quantum leap provided by the next optical and IR telescopes like JWST and EELT (e.g. Zackrisson et al., 2012). Further, instruments like radio instruments like Lofar allow to probe the imprint of the first stars through the imprint on the 21 cm line (e.g. Furlanetto et al., 2006).

At the time of writing this introduction the most distant observed galaxies are probably at redshifts $z \sim 10$ (e.g. Bouwens et al., 2014; Oesch et al., 2014; Zitrin et al., 2014). These are objects selected through a photometric selection using the dropout technique based on extremely deep NIR data with the Wide Field Camera 3 (WFC3) on the Hubble Space Telescope (HST). The highest redshift candidate being a galaxy with a most likely photo-z of $z = 10.7$, whose flux is amplified by gravitational lensing at a foreground galaxy cluster (Coe et al., 2013). A redshift of 10.7 corresponds to a cosmic age of ~ 400 Myr, or 3% of the current age of the universe.

Usually, the photometric selection is followed by the goal to obtain a spectroscopic verification. One possibility is too identify the Lyman break in the spectrum. The detection of the break at the resolution of a spectrum allows for an unambiguous identification. Currently, the most distant object with a spectroscopically detected Lyman break is at redshift $z = 8.2$ (**?**). The continuum measured for this object was not originating from the superposition of the stars in the galaxy but from the afterglow spectrum of a gamma ray burst (GRB). This is the energetic explosion of a single star. A break in the continuum originating from the general stellar population of a galaxy has been recently found in a lensed object at $z = 7.5$ (**?**). While a continuum detection at highest redshifts is only possible for the brightest objects, emission line detections can serve as spectroscopic confirmation also for fainter objects. Usually, Ly α is targeted at these redshifts. The leader is, when a 4σ Ly α line detection is considered enough, a galaxy at $z = 7.62$ (Schenker et al., 2014), or with the more strict requirement of a detection above the 5σ level, a Ly α line at $z = 7.51$ (Finkelstein et al., 2013).

1.3 MEASURING GALAXIES

All our information about galaxies needs to be, at least as a mediator, inferred from the electromagnetic radiation emitted by a galaxy. The radiation that reaches us is a superposition of emission from different sources, which is reprocessed by various scattering and absorption mechanisms both in the emitting galaxy and in unrelated matter intervening the sightline between the galaxy and the telescope. Emission sources include stellar photospheres, nebular emission from H II and photon-dominated regions (PDR) regions, thermal emission from dust heated by the photons, and, if the gas in the galaxy is in the state of accreting onto its central black hole, thermal emission from the accretion disk, non-thermal emission from relativistic electrons, and line emission from broad and narrow line regions. Supernova remnants and X-ray binaries may also contribute significantly (in the radio and X-ray bands respectively). Absorption and scattering processes include absorption and scattering caused by dust particles, resonant scattering, and of course metal line absorption. Dynamical processes inside the galaxies determine the line widths (e.g. motion in gravitational potentials, thermal broadening, turbulence, etc.).

Many of these processes produce clear observational signatures. Measuring these allows to characterize the physical state and chemical composition of a galaxy. As important observational features can be found over the complete electromagnetic spectrum, the use of several different observational techniques is necessary. Out of these techniques and the physical concepts required to interpret the observations, I will in the following only present those most relevant for this thesis.

1.3.1 WHAT IS A GALAXY?

In the favored paradigm for galaxy evolution, a galaxy is considered to be a DM halo with the stars residing at its center. In addition, there is gaseous material both in the volume between the stars, a region referred to as the interstellar medium (ISM), and outside the central region containing stars but still within the halo of the galaxy, know as the circumgalactic medium (CGM). The space between the halos is referred to as the intergalactic medium (IGM).

Based on the assumption that the ISM is in pressure equilibrium, two stable phases exist. These are the cold neutral medium (CNM), where the hydrogen is neutral, and the warm medium, which might either be neutral (WNM, warm neutral medium) or ionized (WIM, warm ionized medium). The energy input from supernovae can create an additional semi-stable phase, meaning that the cooling time is much longer than the reheating time. This phase is known as the hot interstellar medium (HIM) (McKee & Ostriker, 1977).

In addition to these phases of atomic or ionized hydrogen, there is also molecular hydrogen, which can form efficiently in the presence of a small amount dust in the ISM. It is through the formation, collapse, and fragmentation of giant molecular clouds that stars form. Indeed, the star-formation rate (SFR) is directly proportional to the molecular hydrogen density in a galaxy. Once formed, massive, hot stars ionize the gas around them, resulting in so called H II regions. As these regions are the place where the emission lines are formed (cf. section 1.3.3) they are of fundamental importance for the results presented in this thesis.

An isolated galaxy will in most cases eventually use up its gas reservoir and convert it into stars. However, there are sources of replenishment of the gas. Galaxies merge, whereby fresh gas can be brought in from one galaxy to another. Furthermore, it is important to remember that there are many more baryons in the IGM than inside galaxies (e.g. Cen & Ostriker, 1999; Sommer-Larsen & Fynbo, 2008). Cosmological simulations predict that the gas from the IGM may possibly be accreted through so called cold streams (e.g. Dekel et al., 2009), but in any case typically along the filaments of the large scale structure.

The star-formation in galaxies is self-regulated through several feedback mechanisms. Probably the two most important mechanisms are supernovae (SNe) and active galactic nuclei (AGNs). These inject both energy and momentum into the gas both on small and large scales. Subsequently, the star-formation efficiency will be reduced through heating of the gas, the accretion of new gas onto the galaxy will be suppressed, and gas will be removed from the star-forming regions and the ISM through winds. Depending on the momentum input and the depth of the halo's potential well, the gas can be expelled out the CGM or even the IGM. The feedback from SNe is understood to be more relevant in lower mass galaxies, while AGN feedback is dominating for galaxies at the upper end of the mass range.

Therefore, the CGM will have a substantial amount of gas, which might either be strongly metal enriched material ejected from the ISM, or freshly accreted material from the only slightly enriched IGM. The presence of both the fresh and outflowing processed gas can be shown through ionization metal lines in neutral hydrogen absorbers (e.g. Fynbo et al., 2011; Krogager et al., 2013; Lehner et al., 2013; Rubin et al., 2014). Another method to probe the presence of the neutral hydrogen in the CGM is through the scattering of Ly α photons. I discuss this as part of the project presented in chapter 3.

1.3.2 THE SPECTRA OF GALAXIES: STELLAR POPULATIONS

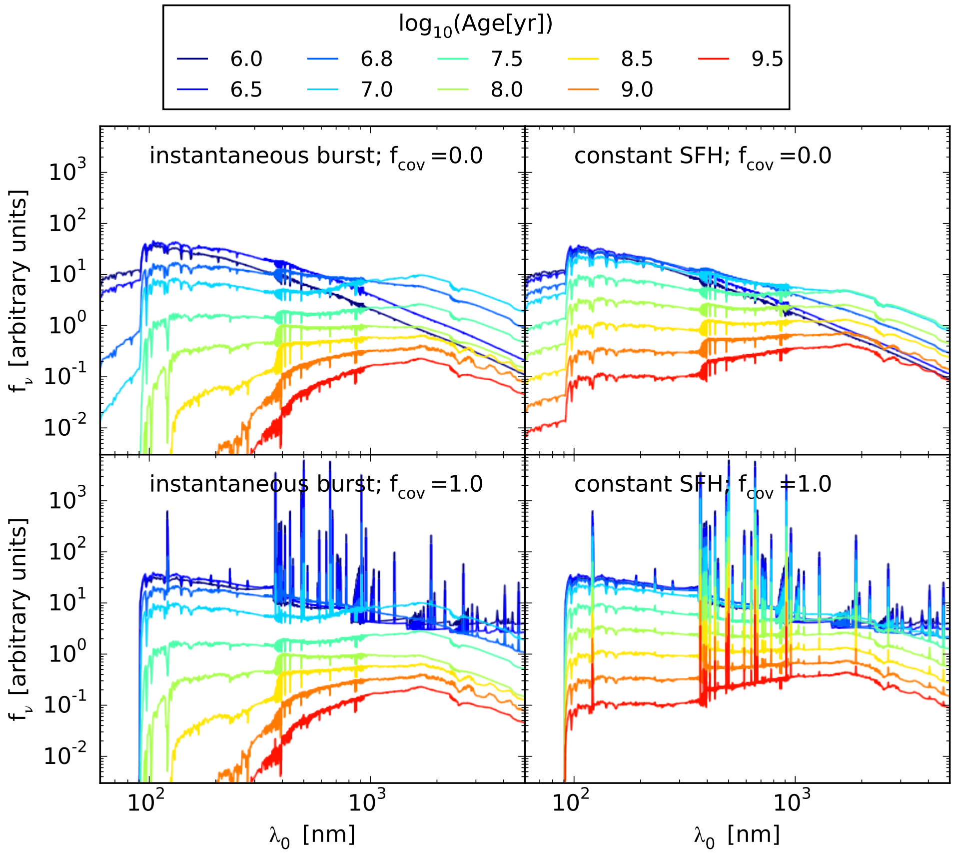

Figure 1.3 Galaxy spectra as obtained from Bruzual & Charlot (2003, BC03) stellar population synthesis models combined with nebular emission following the recipe described by Ono et al. (2010). Spectral energy distributions (SEDs) are shown for nine different ages after onset of star-formation. In the left column, all stellar mass is formed in an instantaneous burst, while for the right column continous star-formation with constant rate is assumed. For the upper row, no hydrogen is in the sightline towards the stars, meaning a covering fraction $f_{\mathrm{cov}} = 0$. Consequently, no H II regions are created and no nebular emission is present. By contrast, in the lower row all ionizing flux is converted into nebular emission within the galaxies.

The Hubble classification has proved successful: since Hubble's time, observations have shown that a wealth of different observational and physical properties of galaxies are correlated with the morphology. E.g. already in the 1950s, Holmberg (1958) has realized that the galaxy color is strongly correlated with the morphology, in the sense that the reddest galaxies are the ellipticals and the bluest are the spiral and irregular (Irr) galaxies. The reason for this is that the Irr and spirals have a lot of cold gas, which is the ingredient for star-formation, and hence have a lot of young stars.

After the stars start burning hydrogen by fusion in their cores, they have luminosities, lifetimes, and photospheric temperatures which approximately scale with the stellar mass as $M^{3.5}$, $M^{-2.5}$, and $M^{0.5}$, respectively (based on values stated in Kippenhahn et al. 2012, chapter 22.1[4]). The probability distribution function for a newly formed star to be of certain mass, the so called initial mass function (IMF), scales approximately with $M^{-2.5}$ (Salpeter, 1955). This means that, even though the actual shape of the IMF might somewhat deviate from the Salpeter power law slope at the low mass end (e.g., Kroupa, 2001; Chabrier, 2003; Bastian et al., 2010), the majority of stars are produced at relatively low masses. Nonetheless, due to the even stronger scaling of the luminosity with mass, the integrated stellar light over a galaxy is dominated by the most massive still living stars (this is not entirely true as the light from RGB and AGB stars can also add significantly to the spectral energy distribution). Assuming the stars to be blackbodies, for which the peak of spectral emissivity is directly related to the photospheric temperature ($\lambda_{peak} \propto T^{-1} \propto M^{-0.5}$), galaxies with a lot of young stars are blue, while those for which the star-formation ceased a long time ago are redder (cf. Figure 1.3).

For a star of a given birth mass and chemical composition, detailed theoretical modeling of stellar structure and atmosphere allows us to predict very accurately the star's mass, luminosity, structure, and chemical composition as a function of time after its formation (e.g. Kippenhahn et al., 2012). Using these stellar evolution tracks combined with either theoretical or empirical spectra at the different evolutionary stages, the integrated spectrum for a single stellar population, $L_\lambda^{ssp}(\lambda, t, Z)$, formed at the same time with a certain IMF out of gas with metallicity Z can be calculated (e.g. Bruzual & Charlot, 2003; Maraston, 2005; Vazdekis et al., 2010).

While the results of these calculation are remarkably accurate, there are still some uncertainties at specific evolutionary stages. A potentially important one is the contribution of stars on the thermally pulsating asymptotic giant branch (TP-AGB), a late evolutionary stage in the life of stars with main sequence masses $\leq 7 M_\odot$. This short phase of stellar evolution can strongly impact the spectrum at IR wavelengths. For SSPs with ages between about 200 Myr and 2 Gyr, the TP-AGB stars might contribute as much as 40% to the total bolometric luminosity of the SSP (Maraston, 1998). Other common SSP implementations, like the BC03 (Bruzual & Charlot, 2003) or the Starburst models (Leitherer et al., 1999) have significantly lower contributions from stars on the TP-AGB (c.f. Maraston et al., 2006). Several results in the thesis are derived using BC03 models. This choice is justified, as observational evidence shows that the BC03 models might be more consistent with observations (Zibetti et al., 2012). Further, as the objects discussed in this thesis are mainly strongly star-forming objects, dominated by stars younger than 200 Myr, the TP-AGB stars have no major impact.

The integrated stellar spectrum for a galaxy, $L_\lambda^{stellar}(\lambda)$, which started forming stars at time t_f and which emitted at time $t = 0$ the light that we observe today, is completely specified through the star-formation rate as a function of time, $\Psi(t_f - t)$ with $t < t_f$, and $L_\lambda^{ssp}(\lambda, t, Z)$.

$$L_\lambda^{stellar}(\lambda) = \int_0^{t_f} \Psi(t_f - t)\, L_\lambda^{ssp}\,(\lambda, t_f - t, Z(t_f - t))\, \mathrm{d}t \tag{1.4}$$

The stellar spectral energy distribution of galaxies, $L_\lambda^{stellar}(\lambda)$, have a few very prominent features (cf. Figure 1.3). For evolved stellar populations this is especially the 4000 Å break (cf. Figure 1.2), which is

---

[4] There more precise values are stated, which slightly depend on mass. The values stated here are crudely rounded.

a combination of the natural blackbody shape for the dominant relatively cool stars[5], combined with additional flux deficit due to blanketing by several metal lines. The sharpness of the break is mainly caused by the strong Ca II H+K absorption lines. For galaxies, which have recently stopped their star-formation, a similar break exists. The spectral classes which dominate a population between about 50 Myr and 1.5 Gyr after quenching[6] of the star-formation (e.g. Poggianti, 2004) have very strong Balmer absorption lines and the continuum opacity due to bound free emission from the $n = 2$ level in hydrogen is high. This causes a break at around 3700 Å, a similar wavelength as the 4000 Å break in the more evolved galaxies.

Finally, there is the Lyman break (e.g. Giavalisco, 2002, and references therein). Galaxy spectra which have ongoing star-formation have a substantial amount of UV photons. However, there is a strong break at 921 nm, as light with wavelengths shorter than this threshold can ionize hydrogen. In addition to a strong hydrogen edge in the stellar spectra due to self absorption in their photospheres, especially the neutral hydrogen in the ISM might almost completely remove the ionizing photons. The absorbed energy will be reemitted in nebular line and continuum emission, as described in the next section. How much of the light shorter than 921 nm ($f_{\rm esc}$) can escape the galaxy depends on the covering fraction of the neutral hydrogen in the sightline to the young stars, which can substantially differ from galaxy to galaxy (observationally e.g. Nilsson et al., 2009; Cooke et al., 2014). In general, an increase of $f_{\rm esc}$ with redshift might be expected (e.g. Razoumov & Sommer-Larsen, 2010), a property required to allow for sufficient ionizing photons escaping into the IGM to facilitate the timely reionization of the universe (e.g Kuhlen & Faucher-Giguère, 2012).

Towards high redshifts the fraction of neutral hydrogen in the intergalactic medium increases or inversely formulated, the universe gets from the neutral state after recombination with time again re-ionized. The ionizing photons are provide by star-forming galaxies and active galactic nuclei, with the latter probably dominating the ionizing background only at $z \lesssim 3$ (e.g. Haardt & Madau, 2012, and references therin). Even so the re-ionization was probably almost complete at $z \sim 6$ (e.g. Fan et al., 2006), the remaining small neutral fraction suppresses the flux-density at wavelengths shorter than Ly α. This absorption is caused by scattering in the resonant Ly α and higher order Lyman lines due to diffuse neutral hydrogen present at redshifts below the observed object's redshift (Gunn & Peterson, 1965). In addition to the diffuse absorption there is absorption at higher column-density systems, which further suppress the flux.

1.3.3 The spectra of galaxies: Nebular emission

In this thesis, when referring to a specific ionization stage of an element, a notation common for stating spectroscopic transitions is used throughout. In this notation the chemical element symbol is combined with a Roman numeral. E.g., O I is neutral oxygen, while O III is double ionized oxygen. An equivalent identifier, which is more common in atomic physics, would be to state O^0 and O^{2+} for the two cases, respectively.

If an emission line originates from a transition between energy levels for which electric-dipole radiation is not allowed due to the violation of the quantum mechanical parity selection rule, the transition is referred to as 'forbidden'. In the notation this is indicated by putting the ion identifier into brackets, e.g. [O III]. The transition probability is not zero for the forbidden lines, as other processes are possible, usually magnetic-dipole or electric-quadrupole transitions. However, these have much lower transition probabilities, and the corresponding excited states have much longer lifetimes than states from which an allowed transition is possible. Consequently, the possibility of a collisional de-excitation of these levels might be important (e.g. Osterbrock & Ferland, 2006).

In addition, there are lines which are referred to as semi-forbidden or inter-combination lines. These

---

[5] Mainly G and K stars which have long enough lifetimes

[6] late B and A stars

originate from transitions which violate a selection rule for the total spin.[7] As the corresponding excited states are in multi-electron atoms or ions not entirely independent from states with other spin-quantum numbers, the small admixture from the other state allows for a transition, yet with significantly decreased probability. Such lines are indicated by one sided bracket, e.g. C III].

When referring to a specific emission line the ion identifier is supplemented by the wavelength corresponding to the transition energy, e.g. [O III]λ5007, with the number being in Å. Due to tradition, these wavelengths are stated in air, as one would measure in a spectrograph on earth under standard conditions. The vacuum wavelengths are somewhat longer. E.g., the line [O III]λ5007 has in vacuum a wavelength of 5008.2Å. All results and plots in this thesis are based on vacuum wavelengths.

Hydrogen recombination lines Due to their high photospheric temperature, massive short-lived stars produce a large number of photons with energies above 13.6 eV, the ionization potential of hydrogen, and as a result hydrogen gets ionized in a region around the star. The resulting free electrons recombine again when they meet a proton. An equilibrium between recombination and ionization will be established in the H II regions, with the recombination rate being naturally proportional to the product between electron density, n_e, and proton density n_p. The latter is for a pure hydrogen nebula the same as n_e. The ionization rate is proportional to the number of ionizing photons, $Q(\mathrm{H}^0)$, emitted by the stars that produce the H II region. Assuming complete ionization within a sphere, the volume of the ionized region, V_S, referred to as a Strömgren sphere, is given by:

$$V_\mathrm{S} = \frac{4\pi}{3} r_\mathrm{S}^3 = \frac{Q(\mathrm{H}^0)}{n_e^2\, \alpha_B} \tag{1.5}$$

α_B is the total recombination coefficient for Case B assumptions (see below). After recombining with some probability to a specific excited level, the electrons will cascade down through different energy levels following the quantum mechanical selection rules and transition probabilities. Transitions from or to the ground level, $n = 1$, of the hydrogen atom are referred to as Lyman-series photons, while those to the first excited level, $n = 2$, are Balmer series photons.[8] Balmer lines are in the optical range of the electromagnetic spectrum, whereas Lyman lines are in the UV range.

For the hydrogen densities typical in the H II regions, the gas is optically thick to Lyman-series photons. These conditions are referred to as Case B (Baker & Menzel, 1938). This means that every emitted Lyman series photon gets essentially reabsorbed immediately. Consequently, the probabilities for the occurrence of the different transitions can be calculated under the assumption that the cascades end at the $n = 2$ level. E.g., for an electron temperature of $T_e = 10^4$ K and density $n_e = 100$ cm^{-3}, typical values for the plasma in the H II regions, the luminosity in the Balmer β strength is given as:[9]

$$L(\mathrm{H}\beta) = 4.78 \times 10^{-13}\ \mathrm{erg\ s}^{-1} Q(H_0) \tag{1.6}$$

As the number of $Q(H_0)$ is proportional to the available mass in heavy and hence very short lived stars, the hydrogen lines are very good indicators of the instantaneous star-formation rate. In Table 1.1 the line strengths for a few hydrogen lines are listed normalized to that of Hβ assuming the same temperature and density as above. These ratios depend, especially within the series, only weakly on T_e and n_e over the range of expected conditions in H II regions (e.g. Osterbrock & Ferland, 2006; Storey & Hummer, 1995).

---

[7] Assuming L+S coupling (e.g. Foot, 2005)

[8] The hydrogen electron orbitals can be completely characterized by the quantum numbers n, l, m_l, m_s, with n being the principal quantum number and l the total angular momentum quantum number. In the hydrogen atom all $2n^2$ states for a given principal quantum number are degenerate, meaning that they have the same energy, at least up to small relativistic fine structure effects.

[9] Calculated using $L_{H\beta} = 4\pi\ j_{H\beta} \times \frac{4\pi}{3} V_\mathrm{S} = \frac{4\pi\ j_{H\beta}}{n_e\, n_p} \times \frac{Q(H_0)}{\alpha_B}$, where $j_{H\beta}$ is the volume emissivity. The appropriate value for $\frac{4\pi\ j_{H\beta}}{n_e\, n_p}$ was taken from Storey & Hummer (1995) and the case B recombination coefficient, α_B, for $T_e = 10^4$ K is based on Hummer (1994).

Table 1.1 Strength of different hydrogen lines normalized to the H β luminosity. Case B recombination for an electron temperature T_e = 10^4 K and an electron density $n_e = 10^2$ cm^{-3} is assumed.

Identifier:	Ly α	H α	H β	H γ	H δ	Pa α
Transition	$2 \rightarrow 1$	$3 \rightarrow 2$	$4 \rightarrow 2$	$5 \rightarrow 2$	$6 \rightarrow 2$	$4 \rightarrow 3$
Flux ratio	23.2[a]	2.86[b]	1[b]	0.47[b]	0.26[b]	0.34[b]

[a] For Case B with T_e = 10000 K 68% of the recombinations end on the 2p level. Therefore, the Ly α luminosity is $L_{\mathrm{Ly}\alpha} = 0.68\, Q(H^0)\, E_{\mathrm{Ly}\alpha} = 1.1 \times 10^{-11}$ erg s^{-1} $Q(H^0)$. The stated flux ratio was calculated by dividing this value with eq. 1.6. The corresponding ratio between Ly α and H α is 8.1, which is slightly lower than the often stated ratio of 8.6. [b] Based on Storey & Hummer (1995)

The case B cascades have one extra step to the ground level after they end on the $n = 2$ level. This last step depends on whether the recombination cascade ends on the 2s or 2p level, where s and p refer to the orbital angular quantum numbers $l = 0$ and $l = 1$ (see e.g. Foot, 2005). As the $2s \rightarrow 1s$ transition is quantum mechanically strongly forbidden, a direct radiative decay to the ground level is only possible through 2-photon decay (e.g. Breit & Teller, 1940). In this decay the energy difference between the $n = 1$ and $n = 2$ levels of 10.2 eV is split between the two photons, creating a continuum with a peak in f_ν at a wavelength of 161.8 nm (Nussbaumer & Schmutz, 1984).

In addition to 2-photon emission, there are two other nebular continuum sources. These are referred to as free-free and free-bound emission. Free-free emission originates from the acceleration of free electrons in the electric field of the ions. Free-bound emission has its origin in the recombination events (e.g. Osterbrock & Ferland, 2006): In the recombination process a photon will be emitted with an energy corresponding to the sum of the kinetic energy of the captured electron and the ionization energy from the level onto which the recombination takes place.

While the electrons ending their cascade on the 2s level will eventually produce 2-photon radiation, those ending on the 2p level can radiatively decay to the 1s level and emit a Ly α photon with λ = 121.6 nm. Under the assumptions of Case B recombination the cascade to the 2p will happen in 68% percent of the recombinations (e.g. Dijkstra et al., 2014). This results in the production of an enormous amount of Ly α photons. Indeed, in strongly star forming galaxies as much as about 5% of the total bolometric luminosity of a galaxy is expected to be in Ly α. This 5% is for the assumption of a typical Pop II metallicity and IMF. Even more extreme values are possible for IMFs including more massive stars or at lowest metallicities (e.g. Partridge & Peebles, 1967; Raiter et al., 2010). This makes Ly α in principle an ideal beacon for very distant galaxies (but compare sec. 1.3.5).

An actual nebula does not only consist of hydrogen, but has also He and metals.[10] The ionization potential to create single ionized He is with 24.6 eV (Kramida et al., 2014) still within an energy range in which the massive O and B stars produce a significant amount of photons. Hence, recombination lines to He I occur in typical conditions of H II regions. However, recombination to the hydrogen like He II is usually not relevant for gas which is illuminated by typical Pop II stellar clusters. Even the most massive stars do not emit a significant amount of photons energetic enough to double ionize He (54.4 eV). By contrast, the spectra of massive Pop III stars might be sufficiently energetic, as they are expected to be

---

[10] In astronomy all elements heavier than He are considered as metal, including several elements which are chemically not considered as metals.

hotter than Pop II stars. The strongest He II recombination line of those with a wavelength above the hydrogen ionization threshold is He II λ1640, the He equivalent of Balmer α. The detection of such a line in a galaxy spectrum might be interpreted as a key signature for a Pop III (cf. also chapter 2).

The excess energy which is set free when an atom gets photo-ionized is converted into kinetic energy of the liberated electrons. As the electrons can quickly thermalize through scattering, the plasma can be characterized through the electron temperature and density. The actual temperature and density structure in the H II regions is determined through the balance between the heating provided by the ionizing photons and the available cooling processes. Despite having very low abundance, lines from ions of C, N, S, O, Ne, etc play an important role in the cooling of the gas. The relevant transitions are for typical temperatures mainly a number of forbidden lines. These have low enough transition energies so that collisions with electrons can excite them. Due to the long lifetimes of the excited meta-stable states, collisional de-excitation becomes important. Therefore, these lines will only be strong below a certain critical density. However, give low enough densities, some of these lines can have emissitivities exceeding those of the hydrogen recombination lines.

One of the most interesting quantities for a galaxy is the mass fraction of metals, the metallicity, Z. The most common measure for the gas-phase metal abundance is through the that of Oxygen, usually stated as:

$$12 + \log(\mathrm{O/H}) \tag{1.7}$$

The oxygen abundance should in principle be inferred from the strength of Oxgygen lines combined with the knowledge of n_e and T_e. n_e and T_e can be measured through line ratios, which are sensitive to one and only one of the two quantities. For n_e these are lines, whose transition have the same excitation energy, but whose critical densities for collisional de-excitation differ (e.g. [O II]$\lambda\lambda$3726, 3729), while for T_e it is levels with different excitation energies, but almost no dependence on the density (e.g. [O III]λ4363, [O III]λ5007). Especially, lines like [O III]λ4363, which are referred to as auroral lines, are for high redshift galaxies usually not accessible with sufficient S/N and hence a direct T_e determination is usually not possible.

Therefore, the most common and crudest method to determine gas-phase oxygen abundances is to use ratios between the available strong lines. These can be put into two groups: either ratios between the collisional excited metal lines and a nearly metallicity independent hydrogen recombination line, or between two of the metal lines with different metallicity dependence (e.g. Kewley & Dopita, 2002). These strong-line ratios are typically calibrated based on measurements for which the direct method described above is available or through photo-ionization modeling. Usually, it is not accounted for differences in the ionization parameter or the hardness of the ionizing spectra, resulting inevitably in substantial uncertainties.

1.3.4 Other ionization sources

Alternatively to very hot stars, the source of ionizing photons can also be accretion on a black hole. The power law like UV spectra of AGNs have a significant number of photons with energies to create double ionized He and can hence produce the He II recombination lines. Further, their spectra also produce high ionization stages of metals, e.g. C IV (47.9eV) and N V (77.4eV), and the gas illuminated by the AGN is heated enough, so that collisional excitation of transitions from their ground states corresponding to photon energies in the UV are likely. These far-UV lines, which shift at high redshifts to the rest-frame optical, can be strong enough to be detectable even at highest redshifts. A further possibility for line excitations are shocks produced by the ejecta from supernovae (e.g. Dopita & Sutherland, 1996).

1.3.5 LYMAN ALPHA

For galaxies at $z \gtrsim 2$, where Ly α shifts into the wavelength range which is observable from the ground (cf. Fig. 1.6), Ly α should due to its strength in principle be an ideal SFR indicator and the best observable spectroscopic feature for very high redshift galaxies. Such a very strong and high equivalent width line can in principle be relatively easily selected with a NB filter, as described in sec 1.6. However, for several reasons Ly α is usually not as strong as expected for Case B recombination assumptions (e.g. Hayes et al., 2010).

Due to being a resonance line,[11] the Ly α optical depth at the line center is very high, about $\tau_0 \approx 3.31 \times 10^{-14}\ T[10000\mathrm{K}]^{-1/2} N_\mathrm{H}$ (e.g. Verhamme et al., 2006), where N_H is the hydrogen column density. With typical H I column densities in galaxies being of the order of $10^{21}\,\mathrm{cm}^{-2}$ (e.g. Zwaan et al., 2005), the optical depth at the line center is enormous. If only a spatial random-walk with scattering in the line center would be possible, each Ly α photon would need to undergo such an enormous amount of scatterings before escape, that despite having a tiny probability, angular-momentum redistribution from the 2p level to the 2s level through collision with ions and the resulting loss of the Ly α photon would become a problem. It is only because the Ly α photons can in addition to a diffusion in real space also diffuse in frequency space that an escape is possible with a small enough number of scatterings (e.g. Osterbrock, 1962; Adams, 1972; Neufeld, 1990):

The frequency dependent absorption cross-section is not a δ function. In the rest-frame of the H atoms it is a Lorentzian, which is a consequence of natural line broadening. In the rest-frame of the galaxy, the cross section is a convolution of this Lorentzian profile with Doppler broadening, as the individual H atoms have a velocity distribution according to the temperature of the gas.[12] After being absorbed, a Ly α photon is re-emitted with exactly the same energy as the incoming photon in the rest-frame of the hydrogen atom (coherent scattering). Importantly, however, if the atom is in motion, the wavelength of the incoming and outgoing photon might not be identical in the rest-frame of the galaxy. The reason is that photons will not be emitted in the same direction as the incoming photon and the atom has different velocity components in the different directions w.r.t to the galaxy rest-frame, meaning different Doppler boosts.

Photons which are absorbed by an atom with large absolute velocity have the chance to obtain a strong enough shift in frequency, so that the probability to meet another atom with Ly α in resonance is substantially reduced. Such an atom would need to have a high velocity, which is rare. Therefore, once a Ly α photon has a frequency in the wings of the Voigt profile, the probability of escape increases.

As a result, the escaping Ly α spectrum has a double peaked profile. The two peaks are shifted w.r.t to the Ly α resonance wavelength in the galaxy's rest-frame symmetrically towards the blue and red. The extent of the shift depends both on the kinetic temperature and the column density of the hydrogen gas (e.g. Neufeld, 1990; Laursen et al., 2009a). However, the picture gets more complicated when the ISM is not static, but outflows or inflows in the ISM are present. Outflows tend to suppress the escape through the blue peak (e.g. Verhamme et al., 2006). In this sense, Ly α can be used as a tracer for the kinematics of the gas. The exact spectral shape depends all on outflow velocity, velocity structure, geometrical structure, and the properties of the gas. All these dependencies are at least to some extent degenerate. Still, by using MCMC radiative transfer simulations parameters can be inferred, especially if constraints from other observables are available (e.g. Krogager et al., 2013).

Even so through the mechanism crudely outlined above, the Ly α photons can mainly escape without being destroyed through the collision with ions, there are two actual reasons why the Ly α luminosity is often lower than expected.

---

[11] Meaning that it is the lowest energy transition from the ground state and can only decay back to the ground state

[12] The resulting profile is referred to as Voigt profile.

First, despite the coupled random walk in real and frequency space, a Ly α photons still covers a very long path before it escapes a region with neutral hydrogen. Therefore, even for a small amount of dust, the probability to get absorbed or scattered by a dust-grain is large. By contrast, the continuum and non-resonant lines can directly pass through the gas and therefore have a much lower probability for such an encounter.[13]

The second effect is the spatial diffusion of the Ly α photons. As Ly α will be scattered at any present hydrogen gas, may it be in the ISM or the CGM, the emitted Ly α light will not be spatially coincident with the continuum emission source. Therefore, measuring the flux within a matched aperture centered on the continuum emission can result in a lower than expected emission for Ly α. The case of scattering in the CGM will be further discussed in chapter 3 of this thesis. Especially at very high redshifts also the IGM is important. There, the IGM is increasingly becoming neutral and the ionized regions around the galaxies are small. Therefore, the damping wing of the Voigt profile of the still neutral IGM might be in redshift space close enough, so that Ly α is scattered out of the line of sight.

1.3.6 The effects of dust

The UV and optical light emitted by the stars and the nebular emission from H II regions is attenuated by the presence of dust in the ISM, where the attenuation for blue light is stronger than for the red light. The amount of the intrinsically emitted light, $I_{\lambda}^{\mathrm{int}}(\lambda)$, which is removed either by absorption or scattering at dust from the sightline, can be given in magnitudes through $A(\lambda)$.

$$-2.5 \log_{10} \mathrm{I}_{\lambda}^{\mathrm{obs}}(\lambda) = -2.5 \log_{10} \mathrm{I}_{\lambda}^{\mathrm{int}}(\lambda) + A(\lambda) \tag{1.8}$$

The wavelength dependent extinction curve might be given through the normalized total extinction, $k(\lambda)$:

$$k(\lambda) \equiv \frac{A(\lambda)}{A(B) - A(V)} = \frac{A(\lambda)}{E(B - V)} \tag{1.9}$$

B and V are two common broadband filters.

When interpreting galaxy dust extinction by means of SED fitting, it is common practice to assume some extinction law. For reasons of comparability, a Calzetti et al. (2000) extinction law was used throughout the projects presented in this thesis. The Calzetti et al. (2000) extinction curve was determined for local starburst galaxies. However, as can be seen from Fig. 1.4, extinction substantially differs from object to object and from sight-line to sight-line. Therefore, the assumption of an extinction law can have substantial effects on the parameters derived by SED fitting.

It is still open to debate, whether the nebular emission suffers from more extinction than the stars or not (e.g. Erb et al., 2006). Calzetti et al. (2000) have found from their sample of local starburst galaxies a relation between nebular $E_N(B - V)$ and stellar $E_S(B - V)$ extinction of $E_S(B - V) = 0.44\, E_N(B - V)$. A physically approach to implement the dust extinction, which can naturally explain the different nebular and stellar extinction, is to assume a different extinction for the short-lived birth clouds of the stars and the ambient ISM (Charlot & Fall, 2000).

The extinct energy needs to be re-emitted by the dust grains in other wavelengths. This is mainly in thermal blackbody emission and some dust line emission of polyaromatic hydrocarbons (PAH) (e.g. Draine, 2003). As the extinction is strongest in the UV, where only massive, short-lived stars contribute, the energy redistribution is strongest for young stellar populations. A combination of measurements for

---

[13] In a clumpy interstellar medium, the Ly α photons might scatter off the dusty neutral hydrogen clumps while the continuum photons will pass through them, with the effect of an increased absorption for continuum photons compared to Ly α photons (Neufeld, 1991). The required physical conditions for a net Ly α boost might however be unrealistic (Laursen et al., 2013).

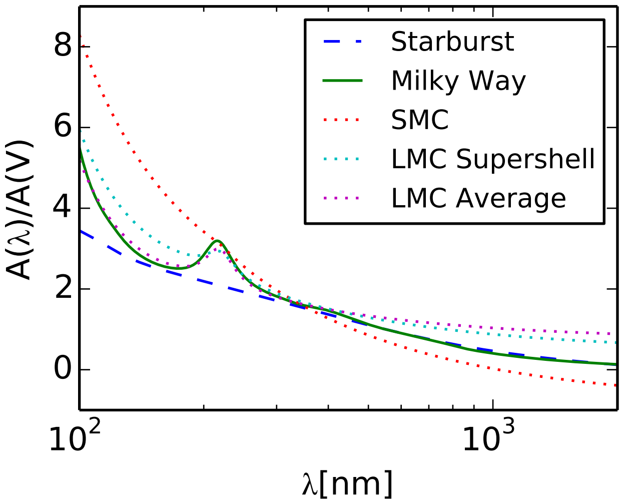

Figure 1.4 Different dust attenuation curves measured for the Milky Way (Cardelli et al., 1989), the Magellanic clouds (Gordon et al., 2003), and for local starburst galaxies (Calzetti et al., 2000).

the UV flux and the total emission in the FIR is a good star formation rate indicator, which is sensitive to the star formation in the last 100 Myr.

1.3.7 How to measure

Important information about galaxies can be gained from the complete electro-magnetic spectrum, which ranges from the high energy gamma-rays to the long wavelength radio data. Each of the wavelength regimes requires specialized telescopes and instruments. While data from the X-ray, far-infrared (FIR), and radio parts are to some extent used in this thesis, the main focus is on the classical optical window and the red extension in the four near-infrared (NIR) transmittance windows Y, J, H, and K (Figure 1.5).

It is noteworthy that the red wavelength end of the Y band coincides with the Si band gap, and the sensitivity of typical optical CCDs is already in the Y band very low. Hence, the high quality Si based CCDs used for optical observations cannot be used in the NIR. However, the IR detector arrays have come close to the optical CCDs, e.g. in quantum efficiency (e.g Rieke, 2007). Nevertheless, cosmetic defects like bad pixels or strong variations in QE, while tractable, are still much more pronounced. One of the main reasons for this is that the structure of the IR arrays is significantly more complex than in optical CCDs. As those semi-conductor materials with low band gaps, which are required for detection of IR photons, do not allow for a CCD implementation within the material, a more complicated hybrid for light detection and readout needs to be constructed. A second reason is that the detection layer needs to be created thicker than at optical wavelength to have sufficient detection efficiency. These imperfections have to be kept in mind when analyzing and interpreting NIR data from e.g. VLT/XSHOOTER, VISTA/VIRCAM, or HST/WFC3, three instruments from which data is used in this thesis.

The flux density $f_\lambda(\lambda)$, which reaches a telescope, is for high redshift galaxies very low. Therefore, telescopes with enormous mirrors combined with advanced instruments are required. The forefront of ground based optical and NIR astronomy are telescopes with mirrors in the 8–10 m class, like VLT (8.2m, 4 telescopes, ESO), Keck (10m, 2 telescopes), and Subaru (8.2m, NAOJ), and dedicated wide

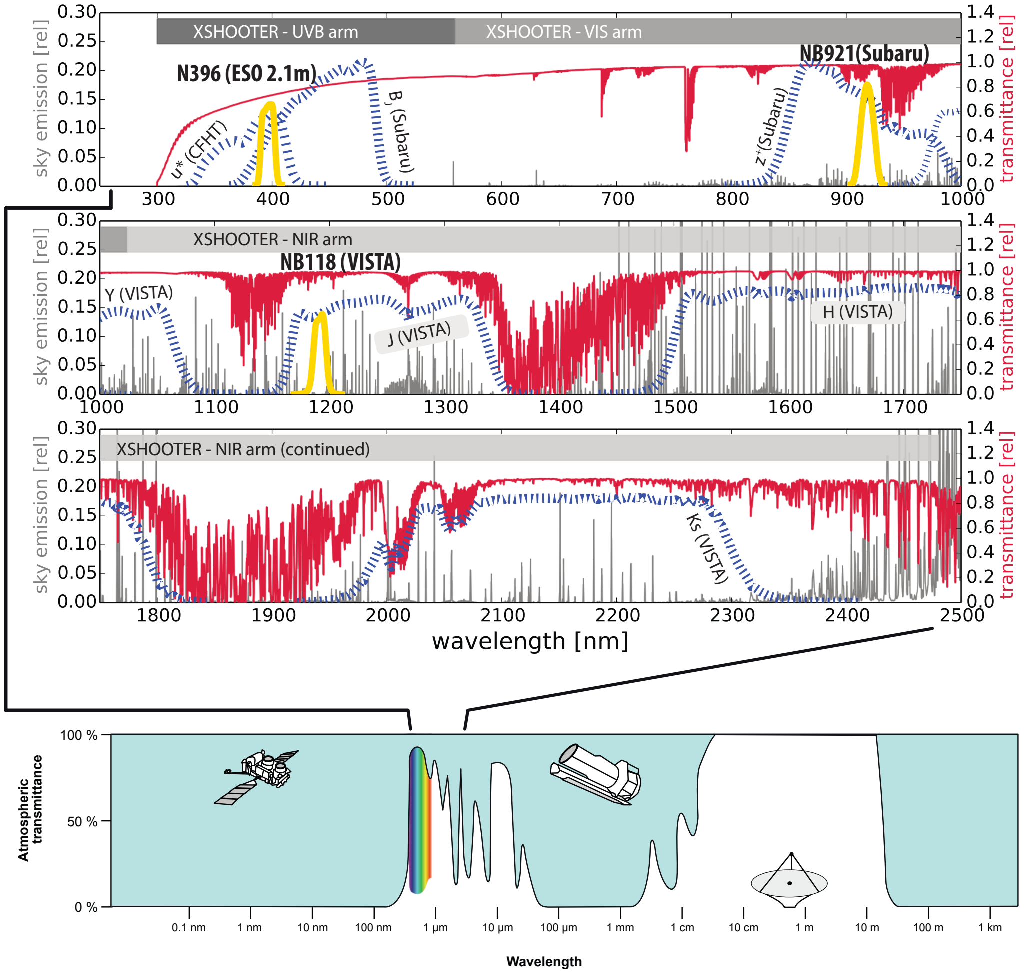

Figure 1.5 In the lower part of the figure the complete electromagnetic spectrum is illustrated. Only a few windows in the optical and IR, and at radio wavelengths can be observed through the earth atmosphere. At all other wavelengths space based telescopes need to be used. For this thesis observations in the optical and near-infrared (NIR) are especially relevant, corresponding to a wavelength range shown as zoom-in in the upper part. The red curve is the atmospheric transmittance while the grey curve is emission by the sky background. Whereas the optical wavelength range is relatively unaffected from both, absorption as well as emission are in the NIR a problem. Filters specifically relevant for the thesis are shown as blue dashed (broadband) and yellow (narrowband) curves. (Image credit: Lower part is a modified figure from wikipedia, originally based on a NASA illustration. In the upper part I have created the atmospheric transmission and absorption curve with SKYCALC/ESO V1.3.9 assuming a zenithal pointing (airmass = 1.0))

field instruments on somewhat smaller telescopes like VISTA/VIRCAM (4.2 m, ESO). Even with these telescopes observation times of several nights can be required to significantly detect objects at the current redshift and low mass frontiers through photometry or spectroscopy.

When observing from earth, astronomical observations are limited by the presence of an atmosphere between the telescope and space. Due to several absorbing atoms, radicals, and molecules (e.g. O_3, O_2, H_2O, CO_2), the atmosphere is only transmitting in certain wavelength ranges. This includes a window at radio wavelengths and a few windows in the IR and the optical (cf. Figure 1.5). Hence, observations at wavelength shorter than the near-UV and most IR observations need to be carried out from space.

The atmosphere has a second negative effect on earth-based observations. In absence of an advanced correcting system referred to as adaptive optics, which is far from being standard for NIR and especially optical observations, the spatial resolution is limited by a wavefront distortion caused by turbulence in the atmosphere. This referred to as *seeing*. Only at the best telescope sides on earth, like Paranal in Chile, Mauna Kea on Hawaii, or Roque de los Muchachos on La Palma, the atmosphere is calm enough to obtain a typical median seeing with a FWHM of around $0''.7$ on a yearly average.[14] This means, that the spatial resolution is for the large telescopes not limited by diffraction at the entrance pupil, which scales with λ/D, but the seeing. E.g. the diffraction limited resolution for a 8 m and a 2.4 m at a wavelength of 500 nm are $0''.02$ and $0''.07$, respectively, values small compared to the typical seeing. Therefore, the Hubble space telescope (HST), with a mirror of 2.4 m significantly outperforms the large 8 m class telescopes in terms of spatial resolution. The spatial extent of high redshift galaxies is very small, both due to their distance[15] and on average smaller sizes of galaxies at a given mass with increasing redshift (e.g. Trujillo et al., 2006a; Mosleh et al., 2012). With the spatial resolution set by the atmospheric seeing to typically around $\sim 0''.7$, high redshift galaxies are at best marginally resolved and little structural information can be inferred.

Observations in the optical and NIR can be subdivided into imaging or spectroscopy.[16] In imaging observations there is simply a detector in the focal plane of the telescope, in the same way as it is in a normal photographic camera. The bandpass of the detected light is controlled by putting a filter into the beam.

From the observation of an object with such a camera one obtains an analogue-to-digital number (ADU), which is related through the gain to the number of electrons freed by detected photons. More specifically the ADU is given by:

$$ADU = \frac{1}{\text{gain}} \int A\ T(\nu)\ f_\nu(\nu) \frac{1}{\text{h}\nu} d\nu \tag{1.10}$$

Here $T(\nu)$ is the passband transmittance as a function of frequency, which includes the filter passband, but also the transmittance of the atmosphere and the QE of the detector, $f_\nu(\nu)$ is the flux density above the atmosphere, and A is the collecting area of the telescope.

Instead of fluxes often magnitudes are stated, which are defined as -2.5 times the decadic logarithm of the ratio between the ADUs measured for the observed object in a specific filter compared to the ADUs expected for a reference object in the same filter.

$$m = -2.5\ \log_{10}\left(\frac{ADU_{\text{obj}}}{ADU_{\text{ref}}}\right) = -2.5\ \log_{10} ADU_{\text{obj}} + \underbrace{2.5\ \log_{10} ADU_{\text{ref}}}_{\equiv ZP} \tag{1.11}$$

Usually this is written in the form of the last equality, where the second summand is referred to as the zeropoint (ZP). The reference object can either be real, often Vega, or an object with a hypothetical spectrum, e.g. a spectrum flat in f_ν, as in the AB magnitudes (Oke, 1974). More specifically in the AB

---

[14] In exceptional nights the seeing can be as good as $\sim 0''.2$.

[15] The angular diameter distance has actually a maximum at $z = 1.6$ for the generic cosmological parameters used throughout this thesis and decreases at even higher redshifts, making sources with the same physical size again a bit larger on the sky at yet higher redshifts.

[16] Additional, but rarely used options are polarimetry and interferometry. Further, modern IFU spectrographs like VLT/MUSE start to smear the fields of imaging and spectroscopy.

magnitude system $f_{\nu;\mathrm{ref}}(\nu) = 3.631 \times 10^{-20}$ erg s^{-1} cm^{-2} Hz^{-1} is chosen, which is about the average flux-density of Vega in the V filter. The AB magnitude systems, which is contemporary at least in extragalactic astronomy the most common magnitude system, has the advantage that it can be easily interpreted.

$$m = -2.5\ \log_{10}\left(\frac{ADU_{\mathrm{obj}}}{ADU_{\mathrm{ref}}}\right) = -2.5\log_{10}\left(\frac{\int T(\nu)\ f_{\nu;\mathrm{obj}}(\nu)\frac{1}{\nu}\ d\nu}{\int T(\nu)\ f_{\nu;\mathrm{ref}}(\nu)\frac{1}{\nu}\ d\nu}\right) = \tag{1.12}$$

$$= -2.5\log_{10}\left(\frac{\int T(\nu)\frac{1}{\nu}\ f_{\nu;\mathrm{obj}}(\nu)\ d\nu}{\mathrm{erg\ s^{-1}\ cm^{-2}\ Hz^{-1}}\int T(\nu)\frac{1}{\nu}\ d\nu}\right) - 48.6 = -2.5\log_{10}\left(\frac{\bar{f}_\nu}{\mathrm{erg\ s^{-1}\ cm^{-2}\ Hz^{-1}}}\right) - 48.6 \tag{1.13}$$

$\bar{f}_\nu$ can be understood as the weighted average of the flux density, with the weights naturally given by the product of the transmittance and the inverse of the energy per photon. Assuming a hypothetical Dirac-δ filter, $\bar{f}_\nu$ is just f_ν. Finally, it is useful to note that $f_\nu(\nu)$ can be replaced by $f_\lambda(\lambda)$, using $|f_\nu(\nu)d\nu| = |f_\lambda(\lambda)d\lambda|$ and $c = \nu\ \lambda$. E.g. for $\bar{f}_\nu$ in eq. 1.13 follows:

$$\bar{f}_{\nu;\mathrm{filter}} = \frac{\int f_\lambda(\lambda)T(\lambda)\lambda\, d\lambda}{\int \frac{c}{\lambda^2}T(\lambda)\lambda\, d\lambda} \tag{1.14}$$

Commonly, filters are chosen from some well defined broadband filter systems (e.g. Bessell, 2005), as this allows for comparability. The various broadband filters have typically a ratio between central wavelength, λ_c, and width of $R = \frac{\lambda_c}{\Delta\lambda} \approx 5$. By using several of these filters, a very low resolution spectrum can be created. In order to increase the resolution of this pseudo spectrum narrower filters can be used. E.g. mediumband filters, which have typically $R \sim 10$, have been employed for this purpose (e.g. van Dokkum et al., 2009).

By comparing the magnitudes, or equivalently the $\bar{f}_\nu$, measured in a set of filters to $\bar{f}_\nu^{\mathrm{model}}$ expected for a model galaxy spectrum, one can statistically decide about the probability of a model being consistent with the data. By doing this for a range of model spectra, one can find the most probable one under the given data. This method of parameter inference is referred to as SED fitting (e.g. Walcher et al., 2010). With a sufficient large number of filters and making certain assumptions, e.g. about the star-formation history and the dust extinction curve (cf. sec. 1.3.2 and 1.3.6), galaxy properties like redshift, stellar mass, population age, amount of dust extinction, and star-formation rate (SFR) can be inferred. It is made use of SED fitting in all chapters of this thesis at least in some form. Details are given at the relevant places.

On the extreme end of the filters are narrowband filters, which have $R \gg 10$. While there exist programs to combine a large number of these filters to construct pseudo continuum spectra (Benitez et al., 2014), a more common use for these filters is to measure emission lines (e.g. Djorgovski et al., 1985; Møller & Warren, 1993; Fynbo et al., 2000; Rhoads et al., 2000; Pascual et al., 2007; Milvang-Jensen et al., 2013): If a strong emission line is both in a matching broadband and a narrowband filter, the $\bar{f}_\nu$ will be larger in the NB filter than in the BB filter. An example for such an observation is shown in the upper part of Figure 1.6. Considering that there is also a continuum, the ratio of $\bar{f}_{\nu\mathrm{BB}}$ and $\bar{f}_{\nu\mathrm{NB}}$, or equivalently the magnitude difference $m_{BB} - m_{NB}$, depends on the observed-frame equivalent width, EW_{obs}. EW_{obs} is defined as:

$$EW = \int\left(\frac{f_\lambda(\lambda)}{f_\lambda(\lambda)^{cont}} - 1\right)\mathrm{d}\lambda \tag{1.15}$$

$f_\lambda(\lambda)^{cont}$ is the flux density of the continuum and $f_\lambda(\lambda)$ includes an emission or absorption line. With this definition, which is used throughout this thesis, $EW_{\mathrm{obs}} > 0$ for emission lines and < 0 for absorption lines. EW might be given either in rest-frame or observed-frame, which are related through $EW_{\mathrm{obs}} = (1+z)\ EW_{\mathrm{rest}}$.

If there is only a single infinitely thin line, a known continuum shape, and a filter with a tophat profile, the *EW* and flux of the emission line can be directly determined from the measured m_{NB} and m_{BB}. However, these assumptions break down for some lines and for NB filters in the majority of wide-field instruments, resulting in large systematic uncertainties. These problems are discussed in more detail in chapter 4, where a method to overcome the problem of non-tophat filters is discussed.

In spectroscopic observations, a slit is usually in the focal plane of the telescope, and the transmitted light is dispersed by an dispersive element, which can be a grating, a prism, or a combination of both (grism). Data from the XSHOOTER (Vernet et al., 2011) spectrograph at the VLT is used in chapter 2 and section 5.4 of the conclusion. XSHOOTER splits the light from the telescope into three wavelength ranges by the use of dichroic mirrors in front of the focal plane. The three intervals are indicated in Fig. 1.5. In each of the three resulting foci is a slit, who are the input to individual Echelle spectrographs. This optical design allows to simultaneously obtain medium resolution spectra over the wavelength range from 300 to 2480 nm. E.g. for the narrowest available slits with $0\farcs4$ and assuming a source which uniformly illuminates this slit in dispersion direction, the resolution in the VIS and NIR arm reaches resolution as high as $R = 17400$ and $R = 10050$. Medium resolution is important in the NIR even for faint high redshift objects, as this allows to efficiently use the wavelength ranges between the bright sky lines.

1.3.8 Selecting galaxies

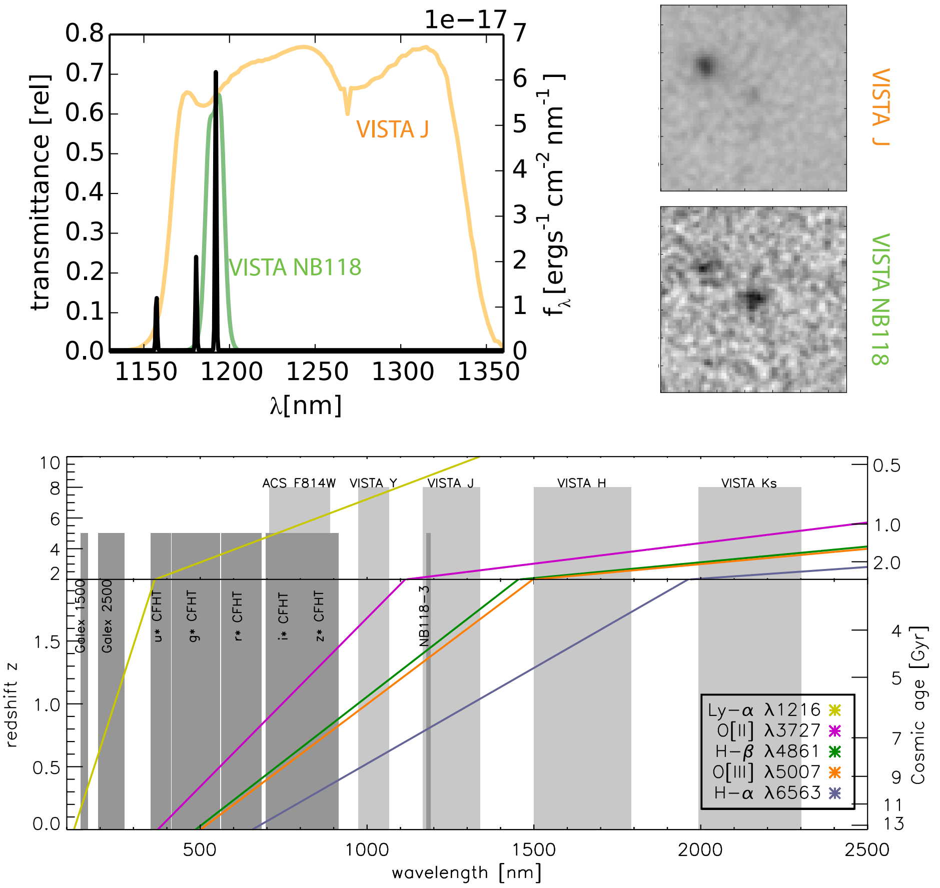

Figure 1.6 In the upper right part 10″x10″ cutouts for an object in the VISTA/VIRCAM NB118 narrowband and J broadband filters are shown. The cutouts, which are scaled to the same specific surface brightness in both cases, are based on data from the UltraVISTA survey (McCracken et al., 2012) (here DR2). The NB excess is with 2.00 ± 0.19 magnitudes one of the strongest measured in the data. Using the BB data (not shown), it can be concluded that it is either Hβ, or [O III] λ4959, or [O III] λ5007, with the latter being due to the extreme *EW* the most likely possibility. Assuming some typical [O III] λ5007 to Hβ ratio and a continuum flat in f_λ, the spectrum which is consistent with the measured magnitudes would look like shown in the upper left panel. In the lower panel of the figure the wavelength of the important rest-frame optical lines is shown as a function of redshift. Several filters are indicated for orientation (Origin for lower figure: my Diplom thesis).

When studying population properties, ideally with follow-up spectroscopy, it is important to select samples with well defined selection criteria at a specified target redshift. Especially for galaxies at $z \gtrsim 0.4$, where the important rest-frame optical emission lines start to get successively shifted into the NIR, only at certain redshifts all important lines are accessible (cf. Figure 1.6, lower part). Therefore, for spectroscopic studies a preselection as precise as possible is important.

NB selection A powerful method is provided by the NB selection method, as used throughout this thesis. The idea is that an emission line causes a stronger increase in the filter averaged flux density in a NB compared to that in a BB (cf. sec 1.3.7). Hence, by explicitly searching for objects which have in matched photometry $m_{\mathrm{BB}} - m_{\mathrm{NB}} > 0$, those galaxies with an emission line in the NB filter can be selected. Typically, this is supplemented by a cut on the statistical significance of this color and a minimum color requirement, corresponding to a minimum EW. Both criteria are applied to avoid false positives, with the first aimed at avoiding statistical flukes and the latter as a veto against pretenders, e.g. caused by a break in the continuum.

After applying such an EW cut, the excess can be in the majority of the selected objects attributed to one of the strong emission lines, including Ly α, Hβ, Hα+[N II] $\lambda\lambda 6548, 6583$, [O II] $\lambda\lambda 3727, 3729$, [O III] $\lambda\lambda 4959, 5007$, at the respective redshifts matching the wavelength of the NB filter. However, also other rarer emission lines might be selected, especially in cases of very high specific star-formation rate (SSFR; ratio between SFR and stellar mass) or the contribution of an AGN.

For a given NB filter of course only those lines with a rest-frame wavelength below the wavelength of the NB filter are possible to select. E.g. in the N396 filter with a central wavelength of 396.3 nm (Nilsson et al., 2009), as used in chapter 3, the only two possibilities out of the strong lines are [O II] at $z = 0.06$ and Ly α at $z = 2.25$. By contrast, the VIRCAM/NB118 filters used in chapter 4 and section 5.4 allow for detection of all the strong rest-frame optical lines, e.g. with $z = 0.81$ for H α and a very high $z = 8.8$ for Ly α (cf. Figure 1.6). Therefore, in order to decide which of the lines causes the excess, the NB excess needs usually to be combined with another selection method. Fortunately, a very low redshift accuracy of this additional selection is enough to discriminate between [O II], [O III] + H β, and H α, and Ly α. Safely deciding between the two [O III] lines and H β on the other hand is difficult.[17]

The atmosphere is not only absorbing, but also emitting. At wavelengths below $\lambda \sim 2$ μm, above which the thermal black-body radiation of the sky-background becomes a problem, the sky-brightness in the NIR is mainly dominated by strong emission lines from molecular transitions, mainly OH (e.g. Rousselot et al., 2000, see also Figure 1.5). Fortunately, due to the narrowness of the NB filters they can efficiently be placed in windows with only a few skylines (e.g. Best et al. 2010; Krug et al. 2012; Clément et al. 2012 and of special important for this thesis Milvang-Jensen et al. 2013). This allows to reach sufficiently deep detection limits to search for Ly α emitters beyond redshifts $z \approx 7$ and a low SFR threshold for the lower redshift emitters.

Broad band selection Using a set of three broadband filters and making use of the characteristics in the spectral energy distributions (SEDs), star-forming as well as passively evolving galaxies can be selected at certain redshifts. Especially important in these selections are the strong breaks, as described in sec. 1.3.2.

An example for this approach is the Lyman break (or dropout) technique used to select high redshift star-forming galaxies. While it was pioneered at redshifts $z \approx 3$ and 4 by Steidel et al. (1999, 2003), it is contemporary used to select such galaxies at redshifts up to $z \sim 10$ (e.g. Bowler et al., 2012; Bouwens et al., 2014). The idea is that a pair of filters with one having a passband above and one below the Lyman break can identify this strong break, and, ideally, a second filter redwards of the break rules out

---

[17] One option is e.g. to use a matched NB filter (e.g. Hayes et al., 2010; Sobral et al., 2012; Nakajima et al., 2012).

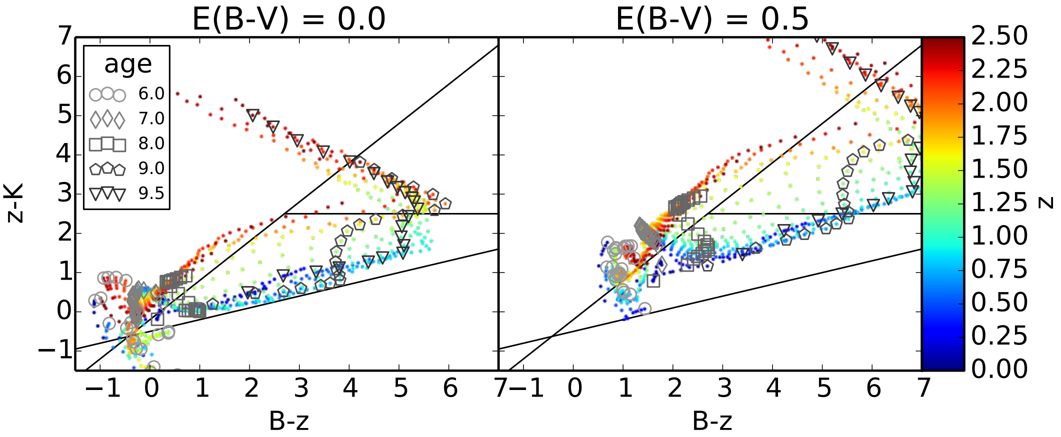

Figure 1.7 BzK selection method to select star-forming and passively evolving galaxies in the redshift range from $1.4 < z < 2.5$ (Daddi et al., 2004). Shown are synthetic magnitudes using BC03 models combined with nebular emission following the description in Ono et al. (2010) over $0 < z < 2.5$ for a range of population ages, starting from very young ages out to the age of the universe at the respective redshifts. A burst of star-formation with an exponentially decaying SFH history with a scale of $\tau = 1$ Myr was assumed. Five (logarithmic) ages are specifically marked
The star-forming galaxies in the target redshift range are above the diagonal line, while the passively evolving galaxies are in the upper right triangle, with little or not contamination from objects at other redshifts. In the right panel, the effect of a substantial dust extinction ($E(B-V) = 0.5$) is shown assuming a Calzetti et al. (2000) law. For BzK, the effect of dust extinction is just a diagonal shift, and hence the star-forming galaxies in the target redshift range are still above the diagonal line even in the case of dust extinction. Lower redshift evolved galaxies would move with the large dust extinction into the region used for selection of such galaxies at the target redshift. However, this is no or a small contamination problem, as passively evolving galaxies usually do not have a significant amount of dust and the models shown are hence rather unrealistic. The reason why the method works so well is that at the specific redshift star-forming galaxies have a relatively blue B-z color, as these two filters probe the Far to NIR UV continuum between Balmer and 4000Å break. On the other hand z-K probes the Balmer break, resulting in a redder z-K color than for galaxies at other redshifts with similar blue B-z colors.

an extremely red galaxy, which could be caused either due to age or more importantly due to strong dust extinction.[18]

Another example for the use of three broadband filters is the BzK technique (Daddi et al., 2004), which allows to select star-forming galaxies and evolved galaxies for the redshift range from $1.4 < z < 2.5$, due to the unique locations of these populations in the (z-K) vs (B-z) space (cf. Fig. 1.7 with some description). Two color selections are very illustrative and can be an easy way to discriminate the different possible redshift solutions in the case of a NB selection (e.g. Kochiashvili et al. 2015 and sec. 5.4 of this thesis). However, while easy too interpret, when observations in a multitude of filters are available, like e.g. in the COMSOS field (Scoville et al., 2007), it makes sense to infer maximum information based on all available data. Therefore, the silver bullet is to find those parametrized theoretical or empirical stellar population template which best fits all available data. When using the technique of SED fitting specifically for determining the most likely redshift, it is referred to as photo-z fitting. In fields like COSMOS, accurate redshift estimations are feasible out to high redshifts (e.g. Ilbert et al., 2013), at least

---

[18] Further contamination candidates are L and T dwarfs, which have sharp breaks in their spectra

for typical galaxy spectra.

When using a selection method it is always important to keep in mind that they are biased towards certain properties. Therefore, these selection criteria should need to be clearly understood and put into perspective to alternative techniques. E.g. when selecting with a NB filter one is selecting for the emission lines, which are a tracer of the instantaneous star-formation rate ($O(10\ Myr)$), while methods making use of the UV continuum or the reprocessed dust emission trace the SFR averaged over a longer time span ($O(100\ Myr)$,Kennicutt 1998). Further, for the NB selection, the mass of previously formed stars is of little importance. Hence, very low mass star-bursting objects can be selected. By contrast, a method like the BzK selection requires a significant detection in three continuum bands and hence a larger threshold stellar mass.

1.4 The journey begins

I will now turn to the three studies of narrowband selected emission-line galaxies.

In the first of these works ("What is the power?", chapter 2), we discuss what can be learned by applying the concepts introduced above to *Himiko*. No, *Himiko* is here not an ancient shaman queen, but a remarkable Ly α emitter at redshift $z = 6.6$, which was found and named by Ouchi et al. (2009). In our study we combined implications from upper limits on rest-frame far-UV lines, which we obtained from extremely deep VLT/XSHOOTER spectroscopy, with results from fitting spectral energy distributions to photometric data. We set out to answer the question: "What is the source of power" for the remarkably strong and extended Ly α emission of this object.

Recent studies have provided strong evidence that weak extended Ly α emission is a generic phenomenon around Ly α emitters (LAE) and star-forming galaxies in general, but the jury is still out. Some Ly α samples seem to show this extended emission, while others do not. As this emission is very weak, it can only be studied through stacking of large samples of LAEs. In chapter 3 ("Together we are deeper") of this thesis, we present a stacking analysis for an independent sample of Ly α emitters at $z = 2.3$.

In the chapter 4 ("The whole is more than the sum of its parts") we apply a unique NB measurement method to a sample of H α emitters at $z = 0.81$, which we selected from the UltraVISTA NB118 data. This measurement technique, which was first developed in my Diplom thesis, makes use of throughput variations between slightly different NB filters, and allows for a redshift and flux estimation significantly more accurate than can be obtained from a generic NB measurement. In the presented work we carefully characterized the method for and through the $z = 0.81$ H α sample.

Finally, I will summarize this thesis in chapter 5. This includes a sneak peak on my currently ongoing projects and my future plans.

2

THE SOURCE OF POWER

Deep rest-frame far-UV spectroscopy of the giant Lyman α emitter ’Himiko’

Johannes Zabl[1], Hans Ulrik Nørgaard-Nielsen[2], Johan P. U. Fynbo[1], Peter Laursen[1], Masami Ouchi[3,4], Per Kjærgaard[5]

[1] Dark Cosmology Centre, Niels Bohr Institute, University of Copenhagen, Juliane Maries Vej 30, 2100 Copenhagen, Denmark
[2] National Space Institute (DTU Space), Technical University of Denmark, Elektrovej, 2800 Kgs. Lyngby, Denmark
[3] Institute for Cosmic Ray Research, The University of Tokyo, 5-1-5 Kashiwanoha, Kashiwa, Chiba 277-8582, Japan
[4] Kavli Institute for the Physics and Mathematics of the Universe (WPI), The University of Tokyo, 5-1-5 Kashiwanoha, Kashiwa, Chiba 277-8583, Japan
[5] Niels Bohr Institute, University of Copenhagen, Juliane Maries Vej 30, 2100 Copenhagen, Denmark

Submitted to Monthly Notices of the Royal Astronomical Society

Abstract

We present deep 10h VLT/XSHOOTER spectroscopy for an extraordinarily luminous and extended Ly α emitter at $z = 6.595$ referred to as *Himiko* and first discussed by Ouchi et al. (2009), with the purpose of constraining the mechanisms powering its strong emission. Complementary to the spectrum, we discuss NIR imaging data from the CANDELS survey.

We find neither for He II nor any metal line a significant excess, with 3σ upper limits of 6.8, 3.1, and 5.8×10^{-18} erg s^{-1} cm^{-2} for C IV λ1549, He II λ1640, C III] λ1909, respectively, assuming apertures with 200 km s^{-1} widths and offset by -250 km s^{-1} w.r.t to the peak Ly α redshift.

These limits provide strong evidence that an AGN is not a major contribution to *Himiko*’s Ly α flux. Strong conclusions about the presence of Pop III star-formation or gravitational cooling radiation are not possible based on the obtained He II upper limit.

Our Ly α spectrum confirms both spatial extent and flux ($8.8 \pm 0.5 \times 10^{-17}$ erg s^{-1} cm^{-2}) of previous measurements. In addition, we can unambiguously exclude any remaining chance of it being a lower

redshift interloper by significantly detecting a continuum redwards of Ly α, while being undetected bluewards.

2.1 INTRODUCTION

An increasingly large number of galaxies is found by their Lyman-α (Ly α) emission in narrowband imaging surveys at redshifts up to $z \sim 7.3$ (e.g. Ouchi et al., 2010; Shibuya et al., 2012)[1]. Searches are ongoing to find Ly α emitters (LAE) at redshifts $z \sim 7.7$ and $z \sim 8.8$ (e.g. Clément et al., 2012; McCracken et al., 2012; Milvang-Jensen et al., 2013), but first results beyond $z \sim 7$ indicate a rapid decline in the fraction of star-forming galaxies showing strong observable Ly α emission (e.g. Konno et al., 2014), in agreement with the low number of Ly α detections in spectroscopic follow-ups for Lyman-break selected galaxies (e.g. Stark et al., 2010; Treu et al., 2013; Caruana et al., 2012, 2014; Pentericci et al., 2014). Such an evolution can be caused either by an increased amount of neutral hydrogen in the vicinity of the galaxies or by a change in galaxy properties, e.g. in the escape of the ionising continuum (e.g. Dijkstra et al., 2014).

Typical LAEs at redshift $z \sim$2–3 are compact and faint (e.g. Nilsson et al., 2007; Grove et al., 2009), but a population of LAEs with emission extending up to 100 kpc has been found (e.g. Fynbo et al., 1999; Steidel et al., 2000; Francis et al., 2001; Nilsson et al., 2006). Currently the most distant object showing characteristics of a Ly α blob (LAB), despite the effects of cosmological surface brightness dimming, is the source *Himiko* found by Ouchi et al. (2009) at a redshift of 6.6 with Subaru/NB921 imaging.

While low surface brightness extended Ly α halos are identified to be a generic property around LAEs (e.g. Steidel et al., 2011; Matsuda et al., 2012), several mechanisms are theoretically proposed to support the much stronger extended Ly α emission of LABs. Each of them might be responsible either alone or in combination. The suggested possibilities include cooling emission from gravitationally inflowing gas (e.g. Haiman et al., 2000; Scarlata et al., 2009; Dekel et al., 2009; Dijkstra & Loeb, 2009; Faucher-Giguère et al., 2010), superwinds produced by multiple consecutive supernovae (e.g. Taniguchi & Shioya, 2000), photo-ionization by AGNs (e.g. Haiman & Rees, 2001), extreme starbursts in the largest overdensities, where the individual galaxies in the proto-cluster are jointly contributing to make up a blob (Cen & Zheng, 2013), and starbursts within major mergers (Yajima et al., 2013a).

Observational evidence from individual objects suggests that several of these mechanisms may contribute. Hayes et al. (2011a) find based on polarisation measurements evidence for Ly α photons to be originating from a central source and being scattered at the surrounding neutral hydrogen. In other cases, evidence for an AGN as a central ionisation source is found directly (e.g. Kurk et al., 2000; Weidinger et al., 2004; Bunker et al., 2003). In a few cases due to the absence of an apparent central ionising source (starburst or AGN) it has been argued for gravitational cooling radiation as the only remaining scenario (Nilsson et al., 2006; Smith & Jarvis, 2007). However, this is a conclusion which can be challenged (Prescott et al., 2015) as halos producing the required amount of cooling radiation would be expected to have a star-forming galaxy at their centre.[2]

Substantial observational efforts have already been devoted to *Himiko* (e.g. Ouchi et al., 2009, 2013; Wagg & Kanekar, 2012). In this paper we present deep VLT/XSHOOTER (Vernet et al., 2011) spectroscopy of this remarkable object, extending over the full range from the optical to the H-band. The main purpose of the observation is to search for other emission lines than Ly α, which helps to shed further light on the origin of the extended Ly α emission. In particular, both a very hot stellar popula-

---

[1] Currently, the spectroscopically confirmed LAE with the highest redshift ($z = 7.5$, Finkelstein et al. 2013) has bee found with HST/WFC3 broad-band data

[2] Prescott et al. (2015) also found a possible ionising source for the Nilsson et al. (2006) object in a hidden AGN offset from peak Ly α emission.

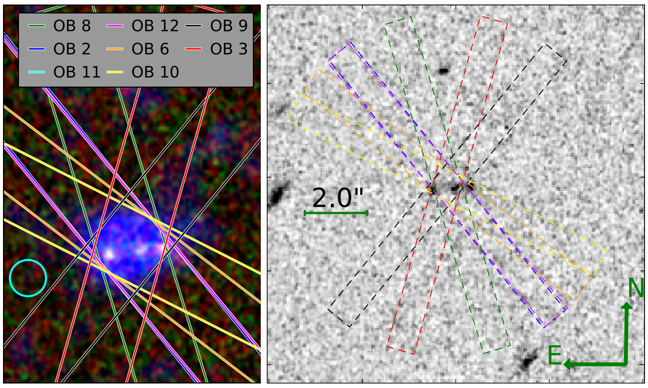

Figure 2.1 Alignment of the slit in the different OBs w.r.t to *Himiko*. A colour composite including CANDELS WFC3 H_{F160W} and J_{F125W} as red and green channels, respectively, and the $NB921$ image as blue channel is shown in the left panel. $NB921$ is a ground based image with a seeing indicated by the $0''.8$ diameter cyan circle. In the right, a larger field is shown. While the left panel shows the $1''.5\text{x}11''$slit, as used in the VIS arm, the right panel shows the $0''.9\text{x}11''$slit as used in the NIR arm. OB11 and OB12 cannot be separated in the plot, as exactly the same position angles were used. The positive slit direction is in all OBs towards the bottom of the figure, so mainly towards the south. The legend lists the OBs in counterclockwise order (along columns).

tion (e.g. Schaerer, 2002; Raiter et al., 2010), as expected for a metal-free Population III (Pop III), and gravitational cooling radiation (e.g. Yang et al., 2006) would give rise to relatively strong He II λ1640 emission. By contrast, due to preceding metal-enrichment, an AGN is expected to display in addition to He II high-ionisation emission lines from C, Si or N. We supplement the spectroscopic data by analysing CANDELS J_{F125W} and H_{F160W} archival imaging (Grogin et al., 2011; Koekemoer et al., 2011).

In section 2.2.1, we describe our spectroscopic observations, while we give details about the data reduction in section 2.2.2, followed by a discussion of the photometry done on archival data (sec. 2.2.3). Results for the Ly α spatial distribution, the spectral rest-frame UV continuum, Ly α flux and profile, and non-detection limits for the rest-frame far-UV lines are presented in sections 2.3.1 through 2.3.4. Subsequently, we discuss in sections 2.4.1 and 2.4.2 implications from the broadband SED, in section 2.4.3 a possible interpretation of the Ly α shape, and finally and most important in section 2.4.4 the implications from our non-detection limits for the mechanisms powering *Himiko*.

Throughout the paper a standard cosmology ($\Omega_{\Lambda,0} = 0.7$, $\Omega_{\mathrm{m},0} = 0.3$, $H_0 = 70\,\mathrm{km\,s^{-1}}$) was assumed. All stated magnitudes are on the AB system (Oke, 1974). Unless otherwise noted, all wavelengths are converted to vacuum wavelengths and corrected to the heliocentric standard. A size of $1''$ corresponds at $z = 6.595$ to a proper distance of 5.4 kpc. The universe was at that redshift 800 Myr young. When stating in the following ‘He II’, ‘C IV’, ‘C III]’, and ‘N V’, we are referring to He II λ1640, C IV $\lambda\lambda$1548, 1551, [C III]C III] $\lambda\lambda$1907, 1909, and N V $\lambda\lambda$1239, 1243, respectively.

2.2 DATA

2.2.1 SPECTROSCOPIC OBSERVATIONS

The XSHOOTER data has been taken at VLT-UT2 (Kueyen) in the second half of the nights starting on 2011 September 2, 3, and 4, subdivided into nine different observing blocks (OB) with integration and observing times summarised in table 2.1. We used the same set of slits for XSHOOTER’s three spectral

Table 2.1 Exposures and exposure times per observing block are listed. Except in OB1 and OB9, exposures were taken with 1200s both in the VIS and UVB arm. In the NIR, each of the exposures was split into two sub-integrations with half the exposure time (e.g. 1200s VIS ⇒ 2x600s NIR). Where not all exposures could be used for the reduction due to passing clouds, both the used and the total number are stated. Numbers in square brackets indicate a differing number of frames used in the NIR reduction.

Date	Obs. Block	# VIS exp.	exp. time[s]	conditions
02.09	OB_H_1-1	0/1	0/1169.7	TK
	OB_H_1-2	4	4800	TN/CL
	OB_H_1-3	2	2400	TN
Summary 02.09:		6/7	7200/8369.7	
03.09	OB_H_1-6	4	4800	TN [1]
	OB_H_1-8	4	4800	TN
	OB_H_1-9	2	[0] 1880 [2]	CL
Summary 03.09:		10/10	[9600] 11480/11480	
04.09	OB_H_1-10	6	7200	CL
	OB_H_1-11	6	7200	CL
	OB_H_1-12	2	2400	CL
Summary 04.09:		14	16800	
Complete Summary:		30/31	[33600]35480 ([9.3]9.9hrs)	

[1] TK E @40° [2] Two exposures were taken with 940 s exposures (VIS) and 2x470 s (NIR). For the NIR reduction, we did not use the 470 s exposures.

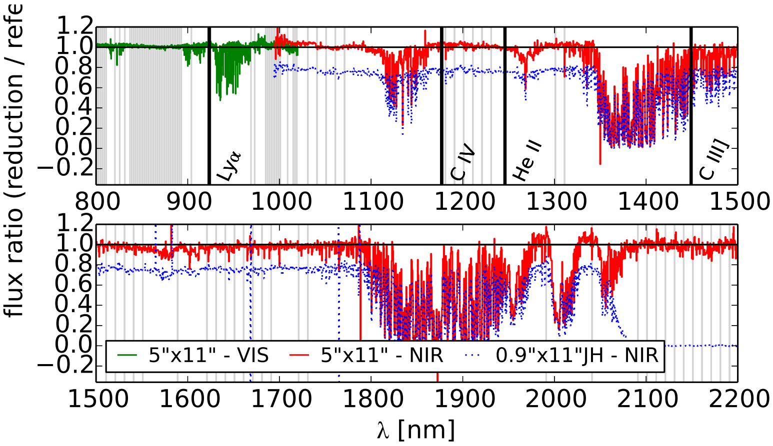

Figure 2.2 Accuracy of flux calibration based on cross-calibrating the spectro-photometric standard LTT7987, taken on September 4, against the response function from our main standard Feige110, taken on the night before. The shown curve gives the ratio between the measured LTT7987 flux and its expectation. In the NIR, results are included both for an observation using the same 5″x11″ slit for LTT7987 and Feige110 and for and observation of LTT7987 with the 0.9″x11″JH slit. Thin vertical lines indicate wavelengths used by the pipeline for fitting a spline.

arms throughout: 1″.6x11″ (UVB), 1″.5x11″ (VIS), and 0.9″x11″JH (NIR), which is a slit including a filter blocking wavelengths longer than 2.1 μm, effectively reducing the impact of scattered light in the NIR spectra. All used data was taken under atmospheric conditions classified as either thin (TN) or clear (CL). After excluding OB1 for being affected by thick clouds, the total usable exposure time was 35480 s. In our NIR reduction, we used only frames with the same exposure time of 600 s, resulting in a slightly smaller total time of 33600 s.

Acquisition on our target's narrowband image (NB921; Ouchi et al. 2008, 2009) centroid in the slit's centre was obtained through a blind offset from a star located $48''.14$ west and $8''.99$ north. We can claim that the pointing accuracy, at least along the slit, was in each of the OBs better than $0''.1$, as can be concluded from the spatial centroid of Ly α in each of the OBs (cf. Table. 2.2). As the NIR is observed in XSHOOTER simultaneously with Ly α in the VIS, we exclude the option of non-detections due to pointing problems.

Spectra were taken with a nod throw of $5''.0$ and a jitter box size of $0''.5$, allowing for an optimal skyline removal. In order to minimise the slit loss, the position angle was set to the parallactic angle at the start of each OB. This is mainly relevant in the NIR, as the VIS and UVB arms are equipped with atmospheric dispersion correctors. The corresponding position angles are shown in Fig. 2.1.

Assuming that emission lines are co-aligned with one or all of the three continuum bright sources, our decision to use the parallactic angle might have resulted in a higher than necessary slit-loss. This can be seen from Fig. 2.1 (right). At the time of the observations no HST/WFC3 data was available.

As *Himiko* is not a point source, it is not possible to measure the seeing directly from the Ly α spectrum. Therefore, we extracted it from the information provided in the FITS header for the seeing measured by the image analysis detector. [3] Corrected to both airmass of the observations and the observed wavelength of Ly α and averaged over sub-integrations, we get a seeing in the individual OBs between $0''.6$ and $0''.8$ (FWHM; Table. 2.2), with a mean value of $0''.65$ for the stacked OBs, or $0''.61$ corrected to the He II wavelength.

2.2.2 DATA REDUCTION

We performed our final reduction using XSHOOTER pipeline version 2.3.0 (Modigliani et al., 2010), where we made a small modification to the pipeline code. This was to additionally mask all pixels neighbouring those pixels identified by the pipeline as cosmic ray hits. Without this precaution, artefacts remain in the stack, which are not indicated in the pipeline quality map. Otherwise, we used mainly standard parameters.

The echelle spectrum was rectified to a pixel size of 0.4 Å and 1 Å in wavelength direction and $0''.16$ and $0''.21$ in slit direction for VIS and NIR arm, respectively. We are only making use of the spectra from XSHOOTER's VIS and NIR arm, as the wavelength range covered by the UVB arm does not contain any information for this object.

While we obtained our final NIR reduction by automatically combining all frames with the pipeline using the nodding recipe,[4] we could improve the result in the VIS reduction somewhat by using our own script. In the latter case we first reduced the VIS frames in nodding pairs with the pipeline, and then combined the frames based on a weighted mean, using the inverse square of the noise maps produced by the pipeline as weights.

A nodding reduction is commonly considered as essential for a good skyline subtraction in the NIR. Nevertheless, we tried also a stare reduction both in the VIS and the NIR, which could give in an idealised case a $\sqrt{2}$ lower noise. In the case of the NIR spectrum, where the use of dark frames taken with the same exposure time as the science frames is necessary for a stare reduction, we used a large enough number of

---

[3] FITS header keyword: *HIERARCH ESO TEL IA FWHM*; available for each sub-integration

[4] *xsh_scired_slit_nod*

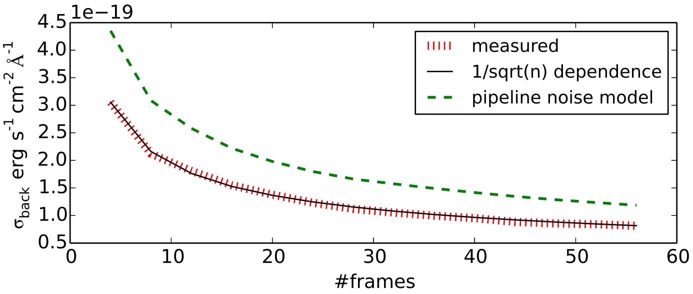

Figure 2.3 Pixel to pixel noise in skyline free regions close to the expected wavelength of He II in the NIR arm. We have successively added 4 frames corresponding to 2 nodding positions to the stack and calculated the $\kappa - \sigma$ ($\kappa = 4$) clipped standard deviation for each of the steps. The result is the solid line. The dotted line shows the noise level as expected from a $1/\sqrt{N}$ dependence based on the noise in the first step (4 frames). It is perfectly in agreement with the data. In addition, the noise prediction from the pipeline noise-model is include.

these to not be limited by their noise.[5]

While the stare reduction worked for the VIS arm, we experienced in the deep NIR stack spatially abruptly changing residual structures, which we could not safely remove by modelling with slowly changing functions. Consequently, we had to decide that a safe stare reduction was not feasible at this point.

By contrast, the pixel to pixel noise decreases as expected with the square root of the number of exposures in the case of the nodding reduction, as shown in Fig. 2.3 for a region around the expected He II line and using only pixels not affected by skylines and bad pixels. Reassuringly, this indicates that the structure seen in the stare reduction is at least within the individual nodding sequences temporarily stable and therefore removed by the nodding procedure. In the relevant VIS arm wavelength range redwards of Ly α, being affected by telluric emission lines and hence requiring a robust sky subtraction, we decided finally to also a use a nodding reduction.

In addition to those pixels flagged as bad in the pipeline, we masked skylines, which we automatically identified by iterative sigma clipping against emission in a stare reduced and non-background subtracted spectrum, and pixels with unexpected high noise, defined as having absolute counts larger than 10 times the 1 σ error. Except in the region of Ly α, where we did not mask these pixels, this assumption is safe in not clipping away any source pixels. Additionally, when determining the S/N within extraction boxes over a certain wavelength region, we excluded those parts of the spectrum with a noise either 1.5 times or 2.0 times larger than the minimal noise within 200 Å of the region's centre. The decision between 1.5 and 2.0 was made based on the amount of pixels remaining for the analysis.

Comparing the calculated pixel to pixel noise to the prediction from the pipeline's noise model, we find for the stack of all 56 NIR frames a rms noise of $1.2{\times}10^{-19}$ erg s^{-1} cm^{-2} Å^{-1} per pixel, while the direct pixel to pixel variations have a standard deviation of 8.1×10^{-20} erg s^{-1} cm^{-2} Å^{-1}. As we are using the error spectra based on the pipeline throughout this paper, stated uncertainties for several quantities might be overestimates. On the other hand, there is correlation in the spectrum due to the rectification, which is difficult to quantify, especially as it varies with the position in the spectrum. A full characterization of the noise would require the propagation of the covariance matrix (e.g. Horrobin et al., 2008), which is currently not available in the pipeline.

The instrumental resolution at the position of Ly α and He II was determined based on fitting Gaus-

---

[5] As ESO does not take by default enough dark frames for such deep observations, we needed to use frames from several days around the observations for this test. In the nodding reduction used for our result no dark frames are required.

sians to nearby skylines. We get in the two cases R=5300 (56 $\mathrm{km\,s^{-1}}$) and R=5500 (55 $\mathrm{km\,s^{-1}}$), respectively.

For the determination of the response function, we used a nodding observation of the standard star Feige110 taken with 5″ slits during the night starting on the 2011 September 3, directly before beginning with the observation of OB_*Himiko*_1-6. We used this response function for all OBs taken within the three nights. In the pipeline, the response function is obtained by doing a cubic spline interpolation through knots at wavelengths having atmospheric transmission close to 100 per cent. For ensuring a very good response function close to Ly α, we had to remove a knot at 9270 Å and add instead another one at 9040 Å.

In order to avoid possible issues of temporal variability of the NIR flat-field illumination, we decided to use the same flat-field observations both for the standard star and the science frame observations, even though they were taken with different slits.[6] Stability and accuracy of the response function were tested by calibrating an observation of the flux standard LTT7987, taken in the second night of our program, based on the response function determined from Feige110 in the first night. The result of this test is shown in Fig. 2.2.[7] We can conclude that the accuracy of the spectrophotometry is about 5 per cent.

In order to reach the maximum possible depth for our science frames, we mainly avoided spending time on telluric standards. Only in the beginning of the observations in the first night we took one telluric standard with the same slit set-up as chosen for our science observations. We used this frame to fit a model telluric spectrum with ESO's MOLECFIT package (Smette et al., 2015), using the input parameters suggested in Kausch et al. (2015). Based on the obtained atmospheric parameters, we created model telluric spectra for the airmass of each individual nodding pair. For the second and third night, we used telluric standards taken for other programs right before the start of our observations to fit the atmospheric parameters. While these observations were based on differing slits, we could use the wavelength solution and line kernel obtained for night one to create appropriate telluric spectra for nights two and three. While we need to make the strong assumption of constant atmosphere over a time-scale of several hours, being unlikely completely correct, the obtained accuracy is appropriate for our purpose. In the case of the optimal combining for the VIS spectrum, we weighted the telluric contributions in the same way as the science spectrum. Errors were adjusted correspondingly.

All 1D spectra were extracted from the rectified 2D frames. As there is no detectable trace in the NIR spectrum, we needed to assess the accuracy of the position of the trace in the rectified frame based on a check on the reduced standard star. We find that the centre of the trace does not differ more than one pixel in slit direction from the expected position over the complete range of the NIR arm.

2.2.3 PHOTOMETRY ON ARCHIVAL DATA

As located in the Subaru/*XMM-Newton* deep field, *Himiko* is covered both by very deep ground and space based imaging, from X-ray to radio, including the $NB921/Subaru$ narrowband image, which allowed to identify *Himiko* as a giant Ly α emitter (Ouchi et al., 2009).

Deep *HST* imaging is available from the CANDELS survey (Grogin et al., 2011; Koekemoer et al., 2011). This includes data from ACS/WFC in V_{F606W} and I_{F814W} and in J_{F125W} and H_{F160W} with WFC3. We performed in this work photometry on the CANDELS data.

It is noteworthy, that recently, both Jiang et al. (2013a) and Ouchi et al. (2013) have published photometry in J_{F125W} and H_{F160W} based on two other observations (*HST* GO programs 11149, 12329, 12616 and GO 12265, respectively), supplemented by deep IRAC 1 & 2 data from *Spitzer*/IRAC SEDS (Ashby

---

[6] Based on comparing different flat-fields we concluded that the throughput of the K-blocking filter in the 0.9x11JH slit is in the J-Band $\gtrsim$ 97 per cent.

[7] We have used the reference spectra from pipeline version 1.5.0, as those from pipeline 2.3.0 do not allow for cross calibrations of the same quality.

Table 2.2 Results of a Gaussian fit to the spatial Ly α profiles as measured in the individual OBs (cf. Fig. 2.5) and the stacked spectrum. The 'centre' column gives the displacement w.r.t to the expected position. In addition, the seeing of the individual OBs, corrected to observed wavelength and airmass, is stated.

OB	centre	FWHM (fit)	seeing	$f_{\mathrm{Ly}\,\alpha}$
	” (slit)	” (slit)	”	10^{-17} erg s^{-1}/cm^2
OB 2	−0.01 ± 0.04	1.24 ± 0.08	0.64	6.1 ± 0.5
OB 3	−0.14 ± 0.07	1.43 ± 0.16	0.58	6.4 ± 0.6
OB 6	−0.07 ± 0.04	1.25 ± 0.10	0.77	6.1 ± 0.5
OB 8	−0.03 ± 0.05	1.23 ± 0.12	0.58	5.6 ± 0.4
OB 9	−0.03 ± 0.08	1.51 ± 0.20	0.60	6.5 ± 0.8
OB 10	−0.08 ± 0.04	1.60 ± 0.08	0.78	6.2 ± 0.4
OB 11	−0.05 ± 0.02	1.26 ± 0.06	0.59	6.2 ± 0.4
OB 12	−0.01 ± 0.05	1.20 ± 0.11	0.62	6.2 ± 0.6
all OBs	−0.02 ± 0.02	1.32 ± 0.04	0.65	6.1 ± 0.2

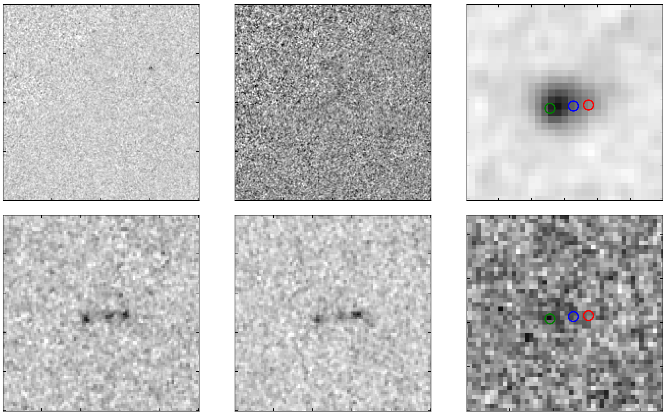

Figure 2.4 Images in following filters in the stated order: V_{F606W}, I_{F814W}, $NB921$, J_{F125W}, H_{F160W}, UKIDSS/UDS K. The images are scaled for optimal viewing from $-3 \times \sigma$ to $1.1 \times max$, where σ and max are the standard deviation and maximum value of the pixels within a circular annulus around the source, respectively. Green, blue, and red circles refer to the three sources visible in the J_{F125W} and H_{F125W} images.

et al., 2013). Especially the analysis of Ouchi et al. (2013) has been targeted at studying *Himiko*, including additional WFC3/$F098M$ intermediate band data allowing to identify peaks in the Ly α distribution and ALMA [ionCII] observations.

Ground based near-infrared (NIR) data in J, H, and K is available from the ultra-deep component (UDS) of the *UKIRT Infrared Deep Sky Survey* (UKIDSS; Lawrence et al. 2007). We are using the UKIDSS data release 8 (UKIDSSDR8PLUS), which has significantly increased depth compared to previous releases.[8]

For our SED fitting in section 2.4.1, we are using NIR photometry determined by us from the CANDELS and the UKIDSS data and supplement it by the IRAC SEDS (1&2) and IRAC SpUDS (3&4) (Dunlop et al., 2007) photometry presented by Ouchi et al. (2013).

---

[8] http://www.nottingham.ac.uk/astronomy/UDS/data/dr8.html

Table 2.3 Magnitudes in $0''.4$ diameter apertures on the CANDELS *HST* images are stated for the three distinct continuum sources identified with *Himiko* (cf. Fig. 2.1). No aperture corrections are applied. The stated UV slope β ($f_\lambda \propto \lambda^\beta$) is based on the estimator $\beta = 4.43(J_{F125W} - H_{F160W}) - 2$ (Dunlop et al., 2012). Upper limits are $1\,\sigma$ values.

	Himiko–E	*Himiko–C*	*Himiko–W*
R.A.	$+2^h17'57''.612$	$+2^h17'57''.564$	$+2^h17'57''.533$
Dec	$-5°08'44''.90$	$-5°08'44''.83$	$-5°08'44''.80$
V_{F606W}	> 29.53	> 29.53	> 29.53
I_{F814W}	28.45 ± 0.64	> 29.02	28.52 ± 0.68
J_{F125W}	26.47 ± 0.07	26.66 ± 0.10	26.53 ± 0.09
H_{F160W}	26.77 ± 0.12	26.97 ± 0.15	26.49 ± 0.10
$J - H$	-0.30 ± 0.14	-0.31 ± 0.18	0.04 ± 0.13
β	-3.33 ± 0.62	-3.37 ± 0.80	-1.82 ± 0.60

We determined magnitudes in several apertures on all optical and NIR images with SExtractor's double image mode (Bertin & Arnouts, 1996), with CANDELS J_{F125W} as detection image. Without unwanted resampling, it is due to the requirement of the same pixel scale in double mode not directly possible to use any of the images as detection image. Therefore, we put fake-sources at the determined positions in images with the appropriate pixel scale and used these as detection images. As the UKIDSS photometric system is in VEGA magnitudes, we use the VEGA to AB magnitude corrections of 0.938, 1.379, 1.900 as stated in Hewett et al. (2006) for J, H, and K, respectively.

Consistent with the visual impression (Fig. 2.1), we detect in the J_{F125W} image three distinct sources at the position of *Himiko*. We refer in the following to these sources as *Himiko–E* (east), *Himiko–C* (centre), *Himiko–W* (west). Their coordinates are stated in table 2.3. The transverse distance between *Himiko–E* and *Himiko–W* is $1''.18$ (6.4 kpc), while the distance between *Himiko–C* and *Himiko–W* is $0''.46$ (2.5 kpc).

In order to obtain accurate error estimates for the fluxes measured within circular apertures, [9] we determined several measurements with apertures of the same size as used for the object, but in non-overlapping source free places. For images exhibiting correlated noise, as being the case for the drizzled or resampled mosaic images used for our analysis, this is the appropriate way to account for the correlation. From the κ-σ clipped standard deviation of these empty-aperture measurements, we obtained the $1\,\sigma$ background limiting flux in the chosen aperture. The clipping with a $\kappa = 2.5$ and 30 iterations makes sure that apertures including strong outlying pixels or which despite the method to find source free places are not really source free are rejected.

We defined source free regions based on the SExtractor segmentation maps and masking of obvious artefacts like spikes or blooming. In addition, we made sure that the used regions have approximately the same depth as the region including *Himiko*. Depending on the available area, we have between 26 and 190 non overlapping empty apertures.

Safely assuming that the noise for the objects is not dominated by the objects, we use these values as errors on the determined fluxes. All stated magnitude errors have been converted from the flux errors by the use of:

$$\sigma_{mag} = 1.0857 \frac{\sigma_{flux}}{flux} \tag{2.1}$$

---

[9] SExtractor keywords (FLUX_APER / MAG_APER)

Table 2.4 Magnitudes as measured in 2″ apertures for the CANDELS/*HST* and the UKIDSS/UDS data. In addition the *Spitzer*/IRAC measurements from Ouchi et al. (2013) are included. First and second column list measurements without aperture correction and the corresponding 1 σ errors. Magnitudes after applying aperture corrections are stated in the third column. Upper limits are 1 σ values. β is calculated as in Table. 2.3.

Filter	Mag (2”)	σ Mag (2”)	Total magnitude
V_{F606W}	>27.47	–	>27.47
I_{F814W}	>26.77	–	>26.78
J_{F125W}	24.71	0.13	24.71
J	25.23	0.26	25.09
H_{F160W}	24.93	0.15	24.93
H	>25.59	–	>25.44
K	24.84	0.22	24.72
$3.6\mu m$ [1]	–	0.09	23.69
$4.5\mu m$ [1]	–	0.19	24.28
$5.8\mu m$ [1]	–	–	>23.19
$8.0\mu m$ [1]	–	–	>23.00
β	-3.0 ± 0.9		

[1] Measurements taken from Ouchi et al. (2013).

In table 2.3, measurements within 0″.4 diameter apertures centred on each of the three peaks are listed for the *HST* images, while magnitudes within 2″.0 apertures are stated for all used images in table 2.4. In the latter case, the apertures are centred on the same position as that stated in Ouchi et al. (2009, 2013). In addition, aperture corrected magnitudes are included. To calculate the appropriate aperture corrections for the images with larger PSFs, we assumed that in all the considered bands the flux is coming from the three main sources and that the flux ratio between the three peaks is the same as in the J_{F125W} *HST* image. This allows us to convolve this flux distribution with the PSF[10] and consequently determine the fraction of the total flux included in the aperture on the created fake image by using SExtractor in the same way as for the science measurements. For the PSF profiles, we assume in the case of the UKIRT/WFCAM NIR images Gaussians determined by a fit to nearby stars. We get for *J*,*H*,*K* FWHMs of 0″.74, 0″.74, and 0″.69, respectively.

Finally, tables 2.3 and 2.4 also include the UV slope β ($f_\lambda \propto \lambda^\beta$). We calculated it based on the estimator $\beta = 4.43(J_{F125W} - H_{F160W}) - 2$ (Dunlop et al., 2012). Both the total object and the two eastern components seem to have very steep slopes of -3.0 ± 0.9, -3.3 ± 0.6, -3.4 ± 0.8, respectively. However, the uncertainties are large.

Interestingly, there seems to exist a tension between the J_{F125W} in the data used by us (CANDELS) and that obtained by Ouchi et al. (2013) with 24.71 ± 0.13 and 24.99 ± 0.08, respectively. This corresponds to a difference of about 1.8 σ. Consequently, they infer a less steep slope of $\beta = -2.00 \pm 0.57$. While Jiang et al. (2013a) have not derived magnitudes for the three individual sources, their total magnitude is with 24.61 ± 0.08 deviating even more. However, they have been using SExtractor *MAG-AUTO* measurements. Therefore, the comparison between their values and those derived by Ouchi et al. (2013) and us should be treated with caution. On the other hand, the ground based UKIDSS J magnitude is with 25.09 ± 0.26 closer to the value obtained by Ouchi et al. (2013).

The greatest difference between the CANDELS data and that from Ouchi et al. (2013) is in the central

---

[10] We created fake images with the IRAF task *mkobjects*

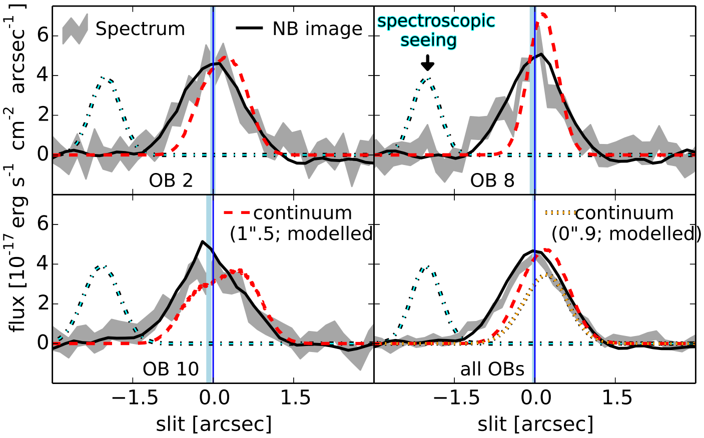

Figure 2.5 Ly α spatial profiles for three individual example OBs (2, 8 and 10) and for the complete stack. Included are profiles directly extracted from the spectrum over the wavelength range from 9227 to 9250 Å and profiles extracted from images under the assumption of the $1''.5$ slit. The latter is shown both for the NB921 image and a J_{F125W} image, which was corrected to the seeing of the individual spectroscopic OBs. Finally, for the stack the expected continuum profile is also shown for the $0''.9$ slit.

component. They get from their data 27.03 ± 0.07 and we derive 26.66 ± 0.10. A subjective visual inspection of the Jiang et al. (2013a) data seems to rather confirm the relatively blue colour in the central blob.

For all stated coordinates, we use the world coordinate system as defined in the CANDELS J_{F125W} image (J2000). We find that this coordinate system is slightly offset w.r.t to the coordinate system used by Ouchi et al. (2009). Their coordinate[11] corresponds to RA, DEC = $+2^h17'57''.581$, $-5^\circ08'44''.72$ in the CANDELS F125W astrometric system. The UKIDSS data appears within the uncertainties well matched to the CANDELS astrometry. Therefore, we do not apply any correction here. Fig. 2.1 (left) includes a R,G,B composite using H_{F160W}, J_{F125W} (both CANDELS), and $NB921$, respectively. Cutouts around the position of *Himiko* for all used images are shown in Fig. 2.4.

2.3 RESULTS

2.3.1 SPATIAL FLUX DISTRIBUTION AND SLIT-LOSSES

The different observing blocks (OBs) taken with different position angles allow to compare the spatial extent of Ly α along the slit to the $NB921$ image for several orientations. To do so, we extracted for each OB a Ly α spatial profile averaged over the wavelength-range from 9227 to 9250 Å, and replicated this for the $NB921$ image by assuming an aperture with the shape of the $1''.5$ slit and calculating a running mean over pseudo-spatial bins of $0''.2$. It should be kept in mind that the $0''.8$ FWHM seeing of the $NB921$ image (Ouchi et al., 2009) is slightly larger than that in the different OBs of our spectral data (cf. Table. 2.2), but almost comparable.

We quantified the centroid and spatial width of Ly α in each of the individual OBs by fitting Gaussians to the spatial profiles. Resulting values and the integrated Ly α flux over the same range are stated in Table 2.2. The centroids imply an excellent pointing accuracy.

For comparison, the expected spatial profile for the continuum within the slit was estimated based

---

[11] RA, DEC = $2^h17'57''.563$, $-05^\circ08'44''.45$ for the centroid of the Ly α emission

on fake J_{F125W} images (cf. Section 2.2.3), convolved with the appropriate seeing for each OB. All three profiles are shown for three example OBs (2, 8, and 10) in Fig. 2.5.

The profiles extracted from the spectrum are as expected in good agreement with the $NB921$ image. For those OBs, like OB8, which are nearly perpendicular to the alignment of the three individual sources, the Ly α profile is significantly more extended than the estimated continuum profile. The main excess in the emission seems to be towards the north. On the other hand, for those OBs like OB10, with the slit aligned closer to the east-west direction, there seems to be an offset of the continuum towards the west. This indicates extended Ly α emission more concentrated on the eastern parts, in agreement with the F098M/WFC3 observations of Ouchi et al. (2013).

Finally, in the lower right panel of Fig. 2.5 the spatial profile of the combined Ly α stack is shown, where the $NB921$ and continuum profiles have been calculated as the average of all contributing frames with their respective position angles. Here, we are showing in addition the profile as expected for the continuum based on the $0''.9$ slit. Noteworthy, we expect the continuum offset with $0''.2$ towards positive slit directions w.r.t to the Ly α centroid being in our slit centre.

Slit-losses both for Ly α and the continuum and both for the $0''.9$ and the $1''.5$ slits were calculated based on the NB921 or the seeing convolved fake J_{F125W} image by determining the flux fraction within slit-like extraction boxes. Identical to the profile determination, we treated the individual OBs separately, and simulated the stack, by combining the slit-losses for the individual OBs weighted with the appropriate exposure times.

Assuming the $1''.5$ VIS arm slit and an extraction width of $4''$ along the slit, being close enough to no loss in slit-direction, results in a slit loss factor of 0.67 (0.44 mag) for Ly α based on the NB921 image.

For the expected continuum distribution we determined the optimal extraction-mask size under the assumption of background limited noise, by maximising the ratio between enclosed flux and the square root of the included pixels. The maximum value is reached in the $1''.5$ VIS slit between 7 and 9 pixels, when keeping the centre of the extraction mask at the formal centre of the slit. For an eight pixel ($1''.28$) extraction width, we derive a slit loss factor of 0.74 (0.32 mag).

The spatial distribution for possible He II or metal line emission is not known. Therefore, we consider hypothetically both the cases that it is co-aligned with the continuum or with the Ly α emission. Assuming the two distributions, we obtain optimal extraction widths around six and eight pixels ($1''.26$ and $1''.68$), respectively, fixing the trace centre at the formal pointing position in both cases. As a compromise, we assumed for the default extraction a width of seven pixels, corresponding in the continuum and the $NB921$ case to slit loss factors of 0.53 (0.69 mag) and 0.38 (1.04 mag), respectively. Certainly, alternative scenarios are possible which could lead to lower or higher slit-losses, e.g. if line emission would be originating mainly from the central or the western-most source, respectively.

2.3.2 SPECTRAL CONTINUUM

We made the continuum hidden in the noise of the rectified full resolution spectrum visible by strongly binning the telluric corrected 2D spectrum in wavelength direction from an initial pixel scale of 0.4 Å pixel^{-1}, as produced with the pipeline, to a pixel scale of 11.2 Å pixel^{-1}. Instead of taking a simple mean of the pixels contributing to the new wavelengths bins, we calculated an inverse variance weighted mean, with the variances taken from the pipeline's error-spectrum. This allows to obtain a low resolution spectrum with relatively high S/N in a region strongly affected by telluric emission or absorption. One caveat with this approach is that the flux is not correctly conserved for wavelength ranges where both the flux density and the noise changes quickly, which is the case at the blue side of the Ly α line (cf. Fig. 2.7). Therefore, we used for our binned spectrum a simple mean in the region including Ly α.

A faint continuum is in the resulting spectrum clearly visible redwards of Ly α and due to IGM

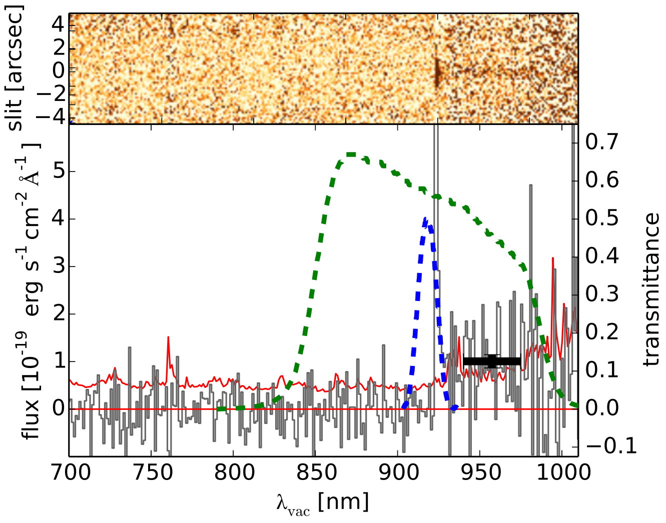

Figure 2.6 VIS spectrum telluric corrected and binned to a pixel scale of 11.2 Å pixel^{-1}. Instead of a simple mean of the pixels contributing to the new wavelengths bins, we calculate (see sec.). Included are the response profiles for the Subaru *NB*921 and z' filters. The trace is shown in black, while the red curve is the error on the trace. The black error bar shows the continuum level from the spectrophotometry. No heliocentric velocity correction was applied for this plot.

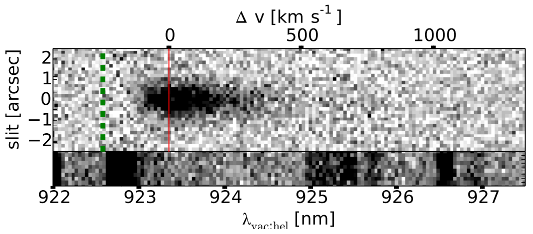

Figure 2.7 2D Ly α spectrum. The green dashed and solid red vertical lines are at the same wavelengths as in Fig. 2.8. Below, a non-background removed spectrum is shown for the same wavelength range, indicating positions of skylines.

scattering not bluewards, as expected for *Himiko*'s redshift (Fig. 2.6). A similar effort in the NIR did not reveal an unambiguous continuum detection.

The detection allows to directly determine the continuum flux density close to Ly α. For the interval from 9400 to 9750 Å (1238 to 1285 Å rest-frame), chosen to be in a region with comparably low noise in our optimally rebinned spectrum, we get with the $1''.28$ extraction mask a flux density of $10.1 \pm 1.4 \times 10^{-20}$erg s^{-1} cm^{-2} Å^{-1} (cf. Fig. 2.6). We used in the calculation a κ–σ clipping with a $\kappa = 2.5$, rejecting one spectral bin.

This is equivalent to an observed magnitude of 25.18±0.15, or after applying the aperture correction of 0.32 mag, of 24.85 ± 0.15, corresponding to a rest-frame absolute magnitude of $M_{1262;AB} = -21.99 \pm 0.15$. The magnitude is slightly fainter than the CANDELS J_{F125W} measurement (24.71 ± 0.13) and slightly brighter than the H_{F160W} magnitude (24.93 ± 0.15), but within the errors consistent with both of them.

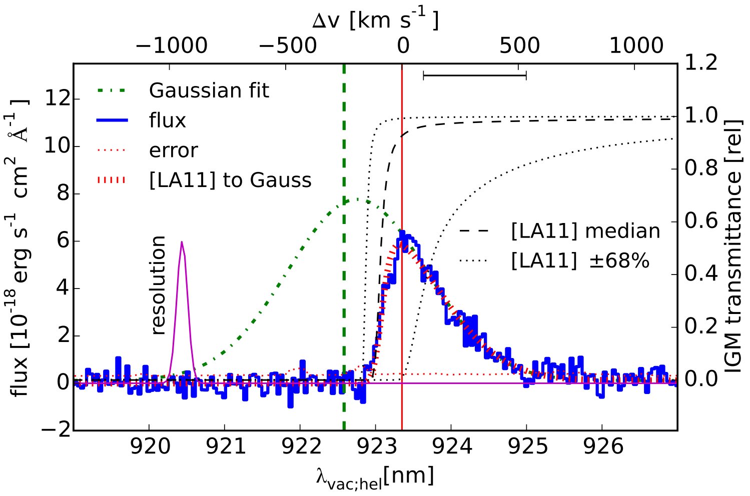

Figure 2.8 Extracted Ly α spectrum based on the stack of all OBs (solid blue). The orange dotted curve gives the errors on the flux density. Red solid and dashed green vertical lines mark the peak of the Ly α line and a velocity offset of $-250\,\mathrm{km\,s^{-1}}$, respectively. The green dot-dashed curve is a fit to the red wing of the Ly α line with the centroid fixed as an example to $-160\,\mathrm{km\,s^{-1}}$. A wavelength range as shown by the bar in the upper right corner was included in the fit. In addition, both the median and the ±68% intervals for the IGM transmission from Laursen et al. (2011) [LA11] at this redshift is plotted. As a test, we have applied the median transmittance to the Gaussian fit, shown as red dashed line. Finally, the magenta Gaussian in the left indicates the instrumental resolution.

2.3.3 Ly α

The final 2D VIS spectrum in the wavelength region around Ly α is shown in Fig. 2.7, from which we extracted the 1D Ly α spectrum. This was done in an optimal way (Horne, 1986), using a Gaussian fit to the spatial profile. The resulting 1D spectrum is plotted in Fig. 2.8. As a sanity check, we compared this result to extractions based on simple apertures of different widths. Large enough apertures converged within the errors to the result from the optimal extraction.

We determined several characteristic parameters of the directly measured Ly α line. All stated errors are the 68 per cent confidence intervals around the directly measured value based on 10000 MC random realisations of the spectrum using the error spectrum. It needs to be noted that this approach overestimates the uncertainties, as the noise is added twice, once in the actual random process of the observation and once through the simulated perturbations. This means that the resulting perturbed spectra are effectively representations for a spectrum containing only half the exposure time. Yet, the values based on this simple approach allow to get a sufficient idea of the accuracy of the determined parameters. A discussion about the loss of Ly α flux in the IGM is presented in sec. 2.4.3.

The pixel with the maximum flux density is at a $\lambda_{\mathrm{vac;hel}}$ of $9233.5^{+1.2}_{-0.4}$ Å. This corresponds to a redshift of $6.5953^{+0.0010}_{-0.0003}$.[12] The peak Ly α redshift, z_{peak}, is due to Ly α radiative transfer effects likely different from the systemic redshift of the ionising source (cf. sec. 2.4.3). For the FWHM of the line we measure $286^{+13}_{-25}\,\mathrm{km\,s^{-1}}$. Ouchi et al. (2009) get for their Keck/DEIMOS spectrum a z_{peak} of 6.595 and a FWHM of $251 \pm 21\,\mathrm{km\,s^{-1}}$, consistent with our result.

Furthermore, we calculated the skewness parameters S and S_w (Kashikawa et al., 2006). For a wavelength range from 9227 to 9250 Å we get values of 0.69 ± 0.07 and $12.4^{+1.4}_{-1.8}$Å for S and S_w, respec-

---

[12] Ly α: $\lambda_{rest} = 1215.7$ Å

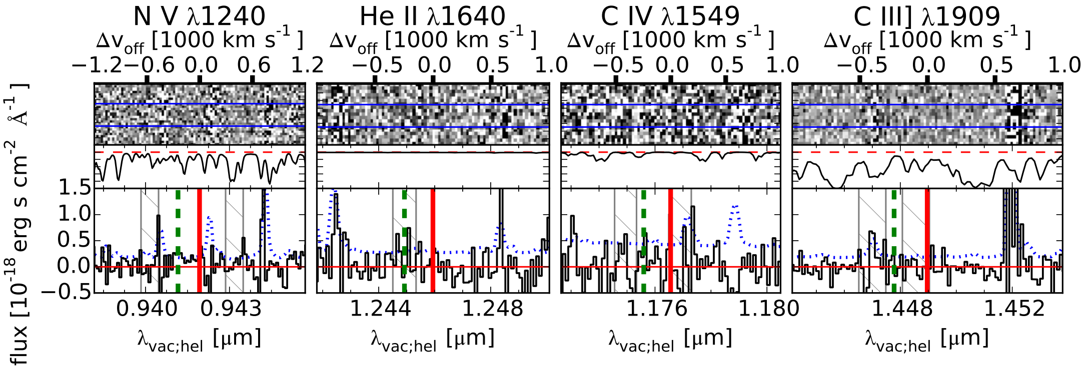

Figure 2.9 2D and 1D spectra for N V λ1240, He II λ1640, C IV λ1549, C III] λ1909. The height of the 2D spectrum is 4″, centred at a slit position of 0″.00 . The 1D spectrum shows a trace extracted with our default extraction mask. The middle panel shows the telluric absorption as derived from MOLECFIT (Kausch et al., 2015), with the red dashed line indicating a transmittance of one and the bottom of the panel being at zero. For the vertical lines in the 1D spectrum, compare Fig. 2.8. All lines, except N V λ1240 are in the NIR arm. For the part of the VIS arm spectrum shown for N V λ1240, we have binned the reduced spectrum by a factor of two. For the example of our narrower fiducial extraction box (200 km s^{-1}), the relevant part is marked as hatched region. In the case of the doublets, both relevant regions are indicated.

.

tively. This is again consistent with the result obtained by Ouchi et al. (2009): $S = 0.685 \pm 0.007$ and $S_w = 13.2 \pm 0.1$Å. Using an increased wavelength range from 9220 to 9260 Å, we measure values of 0.9 ± 0.2 and 16 ± 4 Å for the two quantities, being consistent with the results for the smaller range, but possibly indicating a somewhat larger value. Indeed, the spectrum might show some Ly α emission at high velocities (cf. Fig. 2.7). However, this is weak enough to be due to skyline residuals and we do not discuss it further.

Integrating the extracted spectrum over the wavelength range from 9227 Å to 9250 Å, the obtained flux is $6.1 \pm 0.3 \times 10^{-17}$ erg s^{-1} cm^{-2}. After subtracting the continuum level, the Ly α flux is $5.9 \pm 0.3 \times 10^{-17}$ erg s^{-1} cm^{-2}, or $8.8 \pm 0.5 \times 10^{-17}$ erg s^{-1} cm^{-2} after correcting for the slit-loss factor of 0.67, as derived in section 2.3.1. This corresponds to a luminosity of $4.3 \pm 0.2 \times 10^{43}$ erg s^{-1}. By comparison, Ouchi et al. (2009) derive a $f_{\mathrm{Ly}\,\alpha}$ of $7.9 \pm 0.2 \times 10^{-17}$ erg s^{-1} cm^{-2} and $11.2 \pm 3.6 \times 10^{-17}$ erg s^{-1} cm^{-2} from the $z'/NB921$ photometry and their slit-loss corrected Magellan/IMACS spectrum, respectively. This is in good agreement with our result, considering that the slit loss as calculated from the $NB921$ image is a slight overestimation, as the seeing in our observation was somewhat better (cf. sec. 2.3.1).

From the continuum flux measured in the spectrum and the measured Ly α flux, we derive a Ly α (rest-frame) equivalent width (EW_0) of 65 ± 9 Å, nearly identical to the 78^{+8}_{-6} Å stated by Ouchi et al. (2013). Jiang et al. (2013a) have in their recent study derived a Ly α EW_0 of only 22.9 Å for *Himiko*. The explanation for this discrepancy is that they have fitted a fixed UV slope based on their relatively blue J_{F125W}-H_{160W} and extrapolated this slope to the position of Ly α. However, the continuum magnitude derived from our spectrum is not consistent with this assumption.

2.3.4 Detection limits for rest-frame far-UV lines

As we do not unambiguously detect any of the potentially expected emission lines except Ly α, we focus on determining accurate detection limits. The instrumental resolution of 55 km s^{-1} allows to resolve the

Table 2.5 5σ detection limits for N V λ1240, C IV λ1549, He II λ1640, and C III] λ1909. They were determined as described in sec. 2.3.4. Values are stated in units of 10^{-18} erg s^{-1} cm^{-2}. In addition, we state the flux within the extraction box and the percentage of pixels, which is not excluded in our bad-pixel mapping. Continuum and telluric absorption is corrected. The three different redshift/width combinations refer to peak and FWHM of the measured Ly α line, and two fiducial masks used as examples. The symbols refer to those included in Fig. 2.10.

Δv[1]	0	-250	-250
width[1]	286	600	200
Symbol	cross	circle	diamond
N V	6.9	9.2	4.5
	1.1 [40%]	0.6 [46%]	0.2 [52%]
He II	5.7	7.9	5.1
	0.2 [100%]	1.9 [100%]	1.3 [100%]
C IV	14.3	19.7	11.4
	1.0 [69%]	0.1 [65%]	-0.3 [68%]
C III]	9.5	14.1	9.7
	-1.5 [82%]	-0.7 [59%]	-0.3 [60%]

[1] [km s^{-1}]

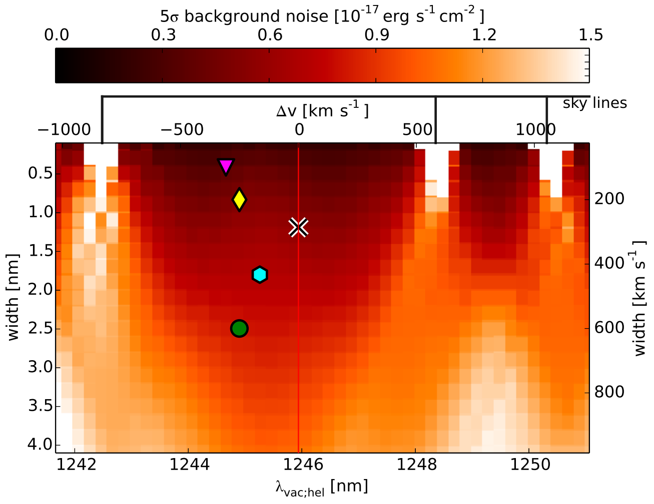

Figure 2.10 5σ detection limits in a region around He II in extraction boxes of different widths and placed at different wavelengths corresponding to different velocity offsets w.r.t to the peak Ly α redshift of 6.595, which is marked by a red vertical line. For all boxes, the extent of the box in slit direction was 7 pixel. Further details are given in sec. 2.3.4. The cross marks redshift and width of the Ly α line, while the yellow diamond and the green circle indicate our two fiducial boxes. Finally, the magenta triangle and the cyan hexagon indicate the two boxes giving the highest positive He II excess.

considered lines for expected line widths. Therefore, detection limits depend strongly both on the line width, and, due to the large number of skylines of different strengths, on the exact systemic redshift. As the systemic redshift is not known exactly from the Ly α profile alone and the search for [CII] by Ouchi et al. (2013) resulted in a non-detection, too, all limits need to be determined over a reasonable wavelength range.

Studies to determine velocity offsets between the systemic redshift and Ly α for LAEs around $z \sim 2$–3 find Ly α offsets towards the red ranging between $100\,\mathrm{km\,s^{-1}}$ and $350\,\mathrm{km\,s^{-1}}$ (e.g. McLinden et al., 2011; Hashimoto et al., 2013; Guaita et al., 2013; Chonis et al., 2013), while the typical velocity offset for $z \sim 3$ LBGs is with about $450\,\mathrm{km\,s^{-1}}$ higher (Steidel et al., 2010). On the other hand, in LABs also small negative offsets (blue-shifted Ly α) have been observed (McLinden et al., 2013).

Whereas offsets at the redshifts of the aforementioned studies are produced by dynamics and properties of the interstellar (ISM) and circumgalactic medium (CGM), we note that at the redshift of *Himiko* an apparent offset can also be produced by a partially neutral IGM (cf. sec. 2.4.3).

Motivated by the lower redshift studies, we formally searched for emission from the relevant rest-UV lines for $-1000\,\mathrm{km\,s^{-1}} < \Delta v < 1000\,\mathrm{km\,s^{-1}}$ from peak Ly α. We calculated for this range the noise for extraction-boxes up to $1000\,\mathrm{km\,s^{-1}}$. The boxes' height in spatial direction was in all cases corresponding to the $1''.47$ trace.

$$\sigma_m = \sqrt{\sum_{\mathrm{i,j} \notin \mathrm{bp\text{-}mask}} \sigma^2_{\mathrm{i,j}}} \quad \underbrace{\times\ (\ 1/f_{\mathrm{included}})}_{\text{applied when stating detection limits}} \tag{2.2}$$

Here, $\sigma_{i,j}$ are the noise values for the individual pixels from the pipeline's error model. Skylines, bad and high-noise pixels, determined as described in sec. 2.2.2, were excluded in the sum, effectively leaving a certain fraction f_{included} of a box's pixels. The signal-to-noise (S/N) was obtained by dividing the spectrum's flux integrated over the same non-excluded pixels by the determined noise. When stating detection limits, we rescaled these errors by the inverse of the fraction of included pixels (cf. eq. 2.2).

In the case of the N V $\lambda\lambda 1238, 1242$, C IV $\lambda\lambda 1548, 1551$, and [C III],C III] $\lambda\lambda 1907, 1909$ doublets we formally calculated values jointly in two boxes centred on the wavelengths of the two components for a given redshift. Wide extraction boxes merge into a single box. Where we state wavelengths instead of redshift or velocity offset, we refer to the central-wavelength of the expected 'blend'. Widths are stated for the individual boxes, meaning that the effective box widths are larger.

While we test over a wide parameter space, we refer in the following several times to somewhat arbitrary fiducial detection limits based on a narrow $200\,\mathrm{km\,s^{-1}}$ and a wider $600\,\mathrm{km\,s^{-1}}$ extraction box, assuming a systemic redshift $250\,\mathrm{km\,s^{-1}}$ bluewards of Ly α, which is as mentioned above a typical value for LAEs. This redshift is also marked in several plots throughout the paper as green dashed line.

We took account for the continuum by removing an estimated continuum directly in the telluric corrected rectified 2D frame. The assumed spatial profiles in cross dispersion direction for the $0''.9$ NIR and $1''.5$ VIS slits are those estimated from the seeing-convolved *HST* imaging (cf. sec. 2.3.1). While we assumed for the region around N V $\lambda 1240$ in the VIS arm a continuum with $f_\lambda(\lambda) = 10.2 \times 10^{-20}\,\mathrm{erg\,s^{-1}\,cm^{-2}\,\AA^{-1}}$, being the flux measured directly from the spectrum as described in sec. 2.3.3 and corrected for aperture loss, we were using for the NIR spectrum a $f_\lambda(\lambda) = 3 \times 10^{-20}\,\mathrm{erg\,s^{-1}\,cm^{-2}\,\AA^{-1}}$ within the slit at the effective wavelength of H_{160W} and a spectral slope of $\beta = -2$.

The used NIR flux density is close to that of the measured H_{F160W}. Due do the difference between our J_{F125W} and the measurement based on UKIDSS J and the J_{F125W} by Ouchi et al. (2013), we decided for the conservative option[13] not to follow the profile shape seen by our data and use a continuum flat in f_ν instead, even so the corresponding $\beta = -2$ is only at the upper end of the uncertainty range allowed from the measurement in our work (cf. also sec. 2.2.3).

In table 2.5, 5 σ detection limits, extracted fluxes, and the fraction of non-rejected pixels are stated all for N V, C IV, He II, and C III] in three different extraction apertures. The spectra for the relevant regions are shown in Fig. 2.9.

---

[13] As the magnitude of Ouchi et al. (2013) is fainter, this results in higher upper limits both for the line-fluxes and the EW_0.

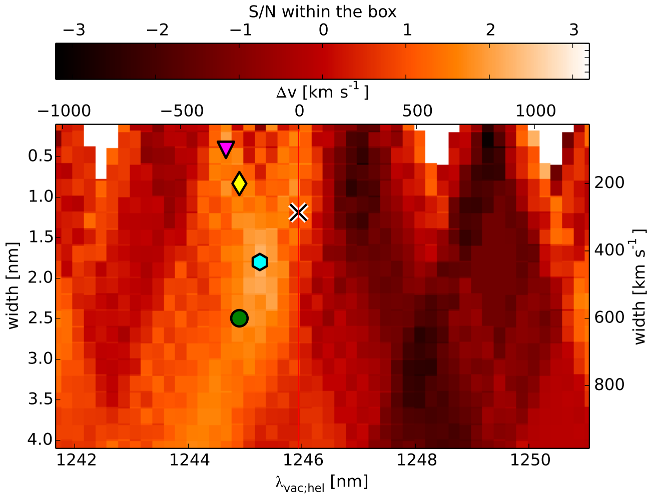

Figure 2.11 Signal-to-Noise ratio (S/N) measured within extraction boxes equivalent to those included in Fig. 2.10. No continuum and telluric correction was applied for this plot. Maximum values are reached for boxes with $\lambda_{hel;vac}$ = 12453 Å with a velocity width of 430 km s^{-1} (cyan hexagon) and $\lambda_{hel;vac}$ = 12447 Å with a velocity width of 100 km s^{-1} (magenta triangle), respectively.

2.3.5 He II

The production of He II λ1640Å photons, which originate like Balmer-α in H I from the transition n = 3 → 2, requires excitation at least to the n = 3 level or ionisation with a following recombination cascade. Whereas the ionisation of neutral hydrogen, H I, requires only 13.6 eV, a very high ionisation energy of 54.4 eV is necessary to ionize He II and consequently only very 'hard' spectra can photo-ionise a significant amount. Such hard spectra can be provided by AGNs, having a power-law SED with significant flux extending to energies beyond the Lyman-limit, nearly or completely metal-free very young stellar populations with an initial mass function extending to very high masses, or the radiation emitted by a shock.

In Fig. 2.10, the 5 σ noise determined as described in sec. 2.3.4 is shown for the relevant central-wavelength/box-width space around the expected He II position and the S/N calculated over the same parameter space is shown in Fig. 2.11. While there might be indication of some excess at velocities between −450 and 0 km s^{-1}, we do not find sufficient signal to claim a detection. The two masks giving the highest S/N [14] are a wider one with a width of 430 km s^{-1} at a central wavelength of 12453 Å (z = 6.591, Δv = −160 km s^{-1}) and a narrower one with a width of 100 km s^{-1} at a central wavelength of 12447 Å (z = 6.588, Δv = −300 km s^{-1}). The S/N in the two cases is after continuum subtraction 1.9 and 1.7, respectively. A somewhat higher S/N can be reached by using a narrower trace more centred on the position of the expected continuum.

The 2D spectrum over the relevant velocity offset range is shown in Table 2.6 in the row labelled 'observed'. The position of the default trace is indicated as magenta dashed lines in the smoothed figure, which is identical in the two columns, while the two extraction boxes giving the highest S/N are indicated by cyan vertical lines in the two columns, respectively. Additionally, a sky-spectrum over the same region and a Gaussian smoothed version are included. In the Gaussian smoothing, we excluded pixels being masked in our master high-noise pixel mask. For a guided eye, it might be possible to identify the

---

[14] Formally, a very narrow box close to the strong skylines at ~ +1000 km s^{-1} gives a similar high S/N. However, this is clearly affected by residuals from strong skylines.

Table 2.6 2D spectrum and fake-source analysis for a wavelength range corresponding to the expected He II wavelength. In the row *observed*, the 2D spectrum in the region around the possible He II excess is shown. The grayscale extends linearly between $\pm 1 \times 10^{-19}$ erg s^{-1} cm^{-2} Å^{-1} (white < black). Above a Gaussian smoothed version is shown with the same scale, at the top of which a sky-spectrum for the same region is included. Both the *observed* and *smoothed* images are identical in both columns. The magenta dashed horizontal lines indicate our default extraction mask. Below the *observed* row, images are shown, where Gaussian fake lines have been added with different strengths for two different FWHM and wavelength combinations. Widths and positions are indicated by the cyan vertical lines. The integrated flux in the respective fake lines is stated in the leftmost column.

flux[1]	100 km s^{-1}	400 km s^{-1}
smoothed	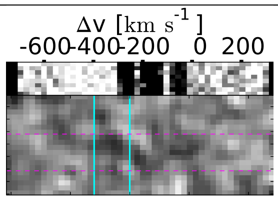	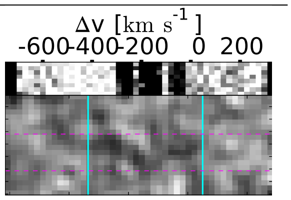
observed	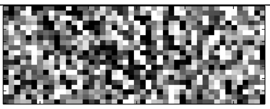	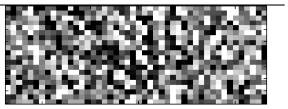
+2.0	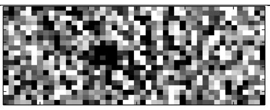	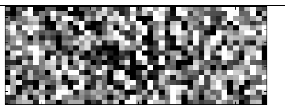
+4.0	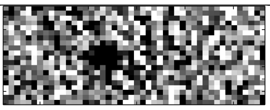	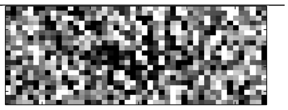
+8.0	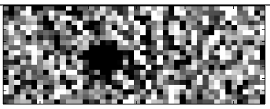	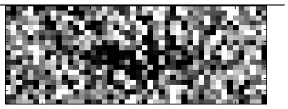

[1] added line-flux [10^{-18} erg s^{-1} cm^{-2}]

excess visually. Yet, it is certainly possible that noise is seen and it cannot be considered a detection. It is noteworthy that there is a triplet of weak skylines in the centre of the region. While these skylines should in principle not increase the noise by much, as also being consistent with the error spectrum, this would assume an ideal subtraction. As can be seen in the figure, there are however some unavoidable residuals, extending over the complete slit.

We tried to understand, which line-flux would be required for an excess to be considered visually a safe detections. We did this by adding Gaussians with FWHMs of 100 km s^{-1} and 400 km s^{-1} centred on the wavelengths of the two extraction boxes leading to the highest S/N and assuming a spatial profile as expected for the continuum. The results are shown in Table 2.6. After visual inspection of four authors, we need to conclude that an additional flux of 2×10^{-18} and 4×10^{-18} erg s^{-1} cm^{-2} would be required in the two cases for a detection considered to be safe, corresponding as expected to approximately a 5σ detection.

Finally, we estimated the 3σ upper limit on the He II EW_0 in our fiducial 200 km s^{-1} extraction box, using the same continuum estimate as used for the continuum subtraction. This is a continuum flux

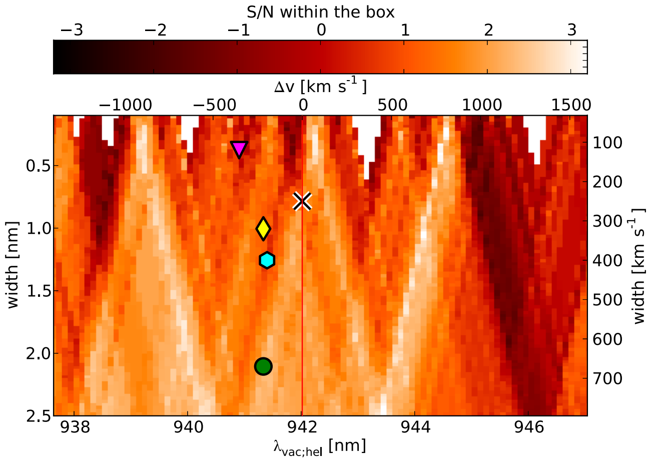

Figure 2.12 Similar plot as shown for He II in Fig. 2.11. A telluric correction was applied to the underlying image and a continuum with a flux as motivated in sec. 2.3.4 was subtracted. The S/N was calculated in two boxes at the respective wavelengths of the two individual lines (1238.82Å and 1242.80Å) w.r.t to the blend centre.

density at the He II wavelength of $4.0 \pm 0.5 \times 10^{-20}$ erg s^{-1} cm^{-2} Å^{-1}, assuming the appropriate slit loss. This results in an upper limit of the observed frame EW of 75 ± 10 Å, which corresponds to a rest-frame EW_0 of 9.8 ± 1.4 Å. The errors are due to the uncertainty in H_{F160W}, not including the uncertainty in the continuum slope β.

2.3.6 High ionisation metal lines

If *Himiko*'s Ly α emission were powered either by a 'type II' or less likely by a 'type I' AGN, being disfavoured from the limited Ly α width, relatively strong C IV λ1549 emission would be expected. This would be accompanied by somewhat weaker N V λ1240, C III] λ1909, He II λ1640, and Si IV λ1400 emission lines (e.g. Vanden Berk et al., 2001; Hainline et al., 2011).

N V

N V λ1240 is a doublet consisting of two lines at 1238.8Å and 1242.8Å, respectively. With their oscillator strength ratio of 2.0 : 1.0, the effective blend wavelength is 1240.2Å. The spectrum around N V is shown in the left most panel of Fig. 2.9. The hatched wavelength ranges mark the regions for the two N V lines under the assumption of our fiducial 200 km s^{-1} wide box at −250 km s^{-1} offset from Ly α. Weak and blended skylines, which are not marked by our skyline algorithm, and telluric corrected absorption causes the noise to vary strongly over the region.

Using the extraction aperture as shown in Fig. 2.9 and subtracting the continuum in the 2D frame as described in sec. 2.3.4, we derive for the wider and narrower of our two fiducial boxes excesses of 0.7 and 0.5 σ, respectively, where we need to exclude a relatively high fraction of pixels due to high noise (cf. Table. 2.11). The result is consistent with zero. Exploring the Δv–*width* parameter space for the S/N (Fig. 2.12), velocity offset and box-width can be chosen in a way to get a higher S/N. E.g. boxes at +450 km s^{-1} with a width of 840 km s^{-1} per doublet component, corresponding to a single merged extraction box of 1324 km s^{-1}, have a S/N of 3.4 with an included fraction of 42%. However, such a

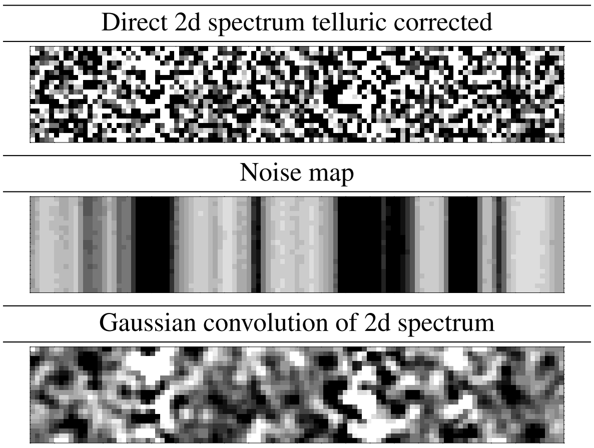

Figure 2.13 Region around the N V λ1240 doublet, as expected based on the Ly α redshift. **Upper:** Telluric corrected 2D spectrum, scaled between ± the minimum rms noise, $\sigma_{\rm min}$, in the shown region. **Middle** Noise map linearly scaled between $\sigma_{\rm min}$ and $3\sigma_{\rm min}$ (white < black). The high noise regions are both due to skylines and due to regions requiring telluric correction. **Lower:** Spectrum smoothed with a one pixel Gaussian Kernel.

relatively large offset towards the red from the Ly α redshift seems not feasible. Restricting the analysis to a more likely range of Δv from -500 to 0 km s^{-1}, we would find a maximum S/N of 2.3 for box widths of 400 km s^{-1} at no velocity offset w.r.t to Ly α, with an included fraction in the box of 45%. The flux within non-excluded pixels is 1.5×10^{-18} erg s^{-1} cm^{-2}. A visual inspection of the relevant region does not allow for the identification of any line (Fig. 2.13).

Other rest-frame UV emission lines

In Fig. 2.9 we are also showing cutouts for two further lines (C IV and C III]). The relevant wavelength range for the two components of C IV $\lambda\lambda$1548, 1551, which have an oscillator strength ratio of 2.0:1.0, is located in a region of high atmospheric transmittance within the *J* band. While there are a few strong skylines, especially between the two components, there is enough nearly skyline-free region available. Visually, we do not see any indication for an excess. Also statistically, considering again the Δv range from -500 to 0 km s^{-1} w.r.t to the Ly α peak redshift, we find a maximum excess of 1.4 σ after continuum subtraction.

By contrast, the C III] doublet is located between the *J* and *H* band, suffering from strong telluric absorption (cf. Fig. 2.9). Nevertheless, it could be possible to detect some signal in the gaps between absorption. Especially, the relevant part bluewards of the Ly α redshift has a relatively high transmission. Both the visual inspection and the formal analysis of the telluric and continuum corrected spectrum indicate no line. Detection limits for our fiducial boxes are stated in Table. 2.5.

Si IV λ1403 is also in a region of high atmospheric transmission. However, here the overall background noise in the spectrum is relatively high and as expected, for this compared to C IV usually weak line, we do not see an excess.

Another line is N IV] λ1486, which has in rare cases been found relatively strong both in intermediate and high redshift galaxies (e.g., Christensen et al., 2012; Vanzella et al., 2010). Unfortunately, the spectrum is at the expected wavelength for N IV] covered with strong skylines (not shown).

The same holds for the [O III] $\lambda\lambda$1661, 1666 doublet, which can be relatively strong in low mass galaxies undergoing a vigorous burst of star-formation (e.g. Erb et al., 2010; Christensen et al., 2012;

Table 2.7 Parameters of the used SSPs, which are the *Yggdrasil* burst models from Zackrisson et al. (2001, 2011) and the BC03 Bruzual & Charlot (2003) models combined with nebular emission following the recipe of Ono et al. (2010) (*BC03-O10*).

Parameter	Values
	Yggdrasil
Metallicities Z ($Z_\odot = 0.02$)	0.0004, 0.004, 0.008 0.02, 0.0 (Pop III)
IMFs	for $Z > 0$: Kroupa (2001, 0.1–100$M_\odot$); for $Z = 0$: Kroupa & log-normal (1–500M$_\odot$, $\sigma = 1\,\mathrm{M}_\odot$, $M_c = 10\,\mathrm{M}_\odot$) & Salpeter (50–500$M_\odot$)
Nebular emission	Cloudy (Ferland et al., 1998)
Using: Schaerer (2002); Vázquez & Leitherer (2005);Raiter et al. (2010)	
	BC03 (Padova 1994); nebular emission as in Ono et al. (2010)
Metallicities Z	0.0001, 0.0004, 0.004, 0.008, 0.02, 0.05
IMF	Salpeter (1955, 0.1–100$M_\odot$)
Nebular emission	following recipe described in Ono et al. (2010)
Using: Ferland (1980); Aller (1984); Storey & Hummer (1995);Krueger et al. (1995)	
	Reddening
Calzetti et al. (2000) extinction law, assuming identical extinction for nebular emission and stellar continuum.	

Stark et al., 2014b). We do not find any excess in the relevant wavelength range. As the region is in addition affected by several bad pixels, we do not state formal detection limits for this doublet.

2.4 Discussion

2.4.1 SED fitting

We performed SED fitting including J_{F125W}, H_{F160W}, K, and $IRAC$1–4, in total seven filters, where for $IRAC$3–4 only upper limits are available. As UKIDSS K and the IRAC data are not resolving the three components and a profile fit is with the available S/N not feasible, we fitted the three sources jointly by using the aperture corrected 2″ diameter photometry (Table 2.4). Throughout our SED fitting we fixed the redshift to $z = 6.590$, a reasonable guess for the systemic redshift based on the Ly α line.

We used our own python based SED fitting code coniecto which allows both for a MCMC and a grid based analysis. Here, we derived our results with the grid based option. The code requires as input single age stellar populations (SSP) for a set of metallicities. Additionally, a pre-calculated nebular spectrum including continuum and line emission needs to be specified for each age–metallicity pair, and can be added to the respective SSP with a scale-factor between 0 and 1. This scale-factor can be understood as covering fraction, f_{cov}, or $1 - f_{\mathrm{ion}}^{\mathrm{esc}}$, with $f_{\mathrm{ion}}^{\mathrm{esc}}$ being the escape fraction of the ionizing continuum. The inclusion of nebular emission has been found crucial for the fitting of redshift $z \sim 6-7$ LAEs and LBGs (e.g. Schaerer & de Barros, 2009, 2010; Ono et al., 2010).

SEDs for a given SFH history are obtained by integrating the single age stellar populations. We were restricting our analysis to instantaneous bursts and continuous star-formation. Due to the lack of deep enough rest-frame optical photometry in *IRAC3–4*, which would be not affected by strong emission lines at our object's redshift, it does not make sense to use more complicated SFHs. Already the used set of parameters allows for over-fitting of the models.

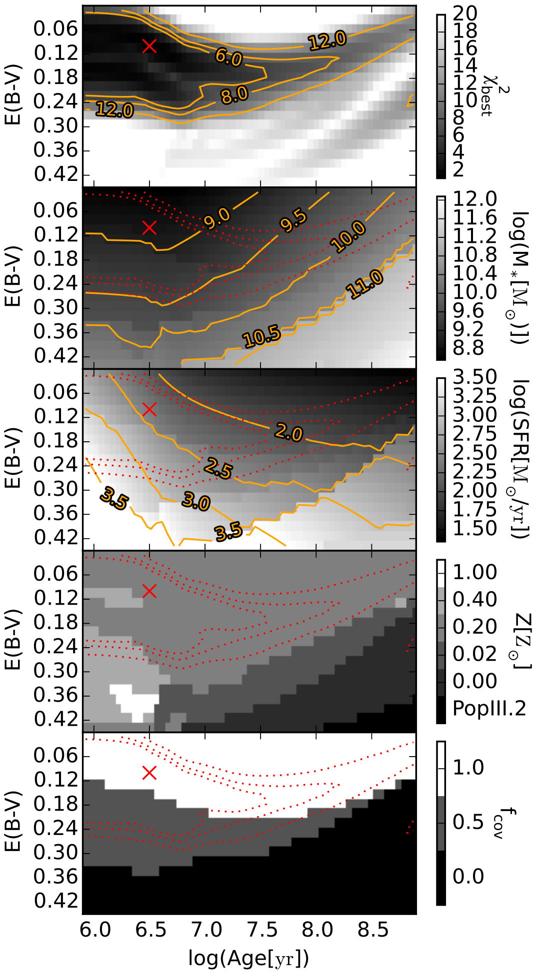

Figure 2.14 SED fitting results under the assumption of continuous SFH using the *Yggdrasil* models. Upper panel shows the lowest possible χ^2 at a given point in the *age*–*E*(B–V) plain. Four physical quantities for the best models are shown below. For orientation, the same χ^2_{best} contours from the top plot are replicated as dotted line in each of the subplots. The model with the absolute minimal χ^2 is marked as cross.

We applied reddening to the integrated SEDs using the Calzetti et al. (2000) extinction law, assuming the same reddening both for the nebular and the stellar emission, motivated by evidence for the validity of this assumption in the high redshift universe (Erb et al., 2006).

As main input SSPs we used the models 'Yggdrasil' (Zackrisson et al., 2011), which include metallicities all from zero (Pop III) to solar ($Z_\odot = 0.02$). Their code consistently treats both nebular line and continuum emission (Zackrisson et al., 2001) by using Cloudy (Ferland et al., 1998) on top of stellar populations. We are here referring to SSPs as their publicly available instantaneous burst models. More details are summarized in Table 4.2.

For reasons of comparison to the SED fitting done by Ouchi et al. (2009, 2013), we also obtained results with input models as used in these works. These are based on BC03 (Bruzual & Charlot, 2003) models, where a nebular emission is calculated by the prescription presented in Ono et al. (2010). We are referring in the following to these models as *BC03–O10*.

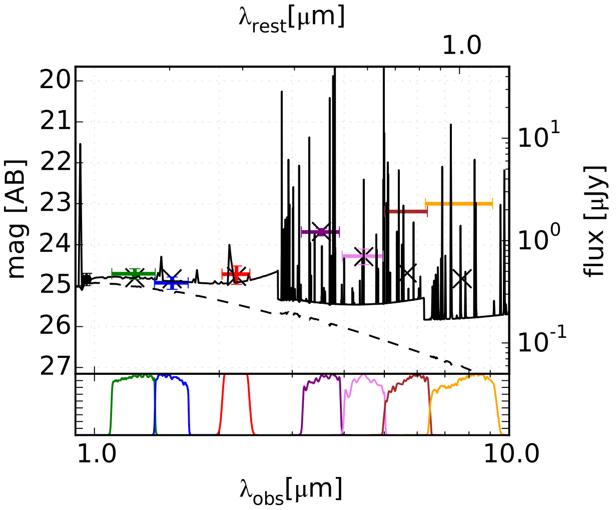

Figure 2.15 Best-fit SED obtained with the Yggdrasil models under the assumption of continuous star-formation. For this very young stellar-population (3 Myr) also the continuum is dominated by the nebular emission, showing the characteristics 'jumps' resulting from the bound-free recombination to different levels in hydrogen. The comparably weak stellar continuum is shown as dashed line. Synthetic magnitudes for the relevant filters are indicated as black crosses. The black circle is the magnitude measured from the spectral continuum.

After calculating synthetic magnitudes on a large *age*–E(B–V)–Z–f_{cov} grid, we have minimized χ^2 w.r.t to mass for each parameter set. The grid covered ages between 0–800 Myr, with the upper limit being the age of the universe at $z = 6.59$, and E(B–V) from 0.00 to 0.45. Used metallicities were those available in the input models (Table 4.2) and for f_{cov} we allowed for three different values (0,0.5,1.0).

In Fig. 2.14, the results are shown for continuous star-formation using the *Yggdrasil* models. For each point in the *age*–E(B–V) space the Z–f_{cov} tuple allowing for the minimal χ^2, χ^2_{best}, is chosen. The resulting $\chi^2_{\rm best}$ contours are indicated in all five subplots, with the five subplots showing χ^2_{best}, stellar mass, star-formation rate averaged over 100 Myr (SFR_{100})[15], metallicity, and f_{cov}, respectively. Stellar masses refer to the mass in stars at the point of observation.

The global best fit SED over the explored parameter space is a very young 3^{+32}_{-2} Myr stellar population, which is strongly star-forming ($SFR_{100} = 2.3^{+26.2}_{-1.2} \times 10^2\ M_\odot\ \mathrm{yr}^{-1}$) and has a stellar mass of $7^{+32}_{-3} \times\ 10^8 M_\odot$ with a $\chi^2 = 1.2$.[16] This best fit model is shown as cross in the maps and as SED in Fig. 2.15. The uncertainties on the estimated parameters were determined based on the range of models having $\chi^2 < 6$. A value of six can be understood as a good fit for seven filters.

Clearly, a large range of parameters is allowed. It is only for metallicity and reddening that relatively strong constraints can be inferred, with mainly $Z = 0.2Z_\odot$ models giving good fits and some $Z = 0.4Z_\odot$ models being allowed within $\chi^2 < 6$. Models with E(B–V) greater than 0.25 are unlikely. Further, at least partial nebular contribution is required. The wide range of solutions can be understood through the interplay of a somewhat evolved population with a 4000Å break and strong nebular emission, combined with small amounts of dust extinction.

The strongest lines in *IRAC1* and *IRAC2* are [O III] $\lambda\lambda$4959, 5007 and Hα, respectively. The [O III]

---

[15] If the age of the stellar population is smaller than 100 Myr, it is averaged over the population age.

[16] Not reduced χ^2

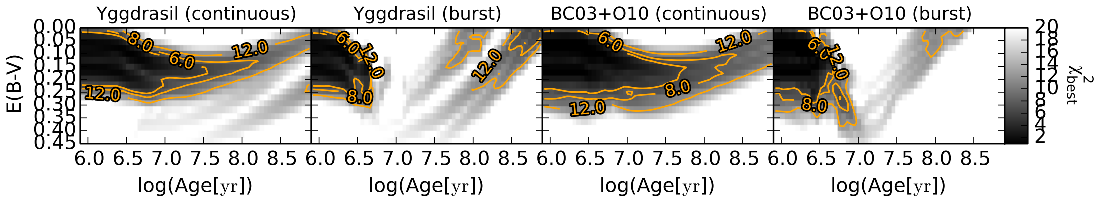

Figure 2.16 The left panel shows the same as the upper panel in Fig. 2.14. For comparison, the χ^2_{best} result using the *BC03+O10* models and the case of burst SFH is shown.

EW_0 is expected to peak at metallicities around $Z = 0.2 Z_\odot$ (e.g. Finkelstein et al., 2013), strong enough to explain the blue *IRAC1* - *IRAC2* colour of -0.6 ± 0.2.

The χ^2_{best} plots are compared for burst and continuous star-formation both using the *Yggdrasil* and the *BC03–O10* model sets in Fig. 2.16. Burst models give acceptable fits only for very young ages, where they are basically identical to the continuous star-formation models. Both model sets give consistent results, with small differences mainly existing where specific metallicities are only available in one of the two sets. E.g., the area of relatively low χ^2_{best} at high ages for burst models using *Yggdrasil* is absent in the *BC03-O10* models, as they require zero metallicity (Kroupa and log-normal IMF). However, these SEDs would require stellar masses in excess of 10^{11} M$_\odot$ and can hence be considered infeasible. In general, biases are possible due to discretized metallicities.

We also tested the impact of substituting our J_{F125W} measurement with that of Ouchi et al. (2013). The fainter J_{F125W} flux shifts the χ^2 best contours slightly towards higher reddening and hence higher required SFRs, or alternatively higher ages. Ouchi et al. (2013) have found from their SED fitting with *BCO3–O10* models under the assumption of continuous SFR a best fit model with a mass of $1.5^{+0.8}_{-0.2} \times 10^9 M_\odot$, an age of $4.2^{+0.8}_{-0.2} \times 10^6$ yr, and an $E(B-V) = 0.15^{+0.04}_{-0.03}$, consistent with our results.[17]

If *Himiko*'s extended Ly α emission was driven by merger activity between the three continuum bright objects, SFRs as high as a few 100 $M_\odot$ yr^{-1} are expected, as seen e.g. in the simulations by Yajima et al. (2013a) focusing on LABs, and consistent with our best fit model.

Importantly, a burst with the same properties as our best fit model having happened 100 Myr before the observed burst, would have faded in all detected filters by at least a factor 20. Hence, there could easily be a moderately young stellar population of a few $10^9 M_\odot$ without significantly contributing to the SED.

While the present work was under revision, Schaerer et al. (2015) also published results from SED fitting for *Himiko*. Most importantly, they made use of the upper limit on the far-infrared luminosity, which can be estimated from the ALMA upper limit for the 1.2mm (observed-frame) continuum presented by Ouchi et al. (2013), in order to constrain the maximum allowed dust extinction.

Their obtained upper limit corresponds assuming a Calzetti et al. (2000) extinction law to $E(B-V) < 0.05 \pm 0.03$, with the uncertainty due to the unknown dust temperature assumed for the conversion from continuum flux density to FIR luminosity. Using this upper limit, a huge part of the allowed parameter space can be ruled out. Schaerer et al. (2015) could argue, using for the SED fitting the photometry of Ouchi et al. (2013), that a young and heavily star-forming solution is disfavoured. However, due to the somewhat bluer $F125W$–$F160W$ measured from the CANDELS data compared to that measured in the data of Ouchi et al. (2013), our fit requires somewhat less extinction and hence very young models consistent with their upper limit can be found.

---

[17] In the original publication a different best fit model was stated $1.5 \times 10^{10} M_\odot$, an age of 1.8×10^8 yr, $E(B-V) = 0.15$, and a SFR of 100 $M_\odot$ yr^{-1}; erratum in preparation

2.4.2 Further SED considerations

As shown in section 2.4.1, the observed broadband magnitudes are compatible with models over a wide age, mass, and reddening range, where the single stellar population fit is likely an oversimplification of the problem. When looking at the J_{F125W} -H_{F160W} colour of the individual components (cf. Table 2.3), there exists a significant difference between the two more eastern and the western-most component, with the latter being about 0.3 mag redder. This can all indicate differing stellar populations, differing escape fractions of the ionising continuum, $f_{\rm ion}^{\rm esc}$, or differing amounts of dust.

Interestingly, the J_{F125W} - $H_{F160W} \sim -0.3 \pm 0.1$ of the two eastern components, corresponding to a $\beta = -3.3 \pm 0.6$, is somewhat difficult to explain with a Pop II when taking account for nebular-emission under the assumption of low ionising continuum escape $f_{\rm esc}^{\rm ion}$ (e.g. Bouwens et al., 2010). Only for complete escape of the ionising radiation, a population with a metallicity as in our best fit SED ($Z = 0.2Z_{\odot}$) would produce a slope as steep as $\beta = -3$, whereas for $f_{\rm esc}^{\rm ion} = 0$ the steepest β is a about -2.5 (cf. also Fig. 2.15).

Our best fit, at least for the joint SED, requires a very low $f_{\rm esc}^{\rm ion}$ to explain the *IRAC* magnitudes. While each of the components does not differ more than 1.5σ from this $\beta = -1.5$, the fact that Ouchi et al. (2013) find at least for the two outer components similar results based on their independent data, increases the probability that the steep slope of *Himiko–E* is real. Certainly, possibilities exist to reconcile the blue colour of the individual components with the low escape fraction required by the SED model. E.g., there could be anisotropic ionising escape in our direction, or the ionising radiation could escape the star-forming regions and the nebular continuum emission is produced somewhat further out, making the nebular emission more extended than the stellar continuum.

Both the visual inspection of Fig. 2.4 and the spatial profiles in the individuals OBs (Fig. 2.5) indicate an offset of the overall continuum light w.r.t to the *NB*921 light distribution, which is dominated by the Ly α emission. The Ly α emission seems least strong around *Himiko–W*. This has been confirmed by the WFC3 / F098M imaging of Ouchi et al. (2013), who find the strongest Ly α emission originating from *Himiko–E*, which is with $EW_0 = 68^{+14}_{-13}$ however not as high that it would put constraints on the escape fraction.

Two-photon, 2γ, continuum (Breit & Teller, 1940), emitted by transitions between the 2s and 1s states of the hydrogen atom, is in the case of nebular emission powered by a central ionising source one among other mechanism contributing to the continuum. In the case of cooling radiation, where the hydrogen atoms are collisionally excited, it would be the sole continuum contribution, though (Dijkstra, 2008). Our data point provided by the spectrophotometry for the rest-frame wavelength range from 1238 to 1285Å could compared to $F125W$ and $F160W$ resemble the typical 2γ dip close to Ly α. Using the frequency-depended emissivities as stated in Table 1 of Spitzer & Greenstein (1951), we calculate the expected J_{F125W} H_{F160W} colour for the two photon continuum at $z = 6.590$. We find a value of J_{F125W} $H_{F160W} = -0.08$. Therefore, it cannot be solely responsible for the found very blue J_{F125W} H_{F160W}. In addition, we estimate for the peak flux density expected from cooling radiation based on the predictions of Dijkstra 2008 and the measured Ly α flux for *Himiko* a value of 28.3 mag. This is more than three magnitudes fainter than the measured flux. Therefore, 2γ emission from cooling radiation is unlikely to significantly contribute to the continuum.

Finally, we note that Ono et al. (2010) have favoured in their SED fitting for the composite of 91 *NB*921 selected LAEs at $z = 6.6$ a very young ($\sim$ 1 Myr) and very low mass ($\sim 10^8$ M$_{\odot}$) model, with significant nebular contribution ($f_{\rm esc}^{\rm ion} = 0.2$). They have only included those objects, which are not detected individually in *IRAC* 1,[18] therefore excluding objects like *Himiko*. The *IRAC* 1 magnitude in their median stack is 26.6 mag. For *Himiko*, the total magnitude after the slightly uncertain aperture correction is 23.69 ± 0.09. Simplifying assuming that the flux in *Himiko* is equally distributed between

---

[18] Based on Spitzer/SpUDS (Dunlop et al., 2007), which is less deep than Spitzer/SEDS

the three sources, each of them would have a magnitude of 24.9. This is only a factor five higher than the median stack. Therefore, the individual components are not as extremely differing from the typical $z = 6.6$ Ly α emitters as the joint photometry suggests.

2.4.3 Lyman alpha profile

Due to resonant scattering the Ly α profile can be modified significantly both in the ISM/CGM and in the intergalactic medium (IGM). A shaping of the profile within the ISM/CGM is likely, with Ly α possibly entering the IGM with a typical double peaked profile observed for lower redshifts LAEs (e.g. Christensen et al., 2012; Krogager et al., 2013) as predicted by theory (e.g. Harrington, 1973; Neufeld, 1990; Verhamme et al., 2006; Laursen et al., 2009a). The blue or red peak is suppressed in the case of outflows or inflows, respectively.

On the other hand, Ly α could leave the CGM also with a nearly Gaussian profile, as seen in several cases for lower redshift LABs (e.g. Matsuda et al., 2006), and explainable theoretically by fluorescent Ly α emission in a fully ionised halo (e.g. Dijkstra et al., 2006).

At $z \approx 6.5$, the IGM is expected to always suppress the blue part of the Ly α line completely, while an extended damping wing might also suppress the red part to some extent, as for example found by Laursen et al. (2011), in accordance with previous observational (e.g. Songaila, 2004) and analytical results (e.g. Dijkstra et al., 2007). Therefore, even when leaving the CGM as a Gaussian, the line might be reprocessed to the observed shape through scattering in the IGM. We tested the feasibility of this scenario for *Himiko*.

Assuming that the red slope of the profile is the nearly unprocessed Gaussian, we fit as a first test a line to this part only, similar to the approach used by Matsuda et al. (2006). We always added to the Gaussian a continuum as measured from the spectrum redwards of Ly α. The wavelength interval used for the fit is shown in Fig. 2.8 and ranges from 9236.4 to 9250.0 Å.

The results from the formal fit are a redshift of $6.589^{+0.003}_{-0.013}$, a line FWHM of $768^{+317}_{-91}\,\mathrm{km\,s^{-1}}$ corrected for instrumental resolution, and a line flux of $2.2^{+8.1}_{-0.7} \times 10^{-16}\,\mathrm{erg\,s^{-1}\,cm^{-2}}$ for this full Gaussian. The best fit flux value would correspond to a Ly α luminosity of $1.7 \times 10^{44}\,\mathrm{erg\,s^{-1}}$ after slit loss correction, and is a factor 3.8 larger than the actually measured one.

The obtained $FWHM$ is not unrealistically high. Matsuda et al. (2006) have found for LABs at $z = 3.1$ $FWHM$s of $\gtrsim 500\,\mathrm{km\,s^{-1}}$. These high values were also confirmed by simulations (Yajima et al., 2013a). For high redshift radio galaxies (HzRGs), the determined width would be still at the very lower limit (e.g. van Ojik et al., 1997).

Then, we tested whether the IGM absorption could indeed produce the observed Ly α profile of *Himiko* by fitting to a model where we apply the median IGM absorption curve of Laursen et al. (2011)[19] to a Gaussian, assuming that the Gaussian's peak corresponds to the systemic redshift and convolving the result with the instrumental resolution (Fig. 2.8). For the fit of this combined model, we used a wavelength range including the full profile, ranging from 9220.3 to 9250.0 Å.

Under these assumptions the best fit underlying Gaussian has a redshift of $6.59052^{+0.00006}_{-0.00004}$, a line FWHM of $702^{+12}_{-13}\,\mathrm{km\,s^{-1}}$, and a line flux of $1.76^{+0.02}_{-0.02} \times 10^{-16}\,\mathrm{erg\,s^{-1}\,cm^{-2}}$, where the uncertainties do not take account for the range of possible IGM absorption curves. The result, which is shown in Fig. 2.8 both before and after applying the median IGM absorption curve of Laursen et al. (2011), is surprisingly close to the observed profile save some small discrepancy at the peak. This demonstrates that IGM absorption alone is a valid option for shaping the Ly α profile of *Himiko*.

Summing it up, it is clear that from the observed Ly α shape alone little can be concluded about the full profile before entering the IGM. Therefore, the fraction of Ly α scattered out of the line of sight by the IGM is highly uncertain and upper limits on the flux ratios between rest-frame far-UV lines and those

---

[19] reionization starting at $z = 10$

of Ly α, as required for the discussion in sec. 2.4.4, need to be treated with caution.

The appropriate loss for Ly α can range from nearly zero, as would be the case for a single red peak produced by scattering of Ly α at an expanding optically thick sphere, to an enormous fraction in the case that we are only seeing a strongly suppressed red peak resulting from an infalling medium. Assuming the Gaussian as used for the model shown in Fig. 2.8 and comparing the flux to the actually measured one, about 38 per cent would pass the IGM.

As a compromise we state in the following upper-limits assuming 50 per cent flux loss in the IGM or alternatively, and more conservatively w.r.t to upper limits, zero flux loss to the IGM. In addition to the IGM absorption, the Ly α emission might also be reduced by dust, even so *Himiko* has been constrained to be very dust poor (Schaerer et al., 2015).

2.4.4 IMPLICATIONS FROM UPPER LIMITS ON REST-FRAME FAR-UV LINES

As already outlined in the introduction, there is a range of possible mechanisms proposed to explain the extended emission around LABs. The most popular are photo-ionisation either by a starburst, a (hidden) AGN, or radiative shocks caused by a burst of Sn IIe following the onset of star-formation. Alternatively, the powering mechanism could be gravitational cooling radiation. Possibly, a contribution from several mechanisms is jointly powering *Himiko*. While our upper limit measurements are not suited to identify minor contributions, we can compare them to the expectations for the different mechanisms assuming these as dominating.

For reference, measurements or upper limits on N V, C IV, He II, and C III] from the literature for a selection of composite spectra and interesting individual LABs and LAEs are listed in Table 2.8 and compared to the upper limits obtained by us for *Himiko*. The stated values are normalised by the respective Ly α fluxes.

As Ly α and the other lines might have different spatial extent we calculated the ratio between these lines and Ly α for *Himiko* in two different ways. In both cases we converted before taking the ratio both Ly α and the upper limits to aperture corrected values, but while assuming in the first case that potential emission is as extended as Ly α, we assumed in the second case that the emission from other lines is co-aligned with the continuum. The ratios for the first case are identical to those one would obtain when measuring Ly α in the same aperture as those used for the upper limits, meaning same slit-width and extraction aperture height.

Stellar population

The range of SED models giving reasonable good fits allows for SFR_{100} ranging from about 100 $M_\odot$ yr^{-1} to extreme 2600 $M_\odot$ yr^{-1}. The Ly α fluxes and rest frame equivalent widths for these models are between 6×10^{-17} and 37×10^{-17} erg s^{-1} cm^{-2} and between 72 and 296 Å. These values were extracted from the *Yggdrasil* SEDs by using the same approach as for the observation, meaning a continuum measurement at a rest-frame wavelength of 1262 Å. The same extinction law as for the rest of the galaxy was assumed for Ly α. These values mean that *Himiko*'s observed Ly α flux and EW_0 can easily be accounted for by the strong Pop II star-formation. Even a relatively strong IGM correction or destruction of Ly α by dust in the ISM would not pose a problem.

Still, an interesting question is whether in this heavily star-forming galaxy Pop III star-formation might be ongoing 800 Myr after the Big Bang or whether our upper limit for He II allows to rule it out. The comparison of a measured He II EW_0 to theoretical models can put very strong constraints on the allowed IMF-metallicity-age parameter space. Combining the information about He II with an intrinsic Ly α EW_0 would allow to tighten the constraints even further. However, Ly α's susceptibility to resonance effects weakens its usefulness for this purpose. He II is not affected by this problem. As we do not detect

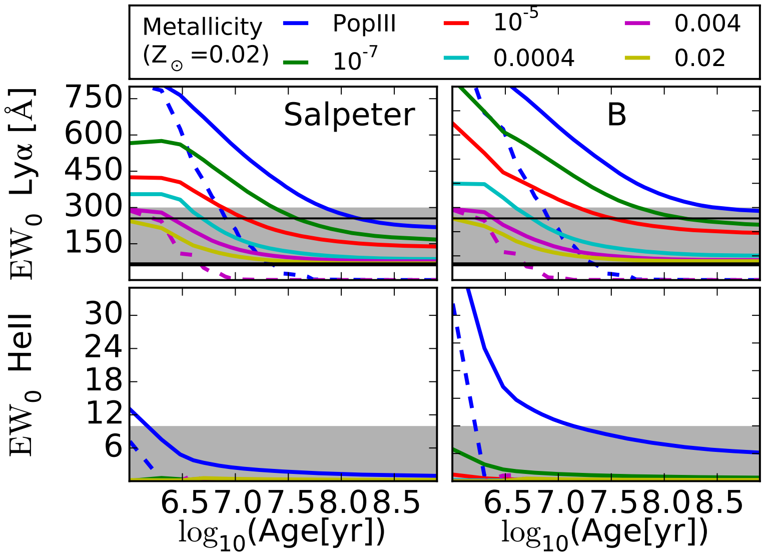

Figure 2.17 Shown are both the Ly α and the He II EW$_0$ for two different IMFs assuming constant star-formation, where B has also a Salpeter slope, but includes stars up to $500 M_\odot$. We are showing the values for 6 different metallicities, ranging from Pop III (Z = 0) to solar metallicity (Z = 0.02). In addition, burst models are included for Pop III and Z = 0.004 as dashed lines. Models have larger EW_0 with decreasing metallicity. The measured Ly α EW_0 is the thick lower horizontal line, while the 3σ upper limit on He II is shown as a shaded area. More details are given in sec. 2.4.4

He II, we can only test whether we would expect for Pop III star-formation He II flux above our non detection limit.[20]

Using the EW_0 prediction for He II and Ly α calculated by Raiter et al. (2010), and following the approach by Kashikawa et al. (2012) for the Lyman-α emitter SDF-LEW-1, we applied this tool to *Himiko*. In Fig. 2.17, the predictions are shown for two different initial mass functions (IMFs) and six different metallicities ranging from zero to solar, and assuming constant star-formation. In addition, both for zero metallicity and $Z = 0.004 = 0.2 Z_\odot$ values are included for burst models. Both IMFs, *Salpeter* and *B*, are power law IMFs with Salpeter (1955) slope of $\alpha = 2.35$, however differing in the mass-range with 1–$100 M_\odot$ and 1–$500 M_\odot$, respectively.

In the figure both the directly observed Ly α EW_0 and the one obtained for the Gaussian fit to the red wing (sec. 2.4.3) are shown as horizontal lines. The range of allowed EW_0's from the SED fitting is indicated as shaded area. For He II, the 3σ upper limit for our fiducial 200 km s^{-1} box is represented as shaded area.

Assuming that the intrinsic Ly α EW_0 is the directly measured one, even a solar metallicity ($Z_\odot = 0.02$) population with standard Salpeter IMF and continuous star-formation would be independent of the age above the observed EW_0. The approximate correctness of the red wing fit would allow for significantly stronger constraints. Then, basically only Pop III and very metal poor models up to $Z = 10^{-5}$ would be allowed for continuous ages larger than about 10 Myr. Populations with higher metallicity would need to be younger. As indicated by our SED fitting, young ages are certainly possible, and very low metallicities are even in the case of the assumed strong IGM absorption not necessarily required.

For a Salpeter IMF with 1–$100 M_\odot$, only an extremely young (< 1 Myr) metal free population could

---

[20] We are referring here as Pop III to a zero metallicity population.

produce a He II EW_0 above the 3σ detection limit of 9.8 Å, independent of IMF, while for the high mass IMF B He II flux would be detectable over a longer period at least for a Pop III. Here, it is important to note that detectable He II would be accompanied by very high Ly α EW_0. Summing it up, it is only a young population combined with an IMF producing very heavy stars, which can be ruled out based on the He II upper limit.

C III], [O III] $\lambda\lambda 1661, 1666$, and at least in some cases also C IV emission, created by photo-ionisation in the H II regions surrounding young high-mass stars, is now understood to be relatively common in low mass galaxies with high specific star-formation rates and low metallicities (e.g. Fosbury et al., 2003; Erb et al., 2010; Christensen et al., 2012; Stark et al., 2014b). While not as strong as in AGNs, the typically strongest of these lines is C III], which has been found with EW_0 up to $\sim$ 15Å (Stark et al., 2014b).[21] A detection of this line seems to be correlated with high Ly α EW, with the correlation probably being a result of both line-strengths depending on metallicity (Stark et al., 2014b).

Our 3 σ upper limit for C III] EW_0 is due to the lines' location between J and H band with $EW_0 <$ 23Å for the 200 km s^{-1} extraction box larger than the observed values. Only if the lines were close to unresolved and the velocity offset with respect to peak Ly α would allow for relatively high transmittance (cf. Fig. 2.9), a detection would have been feasible. Similar, one or both of the [O III] $\lambda\lambda 1661, 1666$ lines, which can be almost as strong as C III], would be only for very specific velocity offsets w.r.t to Ly α within the skylines gaps. Therefore, little can be concluded from these non-detections about the presence of a substantial population of young massive stars, which in principle could help to break the degeneracy in the SED fitting.

Illumination by (hidden) AGN

Quasars are well known to be responsible for strong Ly α emission in so called extended emission line regions, EELRs, spreading in some cases over several 100 kpc. When being switched on during the phase of cold gas accretion, Haiman & Rees (2001) predicted this emission to originate from the illumination of primordial gas. However, at least at lower redshifts, the illuminated gas is more likely ejected galaxy material driven out by either SNe or the jets of the AGN itself (e.g. Villar-Martín, 2007), resulting in the illumination of metal enriched gas and hence a multitude of emission lines.

With *Himiko's* three spatially distinct components all located within about 6 kpc transverse distance and no strong evidence for much difference in the line of sight direction, they are likely in the process of merging and hence triggered AGN activity is not unlikely. Further, Ly α emission powered by AGNs is a common and expected phenomenon. When considering AGNs, it can be useful both to subdivide between radio-quiet and radio-loud (e.g. McCarthy, 1993), and between obscured ('type II') and non-obscured ('type I') by a dusty torus. Extended emission has been found for all cases (e.g. Matsuoka, 2012). In the following we are discussing all four options for *Himiko*, especially w.r.t to our non-detection limits.

As discussed by Ouchi et al. (2009), neither of the existing X-ray (XMM-Newton), 24μm (*Spitzer* MIPS), and sub-mm (850μm SCUBA) data is deep enough to rule out a type I quasar, when scaling the Elvis et al. (1994) quasar template to the rest-frame VIS *IRAC*1 flux. However, there is a strong argument against a type I AGN in the Ly α width, which is even after accounting for IGM absorption too narrow to be originating from a type I AGN (cf. sec. 2.4.3). Another argument against a quasar, at least for the two eastern components, is the continuum slope. Davis et al. (2007) find for SDSS quasars a mean slope of $\beta = -1.63$[22] and very few objects with slopes bluer than $\beta = -2.0$ for the wave-length range between 1450Å and 2200Å. Although the redshifts of this sample is limited to $1.67 \leq z \leq 2.09$, we do

---

[21] In the spectrum of the Lynx arc (Fosbury et al., 2003) higher *EW*s have been measured for these rest-frame UV lines. However, these extreme *EW*s are not in agreement with self-consistent photo-ionisation models and might be a result of differential gravitational lensing between illuminated gas and illuminating stars (e.g. Villar-Martín et al., 2004).

[22] Converted from the ν^{α} as stated in Davis et al. (2007) to λ^{β}

not expected the quasar spectra to be much bluer for higher redshifts. Therefore, in these components the SED is unlikely dominated by direct continuum emission from the accretion disk. Finally, our $3\,\sigma$ upper limit on C IV/Ly α of 0.13, using the $600\,\mathrm{km\,s^{-1}}$ aperture and assuming a crude IGM correction of a factor two is two times below the typical value for type I quasars in the composite spectrum of Vanden Berk et al. (2001). Certainly this comparison falls somewhat short, as a C IV width of $600\,\mathrm{km\,s^{-1}}$ is too low for a type I quasar, while much higher widths are not justifiable based on our observed Ly α line width.

By contrast, *Himiko's* Ly α width is an option for the extended emission line regions around quasars, may it be either a powerful high redshift radio galaxy (HzRG) or radio quiet type II quasar. While typical Ly α line widths of $\sim 1000\,\mathrm{km\,s^{-1}}$ seem somewhat high compared to *Himiko*'s measured one, it might be possible to explain such a width under the assumption of strong IGM absorption (cf. sec. 2.4.3). Further, it is known that HzRGs with very relaxed kinematics exist. MRC 0140–257 has over the complete nebula Ly α $FWHM \lesssim 500\,\mathrm{km\,s^{-1}}$ (Villar-Martín et al., 2007), with very narrow emission in the peaks of Ly α surface brightness ($FWHM \sim 250\,\mathrm{km\,s^{-1}}$). Also, while the extended Ly α emission around HzRGs is usually spatially kinematically disturbed by several $100\,\mathrm{km\,s^{-1}}$, MRC 0140–257 has comparable low velocity offsets. *Himiko* would need to be similar to this rather special object, as we see in our stacked spectrum no evidence for strong velocity gradients (cf. both Fig. 2.6 and 2.7), keeping in mind that the stack is a superposition of different slit angles. However, also in the spectrum of Ouchi et al. (2009), who observed with a fixed slit position, only a small Ly α velocity gradient of $60\,\mathrm{km\,s^{-1}}$ is found over the east-west direction.

Comparing the rest-frame UV and optical photometry, we find that the magnitudes measured for *Himiko* are indeed values reasonable for those expected from HzRGs, when taking the strong and extended emission in the EELRs into account. Assuming a flat continuum in $f\nu$ and H_{F125W} (24.93 mag) as normalisation, we can estimate the flux due to emission lines in IRAC1 and IRAC2 to $14.8\times10^{-17}\,\mathrm{erg\,s^{-1}\,cm^{2}}$ and $4.8\times10^{-17}\,\mathrm{erg\,s^{-1}\,cm^{-2}}$, respectively, corresponding to a ratio of 3.1. Summing up the relevant line fluxes in the HzRG composite spectrum of Humphrey et al. (2008), a typical emission line flux ratio of 3.0 between IRAC1 and IRAC2 would be obtained, [23] consistent with that measured for *Himiko*. Assuming that about 70 per cent of the line flux in IRAC1 is due to [O III] $\lambda5007$, the [O III] $\lambda5007$ rest-frame EW_0 would be 1400 Å. Such a value is not unrealistic for HzRGs (e.g. Iwamuro et al., 2003). Finally, based on the [OIII] flux estimated above, *Himiko*'s Ly α flux would be using the Humphrey et al. (2008) average ratio expected to be a factor 1.7 higher than the actually observed one. This factor is easily within the uncertainty of the IGM absorption.

While this similarity in line ratios is interesting, it is not entirely surprising when considering our best fit stellar SED model. Humphrey et al. (2008) conclude, that the line emission in these HzRGs is not mainly powered by the interaction of the radio lobes with the gas, but rather by photo-ionisation, and that the illuminated gas has typical metallicities of $Z = 0.2Z_{\odot}$.

A means to discern between an AGN or a young stellar population as ionising source would be through the strength and ratios of rest-frame far-UV emission lines. The ratios between these lines and Ly α are in general expected to be stronger, when being powered by an AGN. A complicating factor when interpreting non-detection limits is the extent of the possible line emission. Extended Ly α emission could be a consequence of resonant scattering or of in situ production by ionising radiation escaping the ISM. In the first case other emission lines would be almost co-aligned with the UV continuum, while in the latter case they could be spatially extended as the Ly α emission (e.g. Prescott et al., 2015), resulting for our object in a larger slit-loss.

The typical ratio between C IV and Ly α in the Humphrey et al. (2008) composite is with 0.15 similar to the 3σ upper limit for our target, when assuming the $600\,\mathrm{km\,s^{-1}}$ extraction box and a crude Ly α IGM

---

[23] The relevant lines in IRAC1 are He II $\lambda4686$, Hβ, and [O III] $\lambda\lambda4959, 5007$ and in IRAC2 O I $\lambda6300$, Hα, and [N II] $\lambda\lambda6548, 6583$.

correction of a factor two, which corresponds to C IV/Ly $\alpha < 0.13$ and < 0.18 assuming a spatial extent similar to the continuum or the Ly α emission, respectively. Also the typical He II/Ly α of 0.09 would be detected with at least 3σ even for He II emission as extended as Ly α, assuming again the crude IGM correction and the wider extraction box. The advantage of He II is that it would be present even when assuming primordial composition of the illuminated gas.

Another problem with the interpretation of *Himiko* as a HzRG is the available $100\,\mu$Jy 1.4 GHz VLA upper limit (Simpson et al., 2006). Assuming example radio spectral indices of −0.5, −1.0, and −1.5, with ultra steep slopes more typical for high-z galaxies, this corresponds to $L_{1.4GHz}$ of 1.8×10^{25}, 5.0×10^{25}, 1.4×10^{26} W Hz^{-1}. Converted to 5 GHz the upper limit would be around 1–2$\times 10^{25}$ W Hz^{-1} and hence at the very lower limit of what would be according to the classification by Miller et al. (1990) still be considered a radio-loud galaxy. On the other hand, if the main ionising source for the EELRs is photoionisation by the quasar and not the radio jets, the non detection in the radio data is not ruling out the possibility of a hidden AGN as powering source. Indeed, EELRs have been found around the less known population of radio-quiet type II quasars (e.g. Gandhi et al., 2006; Villar-Martín et al., 2010).

For several among the $z \approx 2$–3 LABs, a hidden AGN has been identified at least as a partial contributor to the Ly α ionising flux. E.g., the blob of Dey et al. (2005) at $z \approx 2.7$ shows clear indication of a dust-enshrouded AGN, producing both He II and C IV emission with relatively narrow width (~ 365 km s^{-1}). Scaling the strength of the lines to our Ly α surface brightness, both lines should be detected.

For the narrow-lined AGNs among those UV selected galaxies by Steidel et al. (2004) at $z \sim 2$–3 (Hainline et al., 2011), the ratios between the rest-frame far-UV lines and Ly α would be even higher.

In addition to the constraints presented here, Baek & Ferrara (2013) have recently argued for a criterion to discriminate between LABs being powered by either star-formation, Compton-thin, or Compton-thick AGNs based on the combined information about the observed surface density profile and skewness of the Ly α line. They seem to conclude that *Himiko* is not in the right region of the parameter space for having an AGN as source.

Gravitational cooling radiation

Early semi-analytical models assumed that the gas feeding a halo is heated to the virial temperature. However, cosmological SPH simulations indicate that the majority of the infalling gas might never reach these high temperatures (Fardal et al., 2001). Under the assumption of primordial element composition, meaning basically only H and He, the major cooling channel of the gas is consequently not through Bremsstrahlung, as for gas with temperatures above $10^6 K$, but through collisional excitation of hydrogen and, depending on the temperature, also through He II. Collisional excitation cooling peaks at $10^{4.3}$K and 10^5K for H I and He II, respectively.

For several observed LABs in the literature, it has been suspected that cooling radiation is the major driver of the extended Ly α emission. For instance, Nilsson et al. (2006) had favoured this scenario for their LAB at $z = 3.16$, as they could not identify an obvious counterpart, even in deep GOODS *HST* imaging. Recent reanalysis of this object based on the extended availability of multi-wavelength data in the field allowed to identify one of the objects in the field, being located at a distance of about 30 kpc from peak Ly α emission as an obscured AGN (Prescott et al., 2015). Unfortunately, no spectrum deep enough to seriously probe He II and the other rest-frame far-UV lines is available for this object.

A LAB, where He II has been observed, is the one by Scarlata et al. (2009). While an AGN can also be identified photometrically within this object, they favour gravitational cooling radiation being at least partially responsible for He II because of the non-detection of C IV.

The He II luminosity of 8×10^{41} erg s^{-1} within their extraction mask would correspond at $z = 6.595$ to a flux of 1.6×10^{-18} erg s^{-1} cm^{-2} , a flux which would not be safely detectable by us. On the other hand, scaling He II to the higher Ly α surface brightness in *Himiko*, we would be able to significantly detect it (cf. Table 2.8).

The question is whether the corresponding high He II luminosity would be at all feasible for cooling radiation and whether a substantial amount of the Ly α emission could originate from cooling radiation. Insight can be gained by comparison to published results from simulations.

As a relatively narrow line is predicted for He II by the simulations (Yang et al., 2006), we compare to the 3σ upper limit of our standard $200\,\mathrm{km\,s^{-1}}$ aperture. This limit corresponds to a luminosity of $L_{\mathrm{He\,II}} = 1.5 \times 10^{42}\,\mathrm{erg\,s^{-1}}$, a value high compared to the luminosities of even the heaviest halos in the simulations of Yang et al. (2006).

Yajima et al. (2012) have run a hydrodynamical simulation combined with Ly α radiative transfer, including all radiative cooling and heating, star-formation in a multi-phase ISM, stellar feedback, and UV background. Their simulation traces a halo developing a Milky Way size galaxy over cosmic times. We have extracted from their presented evolution plots several quantities at redshift $z = 6.6$. A fraction of 65 per cent of Ly α is predicted by them to be due to cooling radiation, mainly created within the cold accretion streams, where the total Ly α luminosity is $L_{\mathrm{Ly}\alpha} = 4.5 \times 10^{42}\mathrm{erg\,s^{-1}}$. Therefore, even before correcting for IGM absorption and before applying a surface brightness threshold, the Ly α luminosity is more than a factor ten lower than *Himiko*'s Ly α luminosity.

Taken this and the fact that the SED fitting suggest vigorous star-formation, it is unlikely that a major fraction of *Himiko's* Ly α luminosity is produced by cooling radiation. Therefore, as each particle in the simulations of Yang et al. (2006) has $f_{\mathrm{He\,II}\lambda1640} \leq 0.1 \times f_{\mathrm{Ly}\alpha}$, the He II flux is not very likely to be detectable and no strong conclusions can be drawn from the non-detection.

Shock ionisation

Another possible explanation for strong and extended Ly α emission are large scale shock-super-bubbles (Taniguchi & Shioya, 2000), which might be the consequence of galactic winds powered by a large number of core-collapse supernovae within the first few 100 Myr after the onset of the initial starburst (Mori et al., 2004; Mori & Umemura, 2007). Assuming that the kinetic energy of the SN ejecta is converted into radiation by fast-shocks and combining information on C IV/He II and N V/He II ratios with a measured line width, one could get insight into the feasibility of this mechanism as contributing power source for the extended Ly α emission by comparison to shock model grids (e.g. Allen et al., 2008). In absence of a significant detection of at least one of the lines, such an analysis is not feasible.

2.5 CONCLUSION

With our analysis we add further hints to the puzzle of what is powering the remarkable Ly α emitter *Himiko*.

First, we have detected a continuum in the spectrum showing a clear break at the wavelength of Ly α, ruling out any remaining chance of it being a lower redshift interloper. The fact that the continuum appears like a single step function indicates that there are no large velocity differences between the three distinct UV bright components.

From SED fitting, including CANDELS J_{F125W} and H_{F160W} data, we argue for a young and heavily star-forming stellar population, with a total stellar mass of the order $10^9 M_\odot$ and a metallicity of $Z = 0.2Z_\odot$, with the bright *IRAC1* magnitude explained by very strong [O III] emission. While we find that similar broadband magnitudes would also be produced by lines in the extended emission line regions around high redshift radio galaxies, this scenario is for several reasons more unlikely. Among them is the most important result of this work. Our upper limits on important rest-frame far-UV lines are clearly disfavouring an AGN as sole powering source for the extended Ly α emission. Due to the natural lack of

Table 2.8 Line ratios of He II, N V, C III], and C IV to Ly α as found in samples and individual objects by various studies. Upper limits are $3\,\sigma$. References: [0] : Line ratios as measured in this study for *Himiko*. The ratios are calculated based on slit-loss corrected fluxes. While we have for Ly α assumed a spatial extent given by the narrowband NB921 image, the other lines were corrected under the assumption that they are distributed as the continuum. If they were as extended as the resonant Ly α line, the upper limits would be a factor 1.5 and 1.4 less stringent for N V and the three lines in the NIR arm, respectively. The non-detection limits are stated for our two fiducial boxes. Values in brackets are assuming a crude IGM correction of a factor two. [1] : SDSS quasar composite spectrum (Vanden Berk et al., 2001) [2] : Composite spectra for AGNs among rest-frame UV selected galaxies (Hainline et al., 2011). The sample is split into those with high and low Ly α EW_0. To convert the values and the spread in the samples stated by Hainline et al. (2011) to values and spreads for the fluxes, we have used the continuum slopes of $\beta = -0.1 \pm 0.4$ and $\beta = -0.5 \pm 0.3$ stated by them for the composite spectra of the high and low EW_0 sample, respectively. [3] : Sample of nine high-redshift radio galaxies (Humphrey et al., 2008) [4] : Prescott et al. (2009) Values are for their night 1. Ly α flux based on same aperture as other lines. [5] : Dey et al. (2005) Ly α flux is based on same aperture as other lines. [6] : Scarlata et al. (2009) referring to component *Ly1*; Ly α flux based on same aperture as other lines. [7] : $1\,\sigma$ He II detection from *HST*/WFC F130N NB imaging (Cai et al., 2011) [8] : He II non-detection for extreme Ly α $EW_0 \approx 900$Å object (Kashikawa et al., 2012) [9] : He II non-detection for SDF J132440.6+273607 (Nagao et al., 2005) [10] : $10^9\,M_\odot$ LAE at z=2.3, showing strong He II and C III] emission likely powered by star-formation (Erb et al., 2010).

	Ly α	N V	C IV	He II	C III]
			Himiko		
Based on aperture corrected line-fluxes and upper limits without (with) IGM correction.					
box: 200 km s^{-1}; $v_{\rm off} = -250$ km s^{-1}	1.00	< 0.04 (< 0.02)	< 0.15 (< 0.07)	< 0.07 (< 0.03)	< 0.12 (< 0.06)
box: 600 km s^{-1}; $v_{\rm off} = -250$ km s^{-1}	1.00	< 0.08 (< 0.04)	< 0.25 (< 0.13)	< 0.10 (< 0.05)	< 0.18 (< 0.09)
			Composite spectra		
Broad-line AGN [1]	1.00	0.03	0.25	0.005	0.16
Narrow-line AGN [2] $EW_{Ly\alpha} > 63$ Å	1.00	0.05 ± 0.01	0.20 ± 0.04	0.07 ± 0.02	0.16 ± 0.07
Narrow-line AGN [2] $EW_{Ly\alpha} < 63$ Å	1.00	0.16 ± 0.05	0.25 ± 0.09	0.17 ± 0.06	0.17 ± 0.09
Radio-galaxies ($z \sim 2.5$) [3]	1.00	0.04	0.15	0.09	0.06
			Example LABs		
LAB PRG1 ($z = 1.67$) [4]	1.00	< 0.39	< 0.09	0.12	< 0.07
LAB ($z = 2.7$) [5]	1.00	< 0.02	0.13	0.13	0.02
LAB ($z = 2.38$) [6]	1.00	N/A	< 0.45	0.36	N/A
			Example LAEs		
LAE IOK ($z = 6.96$) [7] N/A	1.00	N/A	N/A	0.06 ± 0.05	N/A
LAE SDF-LEW-1 ($z = 6.5$) [8]	1.00	N/A	< 0.013	< 0.015	N/A
LAE SDF ($z = 6.33$) [9]	1.00	N/A	< 0.675	< 0.340	N/A
BX418 [10]	1.00	N/A	abs	0.034	0.048

knowledge about the appropriate slit-loss, line-width, and systemic redshift and the spread in line-strength for AGNs, it is not entirely impossible that an AGN has escaped our detection.

2.6 ACKNOWLEDGMENTS

Based on observations made with ESO telescopes at the La Silla Paranal Observatory under programme ID 087.A-0178(A). The Dark Cosmology Centre is funded by the DNRF. JPUF and PL acknowledge support from the ERC-StG grant EGGS-278202. This work is based on observations taken by the CANDELS Multi-Cycle Treasury Program with the NASA/ESA *HST*, which is operated by the Association of Universities for Research in Astronomy, Inc., under NASA contract NAS5-26555. This research made use of Astropy, a community-developed core python package for Astronomy (Astropy Collaboration, 2013). We thank Martin Sparre for providing us with his python XSHOOTER pipeline manager, and Nobunari Kashikawa and Yoshiaki Ono for providing us with information.

3

TOGETHER WE ARE DEEPER

Searching for neutral hydrogen halos around LAEs at z = 2.3

Johannes Zabl[1], **Sangeeta Malhotra**[2], **James Rhoads**[2], **Lise Christensen**[1], **Johan P. U. Fynbo**[1], **Palle Møller**[3]

[1] Dark Cosmology Centre, Niels Bohr Institute, University of Copenhagen, Juliane Maries Vej 30, 2100 Copenhagen, Denmark
[2] School of Earth and Space Exploration, Arizona State University, Tempe, AZ 85287
[3] European Southern Observatory, Karl-Schwarzschild-Straße 2, 85748 Garching bei München, Germany

Prepared for submission

Abstract

Observational studies have with increasing strength over the last two decades shown that star-forming galaxies are surrounded by extended Lyman-α halos, most likely due to resonant scattering of Ly α photons on or ionization and subsequent recombination of extended reservoirs of hydrogen surrounding high-z galaxies. A possible decrease in the extended Lyman α emission from higher redshifts to $z \sim 2$ is widely debated, as contradicting results about the existence of halos at this redshift have been found. Motivated by this, we present here results for a search of extended Ly α halos in an independent sample of typical field Ly α emitters at $z = 2.26$. Our results are based on a sample of 73 objects. Despite the relatively small sample size, we detect statistically significant extended emission with a scale length of 11.2 ± 1.7 kpc and a central surface brightness of $5 \pm 2 \times 10^{-18}$ erg s^{-1} cm^{-2} arcsec^{-2}, which is consistent with other studies at several redshifts. Hence, we do not find evidence for a strong redshift evolution in the redshift range from 2 to 3.

3.1 Introduction

Star-forming galaxies have by definition a young stellar population and hence a substantial amount of massive and hot stars, which produce a significant amount of photons with energies capable of ionizing hydrogen. Surrounding the young stars, in so called H II regions, hydrogen ionization and recombination rates are in equilibrium. During each recombination, hydrogen emission lines corresponding to different transitions are created in the cascade (e.g. Pengelly, 1964; Brocklehurst, 1971). The strongest line by far is Ly α, being produced in 68% of the recombinations assuming generic Case B assumptions (e.g. Dijkstra, 2014), and carrying as much as 10% of the galaxy's bolometric luminosity (e.g. Partridge & Peebles, 1967).

Yet, Ly α is often not as strong as expected. For example, only about 25% of the Lyman break selected galaxies show Ly α emission with a rest-frame EW_{rest} above 20 Å (e.g. Shapley et al., 2003). Star-forming galaxies with Ly α emission above this equivalent-width threshold are typically referred to as Lyman α emitters (LAE). The volume averaged, global Ly α escape is at $z = 2.2$ about 5% (Hayes et al., 2010). This escape fraction decreases towards lower redshifts and increases towards higher redshifts with a peak at around $z = 6$ (e.g. Hayes et al., 2011b; Blanc et al., 2011), above which the increasingly neutral IGM becomes important. It is important to keep in mind that LAE samples have by construction high Ly α escape. The average escape fraction for individual LAEs has large scatter but seems relatively constant with redshift, as found by Blanc et al. (2011) for the range $1.9 \lesssim z \lesssim 4$ with a median value of about 30%. This value was derived by comaprison to reddening corrected UV star-formation rate (SFR) estimates. The value is consistent with lower limits obtained from comparison to other SFR estimators, like X-ray (Zheng et al., 2012) or far-infrared (Wardlow et al., 2014).

The reason for the suppression is that Ly α, due to its resonance nature, is susceptible to scattering at each hydrogen atom in the ground state. The resulting increased path length increases the chance for a Ly α photon to be destroyed by a dust grain substantially compared to that for a continuum photon at similiar wavelength, at least as long as the interstellar medium (ISM) is not clumpy (Neufeld, 1991). It is still open to debate how much dust exists in those objects which actually show Ly α (e.g. Laursen et al., 2009b; Nilsson et al., 2009; Pentericci et al., 2009; Finkelstein et al., 2009; Blanc et al., 2011; Song et al., 2014).

When Ly α is not destroyed by dust, the multiple scatterings will have the effect that Ly α diffuses. Hence, galaxies might present themselves as diffuse halos in Ly α with a larger extent than in the ionizing radiation. Depending on the kinematics and geometry of the interstellar medium (ISM), this dillution can be on smaller scales within the ISM, but the light might also be scattered within the CGM or the IGM, as predicted by simulations (Laursen & Sommer-Larsen, 2007; Zheng et al., 2011).

During the last decade it has become observationally clear that emission more extended than the continuum is indeed not a rare phenomenon, observed both in the high spatial resolution UV images of local galaxies (Östlin et al., 2009; Hayes et al., 2013) and at redshifts allowing for Ly α imaging in the rest-frame optical (Møller & Warren, 1998; Fynbo et al., 2001, 2003). However, in other individual LAEs no clear detection of extended emission has been found (Bond et al., 2010), an indication for the heterogeneity of the LAE population.

Individual LAEs with extraordinary extended strong Ly α emission have been found at all cosmic times between $2 \lesssim z \lesssim 7$ (Steidel et al., 2000; Matsuda et al., 2004; Saito et al., 2006; Yang et al., 2009; Ouchi et al., 2009; Prescott et al., 2012), with LAEs above a somewhat arbitrary size threshold often referred to as a separate class of objects, so called Lyman α blobs (LAB). Different physical mechanisms for the extended Ly α production have been discussed, being gravitational cooling radiation (Dijkstra & Loeb, 2009), galactic super winds (Taniguchi & Shioya, 2000), or photo-ionization by a central ionization source. In the latter case this might be an AGN (Haiman et al., 2000), for which in several cases direct evidence has been found (e.g. Weidinger et al., 2004), but young stars being produced in a burst of star-

Table 3.1 SExtractor parameters used at different steps in the analysis.

	Centroid	Background	Object mask
DETECT_THRESH	1.2	0.55	0.55
DEBLEND_MINCONT	0.005	0.005	0.001
DEBLEND_NTHRESH	32	32	64
DETECT_MINAREA	4	9	9
WEIGHT_TYPE	BACK	BACK	BACK
BACK_SIZE	64	240	512
BACK_FILTERSIZE	3	5	3
BACKPHOTO_TYPE	LOCAL	GLOBAL	GLOBAL

formation might be the most likely explanation for other LABs (Yajima et al., 2013b; Geach et al., 2014). Apparent extended emission might also be the result of Ly α emission from clustered objects below the individual detection threshold in the continuum (e.g. Zheng et al., 2011).

Rauch et al. (2008) found based on a blind long-slit search for Ly α emission a population of low luminosity Ly α emitters at $z \sim 3$, showing in the stack of their Ly α spectra radially extended surface-brightness profiles out to 30 kpc. Recently, stacking analysis of Ly α narrowband (NB) images have revealed that low surface-brightness extended emission over several tens of kpc is a typical property of LAEs and even of star-forming galaxies, which are not classified as LAEs based on typical aperture photometry (Steidel et al., 2011). The presence of the halos might be even anti-correlated with the central Ly α EW (Feldmeier et al., 2013). A clearer correlation has been found between the LAE overdensity and the strength of these Ly α halos (Matsuda et al., 2012), in a sense that for fixed continuum magnitude the Ly α halos are brighter the denser the environment. In this picture, at least some of the LABs might just be objects in the densest environments, where more of the iceberg is visible above the surface brightness threshold of the observation.

Based on the study of Feldmeier et al. (2013) the question arose whether there might be some evolution of the halos between $z = 3$ and $z = 2$, as they did not find halos at $z = 2$, but some indication at $z = 3$, adding to the controversial discussion about the evolution of LAEs between $z = 3$ and $z = 2$ (e.g. Nilsson et al., 2009, 2011; Acquaviva et al., 2011). One possible explanation for the non-finding of these halos is the depth of the samples. In a recent study Momose et al. (2014) have found based on their very large sample of LAEs halos with similar extent at all redshifts between $z = 2$ and $z = 6.6$, with little evolution of the halo properties. Further evidence against the omnipresence of strong halos was given at high redshifts by the study of Jiang et al. (2013b). By carefully discussing possible systematics Feldmeier et al. (2013) also opened the question, whether detected halos may at least be partially the consequence of systematics existing in data taken with wide-field instruments.

Considering the heterogeneous properties of LAEs, especially at $z \sim 2$ it is important to compare results from as many different samples as possible. One of the Ly α samples at this redshift is the sample of Nilsson et al. (2009). Nilsson et al. (2009) and Nilsson et al. (2011) have performed a detailed analysis of the physical properties of these galaxies, mainly through SED fitting. In our study we revisit this sample to study the extension of the Ly α emission on large spatial scales through a stacking analysis.

Throughout the paper a $\Omega_{\mathrm{m},0} = 0.3$, $\Omega_{\Lambda,0} = 0.7$, $H_0 = 70$ km s^{-1} Mpc^{-1} cosmology is assumed, in which 1$''$ corresponds at $z = 2.26$ to 8.23 kpc.

3.2 DATA

We were using for our analysis 27.7 h data taken with a NB filter in the Wide-Field Imager (WFI) at the MPG/ESO 2.2m telescope. The filter has a FWHM of 129 Å at a central-wavelength of 3963 Å (Nilsson et al., 2009) and is referred to as N396. The covered area, being a part of the COSMOS field, is centered on RA = +10°:00′:27″.5 and Dec = +02° :12′:23″, and has a size of 33′ × 32′.

These N396 data have been used in previous publications (Nilsson et al., 2009, 2011) and we refer to Nilsson et al. (2009) for details about the reduction. As a starting point for our work, we used the fully reduced but not background subtracted N396 image. In addition, we made use of the COSMOS mosaics for u^* based on observations with CFHT/Megaprime, and B_J and V_J taken with Subaru/Suprime-Cam (Taniguchi et al., 2007; Capak et al., 2007).

We put the N396 image on the same astrometric system as used for the COSMOS mosaics. More specifically, we matched the N396 image to the B_J image by finding the astrometric solution using scamp (Bertin, 2006, V2.0b12) and then resampling the N396 image using swarp (Bertin et al., 2002, V2.17.6). The matching was done based on objects having in B_J a SExtractor *CLASS_STAR* > 0.7 and S/N between 30 and 2000 and for the resampling *LANZCOS3* interpolation was employed. We remark that the N396 mosaic available to us has been resampled for a first time with a pixel scale of 0″.2 for the original reduction (Nilsson et al., 2009), differing from WFI's native pixel scale of 0″.238. As the PSF with a FWHM of 1″.1 or 4.6 native pixels is oversampled, resampling is not expected to impact the search for extended emission.

The N396 photometric zeropoint (ZP) was determined w.r.t to photometry in the COSMOS u^* and B_J mosaics, the ZPs of which we corrected by the ZP offsets found by Muzzin et al. (2013) based on comparing photo-z fitting to a spectroscopic training sample. From the photometry (MAG_AUTO) in these two bands we estimated the magnitude at the wavelength of the N396 filter determined as a linear combination of the magnitude in u^* and B_J, $N396_{\rm est} = u^* - 0.17(u^* - B_J)$, which would be for power law spectral energy distributions exactly correct, independent of the slope. We then obtained the N396 ZP by imposing the requirement $N396 - N396_{\rm est} = 0$ to point sources with sufficient S/N but no saturation in either of the filters. As there was only a small overlap between suitable point-sources in the three filters (55), the determined ZP might have some uncertainty. Fluxes and magnitudes for the galaxies are further corrected for galactic extinction using a Cardelli et al. (1989) Milky Way extinction curve assuming an $E(B - V) = 0.019$, a value appropriate for the region covered by the observations (Schlegel et al., 1998).

As the background in the image has non-negligible structure (cf. also Nilsson et al. 2009), we removed the background carefully. As a first step we determined a global background map by fitting a bicubic spline to a 36″x36″ mesh smoothed with a 4x4 median filter. This was done with SExtractor using the parameters 'background' in Table 3.5.

3.3 SAMPLE

Our analysis is based on the sample of LAE candidates as first discussed in Nilsson et al. (2009) and refined in Nilsson et al. (2011). The initial sample consisted of 187 objects selected by means of a NB excess to have a Lyα equivalent width of $EW_0 > 20$Å ($EW_{obs} > 65$Å).[1] Nilsson et al. (2009, 2011) identified objects which were found not to be LAEs at $z = 2.26$, excluded through VIMOS spectroscopy, or found to be AGNs, identified from detections in X-ray data by Chandra or XMM and in radio data from the VLA. This results in the removal of 43 objects.[2] About 40% of the initial objects are without

---

[1] We did not include 11 objects, which have been added to the Nilsson et al. (2009) sample based on spectroscopic results for the Nilsson et al. (2011) sample.

[2] In the list available to us we are missing one not confirmed in each of the four categories: LAE best, GALEX only, AGN only, GALEX+AGN of Table 1 in Nilsson et al. (2011)

Table 3.2 Listed is the number of LAEs in the sample, subdivided by different criteria. The two visual classification groups, A and B, are described in sec. 3.3.

Visual group	A	B	Σ^{a}
LAE + AGN [b]	101	39	140
LAE	83	36	119
LAE ($m[N396; 1'' > 25.1]$)	73	33	106
LAE GALEX	4	5	9

[a] A + B [b] Classification based on criteria in Nilsson et al. (2011)

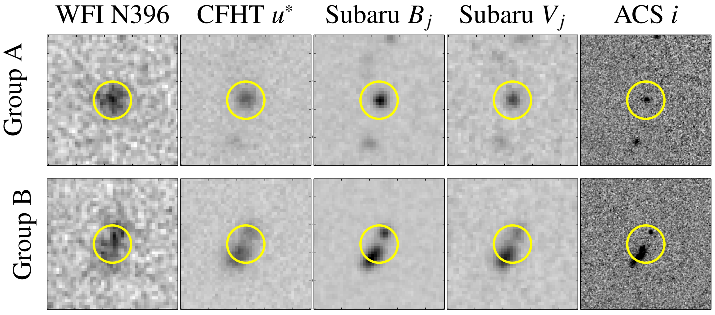

Figure 3.1 Examples for objects in the visual classification groups A and B (cf. sec. 3.3). 7″ cutouts are shown for both objects in five filters. *ACS i* is the COSMOS HST ACS/F814W filter. The images are not seeing convolved. The yellow circle has a radius of 1″.

follow-up spectroscopy and therefore a fraction of interlopers is possible.

We created for this work a very strict visual mask, which we not only use during the creation of the stacks, but also for refining the sample. This mask excludes regions in the data affected by visible

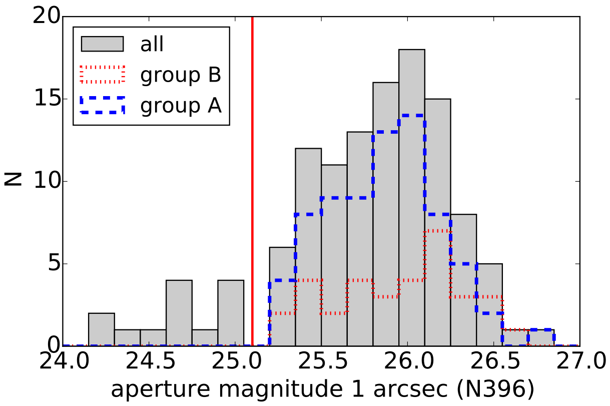

Figure 3.2 The magnitude histogram of all 119 LAEs in the sample. Subhistograms are shown for those non-rejected LAEs, being in group A (isolated) or group B (close partner(s)), respectively, and not being in the bright tail. Indicated is the magnitude cut used to separate the bright from the typical objects.

blooming and reflections. Regions around bright stars are in general masked very conservatively. As we created stacks for the same objects also in three broadband (BB) filters, region masks for the four filters were exclusively combined to create a master region mask. In cases where a LAE was coincident with a masked region, we excluded this object completely. Further, we removed all objects, which had a saturated pixel within 30″ around the object in the N396 filter or which are close to the field boundary. These strict criteria exclude 25 further objects from the sample, leaving a sample of 119 LAEs.

The remaining objects were further subdivided by visually classifying each of the objects into one of two groups. As the $\mathrm{B_J}$ data is about 1.3 magnitudes deeper than the N396 data (Capak et al., 2007; Nilsson et al., 2009), we used for the visual classification the $\mathrm{B_J}$ data.

- *Group A:* Objects which appear in the optical $\mathrm{B_J}$ imaging as compact sources, with the closest neighbor separated more than 1″ at the lowest visibly discernible surface-brightness level. Such objects could have in HST/ACS F814W either a single peak or multiple densely clustered H II regions.

- *Group B:* Objects, where a close-by component is visible in the deep $\mathrm{B_J}$ image, often with a morphology strongly indicating merging. We put objects into this group, either if the objects are less than 1″ separated based on the visible extent in $\mathrm{B_J}$, and/or if the NB centroid lies between the sources identifiable in $\mathrm{B_J}$. The group also includes one object which is extended in the continuum. Examples both for group A and B are shown in Figure 3.1.

Finally, we subdivided the sample by the N396 aperture magnitude within 1″, where we used a 25.1 mag cut, motivated by the magnitude distribution of the objects (Figure 3.2). The small number of 13 objects brighter than the magnitude cut contain 27% of the total flux obtained by summing up the flux of all objects. Therefore, it makes sense to exclude them, when doing a non-scaled mean stack.

We refer in the following to the subset of 73 LAE with $m[N396; 1" > 25.1]$ in group A as the *stacking sample*. All centroids, magnitudes, and $R_{1/2}$ were determined with the SExtractor parameters referred to as 'centroid' in Table 3.1. Nilsson et al. (2009) derived for the sample a 90% luminosity completeness limit of $\log_{10}(L_{\mathrm{Ly}\alpha}) = 42.44$. Four out of the 73 objects in our sample are below this limit.

The half-light radii, $R_{1/2}$, as determined with SExtractor from the N396 image of the objects in the *stacking sample* have a median of 0″.75, which is above the extent of the PSF ($R_{1/2} \approx 0''.55$). The three objects with the maximal extent have half light radii of $R_{1/2} = 1''.10$, 1″.12, and 1″.31, respectively.

In the following we also make use of the COSMOS multi-wavelength data by using the r^+ selected version of the publicly available photometric catalogue of Muzzin et al. (2013) using PSF homogenized data.[3] We cross-matched this catalogue with our N396 centroids, and find except in four cases for the 140 objects a match within 1″.0, with a mean absolute separation of 0″.14 for all objects and 0″.13 for group A objects.

3.3.1 Additional subsamples

We further subdivided the *stacking sample* by three more criteria, where the cuts were in each case chosen to split the sample into two equal sized subsamples. We neglected here the three group A objects, for which we did not find a match within 1" with the catalogue of Muzzin et al. (2013). This means for each of the subsamples 35 objects.

First, we split by the rest-frame UV color. We chose for this purpose a cut in $V_{\mathrm{J}} - i'$. As discussed by Nilsson et al. (2009), the sample has a relatively large fraction of dusty or evolved objects, indicated by a

---

[3] The r^+ selected catalogue is available from `http://www.strw.leidenuniv.nl/galaxyevolution/ULTRAVISTA/Ultravista/R-selected.html` and is except the selection image produced in an identical way as the Ks selected catalog described in Muzzin et al. (2013).

high $V_J - i'$ color. The color dividing the blue and red halves is $V_j - i' = 0.00$ mag, with the blue and red subsamples having median colors of -0.08 mag and $+0.18$ mag, respectively. This cut turns out to match that of Nilsson et al. (2009, 2011).[4] It should be noted that these subsamples are neither identical to those in Nilsson et al. (2009) nor to those in Nilsson et al. (2011): we do not separate between objects which are individually detected in K and have a substantial amount of objects excluded due to our conservative region masking tailored for the search of the extended halos.

Secondly, we split by the rest-frame EW_0. We used here the first order values as derived by Nilsson et al. (2009). These EW_0 estimates are underestimates, as they were calculated assuming overestimated continuum flux densities: these continuum flux densities were calculated as linear combination of u* and B_J flux densities, without correcting for the contribution of Ly α in these filters. The median of all objects in the stacking sample has based on the values of Nilsson et al. (2009) an EW_0 of 56 Å and the medians for the objects above and below this cut are 37 Å and 85 Å, respectively. It is noteworthy that there is a large overlap between the EW and the color classification, with 24 objects of the low EW sample also within the red sample.

Finally, we split by stellar mass. Nilsson et al. (2011) performed fitting of the spectral energy distributions (SED) for those objects with individual K or IRAC detections individually and to stacked data for those without.

Through the UltraVISTA survey (McCracken et al., 2012) substantially deeper NIR data has become available than that included in Nilsson et al. (2011). This makes it feasible to fit all objects individually. We did so using the PSF homogenized $2\farcs1$ aperture photometry of Muzzin et al. (2013), corrected to total magnitudes, which includes UltraVISTA DR1 data in Y, J, H, and K. For the fit we assumed a constant star-formation history (SFH), a Calzetti extinction law (Calzetti et al., 2000), and searched for the model allowing for the minimal χ^2 when normalizing with the mass on a grid for different metallicties, ages, and E(B-V)s. Nebular line and continuum emission were implemented in a similar way as described in Schaerer & de Barros (2009) and Ono et al. (2010) (cf. also sec. 4.5.6 of this thesis).

The estimated masses must be understood as the best fit masses under the specific assumption for the assumed SFH and the reddening law. Even so we take account for the nebular contribution, a degeneracy between a solution favoring strong emission lines and a more evolved population with a strong Balmer/4000 Å remains. As the [O II], [O III]+Hβ, and H α fluxes contribute in J, H, Ks, respectively, none of the NIR data longwards of the 4000 Å is unaffected from nebular emission. The available Spitzer data, which would in principle allow to break the degeneracy, is not in all cases deep enough to do so. This can lead to differing mass estimates. The derived median mass is $10^{8.92}$M$_\odot$ with the median in the upper half being $10^{9.70}$M$_\odot$ and that of the low half $10^{8.22}$M$_\odot$.[5]

3.4 Stacking

3.4.1 Method: 2D stack

Differing from other studies (e.g Steidel et al., 2011; Matsuda et al., 2012; Momose et al., 2014) we did not stack continuum subtracted Ly α images, but the NB images that include both continuum and line emission. This is similar to what Feldmeier et al. (2013) did. The main reason was that we compared data from different instruments and hence strongly differing PSFs (cf. sec. 3.4.4). Matching such PSFs poses a possible source of introducing spurious halos (e.g. Feldmeier et al., 2013). We still created PSF matched continuum stacks for comparison (cf. sec. 3.5.3), but discuss them with the necessary caution.

---

[4] We note that the ZP corrections of -0.10, -0.12, +0.03, -0.03 for u^*, B_j, V_j, i^+, respectively, applied by Muzzin et al. (2013) and the galactic extinction corrections slightly modify the colors of the objects compared to those in Nilsson et al. (2009).

[5] There are conflicting statements about the masses of the stacks between text and table in Nilsson et al. (2011), likely due to a typo. Therefore, we forego here a comparison.

For the stacking, we created cutouts with a size of $50'' \times 50''$ or 411 kpc × 411 kpc around the integer pixel nearest to the objects' centroids using IRAF/imcopy. The oversampled pixel scale is $0.15''$ pixel^{-1}, which is small enough to render an additional shift unnecessary. The typical centroid determination error is of the same order for the relevant magnitude range, as we verified by using test sources.

When creating stacks with the goal of finding extended halos, both the background subtraction and the stacking should be done using the same object masks. The spatial distribution of unrelated objects is for our relatively small sample far from uniform and therefore masking of these objects is very important.

We masked all detectable objects in the field by creating object masks based on the segmentation mask output by SExtractor using the parameters 'Mask' in table 3.1. The use of SExtractor allowed us to use a very low detection threshold, but at the same time counteract a clipping of the background noise distribution by using a relatively high minimal detection area (*DETECT_MINAREA*) and Gaussian filtering. Furthermore, it allowed for a consistent de-blending of the central object from its neighbors. We chose for the masking lower thresholds than for the centroid determination. We implemented masks both for the N396 image and the BB images individually. Due to the greater depth for continuum sources, the latter mask more objects. While this might introduce a minimum inconsistency between the masks used for the BB and NB filters, it is justified, because we need to reach deeper continuum limits to compare the profiles.

To keep the stacking and background subtraction masks consistent, we refined the background subtraction before the actual stacking by locally removing an average background for each cutout. As local, we defined an area with an inner circular boundary of $25''$ (206 *kpc*) diameter and an outer boundary defined by a rectangular box with side length of $40''$. This area included 50736 pixels before object and region masking. The inner radius was chosen for reasonable Ly α profiles to be sufficiently away from the center to not impact a possible measurement. The outer box was chosen to avoid in the local background subtraction regions, where the segmentation map might be effected by boundary effects, and hence not be completely representative for the object masks used in the stacking of the science part.

Different biases might without careful masking lead to an excess of flux due to unrelated or related neighboring objects. When comparing with theoretical studies, we stress that our method removes not only spatially unrelated but also spatially related objects.

Deep and consistent masking both in the background subtraction and stacking is also important to avoid negative profiles close to the LAEs, which can result from a selection bias: Objects with a close neighbor, be it spatially related or unrelated, would not be selected to be part of the *stacking sample*, and might not even be selected as LAEs initially, as the neighbor can reduce the effective equivalent width within the measurement aperture. We can naturally only take care of this effect down to the detection limit of individual objects.

Finally, we stacked the 2D frames, excluding masked pixels in each frame, using the mean. The use of the mean is essential to reach the required depth despite the relatively small sample. We checked that our result is not impacted by a few extreme profiles. In addition to the object masking, we also applied σ-clipping with $\kappa = 3$ and 5 iterations. We created stacks using individual masks for each filter.

3.4.2 Method: 1D profiles

From the determined 2D stacks we extracted the surface brightness as a function of radius by azimuthally averaging over radial bins with bin widths of $0''.30$. In the averaging we used an additional σ-clipping with $\kappa = 3$ and 5 iterations. The width of the bins was chosen to be a compromise between sampling of the profile and enough pixels to reach enough depth at the relevant radial bins.

In the following we state our resulting N396 profiles both in units of flux-density surface brightness and line-flux surface-brightnesses. The latter are calculated using:

$$f_{SB} = \frac{c_0 \Delta_f}{\lambda_{0;f}^2} \times 10^{-0.4\cdot(\mathrm{ZP}+48.6)} \frac{c_{SB}}{\mathrm{pixelscale}^2} \tag{3.1}$$

Here, c_0 is the speed of light, Δ_f and $\lambda_{0;f}$ are filter width and central-wavelength, respectively, c_{SB} are counts in units $ADU/pixel$, and ZP is the zeropoint on the AB system. In this calculation it is assumed that all flux in the NB filter is from the line itself. However, as we were not using continuum subtracted images, for an observed frame equivalent width, EW_{obs} of 65 Å, only $\sim \frac{1}{3}$ of the flux in the NB filter is due to Lyα and the rest is continuum. If extended Ly α profiles are only a consequence of resonant scattering, the extended halos would show no continuum emission. In this case the stated values are nearly identical at large radii to the actual Ly α surface flux-densities.

3.4.3 Depth characterization

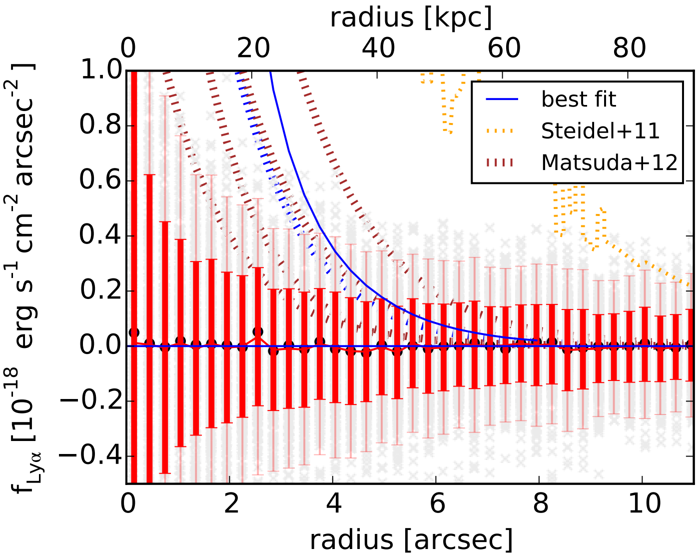

Figure 3.3 Scatter in the background measured within azimuthally averaged radial bins as a function of radius. The scatter was derived from 300 realization of background stacks with the same number of cutouts as in the 'stacking' sample. The values obtained for each realization are shown as light grey crosses in the background. The mean of the 300 stacks is shown as red curve, while the median is given by blue points. The standard deviation is shown as thick red error bars, and twice the standard deviation as light red thin error bars. For comparison five different extended Ly α halos from the literature are shown. The orange curve is for the stack of Ly α emitters in (Steidel et al., 2011), while the other lines are exponential profiles found for four different rest-frame UV magnitude bins by Matsuda et al. (2012) at $z \sim 3$. The literature profiles are corrected to the redshift of our study ($z \sim 2.26$). The solid blue curve is the best fit profile as obtained for our data (cf. fig. 3.6), whereas the dashed blue curve is our best fit outer exponential profile not convolved with the PSF.

To estimate the expected depth for our *stacking sample*, we chose 73 random positions for the stacking sample and 35 for the subsamples, corresponding to the number of objects in the actual samples. None of the chosen positions were allowed to be excluded when applying the same region mask as used for the actual objects. We created cutouts at these random positions and removed the local background in the same way as for the actual data, with the only difference that no object was required to be at the center.

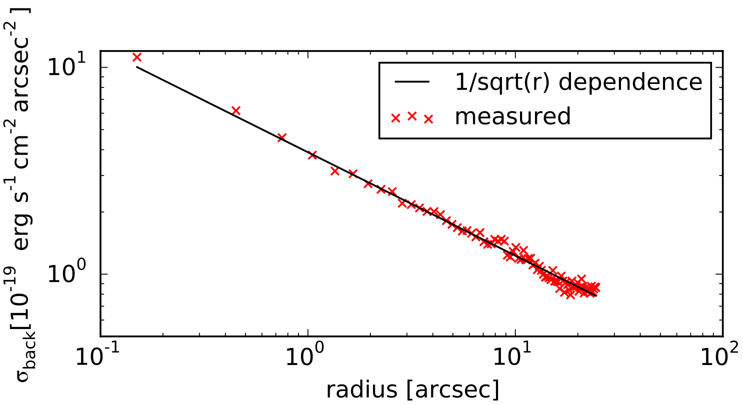

Figure 3.4 The standard-deviation between different realizations of the background noise as a function of the radius

If this was randomly the case, the central object was kept masked. By creating 300 realization of these random stacks, we found the standard deviations. Mean, median, and one and two σ values for the 300 realizations are shown for each of the radial bins over which we azimuthally average in Figure 3.3. This standard deviation includes all effects from the flat-fielding and deviations from a constant background within the 50″cutouts. At the important radii between 3″ and 5″ the 1 σ uncertainty in each of the radial bins is about 0.2×10^{-18} erg s^{-1} cm^{-2} arcsec^{-2} for the full 73 object stacking sample.

As the number of pixels within an annulus with fixed radial width scales linearly with the annulus's central radius, the total noise divided by the area is expected to be inverse proportional to the $\sqrt{radius}$, if the assumption of Poissonian noise holds.

The noise dependence measured from the different realizations is shown as a function of the radial bin in Figure 3.4 and is consistent with this expectation. The resultbroadband illustrates that the noise in the stack behaves almost ideally and that large scale flat-fielding uncertainties do not dominate the noise at any radius down to the depth we are reaching.

Following the same procedure as described above for the N396 image, we determined the uncertainties for the stacks in the three broadband filters u*,B$_J$, and V$_J$, as used later in this manuscript.

3.4.4 PSF stacks

As discussed thoroughly by Feldmeier et al. (2013), effects of the large scale PSF might possibly fake Ly α halos. Therefore, we determined the PSF to large radii. To do so we stacked stars, where we selected the stars by means of their position in the SExtractor based *MAG_AUTO* - $R_{1/2}$ space. From these plots we also decided about the saturation.

For this star stacking, we rescaled the stars to a common reference magnitude, a step which we did not do for the actual data. For the very deep B$_J$ and V$_J$ images, where the saturation is relatively low, we combined two different stacks for the inner and outer part. The stacks for N396, u*, B$_J$, and V$_J$ include the magnitude ranges from 18.0–20.0, 18.0–20.0, 22.0–24.0 plus 18.0–22.0, and 20.5 – 22.5 plus 18.0–20.5, respectively. The resulting stacks and the corresponding radial profiles are shown in Figure 3.5.

Finally, we determined radial symmetric convolution kernels based on the stacks. As the N396 image has the most extended PSF, convolution kernels were calculated for the transformation from the BB filters to the N396 filter. For the Kernel determination we followed Alard & Lupton (1998), using a linear combination of the product of Gaussians and polynomials. We get reasonable agreement out to radii relevant for our study, as can be seen from the green dotted curves in Fig. 3.5, which show the convolved

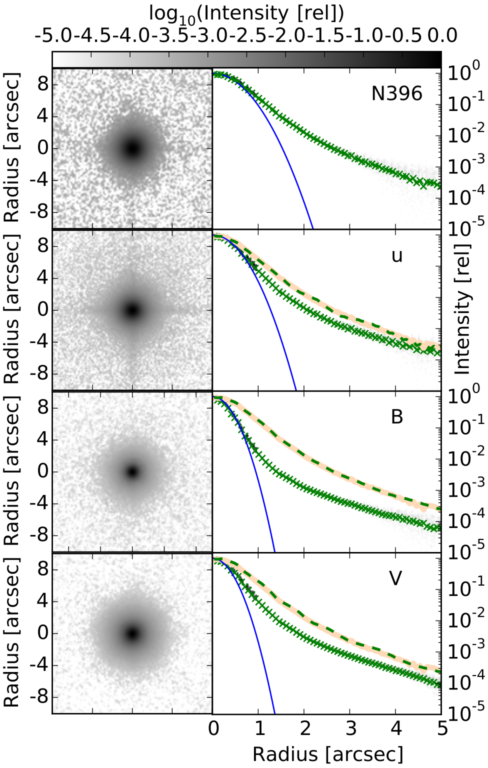

Figure 3.5 PSFs as obtained from stacks of stars for all four used filters. The stacks are shown in the left panels, while the azimuthally averaged profiles are shown as the green crosses in the right. The N396 PSF is shown in the panels for the three broad band filters as peach thick line. The results from matching the large scale PSFs for the stacks to the N396 stack is shown as green dashed line. A Gaussian with the same FWHM as the PSFs is shown as solid blue line.

profiles.

3.5 Results

3.5.1 N396 profile

For the stacking sample of 73 objects, the resulting N396 profile is shown in Fig. 3.6, with the uncertainties determined as in sec. 3.4.3. In order to obtain scale length and normalization of the extended profile common practice in other works has been to exclude the part affected by the PSF, where the size of exclusion was chosen differently. E.g. Matsuda et al. (2012) have fitted a simple powerlaw profile at radii larger than 3″and Momose et al. (2014) between 2″ and 40 kpc, respectively. In contrast, we actually fit the profile including effects of the PSF. In detail, we convolved exponential profiles with the N396 stack PSF. Then we fit for a double powerlaw, where we determined the uncertainties based on a MCMC chain. The MCMC results, indicating the degeneracies between the parameters are shown in Figure 3.7.

For the inner profile we get a scale length of $1.54^{+0.08}_{-0.07}$ kpc, corresponding at $z = 2.26$ to 0.19″ or a half light radius of 0.31″. For 52 out of the 73 objects in the stacking sample we have half-light radii from the analysis of Malhotra et al. (2012) using the ACS F814W filter. The mean F814W based half

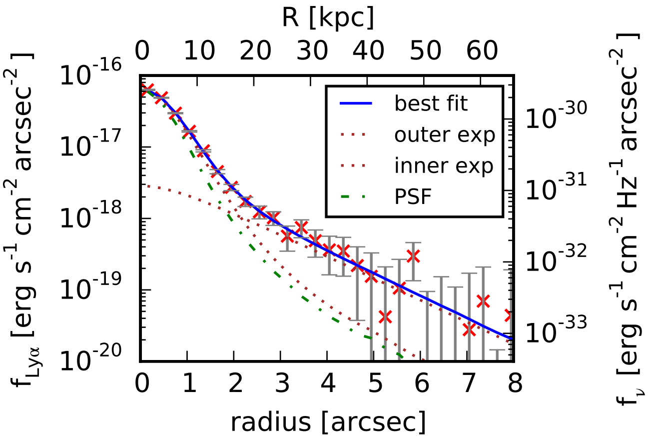

Figure 3.6 The radial profile as extracted from the N396 stack. The measured surface brightnesses is shown as a function of radius as red crosses, together with the error bars derived from the depth test described in sec. 3.3. The best fit double-powerlaw convolved with the PSF is shown as blue curve, where the PSF is shown as green dash-dotted curve. The two individual powerlaws are also plotted separately.

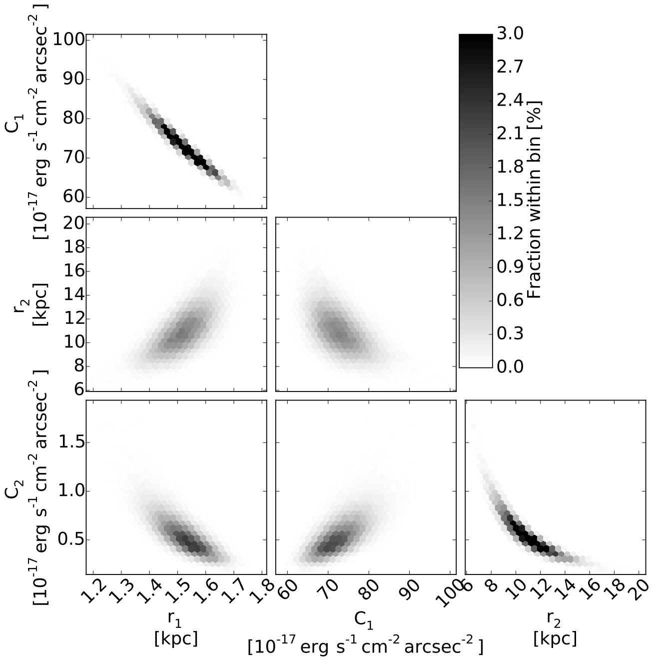

Figure 3.7 Result for fitting a double-power law to the the N396 profile obtained for the stack of the 73 Ly α emitters. C_i and r_i are normalization and scale length of the exponential profiles, with $i \in 1, 2$ for the two profiles.

light radius for these objects is 0″.15. This is about a factor two smaller than the value for the inner N396 profile. The discrepancy has three main explenations. First, there is expected to be some positional widening from centroiding uncertainties. Secondly, Malhotra et al. (2012) have excluded objects with clumpy F814W morphology. Finally, also the inner profile is expected to be more extended than the pure continuum profile due to resonant scattering.

The outer exponential profile, which we interpret as the extended Ly α halo, has a scale length of $11.2^{+1.8}_{-1.7}$ kpc and a central surface brightness of $4.9^{+2.1}_{-1.2} \times 10^{-18}$ erg s^{-1} cm^{-2} arcsec^{-2}.[6]

Even before subtracting a continuum, the profile is significantly weaker than the profile seen in the stack of Steidel et al. (2011) (cf. Fig. 3.3). By contrast, this visual comparison clearly indicates that the halo is of comparable extent to the halos found for field LAEs by Matsuda et al. (2012).

3.5.2 Robustness of excess

To alleviate concerns that the halo detected at radii larger than $2''$ might be a typical result of the stacking procedure applied to our data, we performed a robust test.

The first step of this test was to chose for each of the LAEs in the stack a comparison object with similar $R_{1/2}$ ($|\Delta R_{1/2}| < 0''.15$) and magnitude ($\Delta mag[1''] < 0.1$). The redshifts of the comparison objects were arbitrary, but they were not allowed to be selected as emission line galaxies in the N396 filter.

We then created a stack based on the picked comparison objects in the same way as for the LAEs. The process of selecting a random comparison sample and creating a stack was repeated 100 times, the results of which are shown in Fig. 3.8.

The extended Ly α profile is reassuringly found to be stronger than the comparison samples at the relevant radii between $2''$ and $4''$. All those comparison stacks, which have in one or more of the seven radial bins between $2''.25$ and $4''.05$ a value above the 95% confidence interval, have at least two bins where they are not above the 68% interval. By contrast the LAE stack has no value below the 68% interval.

We stress that the presented test needs to be understood as a conservative check for the presence of Ly α halos at large radii. We also note that no PSF matching has been applied, which could introduce spurious effects.

3.5.3 Stacks for the different filters

We created also stacks for u*, B$_\mathrm{J}$, V$_\mathrm{J}$. The BB stacks we matched to the PSF of the NB396 filter using the convolution kernels as derived for the averaged PSFs (cf. sec. 3.4.4). The resulting stacks are shown in Figure 3.9. The convolved BB stacks need to be treated with caution, as the difference between the PSFs are large and especially the N396 PSF has some variation over the field. Further, the BB stacks, especially for B$_\mathrm{J}$ and V$_\mathrm{J}$ have some negative dip around the stacked source. This makes the interpretation of the halos difficult. We note that a similar dip seems also to appear in the V$_\mathrm{J}$ stack of Momose et al. (2014) for their sample of Subaru $z = 2.2$ Ly α emitters, which are also partially in the COSMOS field. One possible explanation is an underdensity of objects below the detection thershold of individual objects compared to the average background close to the LAEs. We consider it also as a possiblity that this is a result of the masking used for the COSMOS BB data described in Capak et al. (2007), which might be worth further investigation.

The N396 Lya object stack is clearly extended compared to the N396 PSF. Compared to the BB stacks, the excess is especially significant at radii larger than $2''$. When interpreting the differences between the profiles, it is important to keep in mind that the Ly α emission would also need to contribute in u* and B$_\mathrm{J}$. In Figure 3.9 we indicate how the outer Ly α profile, as determined from fitting in sec. 3.5.1, would look like in u* and B$_\mathrm{J}$. It can be concluded that the extended Ly α emission is consistent within the errorbars

---

[6] The central surface brightnesses correspond to the profiles before convolving with the PSF.

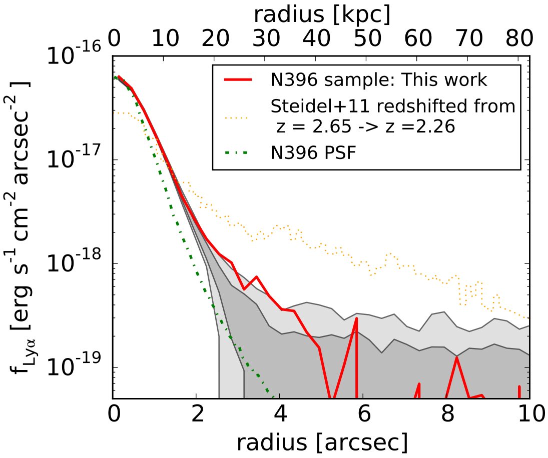

Figure 3.8 The profile as obtained for our stacking sample is shown as solid red line. We have calculated 100 comparison stacks, each of which has the same number of objects as the Ly α stack with the same half light radius and magnitude distribution, but not being part of the Ly α sample. 68% and 95% intervals around the mean of these realizations are shown as light and dark-grey regions. In addition, the PSF is included as green dash-dotted curve. The yellow dotted line the Ly α profile by Steidel et al. (2011) for LAEs in their sample, corrected here for the difference in redshift between their sample and our sample.

with the profile in the BB filters.

We derived the EW_0 of the stack within several apertures sizes ranging from diameters between 1″ to 12″ in two different ways. First, we used the simple approach to estimate the continuum based on the linear combination between u^* and B_J. This, however, underestimates the EW_0s as the contribution of Ly α to B_J and especially u^* is ignored. Therefore, we also determined EW_0 by consistently fitting a model consisting of a powerlaw continuum attenuated blueward of Ly α by the redshift typical IGM attenuation (Inoue et al., 2014), a Gaussian emission line, and assuming the actual filter curves. We assumed a precise redshift at the peak of the filter. If the actual redshift corresponds to the wings of the filters or if the Ly α line would extend in wavelength over the edges of the passband, the derived EW_0s will still be lower limits. As there are some remaining uncertainties in the ZPs and mismatch between model and actual profile can be a problem, we added a somewhat arbitrary 5% uncertainty to the measured flux uncertainties.

The EW_0 changes substantially from 48 ± 8 Å to 94 ± 15 Å from the smallest to the largest aperture, due to the presence of the extended Ly α emission. Reassuringly, the best-fit continuum slope is not changing significantly over the complete aperture range with a value of $\beta \approx -1$ ($f_\lambda \propto \lambda^\beta$)

As a consistency check we compared our stack magnitudes to the mean of the magnitudes in the Muzzin et al. (2013) catalogue, corrected to total magnitudes based on the correction between 2″1 and *SExtractor* MAG_AUTO in r^+ provided by Muzzin et al. (2013). While the agreement in B_J and V_J is excellent, there is a small difference in u^*. At least part of the deviation can be explained, since the aperture correction for the extended Ly α emission is based on r^+ and therefore not completely correct for u^*, which has a significant Ly α contribution.

Finally, we created stacks for the subsamples split by the three criteria, UV-color, EW_0, and mass, as described in sec. 3.3.1. The resulting sub-stacks are shown in Figure 3.10. To the depth of our data, there is no significant difference between the high and low EW_0 and the UV blue and red subsamples. At best, there is an indication of slightly stronger halos at large radii for the low EW_0 and red sample. The difference between low and high mass subsamples is slightly stronger but still marginal.

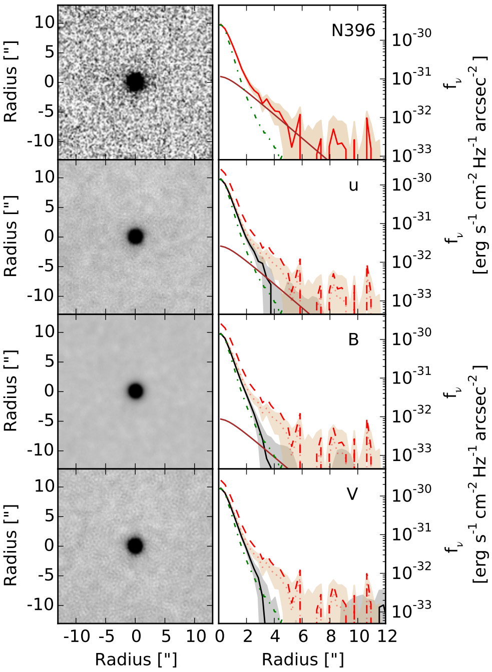

Figure 3.9 In the left cutouts of the stacks in the NB396 filter and the three broadband filters after PSF matching are shown. The extracted radial profile is shown in red for the N396 filter and is repeated in the panels for the BB filters as red dashed line. The profile extracted for the broadband filters are shown as solid black lines. The N396 profile is also shown scaled to the peak brightness of each of the broadband filters as red dotted line. The N396 PSF, to which the other filters are matched, is shown in all panels as green dashed-dotted line. In addition, the contribution of the extended Ly α halo, as determined from the N396 stack, is also shown for the u and B filters.

3.6 Discussion & Conclusion

The presence, strength, and evolution of extended Ly α halos around LAEs is an important question to answer. Especially the time window from $z = 3$ to $z = 2$, covering about 1 Gyr around the peak of cosmic star-formation activity is of interest. The evolution of other properties, like dust content and mass of the LAE population during this time window is under debate (e.g. Nilsson et al., 2009; Finkelstein et al., 2009; Blanc et al., 2011; Song et al., 2014). Therefore, it is important to study this period for as many quantities and with as many independent samples as possible.

With our analysis we demonstrated the presence of extended Ly α halos in the $z \sim 2.26$ sample of Nilsson et al. (2009). As we used only relatively isolated objects and masked objects down to a low detection threshold, the detection can be considered as save.

Already Nilsson et al. (2009) noted a larger extent in the N396 images compared to the continuum extent by analyzing the half light radii of individual objects. In our work, we showed for the stack of LAEs in the NB filter that the surface-brightness profile is even more extended than a stack of continuum objects with the same half-light radius and magnitude distribution. This very conservatively demonstrated the presence of extended Ly α emission originating in the circumgalactic medium in the halos hosting the LAEs.

We also created stacks in u*, B$_\mathrm{J}$, and V$_\mathrm{J}$. After matching the stacks to the PSF of the NB image,

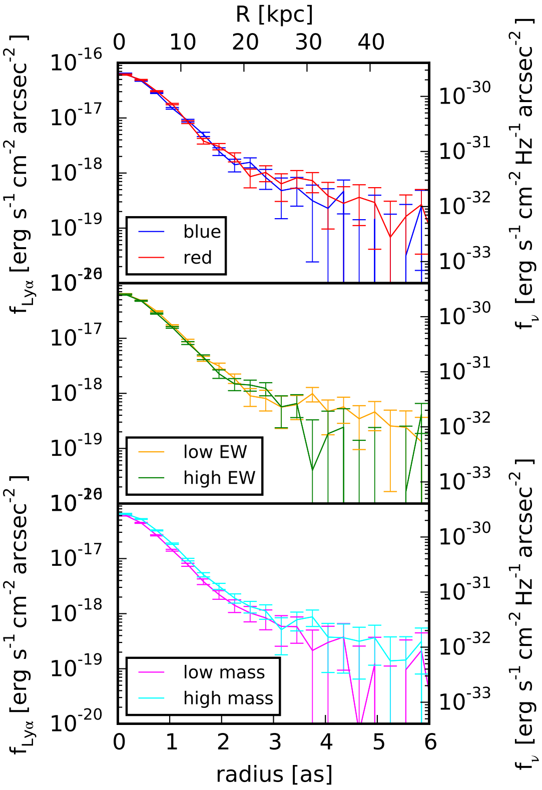

Figure 3.10 Shown are profiles obtained for six different sub-stacks, where the stacking sample was split into objects with blue and red continuum slopes, low and high Ly α equivalent width, and low and high mass (cf. sec. 3.3.1)

.

we can clearly conclude that the Ly α emission is more extended. Considering that the centroids were determined on the Ly α image, remaining uncertainties on the astrometry and possible offsets of the Ly α emission compared to the continuum emission would only widen the profiles in the broadband stacks.

Somewhat worrying is that all three broadband images seem to have a slightly negative dip at the relevant radii between 4″ and 6″. A possible reason is a selection bias: Due to analyzing only relatively isolated objects, there might be a local over-subtraction of the background. We do on average see no negative bias for the comparison random position stacks.

3.6.1 Comparison to other studies

Normalization and size of our halo is with

$$C_n = 4.9^{+2.1}_{-1.2} \times 10^{-18} \text{ erg s}^{-1} \text{ cm}^{-2} \text{ arcsec}^{-2} \quad \text{and} \quad r_n = 11.2^{+1.8}_{-1.7} \text{ kpc}$$

similar to that of other LAE field samples at $z = 2$ and $z = 3$, except that of (Feldmeier et al., 2013). Momose et al. (2014) find in the large sample of 2115 LAEs at $z = 2.2$ a

$$C_n = 1.5 \times 10^{-18} \text{ erg s}^{-1} \text{ cm}^{-2} \text{ arcsec}^{-2} \quad \text{and} \quad r_n = 7.9^{+0.56}_{-0.49} \text{ kpc}$$

Table 3.3 Magnitudes in circular apertures of ten different sizes all for the u*, $\mathrm{B_J}$, $\mathrm{V_J}$, and N396 stacks. For each radius the Ly α restframe EW_0 is stated, calculated in two different ways.

Aperture radius[a]	N396	u*	$\mathrm{B_J}$	$\mathrm{V_J}$	$\mathrm{EW_0}$ (simple)[b,c]	$\mathrm{EW_0}$ (fit)[b,d]	β (fit)[d]
0.5	25.78±0.05	26.44±0.05	26.43±0.05	26.31±0.05	33±5	48±8	−1.2±0.3
1.0	24.77±0.05	25.47±0.05	25.50±0.05	25.36±0.05	36±5	55±9	−1.1±0.3
1.5	24.42±0.05	25.16±0.05	25.21±0.05	25.05±0.05	39±5	62±10	−1.0±0.3
2.0	24.28±0.05	25.04±0.05	25.09±0.05	24.94±0.05	41±5	65±10	−1.0±0.3
2.5	24.21±0.05	24.98±0.05	25.05±0.05	24.89±0.05	42±5	68±11	−1.0±0.3
3.0	24.16±0.05	24.95±0.05	25.03±0.05	24.87±0.05	43±5	71±11	−1.0±0.3
3.5	24.12±0.05	24.93±0.05	25.02±0.05	24.87±0.05	45±5	75±11	−1.0±0.3
4.0	24.09±0.05	24.92±0.05	25.02±0.05	24.87±0.05	47±6	79±12	−1.0±0.3
5.0	24.05±0.05	24.93±0.05	25.02±0.05	24.90±0.05	51±6	87±13	−0.9±0.3
6.0	24.03±0.05	24.94±0.05	25.04±0.05	24.94±0.05	54±6	94±15	−1.0±0.3
mean (Muzzin et al., 2013)		25.08	25.01	24.87			

[a] [arcsec] [b] [Å] [c] Simple refers to a calculation ignoring the contribution of Ly α to u and B.

[d] *Fit* means that a model including a (Gaussian) line, a powerlaw continuum ($f_\lambda \propto \lambda^\beta$), and IGM attenuation (Inoue et al., 2014) was fit simultaneously to all four filters.

and for 316 LAEs $z = 3.1$ a

$$C_n = 5.3(24) \times 10^{-18}\ \mathrm{erg\ s^{-1}\ cm^{-2}\ arcsec^{-2}} \quad \text{and} \quad r_n = 9.3^{+0.48}_{-0.53}(8.6)\ \mathrm{kpc}.$$

For the $z = 3.1$ halo we state in brackets values, where C_n has been corrected to $z = 2.26$ by assuming the $(1 + z)^4$ cosmological surface brightness dimming, and r_n by taking account for the difference in angular diameter distance. The samples of Momose et al. (2014) are chosen to be complete to $\log_{10}(L_{\mathrm{Ly}\alpha}) = 42.00$, and hence factor of 2.8 fainter than the 90% completeness limit of the sample of Nilsson et al. (2009) used in our analysis.

Matsuda et al. (2012) split their sample by UV magnitude. The continuum of our best fit powerlaw for an aperture radius of 3″.5 would correspond at $z = 3.1$ to a continuum magnitude of 25.81 ± 0.08 at the Ly α wavelength. For their stack of objects with continuum magnitudes between 25 mag and 26 mag, Matsuda et al. (2012) find

$$C_n = 1.8(4.6) \times 10^{-18}\ \mathrm{erg\ s^{-1}\ cm^{-2}\ arcsec^{-2}} \quad \text{and} \quad r_n = 13.2(12.2)\ \mathrm{kpc}.$$

In brackets are again values stated, which are corrected to the redshift of our sample.

The normalization of our profile is a bit higher than the profile of Momose et al. (2014) at $z = 2.2$. The difference could be explained through the fainter detection limit of their sample. The profile of Matsuda et al. (2012) at $z = 3.1$ has also a smaller observed normalization. However, after correcting for surface-brightness dimming, it would be very similar to our profile. As our and their subsample are well matched in continuum magnitude, this indicates that there is no clear evolution between $z \sim 3$ and $z \sim 2$.

By contrast, the profile found for LAEs in the sample of Steidel et al. (2011) is significantly stronger and much more extended. This can be seen in Figures 3.3 and 3.9, where we have included this profile, which we converted from $z = 2.65$ to our redshift of $z = 2.26$ by taking account for the $(1+z)^4$ dependence and the different angular diameter distances.

The fact that the halo for our field LAE sample is similar to the halos of Momose et al. (2014) and Matsuda et al. (2012) both at $z = 2.2$ and $z = 3.1$, but much weaker than the halo of Steidel et al. (2011), which includes objects from three highly over-dense regions, confirms the interpretations by previous studies (Momose et al., 2014; Matsuda et al., 2012) that the sizes of the Ly α halos do not evolve strongly with redshift, but are strongly impacted by the environment.

Further investigations are certainly necessary to establish whether there are additional correlations. While we tested for differences of the halo as a function of UV color, EW_0, and mass, the depth of our stack would have allowed only for the detection of extreme differences. We do not see a significant difference, and can at best identify a trend towards somewhat more extended halos for low EW and red objects, which would be in line with the results of Feldmeier et al. (2013) at $z \sim 3$.

The question remains, why Feldmeier et al. (2013) did not see halos at $z \sim 2$. It is possible that the depth provided by their median stacking approach was not sufficient. However, their objects seem to be consistent with the PSF over the full profile. By contrast, we see clear deviations from the PSF already significantly above the detection limit for individual objects, in line with the previous findings by Nilsson et al. (2009) for our sample. This makes the depth interpretation as the sole difference questionable.

3.6.2 Implications from equivalent width and how to proceed

In section 3.5.3 we have determined for our stack the EW_0 as a function of aperture size. It is clear that measurement apertures with diameters between $\sim 1\rlap{.}''0$ and $3\rlap{.}''0$, which are typically used for high redshift studies, significantly underestimate the total Ly α EW. We find almost a factor of two between the $2''$ aperture and the $12''$ aperture.

The question is whether the increase of the Ly α EW_0 is only a consequence of the scattering of Ly α photons by the neutral gas of the CGM, with the Ly α photons originally produced by recombination in the H II regions of the LAE located at the center of its halo, or whether other processes play a role.

While the maximum Ly α EW_0 of 94 ± 15 Å is certainly in the range of EW which can be produced by young star-forming galaxies (e.g. Malhotra & Rhoads, 2002), it needs to be considered that our stack is with a UV slope of $\beta = -1.0 \pm 0.3$ moderately red, indicating dust extinction or alternatively larger age or very high metallicity. Using the relation between the extinction at 1600Å and β of (Meurer et al., 1999) of $A_{1600} = 4.43 + 1.99\beta$ we find for our slope $A_{1600} = 2.4$ mag. This corresponds for a Calzetti et al. (2000) extinction law to an $E(B-V)$ of 0.25. Using the difference in exctinction between Ly α and continuum, as determined by Hayes et al. (2010), this would result in the suppression of the EW by about 70% and the value of 94 Å would be difficult to explain based on star-formation alone. This comparison has however in addition to a possible selection effect a caveat. The results of Hayes et al. (2010) was derived based on SExtractor MAG_AUTO apertures for the individual objects, which cannot take correctly account for the extended low-surface-brightness emission.

If it is not only scattered light there are several possibilities. One possibility would be the escape of ionizing photons from the central Ly α emitter. While this cannot increase the maximum EW_0 produceable by a stellar population, the escaping photons might experience less dust extinction. In contrast to the scattering scenario, the extended Ly α emission would be produced by recombination directly in the CGM. As a consequence, there would be also extended halos in the non-resonant emission lines, like H α. This is in principle testable; but it will be challenging to do so, as even H α is about a factor eight weaker than Ly α, somewhat depending on the temperature of the cloud where the recombination takes place. Another possibility would be star-formation in smaller structures in the CGM (e.g. Lake et al., 2015). While this would also produce both Ly α and other non-resonant recombination lines, it would be accompanied by relatively strong stellar UV continuum. In the case of the escaping ionization radiation only nebular continuum, including bound-free, free-free and 2-photon emission would be detectable (e.g. Osterbrock & Ferland, 2006). Finally, another possibility for the extended Ly α emission would be gravitational cooling radiation. As the excitation is here caused by collisions, the only continuum source is 2-photon emission (e.g. Dijkstra & Loeb, 2009).

Recently, Lake et al. (2015) have argued that the scattering of photons from the central LAE in the halo alone is not sufficient to explain the extended profiles found by Momose et al. (2014), while strong star-formation within the outer parts of the halo was identified to be not consistent with the strength of the UV continuum. Therefore, they prefer a significant contribution of Ly α produced by gravitational cooling radiation. Here it might however be important to consider that profiles as flat as those predicted by Lake et al. (2015) for background star-formation and background gravitational cooling radiation would pose a significant challenge to background subtractions in actual observations due to the profile flatness. Our sample is not deep enough to test any of these options conclusively.

4

THE WHOLE IS MORE THAN THE SUM OF ITS PARTS

A Method to improve line flux and redshift measurements with narrowband filters

Johannes Zabl[1], **Wolfram Freudling**[2], **Palle Møller**[2], **Bo Milvang-Jensen**[1], **Kim K. Nilsson**[2], **Johan P.U. Fynbo**[1], **Olivier Le Fèvre**[3], **Lidia A.M. Tasca**[3]

[1] Dark Cosmology Centre, Niels Bohr Institute, University of Copenhagen, Juliane Maries Vej 30, 2100 Copenhagen, Denmark
[2] European Southern Observatory, Karl-Schwarzschild-Straße 2, 85748 Garching bei München, Germany
[3] Aix Marseille Université, CNRS, LAM (Laboratoire d'Astrophysique de Marseille) UMR 7326, 13388, Marseille, France

Prepared for submission in Astronomy & Astrophysics

Abstract

High redshift star-forming galaxies are discovered routinely through the presence of a flux excess in narrowband filters caused by an emission line. In most cases, the width of such filters is broad compared to typical line widths, and the throughput of the filters varies substantially within the bandpass. This leads to substantial uncertainties in redshifts and fluxes that are derived from the observations with one specific narrowband filter.

The uncertainty in measured line parameters can be sharply reduced by using repeated observations of the same target field with filters that have overlapping passbands but differ slightly in central wavelength or wavelength dependence of the effective filter curve. Such data are routinely collected with some large field imaging cameras that use multiple detectors and a separate filter for each of the detectors. An example is the European Southern Observatory's VISTA InfraRed CAMera (VIRCAM).

We developed a method to determine more accurate redshift and line flux estimates from the ratio of apparent fluxes measured from observations in different narrowband filters and one or several matching broadband filters. A parameterized model of the line and continuum flux is used to predict the flux ratios as a function of redshift based on the known filter curves. These model predictions are then used to determine the most likely redshift and line flux.

We tested the obtainable quality of parameter estimation for the example of Hα in the VIRCAM NB118 filters both on simulated and actual observations, where the latter were based on the UltraVISTA

DR2 data set. We combined the narrowband data with deep broadband data in Y, J, and H. We find that by using this method, the errors in the measured lines fluxes can be reduced up to almost an order of magnitude.

We conclude that existing narrowband data can be used to derive accurate line fluxes if the observations includes images taken with sufficiently different filter curves. For the UltraVISTA survey, the best suited narrowband filter combinations allow to achieve an accuracy in wavelength of better than 1 nm, and in flux of better than 15% at any redshift within the bandpass of the filters. By contrast, analyzing the data without exploiting the difference in filter curves leads to an uncertainty in wavelength of 10 nm, and up to an order of magnitude errors in line flux estimates.

4.1 INTRODUCTION

Strong emission lines, which are the key signature in the spectra of star-forming galaxies, are important tools. The hydrogen Balmer lines are useful for determining the instantaneous SFR, as their strength is after correcting for dust directly proportional to the SFR (e.g. Kennicutt, 1998). Other strong emission lines, like [O II] $\lambda3727$, are due to their metallicity dependence less accurate SFR indicators (Moustakas et al., 2006; Kewley et al., 2004), but certain ratios between these lines and the metallicity-independent Balmer lines can be gauged as proxies for the gas-phase metallicity (e.g. Pagel et al., 1979; Kewley & Dopita, 2002).

Wide-field surveys with narrowband (NB) filters provide large line flux limited samples down to low equivalent widths at well defined redshifts. The idea behind the NB selection is to identify objects through an excess of the filter-averaged NB flux density over the underlying continuum flux density, with the latter being inferred from one or more suitable broadband (BB) filters (e.g. Djorgovski et al., 1985; Møller & Warren, 1993; Pascual et al., 2007). When the NB observations are in a field with extensive multi-wavelength data, photometric redshifts allow to discern between the different lines which could be the cause for the NB excess (e.g. in the COSMOS field: Ilbert et al., 2013; Muzzin et al., 2013).

A vast number of NB surveys have been performed, targeting H α, [O II], and Lyα at different redshifts. While many studies have been using observed-frame optical NB filters (e.g. Fujita et al., 2003; Dale et al., 2010; Takahashi et al., 2007; Ly et al., 2012; Rhoads et al., 2000; Ouchi et al., 2003; Nilsson et al., 2007), currently a strong focus is put on the exploitation of the airglow windows in the near-infrared (NIR) (e.g. Best et al., 2010; Ly et al., 2011). This is essential for high redshifts, as the important rest-frame optical lines shift into this wavelength regime. Among the deepest wide-field NIR surveys are the NB118 observation by Milvang-Jensen et al. (2013) and the NB118 part of UltraVISTA (Ultra Deep Survey with VISTA; McCracken et al. 2012), both of which are performed with the near-infrared camera VIRCAM (VISTA InfraRed CAMera, Dalton et al. 2006) at ESO's 4.1m survey telescope, VISTA (Visible and Infrared Survey Telescope for Astronomy, Emerson et al. 2006).

All these observational efforts are eventually used to estimate from the measured NB excesses line fluxes and, with the knowledge of the redshift, line luminosities. Obtaining these for large samples of galaxies at well defined redshifts allows to get important insights into galaxy evolution, e.g. by means of determining H α luminosity functions, which can be converted to SFR densities. Understanding can also be gained by relating other properties like galaxy mass, environment, and spatial clustering to the line luminosities (Sobral et al., 2010, 2011), and line based SFR estimates might be compared to SFR estimates obtained by other means, allowing to characterize the galaxies' star formation histories (Domínguez et al., 2014).

Unfortunately, line flux measurements obtained from NB filters can have substantial uncertainties. As the transmittance curves are often far from flat, a flux measured in the filter is consistent with a range of intrinsic line fluxes. While for sample based statistics it is often possible to overcome this problem to some extent by statistical means, other applications, like the identification of high redshift candidates, need the best possible flux determination for individual objects.

In this paper we discuss a method which both overcomes this flux measurement problem and allows at the same time for a wavelength resolution an order of magnitude below the NB width. This can be achieved by the use of slightly different filters, which allow to break the degeneracy between central wavelength and line flux.

We demonstrate the suggested method specifically for H α in the VISTA NB118 filters. In VIRCAM, there is one individual copy of the NB118 filters above each of its 16 non-contiguous detectors. Although produced to be as similar as possible, the transmittance curves of the individual filters are unavoidably slightly different from each other, and hence useful for the proposed method. The extremely deep and homogeneous BB data also available from the UltraVISTA survey are well suited to constrain the continuum.

The paper is organized as following: In sec. 4.2, we motivate the throughput-variations method (TPV). After describing estimation algorithm and estimation model in sec. 4.3, we test usefulness and caveats of the technique based on simulations, which emulate UltraVISTA DR2 observations of H α emitters (sec. 4.4). An application of the method to actual UltraVISTA DR2 data is presented in sec. 4.5. Finally, we discuss a possible modification to the UltraVISTA NB118 observing pattern for the purpose of the TPV (sec. 4.5.9).

Where needed, a (flat) standard ΛCDM cosmology with $H_0 = 70$ km s^{-1} Mpc^{-1}, $\Omega_{\mathrm{m},0} = 0.3$ and $\Omega_{\Lambda,0} = 0.7$ was assumed. Furthermore, we used throughout this paper AB-magnitudes (Oke, 1974). All numbers referring to specific VISTA NB118 filters are in line with the standard VISTA detector (filter) numbering scheme (cf. Ivanov & Szeifert, 2009; Milvang-Jensen et al., 2013).

All stated wavelengths are in vacuum, except when we use common identifiers like [O III]λ5007, which are based on wavelengths in air.

All assumed VISTA/VIRCAM filter curves include quantum-efficiency and mirror reflectivities, and the broadband filters curves include in addition an atmosphere with $PWV = 1$ mm at airmass 1. For the broadband filters, Y, J, and H, we used the same filter curve for all 16 detectors, as available from the ESO webpage.[1] Details about the individual NB118 filter curves are given in Appendix A.1. Parts of the field covered by the joint stack include data from a single filter/detector, while other parts include data from two filters (cf. sec. 4.5.1). Throughout this paper we will refer to 'combined effective filters', which are the effective filter responses, if data from two similar filters is combined into a single stack.

4.2 METHOD

4.2.1 ESTIMATING LINE FLUXES FROM NB OBSERVATIONS

Narrowband surveys, which aim at identifying emission line galaxies and measure their line fluxes, typically use one NB filter in combination with one or two broadband (BB) filters at wavelengths similar to the NB. In the simplest case the NB passband is the at the center of a BB passband, minimizing the impact of a sloped continuum. Then, a $BB - NB > 0$ indicates the presence of an emission line, as the impact of a line on the filter-averaged flux density is significantly larger in the narrower filter.

When relating the measured magnitudes to an emission line, it is useful to describe the line spectrum through the line's flux, f_0, its observed-frame equivalent width, EW_{obs}, and its central wavelength, λ_0, or equivalently its redshift. Using these three quantities, the object's spectrum can be written as:

---

[1] Filter curves, detector QE and mirror reflectivities were downloaded from `http://www.eso.org/sci/facilities/paranal/instruments/vircam/inst/Filters_QE_Atm_curves.tar.gz`

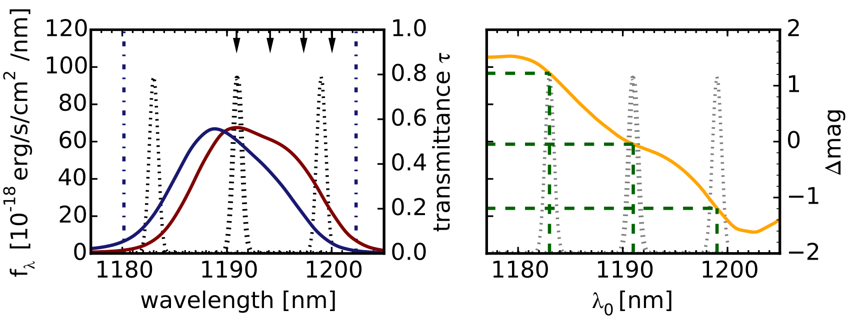

Figure 4.1 Illustration of how to obtain accurate line fluxes by the use of two NB filters. The left panel shows the throughput curves of two similar NB filters, superimposed on an emission line shifted to different wavelengths. The right hand panel shows the corresponding differences between the magnitudes measured with the two filters, Δmag, as a function of the wavelength of the emission line, λ_0. Here, the green dashed lines indicate how a measurement of Δmag can be used to determine the wavelength of the line, which in turn can be used to estimate its flux using the throughput curves on the left. The shown filter combination is the filter pair 14 & 15 of the NB118 filters, with 15 being the bluer. The meaning of the small arrows and the two vertical lines in the left panel is described elsewhere in the paper.

$$f_\lambda(\lambda; f_0, EW_{obs}, \lambda_0) = \zeta_\lambda(\lambda; \lambda_0)\frac{f_0}{EW_{obs}} + f_0 \cdot \mathcal{L}_\lambda(\lambda; \lambda_0) \tag{4.1}$$

$\zeta_\lambda(\lambda)$ and $\mathcal{L}_\lambda(\lambda)$ are the dimensionless spectral shape of the continuum and emission line spectrum, respectively. $\zeta_\lambda(\lambda)$ is normalized at the wavelength of the relevant line and $\mathcal{L}_\lambda(\lambda)$ can include additional lines, but it is scaled so that the integrated flux over the relevant line is one. f_λ is related to the observed magnitudes through (e.g. Buser 1986):

$$\mathrm{f}_{\nu;\mathrm{filter}} = \frac{\int f_\lambda(\lambda)T(\lambda)\lambda\, d\lambda}{\int \frac{c}{\lambda^2}T(\lambda)\lambda\, d\lambda} \tag{4.2}$$

$$\mathrm{m}_{\mathrm{AB;filter}} = -2.5\log_{10}\mathrm{f}_{\nu;\mathrm{filter}} - 48.6 \tag{4.3}$$

However, there is a problem when trying to estimate line fluxes from a single NB observation because the observed flux depends on the wavelength of the line. This problem can be understood from the left panel of Fig. 4.1 for the hypothetical example of a line without continuum. It is not possible to constrain both f_0 and λ_0, leading to order of magnitude uncertainties on the flux measurement. Further, the accuracy of the central wavelength estimation is limited to ’somewhere within the passband’, which might be for 1% filters, depending on the redshift, not much improvement over state of the art photometric redshifts.

Only if the NB filter’s passband was top-hat and if it was wide compared to the typical line width, the precise value of λ_0 could be ignored for the flux estimation. Effective top-hat filters are however in the fast convergent beams of large survey telescopes such as as VISTA, CFHT, and UKIRT physically impossible (cf. also Appendix A.1).

4.2.2 OBSERVATIONS WITH SEVERAL NB FILTERS

One way to solve the problem described in sec. 4.2.1 is to use observations in more than one, slightly differing NBs. Then, two magnitude equations (eq. 4.3) are available for determining the two unknowns,

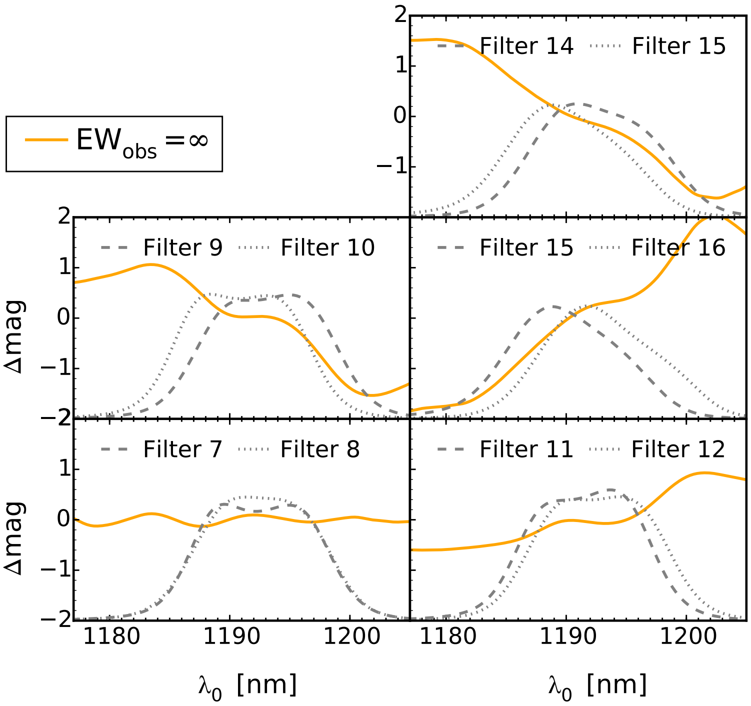

Figure 4.2 Δmag–λ_0 curves for five different NB118 combinations assuming an infinite $EW_{\rm obs}$ emission line. The passbands of the respective NB118 filters, for which the Δmag–λ_0 are shown, are also indicated in the different panels. The axis scaling for the filter passbands is linear.

f_0 and λ_0. f_0 can be eliminated from the equation and it can subsequently numerically solved for λ_0 as a function of the measured magnitude difference between the two filters, Δmag, as illustrated in Fig. 4.1.

With a well matched pair of NB filters, it is possible to determine the wavelength of a line within the range of wavelengths covered by the passband of the NB filter very accurately. Suitable filter pairs are those that result in Δmag–λ_0 relations that are monotonous and steep, allowing for a good wavelength resolution, even when considering realistic uncertainties in Δmag.

By means of such Δmag–λ curves we characterized the suitability of the various combinations between the 16 UltraVISTA NB118 filters for our method to determine the line fluxes from two filters. As discussed in more detail in sec. 4.5.1, for 12 out of the 120 theoretically possible combinations of these 16 filters, observations become directly available as part of the standard UltraVISTA observations. One of these combinations is 14 & 15, which was used for illustration in Fig. 4.1.

While this specific pair is very well suited for the method, not all the possible NB118 combinations are so in the same way. In Fig. 4.2 four further of the 12 relevant NB118 combinations are shown, where 15 & 16 is as good, and 9 & 10 almost as good as 14 & 15. The two filters 7 & 8 are too similar to be useful for the presented method, whereas in the Δmag-λ_0 curve of 11 & 12 still some information is contained. A quantitative characterization of the Δmag-λ_0 curves for all 120 combinations is given in Appendix A.2.

4.2.3 CONTINUUM ESTIMATION

In sec. 4.2.2, we have discussed the throughput variation method neglecting the continuum. But the continuum contributes for typical emission line galaxies significantly to the flux in NB filters. Hence, the magnitude differences measured for emission lines with the same f_0 and λ_0 also depend on the equivalent width, $EW_{\rm obs}$.

A measurement of the contribution of the continuum to the NB fluxes is required; consequently, continuum-corrected NB magnitudes can be used to estimate f_0 and λ_0 from the Δmag-λ_0 curves for infinite $EW_{\rm obs}$. An accurate continuum estimate at the wavelength of the NB filter could be obtained from measurements in additional narrowband or mediumband filters bracketing the main NB filter. Typically, for reasons of time and cost efficiency, it is resorted to BB filters. If a BB which has a passband covering the emission line is included in the estimation, f_0 , λ_0, and EW_{obs} need to be estimated simultaneously and the Δmag-λ_0 curves cannot be used directly. We describe a statistical approach of fitting the parameters in the next section.

4.3 ESTIMATION ALGORITHM

4.3.1 CONCEPT

Δmag - λ_0 curves, as motivated in section 4.2.2, allow to get a quick insight into the suitability of a specific filter-combination for the throughput variations methods (TPV). In this section, we describe how to infer central wavelength, λ_0, line flux, f_0, and equivalent width, $EW_{\rm ons}$ simultaneously using a statistical approach.

From the observation in the different filters a set $\mathbf{M}$ of observed magnitudes, $m_{\rm i}$, and estimates on their uncertainty, $\delta m_{\rm i}$ is obtained. A model relates a set of parameters, $\mathbf{p}$, to a spectrum, $f_\lambda(\lambda; \mathbf{p})$, from which synthetically model magnitudes in the relevant filters, $m_{\rm i;theo}[\mathbf{p}]$, can be calculated.

Then, the parameter set being most probable under this data needs to be found ($\mathbf{p}^{\rm est}$). This is to minimize the Bayesian posterior probability $\mathcal{P}(\mathbf{p}\,|\,\mathbf{M})$. $\mathcal{P}(\mathbf{p}|\,\mathbf{M})$ is related to the Likelihood, $\mathcal{L}(\,\mathbf{M}\,;\,\mathbf{p})$, and the prior on the parameters, $\mathcal{PRI}(\mathbf{p})$, by:

$$\mathcal{P}(\mathbf{p}\,|\,\mathbf{M}) = \alpha\,\mathcal{P}(\mathbf{M}\,|\,\mathbf{p})\,\mathcal{PRI}(\mathbf{p}) \tag{4.4}$$

α is a normalization constant. As we are assuming the errors in the measurements of the different magnitudes to be independent and Gaussian, the total likelihood is given by the product of the normal distributions for the individual measurements. Consequently, the negative log-likelihood is, safe a factor 1/2, the well known χ^2:

$$\chi^2 = \sum_i \left(\frac{m_{\rm i;obs} - m_{\rm i;theo}[\mathbf{p}]}{\delta m_{\rm i}} \right)^2 \tag{4.5}$$

The weight of individual filters can be artificially decreased by increasing the respective δm_i in the calculation of χ^2. In practice we chose a minimum δm_i for the broadband filters, $\Delta m^{\rm est}_{\rm BB}$, which we default to 0.01 mag. The implications from this choice are analyzed in sec. 4.4.3.

4.3.2 CHOICE OF INPUT MODEL

Continuum shape

Both the continuum shape and the ratios between the various emission lines will differ from galaxy to galaxy, even so they are selected by the combination of NB excess and photometric redshifts to be star-forming galaxies at a well defined redshift. If $f_\lambda(\lambda;\mathbf{p}_{\text{free}})$ is parametrized by eq. 4.1, educated guesses need to be made for ζ_λ and $\mathcal{L}_\lambda$. Ideally, these generic choices for ζ_λ and $\mathcal{L}_\lambda$ approximate the range of actual spectral energy distributions (SED) so well that the estimation of the free parameters is not impacted.

While the simplest form for $\zeta_\lambda(\lambda)$ is a continuum flat in f_ν or f_λ, a useful first order correction is to add an additional parameter in form of the power law slope β ($\zeta_\lambda(\lambda,\beta) \propto \lambda^\beta$). This inclusion of the slope is especially relevant, when the NB is off-centre from the BB passband, as it is the case for NB118 and J.

A power law continuum will not be sufficient if the wavelength range around the considered line includes a strong spectral break, like the 4000 Å or Balmer break in the case of [O II] λ3727, but is a good assumption for Hα in the NB118 filters, as discussed in sec. 4.4.2. We will issue the problematic of the break on selection and measurement of [O II] emitters in the NB118 data as part of a forthcoming publication.

Line shape and [N II] contribution

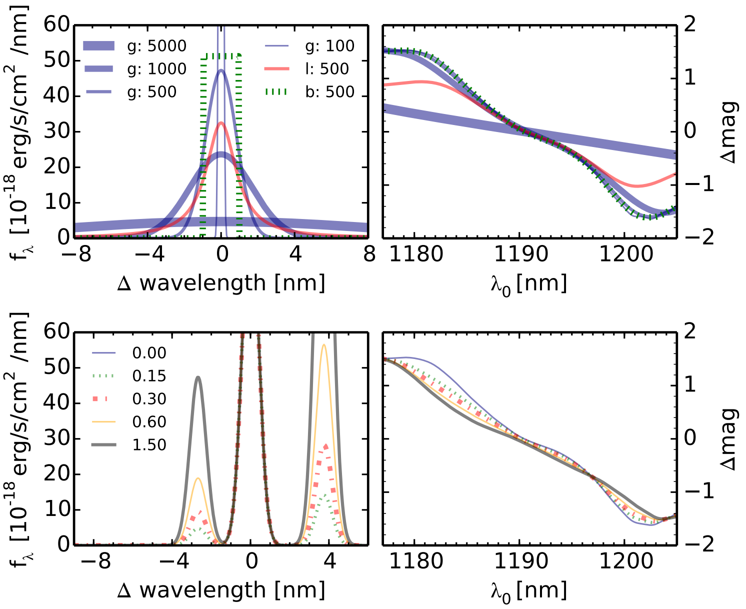

Figure 4.3 Impact of the line shape (upper panels) and the presence of multiple lines (lower panels) on the predicted Δmag - λ_0 curves. The left panels show different input spectra, and the right panels the corresponding Δmag - λ_0 curves. 'g', 'l', and 'b' in the legend refer to Gaussian, Boxcar, and Lorenzian, respectively, with the succeeding numbers stating the line $FWHM$ in km s^{-1}. The presence of multiple lines is demonstrated for the relevant example of the [N II] doublet bracketing H α, with the values in the legend corresponding to the assumed [N II] λ6583 to H α ratios. All shown results are based on the same filter combination as used for Fig. 4.1.

When observing H α in a NB filter, there is contamination from the collisional excited, forbidden [N II] lines at 655.0 and 658.5 nm, which have to be included in $\mathcal{L}_\lambda$. In the NB118 filters, where Hα is observed at a redshift of $z \sim 0.81$, the lines are at a difference of 2.7 nm and 3.6 nm from Hα, respectively. While the ratio between the fluxes in the two [N II] lines, $f_{[\text{NII}]\lambda6583}/f_{[\text{NII}]\lambda6548}$, is theoretically fixed to ~ 3 (Osterbrock, 1989, p.61), the flux ratio $w_{6583} = F_{[\text{NII}]\lambda6583}/F_{H\alpha}$ does substantially differ from galaxy to galaxy. Values vary for pure star formation depending on the metallicity and the ionization parameter between 0.0 and almost 1.0 (e.g. Kewley & Dopita, 2002), with even higher ratios possible for spectra with AGN contribution (e.g. Kauffmann et al., 2003). Based on low redshift data, a typical value has been shown to be $w_{6583} = 0.3$ (e.g. Pascual et al. 2007 and references therein). In the absence of knowledge about the metallicities, correlations between w_{6583} and EW or mass can be used for a more sophisticated estimate. Using such relations in our estimation might bring some improvement, which we consider for further investigation. Throughout this work we assumed a ratio of 0.3.

A wrong assumption on w_{6583} naturally impacts both the f_0 and λ_0 estimation, where the impact on the latter can be examined by comparing Δmag–λ_0 curves for different w_{6583}. Curves for five different w_{6583} between 0.0 and 1.5 are shown for the example filter combination 14 & 15 in the lower panel of Fig. 4.3. We can conclude, while the impact is not negligible, the resulting systematic wavelength errors are even in the worst case not larger than $\sim$ 3 nm, compared to the assumption of $w_{6583} = 0.3$.

In addition to w_{6583}, also the shape of the Hα line could differ.[2] Whereas line widths beyond 1000 km s^{-1} are not expected for solely star-forming galaxies, line-widths of several 1000 km s^{-1} are possible when originating from a type I AGN. AGNs can be recognized by the use of the extensive multi-wavelength data available in fields like COSMOS.

We tested the impact of the line width on the λ_0 estimation by determining Δmag–λ_0 curves for Gaussians with $FWHM$ of 100, 500, 1000, 5000 km s^{-1}, as shown in the upper part of Fig. 4.3. While a line with a width of several 1000 km s^{-1} skews the result as expected, the difference all the way between 100 and 1000 km s^{-1} does not strongly impact the parameter estimation. Only, if the line had broader wings than a Gaussian, the deviations will be visible at lower $FWHM$. A 500 km s^{-1} boxcar line gives essentially an identical Δmag–λ_0 curve as a Gaussian with the same $FWHM$, but a Lorenzian will cause stronger deviations from the estimated wavelength especially at low filter transmittances.

4.3.3 Choice of broadband filters

In order to put observationally a constraint on the continuum slope β, at least two flanking BBs need to be used. This is in the case of the VISTA NB118 filters in addition to J naturally Y, but also H might be included, allowing for a stronger constraint on β. For the analysis presented in the following we use all three filters.

As Y and H alone are theoretically enough to constrain a power-law continuum, and any strong emission line in the NB118 filter also contributes to the flux in J, J can in principle be used as an estimator of the emission line flux. Whether it is actually feasible to obtain an accurate estimate from the J excess depends on two main criteria:

First, the contribution of the line to the filter-averaged signal needs to be high enough compared to the total noise in J. For the UltraVISTA DR2 data the S/N for an infinite EW line is in J a factor 4.1 lower than e.g. at the peak of NB118 filter 15 (For more details see Appendix A.4). Therefore, the J estimate will be for the faintest lines detectable in the NB filters not very useful.

Secondly, it needs to be possible to determine the continuum contribution to J with very high precision. For example, a $EW_{\mathrm{obs}} = 10$ nm line has a J excess of only 0.06 mag, while the same object causes an excess of 0.64 mag at the peak of NB118 filter 15. Hence, deviations between estimation power law and actual continuum SED are for fluxes measured through the broadband excess more critical. It is important to note that this statement also holds, even so an accurate flux estimate in the NB118 filters can only be obtained through the TPV, as more quantitatively discussed in sec. 4.4.3.

Table 4.1 Range of parameters used for the pre-grid in the parameter estimation with the Nelder-Mead implementation of our code.

	λ_0 [a]	$\log_{10}(f_0$[b]$)$	$log_{10}(EW_{obs}$[a]$)$	β
start	1170	-17	-1	-3
end	1210	-15	2.5	5
steps	15	10	10	8

[a] [nm] [b] [erg s^{-1} cm^{-2}]

4.3.4 IMPLEMENTATION OF ESTIMATION CODE

Finding the right, global, minimum in a complicated χ^2 landscape is not always easy. We implemented two versions of a *python* code to determine the parameter-set $\mathbf{p^{est}}$ maximizing the posterior probability for a given set of measured magnitudes, $\mathbf{M}$. One version makes use of the implementation of the Nelder-Mead algorithm (Nelder & Mead, 1965) within *python/scipy.minimize*. Using the downhill simplex method, it allows to efficiently determine the minimum. In order to improve the success rate of finding the global minimum, we combined it with a pre-calculation on a coarse grained grid. The parameter-range of this pre-grid is given in Table 4.1. Then, we run the Nelder-Mead algorithm three times, starting from the grid points with the three smallest χ^2 values. After comparing the found posterior probability form each run, we assumed in case of differing minima the found minimum with the highest probability as the global minimum and designate the corresponding parameters as $\mathbf{p^{est}}$. If all three sub-runs were not converging, or if λ_0 for the best-fit parameter set was within 1 nm of the prior boundaries, we assumed the parameter estimation as failed.

The Nelder-Mead implementation is relatively efficient, but it does not allow for a direct assessment of the credibility intervals. When having actual observations, where the experiment cannot be repeated as in simulations, the correct way to state uncertainties is to determine the posterior probabilities, e.g. based on a Markov chain Monte Carlo (MCMC) approach. Therefore, we implemented also a version based on the Metropolis-Hastings algorithm (Metropolis et al., 1953). The code makes use of adaptive proposal distributions based on repetitively recalculated covariance matrices, allowing for optimal efficiency (Roberts & Rosenthal, 2001; Rosenthal, 2014). We run six separate chains with 100k proposal steps in each chain, where the initial proposal distribution was chosen wide enough to explore the complete parameter space.

Altogether, the set of four free fitting parameters, $\mathbf{p}$, does include the central wavelength of the main line, λ_0, its integrated flux f_0, the observed frame equivalent width, EW_{obs}, for the main line, and the slope β of the continuum. Within the prior, we constrained f_0 to a physically reasonable range in order to exclude combinations of unreasonably high f_0 and λ_0 at low transmittances of the filters.

The range of acceptable $\mathbf{p}$ was set for our specific test case of Hα in the NB118 filters to $1171\,\mathrm{nm} < \lambda_0 < 1206\,\mathrm{nm}$ and $0.5 \times 10^{-17}\,\mathrm{erg\,s^{-1}\,cm^{-2}} < f_0 < 100 \times 10^{-17}\,\mathrm{erg\,s^{-1}\,cm^{-2}}$, respectively. Further, we constrained $0\,\mathrm{nm} < EW_{\mathrm{obs}} < 300\,\mathrm{nm}$.

Assuming a flat prior for the line flux is from are rigorous Bayesian point of view not the right choice, as this does not reflect our complete state of prior knowledge. The line-luminosities are known to be approximately distributed by a Schechter luminosity function (Schechter, 1976). However, for clarity of the results we still used a flat priors in this work.

---

[2] We assume that the [N II] lines have the same width as the H α line.

4.4 APPLICATION TO SIMULATED OBSERVATIONS

4.4.1 MOCK OBSERVATIONS

For testing the proposed TPV method systematically, we were using in this first part simulated observations for a range of spectra. The inputs into the simulation were chosen to closely resemble available UltraVISTA DR2 data.

This means that we used as inputs VIRCAM filter curves, the characteristics of the VIRCAM IR-arrays (gain, ZP), and realistic sky brightnesses in the NB118 and the three VIRCAM BB filters.

The sky-brightnesses in the individual NB118 filters were taken from Milvang-Jensen et al. (2013) and significantly differ between the individual copies, ranging from 21.2 e^{-} s^{-1} $pixel^{-1}$ to 51.5 e^{-} s^{-1} $pixel^{-1}$ s^{-1} $pixel^{-1}$. For Y, J, and H we assumed 150, 650, 4700 e^{-}, respectively, values typical for the UltraVISTA observations. We set the detector gains to 4.2 and the zeropoints on the AB system to 21.78, 24.12, 24.73, and 25.29 for NB118, Y, J, and H zeropoints [3], respectively.

Further, we were assuming point sources observed in $2''$ diameter circular apertures. The corresponding enclosed flux fraction within the aperture is about 75% for the UltraVISTA NB118 and J PSFs. For simplicity, the same enclosed fraction was also used for Y and H, even so the PSFs in these filters slightly differ for the actual observations.

Based on a chosen spectrum and these inputs, we synthetically calculated with eq. 4.3 the expected aperture magnitudes, m_{expect}, and from the corresponding signal-to-noise ratio (S/N) we derived by $\Delta m_{\text{expect}} \approx 1.086 \frac{1}{S/N}$mag the expected magnitude errors Δm_{expect}.

The S/N was estimated from the CCD equation (e.g. Howell, 2000; Chromey, 2010). Neglecting justifiably uncertainties from read-out noise, dark-current, linearity corrections, flat fielding, background subtraction, and converting electrons through the gain, g, to digital-units, DN, the S/N can be calculated as:

$$S/N = \frac{\dot{N}^{*}_{\text{DN}} \sqrt{g} \sqrt{t}}{\sqrt{\dot{N}^{*}_{\text{DN}} + n_{\text{pix}} \dot{b}^{*}_{\text{DN}}}} \tag{4.6}$$

Here $\dot{N}^{*}_{\text{DN}}[n_{\text{pix}}]$ is the total number of DN per second created within the aperture due to the source, while $\dot{b}^{*}_{\text{DN}}$ is the number of DN produced per pixel and second by the sky-background. n_{pix} is the number of pixels constituting the aperture and t is the exposure time.

We assumed an observation time of 11.4 hr in each of two NB118 filters through which an objects is simulated to be observed, which sums to the typical per-pixel integration time available in the UltraVISTA DR2. The expected per-pixel integration time in the finished survey will be 112 hr, meaning that the DR2 NB118 data includes only $\sim$ 20% in time or 45% in depth of the final UltraVISTA survey goal. Similarly, we assumed for Y, J, H the 56, 34.9, 29.4 hrs available in the DR2 for the same field as the NB118 data, with the time in the finalized survey expected to be 210 hr in each of the BB filters.

While we tested correctness and stability of our estimation code by using spectra as input models, which could be exactly matched by the estimation model, the mock observations used in the following were based on realistic galaxy SEDs. We were using for the tests the high resolution BC03 models (Bruzual & Charlot, 2003) based on the $R \sim 2000$ STELIB (Le Borgne et al., 2003) library assuming a Salpeter IMF ($M = 0.1 - 100 M_{\odot}$, Salpeter 1955).

Table 4.2 Grid of spectral energy distributions used in this work for testing biases from the continuum estimation and for SED fitting. The larger grid used for the SED fitting is given in brackets.

Parameter	Values
Stellar population:	BC03 Bruzual & Charlot (2003) based on STELIB (Le Borgne et al., 2003) (BC03 based on BaSeL3.1 (Westera et al., 2002))
Nebular emission:	Recipe described in Ono et al. (2010)
IMF	Salpeter 0.1 – 100 $M_\odot$
Metallicities Z^a	0.008, 0.02, 0.05 (0.004,0.008, 0.02, 0.05)
$\log_{10}(Age[yr])^b$	6–9.9 with 14 steps (7–9.8 in steps of 0.1
${f_{cov}}^c$	0 (0.7,1)
$E_S(B-V)^d$	0.2 (0.0–1.0 in steps of 0.02)
SFH: $\log_{10}(\tau[yr])$	8, ∞ (7.9–10.5 in steps of 0.2)
α^e	None (1.75)

[a] $Z_\odot = 0.02$ [b] Age of the universe at $z = 0.81$ was 6.59 Gyr ($\log_{10}(Age[yr]) = 9.82$)

[c] We assume that the covering fraction of the gas, $f_{\rm cov}$, is related to the escape of the ionizing radiation, $f_{\rm esc;ion}$, through $f_{\rm esc;ion} = 1 - f_{\rm cov}$ [d] Stellar extinction assuming Calzetti et al. (2000) extinction law. Assumed to be 0.7 times lower than the nebular extinction.

[e] Parameter α of Dale & Helou (2002) models used for dust emission.

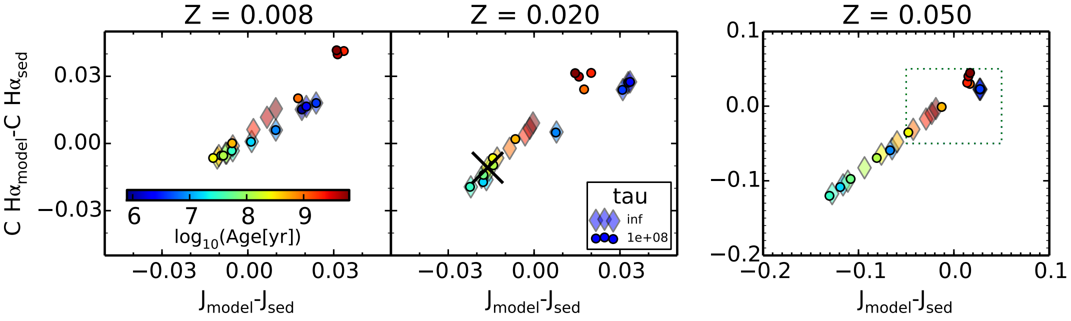

Figure 4.4 The figure shows the difference between the continuum of synthetic spectral energy distributions (SED) and the estimate obtained from a power-law fit to these SEDs (model) using Y,J, and H filters. The magnitude difference between J_{SED} and J_{model} is plotted against the magnitude difference between SED and model directly at the wavelength of H α (cf. sec. 4.4.2). The range of SED parameters, for which results are shown, is summarized in Table 4.1. For the $Z = 0.05 = 2.5Z_\odot$ panel, a wider axis scale was chosen than in the other two cases. The narrower range used for $Z = 0.008$ and $Z = 0.020$ is indicated as dotted box in the $Z = 0.05$ case.

4.4.2 Quality of continuum estimation from simulations

We are using in the TPV estimation three BB filters, Y, J, H. This means that a relatively large wavelength range is included. The range from the blue end of Y to the red end of H corresponds at $z = 0.81$ to a rest-frame wavelength range from 540 to 990 nm.

When estimating f_0 and λ_0 from the throughput variations, the constrains on the continuum at the

---

[3] Based on Vega ZPs from `http://casu.ast.cam.ac.uk/surveys-projects/vista/technical/photometric-properties` and Vega to AB corrections calculated by us for the assumed filter curves.

wavelength of the NB filter need to be precise. Further, as H α is also contributing to J, an excess in J impacts the estimation results with the algorithm described in sec. 4.3.1. Hence, the continuum needs also to be precisely estimated averaged over the complete J passband.

Therefore, it is important to carefully assess the expected deviations between the power law fit and the actual continua both in NB118 and J. Features in the spectral energy energy distributions (SEDs) could in principle cause deviations. These are not necessarily of the same extent exactly at the wavelength of H α and averaged over J, especially as the NB118 passband is at the blue end of the J passband.

While no strong spectral features are expected over the covered wavelength range, only a formal test can give a clear answer. Therefore, we fit power law continua to synthetic magnitudes calculated for a grid of model SEDs at without nebular emission applied (Table 4.2). For consistency, we had scaled all input model SEDs to a $f_\lambda = 1 \times 10^{-17}$ erg s^{-1} cm^{-2} nm^{-1} at the wavelength of Hα, before calculating input magnitudes and uncertainties as in sec. 4.4.1.

In Fig. 4.4 the difference between the continuum magnitude at H α from the best-fit power law continuum, $C\,H\alpha_{model}$, and that measured directly from the input SED, $C\,H\alpha_{sed}$, is shown for a range of SEDs. $C\,H\alpha_{sed}$ was determined by averaging the flux-densities over two 8 nm wide intervals at 1172 nm and 1205 nm, corresponding to rest-frame wavelengths of 647.5 nm and 665.7 nm, respectively, chosen to exclude Hα absorption. On the other axis, the differences between input and estimation are shown for J. The deviations averaged over the J passband are of similar extent as those for the continuum magnitudes directly at H α.

Both for stellar populations with solar and sub-solar (Z=0.4$Z_\odot$) metallicity these deviations are very small. Except for very young ages and for populations without ongoing star-formation, the differences between fit and input magnitude are below 0.02 mag. On the other hand, strong deviations exist for super-solar metallicities, exceeding 0.1 mag for expected population ages. While this is cause for some concern, star-forming galaxies with stellar metallicity as high as $Z = 2.5Z_\odot$ are expected to be very rare (e.g. Gallazzi et al., 2014, at $z = 0.7$), even at highest masses. Most of our selected galaxies will have stellar masses $\lesssim 10^{10} M_\odot$ and hence not be among the most metal rich systems according to the mass-metallicity relations (e.g. Tremonti et al. 2004; at $z \sim 0.7$: Savaglio et al. 2005; Lamareille et al. 2009). [4]

We can conclude that the continuum estimate is expected to be excellent, making both the TPV and, at least to some extent, also the use of the J excess feasible.

4.4.3 QUALITY OF FULL PARAMETER ESTIMATION FROM SIMULATIONS

We assessed the expected accuracy of H α estimations at different wavelengths for different f_0 and EW, different filter combinations, and different assumptions in the estimation algorithm. For this purpose we created in each considered case 500 realizations of observed magnitudes: we calculated for a given input spectrum the synthetic magnitudes and uncertainties, and randomly disturbed each of the magnitudes.[5]

Then, we ran our Nelder-Mead TPV code (cf. sec. 4.3.4) on each of the realizations. In this way, we found the expected distribution of best fit parameters for hypothetical repeated observations of the same object. Finally, the determined 4d distributions in the λ_0–f_0–EW–β space were reduced to 1d distributions for each of these four $\mathbf{p}_{\mathrm{free}}$ by marginalization over the three other parameters.

In all cases we used as input continuum a constantly star-forming solar metallicity SED with $E(B-V) = 0.2$ and an age of 3×10^8 yr. This SED might be considered as a typical example for the $H\alpha$ emitters selected in the UltraVISTA data. The expected offset between power law continuum and this model continuum is marked in Fig. 4.4 as a cross. It is important to note, that this chosen continuum SED

---

[4] Typically stellar metallicities are, at least for local galaxies, 0.5 dex below the gas-phase metallicity (Gallazzi et al., 2005).

[5] More precisely, we disturbed the flux densities.

has a H α absorption EW_{obs} of 0.7 nm at $z = 0.81$.[6] Therefore, even perfectly estimated H α emission fluxes, $f_{0;est}$, are too low by 16%, 8%, 5%, 3%, and 1% for H α emission with EW_{obs} of 4, 7, 10, 20, and 100 nm, respectively, as the TPV code does not correct for the H α absorption.[7] We added a Hα line with chosen f_0 and $w_{6583} = 0.3$ to this continuum. The continuum was scaled so that that the added line has a specific H α EW_{obs}. We remark that adding H α to a somewhat arbitrary continuum is not completely self-consistent, but using the same continuum allows for a clearer comparison of the results.

Line fluxes refer in the simulation parts of this paper to total fluxes, even so all measurements and estimations are simulated to be performed within the 2″ apertures.

Different line parameters

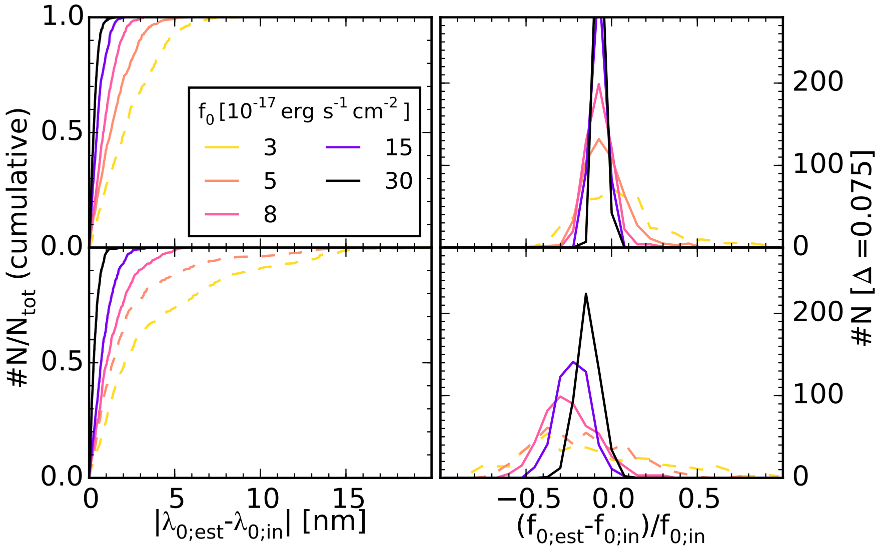

Figure 4.5 Distributions of the best fit wavelength $\lambda_{0;\mathrm{est}}$ (left panels; cumulative) and flux $f_{0;\mathrm{est}}$ (right panels) for input spectra with an emission line at the effective wavelength (top panels) and at 50% transmittance (bottom panels) of the two NB118 filters' combined passband. In each panel, distributions are shown for five different Ha fluxes. The respective values are listed in the legend in units of erg s^{-1} cm^{-2}. The input EW_{obs} was in all five cases 10 nm. Fits were obtained at both transmittances for 500 realizations of simulated observations in NB118 14&15, Y, J, and H. Dashed lines indicate that the objects would not be selected as NB excess objects.

Ideally, a robust parameter estimation is possible for the complete range of f_0–EW_{obs}–λ_0 existing in objects selected to be Hα NB118 emitters. Therefore, we performed tests based on mock observations for a set of five input line fluxes, $f_{0;\mathrm{in}}$, over the complete relevant flux range from 3.0–30.0 × 10^{-17} erg s^{-1} cm^{-2} and for five input $EW_{\mathrm{obs;in}}$ over the range from 4.0–100.0 nm. In the two cases, we fixed the respective other quantity to $EW_{\mathrm{obs;in}} = 10$ nm and $f_{0;\mathrm{in}} = 10.0 \times 10^{-17}$ erg s^{-1} cm^{-2}. Throughout this section we were assuming observations in filter combination 14 & 15, which is well suited for the TPV.

---

[6] Measured from the SED with *IRAF/splot*

[7] The factors were calculated assuming an additional [N II] contribution with $w_{6583} = 0.3$. As the measured contribution of the [N II] lines is for the actual NB118 filters redshift dependent, the expected underestimation factors also depend somewhat on the redshift.

Table 4.3 Mean and standard deviations of best estimates for H α fluxes $f_{0;est}$ and wavelengths $\lambda_{0;est}$ using the TPV on repeated simulations of observations of the same H α emitters at $z = 0.81$. More precisely, the values are for the distributions of $(f_{0;est} - f_{0;in})/f_{0;in}$ and $(\lambda_{0;est} - \lambda_{0;in})$, where 'in' is referring to the true input values. Results are stated for different $f_{0;in}$, different $EW_{\mathrm{obs;in}}$ (cf. sec. 4.4.3), different assumptions in the estimation (cf. sec. 4.4.3), and different filter combinations (cf. sec. 4.4.3). For each of the assumptions, results are given at the combined effective filter's mean wavelength (A) and three different wavelengths redwards of it (B,C,D). At 'C' and 'D' the combined effective filter's wavelength has dropped to 50% of its peak value. 'B' is halfway between the 'A' and 'C' wavelengths. Results for input parameters, where objects are not selected by the NB118 selection criteria in sec. 4.5.3 are in brackets. The full distributions, to which the stated mean and standard deviation correspond, are shown for 'A' and 'C' in Fig. 4.5 – Fig. 4.8.

	$(f_{0;est} - f_{0;in})/f_{0;in}$				$(\lambda_{0;est} - \lambda_{0;in})$ $[nm]$			
	A	B	C	D	A	B	C	D
	Different input fluxes (Fig. 4.5)							
3^a	(0.07 ± 0.28)	(−0.01 ± 0.32)	(−0.11 ± 0.41)	(−0.18 ± 0.45)	(0.11 ± 2.88)	(−1.50 ± 3.47)	(−2.68 ± 4.63)	(−5.09 ± 7.37)
5^a	−0.04 ± 0.13	−0.11 ± 0.19	(−0.18 ± 0.26)	(−0.27 ± 0.32)	−0.34 ± 1.79	−1.27 ± 2.35	(−1.78 ± 3.07)	(−2.84 ± 5.40)
8^a	−0.07 ± 0.07	−0.14 ± 0.12	−0.24 ± 0.16	(−0.32 ± 0.23)	−0.27 ± 1.13	−0.96 ± 1.49	−1.14 ± 1.38	(−9.12 ± 9.05)
15^a	−0.08 ± 0.04	−0.14 ± 0.07	−0.23 ± 0.10	−0.33 ± 0.12	−0.15 ± 0.67	−0.70 ± 0.89	−0.81 ± 0.70	−0.70 ± 0.70
30^a	−0.07 ± 0.02	−0.08 ± 0.04	−0.14 ± 0.06	−0.29 ± 0.07	0.00 ± 0.39	−0.10 ± 0.43	−0.25 ± 0.36	−0.53 ± 0.31
	Different input EW (Fig. 4.6)							
4^b	−0.16 ± 0.06	−0.22 ± 0.11	(−0.36 ± 0.14)	(−0.64 ± 0.14)	−0.08 ± 1.10	−0.70 ± 1.37	(−1.14 ± 1.40)	(−2.35 ± 2.63)
7^b	−0.10 ± 0.05	−0.18 ± 0.09	−0.30 ± 0.13	(−0.44 ± 0.16)	−0.32 ± 0.90	−1.00 ± 1.17	−1.22 ± 1.14	(−1.38 ± 2.34)
10^b	−0.08 ± 0.05	−0.15 ± 0.10	−0.23 ± 0.13	(−0.32 ± 0.17)	−0.22 ± 0.92	−0.99 ± 1.18	−0.96 ± 1.06	(−1.02 ± 2.58)
20^b	−0.03 ± 0.06	−0.07 ± 0.11	−0.12 ± 0.14	(−0.16 ± 0.17)	−0.07 ± 0.96	−0.47 ± 1.16	−0.50 ± 0.89	(−0.69 ± 2.41)
100^b	0.01 ± 0.07	−0.01 ± 0.11	−0.03 ± 0.15	(−0.05 ± 0.18)	−0.01 ± 1.10	−0.24 ± 1.21	−0.27 ± 0.90	(−1.04 ± 3.64)
	Different assumptions in the estimation (Fig. 4.7)							
0.01^c	−0.08 ± 0.05	−0.15 ± 0.10	−0.23 ± 0.13	(−0.32 ± 0.17)	−0.22 ± 0.92	−0.99 ± 1.18	−0.96 ± 1.06	(−1.02 ± 2.58)
0.05^d	−0.04 ± 0.08	−0.05 ± 0.14	−0.05 ± 0.25	(−0.24 ± 0.28)	0.19 ± 1.26	−0.13 ± 1.38	−0.14 ± 1.35	(−0.97 ± 2.46)
eff.^{e}	−0.11 ± 0.05	−0.24 ± 0.11	−0.31 ± 0.17	(−0.31 ± 0.19)	−0.96 ± 0.61	−4.20 ± 1.99	−5.97 ± 5.19	(−6.61 ± 8.62)
	Different filter pairs (Fig. 4.8)							
$14/15^f$	−0.08 ± 0.05	−0.15 ± 0.10	−0.23 ± 0.13	(−0.32 ± 0.17)	−0.22 ± 0.92	−0.99 ± 1.18	−0.96 ± 1.06	(−1.02 ± 2.58)
$7/8^f$	−0.08 ± 0.06	−0.17 ± 0.08	−0.32 ± 0.19	(−0.31 ± 0.19)	−1.43 ± 0.99	−4.99 ± 1.83	−5.63 ± 5.33	(−6.61 ± 7.92)
$11/12^f$	−0.06 ± 0.06	−0.15 ± 0.08	−0.27 ± 0.14	(−0.32 ± 0.17)	−1.32 ± 1.47	−2.83 ± 2.33	−1.07 ± 1.79	(−1.88 ± 4.45)

[a] $f_{\mathrm{0;in}}$ [10^{-17} erg s^{-1} cm^{-2}] [b] $EW_{\mathrm{obs;in}}$ [nm] [c] $\Delta m_{\mathrm{BB}}^{\mathrm{est}} > 0.01$ mag [d] $\Delta m_{\mathrm{BB}}^{\mathrm{est}} > 0.05$ mag

[e] one NB118 filter; assuming effective combined NB118 filter 14 + 15 [f] Filter pair

The resulting marginalized distributions for the best fit $f_{\mathrm{0;est}}$ and $\lambda_{0;est}$ are presented for each of the input $EW_{\mathrm{obs;in}}$–$f_{\mathrm{0;in}}$ combinations at two different input wavelengths in Fig. 4.5 and 4.6. Mean and standard deviation of these distributions are stated in Table 4.3.

The two wavelengths correspond to the mean wavelength of the two filter's combined effective passband and the wavelength where the transmittance of this passband is 50% of its peak value. The mean wavelength was calculated as in eq. 6 of Milvang-Jensen et al. (2013). Table 4.3 includes results for two additional wavelengths. One is in the middle of the interval between mean wavelength and the 50% transmittance, and the other is at 20% transmittance. The four wavelengths are indicated as small arrows in Fig. 4.1.

We note that not for all EW_{obs}–f_0–λ_0 combinations objects would also be selected as NB excess objects when applying selection criteria (cf. sec. 4.5.3), either because of not having enough S/N or not

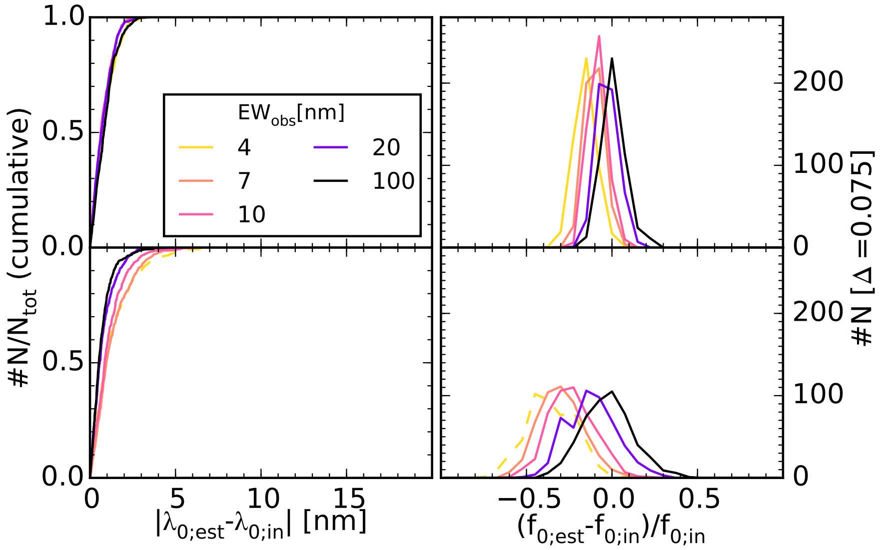

Figure 4.6 Distributions of best fit wavelength and flux similar to Fig. 4.5. Here, distributions for five different $EW_{\rm obs}$ are shown. $EW_{\rm obs}$ values stated in the legend are in units of nm. The input flux was in all cases 10×10^{-17}erg s^{-1} cm^{-2}.

a high enough NB excess. These cases are indicated both in the plots and the table.

Several important things can be inferred from this analysis. The bias in the λ_0 estimation is $\leq$ 1 nm for all those among the tested EW_{obs}–f_0 combinations, which would be selected as NB excess objects. Further, the spread in the estimation, $\sigma_{\lambda_{0;est}}$, is in all cases with selection below 3 nm. For $f_{0;in}$ = 10.0×10^{-17} erg s^{-1} cm^{-2} the spread is even $\leq$ 1 nm over the complete relevant $EW_{\rm obs}$ range, with little dependence on the $EW_{\rm obs}$.

While the $f_{0;\rm est}$ seems to significantly change with EW_{obs}, it is important to keep here the Hα absorption in our assumed model SED in mind. At the mean wavelengths of the combined effective filter almost all apparent bias is only for this reason, whereas at lower transmittances there is some additional bias. This additional bias is resulting from the mismatch in the continuum.

Different estimation assumptions

As discussed in sec. 4.3.3, the J excess is providing a flux estimate, as Y and H alone allow for a very good continuum estimate. In the case of a single NB118 filter, this would be supplemented by an additional lower limit. Therefore, one might wonder how much additional estimation power is really coming from the use of two NB filters.

In order to asses this, we performed the parameter estimation simulation for a galaxy with EW_{obs} of 10 nm and a Hα line with f_0 of 10×10^{-17} erg s^{-1} cm^{-2} using the three BB filters either combined with the pair 14 & 15 or a single NB118 filter. For the latter we assumed the combined effective filter for 14 & 15. While this does not correspond to an actual filter, it is the applicable wavelength response when analyzing a joint stack of data coming from both 14 & 15.

Estimation histograms for both cases are shown in Fig. 4.7. Clearly, making use of the throughput variations between the two NB118 filters allows for an excellent λ_0 estimation over the complete relevant wavelength range. By contrast, no robust estimation is possible when using only the single filter.

This is due to two main reasons. First, while in principle a wavelength resolution is possible when

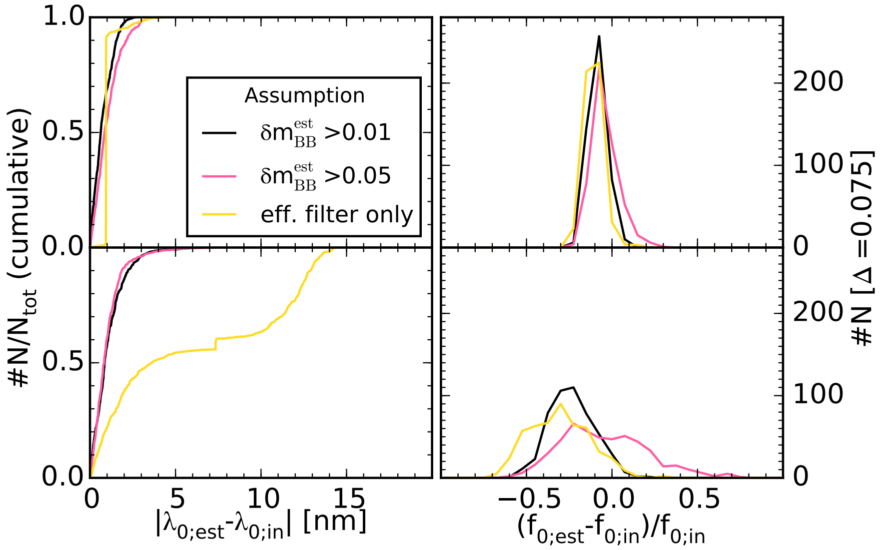

Figure 4.7 Similar to Fig. 4.5, but here estimation results for three different assumptions in the TPV algorithm are presented. First, results are shown both for assuming the default minimal BB estimation uncertainty (cf. eq. 4.5), $\Delta m_{\rm BB}^{\rm est}$ = 0.01, and an alternative $\Delta m_{\rm BB}^{\rm est}$ = 0.05. Secondly, results are presented for the case of using the data from the combined NB118 stack in the estimation (eff. filter. only), instead of the data from the two NB118 filters separately.

combining one NB filter with the flux measured based on a BB filter, a bimodality between a blue and a red solution is unavoidable. Secondly, at 50% transmittance another effect is obvious. As for the specific continuum SED, the continuum magnitude is estimated slightly too bright, the H α flux which is estimated from the J excess alone is underestimated. Therefore, even for a line several nm away from the peak, the lower limit from the NB filter indicates a stronger flux than estimated from the excess in J. Hence, the best possible reconciliation with the NB excess is for the estimation algorithm a solution being at the peak of NB filter. This is why the cumulative histograms in Fig. 4.7 jumps at around 7 nm.

The difference between using the two NB filters separately and using the single combined effective filter is not as dramatic for the flux estimate, but still results in a huge improvement. At 50% transmittance, where the line still contributes significant signal to the NB data, the reduction of the bias due to the two NB filters corresponds for our standard $\Delta m_{\rm BB}^{\rm est}$ to a factor of 1.4. At higher NB transmittances the effect is even larger. Halfway between the combined filter's mean wavelength and 50% transmittance (cf. 'C' in Table 4.3) it is a factor of 1.6. The difference is at 20% negligible ((cf. 'D' in Table 4.3), as at the corresponding low transmittances in the NB filters the flux estimation is mainly relying on the J excess. Objects at this wavelength would not be part of our NB excess sample at the given $EW_{\rm obs}$.

We also investigated the consequences of increasing $\Delta m_{\rm BB}^{\rm est}$ to 0.05, i.e. giving less weight to the BB filters. Clearly, the bias is significantly reduced. Even at 50% transmittance, the bias is close to zero, keeping in mind the H α absorption. On the other hand, the scatter is significantly increased.

Different filter combinations

As a third test, we compared the estimation quality for three different filter combinations, including 14 & 15, which was used throughout sections 4.4.3 and 4.4.3, 7 & 8 and 11 & 12. All three combinations were discussed through Δmag–λ_0 curves in sec. 4.2. The pairs are well suited for a fair comparison, as

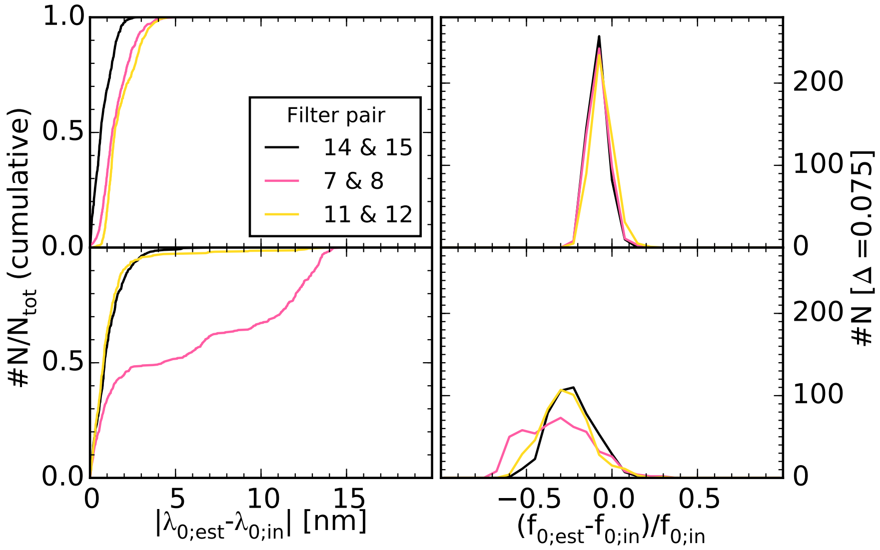

Figure 4.8 Similar to Fig. 4.5, but here results are shown for different filter combinations. An $EW_{\mathrm{obs;in}}$ = 10 nm and a $f_{0;\mathrm{in}} = 10 \times 10^{-17}$ erg s^{-1} cm^{-2} were assumed.

the sky-brightnesses are with 36 & 32, 38 & 30, 33 & 28 e^{-} s^{-1} pixel^{-1}, respectively, similar in the three pairs.

The resulting distributions for the three different filter combinations, simulated for $EW_{\mathrm{obs;in}}$ = 10 nm line with $f_{0;\mathrm{in}} = 10 \times 10^{-17}$ erg s^{-1} cm^{-2}, are shown in Fig. 4.8. It needs to be noted that both 7 & 8 and 11 & 12 are more top-hat than 14 & 15, which means that a one filter estimation is correct over a larger wavelength range.

We are showing in Fig. 4.8 the histograms for the mean wavelength and the 50% transmittance for the respective combined effective filters.

Combination 7 & 8 behaves as expected overall similar to a single effective filter, meaning that it is not very useful for an improved wavelength resolution. The wavelength resolution from 11 & 12 is also not as precise around the peak as for 14&15, as the Δmag–λ_0 curve is relatively flat there. At intermediate transmittances, where the slope is similar to that of 14 & 15, the wavelength resolution is on the other hand similar good.

4.5 Application to UltraVISTA data

4.5.1 UltraVISTA NB118 observing pattern

VISTA NB118 narrowband observations are already available from the NB118 GTO observations (Milvang-Jensen et al., 2013) and the intermediate UltraVISTA data releases (McCracken et al., 2012)[8], and more data is continuing to become available within the ongoing UltraVISTA observations.

Interestingly, some parts of the covered field are becoming directly applicable to our method. VIRCAM covers with a single pointing a non contiguous area on the sky that consists of 16 separate patches, corresponding to the individual detectors. They total 0.59deg^2 (Ivanov & Szeifert, 2009, p.11). This single-pointing field coverage is referred to as a pawprint. In order to cover an area on the sky contigu-

---

[8] McCracken et al. (2012) are describing the UltraVISTA DR1. The current release is DR2: `www.eso.org/sci/observing/phase3/data_releases/uvista_dr2.pdf`

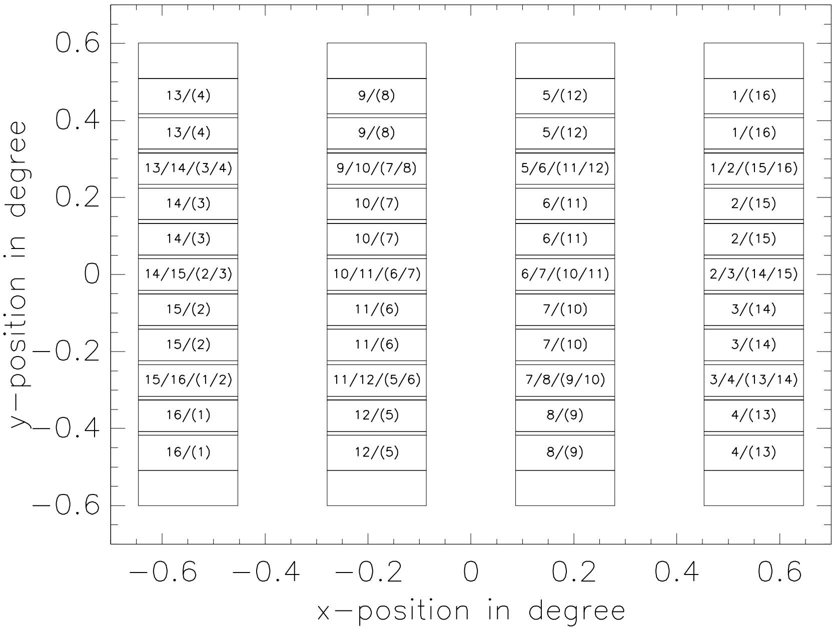

Figure 4.9 Diagram showing which copies of the NB118 filters contribute to the different parts of the field covered by the UltraVISTA NB118 tile. The numbers in brackets are only relevant, when using the suggested modification of the observing pattern, as discussed in sec. 4.5.9.

ously, a so called tile consisting of six pawprints is required.

The six contributing pawprints are three steps in one direction of the sky (y), which are performed for two steps in the perpendicular direction (x). For the NB118 part of UltraVISTA, only one of the two x-positions is observed, resulting in four stripes (cf. Fig. 4.9).

Each pointing in the y-direction is separated by 47.5% of a detector (or 5.5′).[9] Consequently, observations of at least two pawprints contribute to the covered field with the exception of the outermost parts. The filter numbers in the different patches of the pawprint can bee seen in Fig. 4.9. Most important for our method, in 20.5% percent of the stripes two pawprints contribute with two different filters. In addition for 6 tiny patches, which total 4.8% percent of the stripes, two pawprints contribute with one filter, while one pawprint contributes with a second filter. Due to the random jitter within a $2' \times 2'$ box, the regions are somewhat smeared out.

4.5.2 DATA

The controlled environment of our simulations demonstrated that the TPV is expected to work. Here, we apply the method to the actual UltraVISTA DR2 data. As part of this data release a stack of NB118 data is available. In regions of overlap, this stack includes data from both contributing NB118 copies. For the purpose of the TPV, we need these data separately. Therefore, we produced 16 custom NB118 stacks, each of which including only the data from one filter/detector. Reduction, stacking, and flux calibration were basically done in the same way as for the publicly available joined NB118 DR2 stack (cf. Milvang-Jensen et al. 2013; McCracken et al. 2012[8]) and the same observations were included.

Employing SExtractor's (Bertin & Arnouts, 1996) double-image mode, we obtained in each of the

---

[9] Each of the 16 detectors is a 2048x2048 Raytheon VIRGO HgCdTe array. 100% of a detector corresponds with the average pixel-scale of $0.34''$ pixel^{-1} to $11.6'$.

individual NB118 filters photometry in the same 2″circular apertures as in the detection image, where the latter was the joined NB118 DR2 stack including data from all 16 filters. Matching dual image photometry was also obtained for the Y, J, and H DR2 stacks. All SExtractor aperture flux and magnitude errors were corrected for correlation by means of empty aperture measurements. This was necessary, as the stacks were produced on the non-native 0".15 pixel scale and interpolation was required in the reduction as a consequence of the dithering strategy.[10] Stated observed magnitudes are aperture magnitudes in 2″ and are written in italic, where $NB118[x]$ ($x \in [1, 16]$) is referring to the magnitude in an individual NB118 filter and $NB118[s]$ is referring to the magnitude in the joint stack.

We corrected the aperture magnitudes in the different filters to the J aperture based on the enclosed fractions for point-sources. Moreover, we made sure that both remaining ZP variations in the different NB118 filters and small seeing variations in the different pawprints were accounted for. As different pawprints contribute to different parts of the per-detector stacks, the correction was done for those filters, which contribute to two different regions with overlapping filters, for each of the regions separately.

4.5.3 SAMPLE SELECTION

Selection criteria

We used following criteria to select NB excess objects in the regions of overlapping filters.

- Position in field:

  $$\text{Observed in at least two different filters} \tag{4.7}$$

- Color-cut, which must be satisfied in at least one of the two contributing NB118 filters.

  $$J_{\text{corr}} - NB118[\text{i}] > 0.2 \tag{4.8}$$

  The index i refers generically to the number of this filter and the second filter in the pair is referred to as j.

- Significance of NB excess at the four σ level ($\kappa = 4$) at least in one filter, which satisfies also eq. 4.8

  $$f_{NB118[\text{i}]} - f_{J_{\text{corr}}} > \kappa \times \delta(f_{NB118[\text{i}]} - f_{J_{\text{corr}}}) \tag{4.9}$$

  This criterion corresponds to the often used Σ criterion (Bunker et al., 1995). $\delta(f_{NB118[\text{i}]} - f_{J_{\text{corr}}})$ is the one sigma uncertainty on the flux difference.

- Significance of NB118 detection in the second filter at the 2.5 σ ($\kappa = 2.5$) level.

  $$f_{NB118[\text{j}]} > \kappa \times \delta f_{NB118[\text{j}]} \tag{4.10}$$

- Mask

  $$(\alpha, \delta) \not\subset \mathcal{M}, \tag{4.11}$$

  where (α, δ) are the coordinates of the object, and $\mathcal{M}$ are regions which are excluded due to bright stars, reflections, being close to detector boundaries, and a defect region in detector 16. We require additionally that the SExtractor flags in both contributing NB118 filters and Y and J are smaller than 4.

---

[10] Correlation correction were previously determined based on UltraVISTA DR1 data.

$f_{J_{\rm corr}}$ is the broadband flux density corrected to the position of the NB118 filter and $J_{\rm corr}$ was calculated from $f_{J_{\rm corr}}$ in the usual way by eq. 4.3. $f_{J_{\rm corr}}$ was approximated, depending on the S/N in Y and J, and the $Y-J$ color, as:

$$\begin{aligned}
\text{If } f_J/\delta f_J < 1.0 \text{ then} \quad f_{J_{\rm corr}} &= 0, && (4.12)\\
\text{else if } f_Y/\delta f_Y < 2.0 \text{ then} \quad f_{J_{\rm corr}} &= f_J \cdot 10^{-0.4 \cdot 0.07}, && (4.13)\\
\text{else if } Y-J > 0.45 \text{ then} \quad f_{J_{\rm corr}} &= f_J \cdot 10^{-0.4 \cdot 0.153}, && (4.14)\\
\text{else} \quad f_{J_{\rm corr}} &= f_J^{0.75} f_Y^{0.25}. && (4.15)
\end{aligned}$$

Equation 4.15 corresponds in magnitudes to:

$$J_{\rm corr} = J + 0.25\,(Y - J) \tag{4.16}$$

The selection criteria described above are motivated by those in Milvang-Jensen et al. (2013), but they are not identical. E.g. the 0.25 used in eq. 4.16 differs from the factor 0.34 in their work. We determined the optimal correction factor theoretically for the assumption of a power law in the Y, J, and $NB118$ filters. Milvang-Jensen et al. (2013) have determined the correction factor empirically. However, the zeropoints have been adjusted between the UltraVISTA DR1, which was used by them, and the DR2 used by us. Further, we use in this work corrections between the Vega magnitude system and the AB system, which differ slightly from those used for both UltraVISTA data releases and the work of Milvang-Jensen et al. (2013).[11] After a we applied these changes, an empirical analysis, similar to that performed by Milvang-Jensen et al. (2013), resulted in an empirical correction factor consistent with the theoretical factor of 0.25.

Another difference is that we determined the color significance based on the flux. This makes the treatment of $J_{\rm corr}$ non-detections straight-forward. Most importantly, however, we adjusted the color significance criterion (eq. 4.9) for the use of two different NB118 filters, by requiring two sub-criteria. The $4.0\,\sigma$ & $2.5\,\sigma$ combination corresponds to a combined detection of at least $4.7\,\sigma$.

The NBES sample

Our main NB-excess sample (NBES) was selected based on the criteria in eq. 4.7 – 4.11, resulting in 244 objects. Matching to the photo-z catalog of Ilbert et al. (2013), we can identify as the cause of the NB excess in 88 cases Hα+[N II] or [S II], 58 Hβ or [O III], 28 [O II], and six [S III], where the redshift cuts of $0.6 < z < 0.95$, $1.25 < z < 1.55$, $2.1 < z < 2.4$, and $0.2 < z < 0.4$ were applied, respectively. The remaining 64 objects could either not be matched to the Ilbert et al. (2013) catalogue or do not have a photo-z within the four intervals. Based on a full simulation of the NB118 observing pattern, as presented in Appendix A.3, we expect for the selection criteria about 100–250 Hα emitters, where the number depends on the chosen literature Hα luminosity function, the equivalent width distribution, and the w_{6583} distribution. In the final UltraVISTA data we expect to select about twice as many Hα emitters.

In addition to the NBES, we picked 100 comparison samples, each of which having in each of the filters the same number of objects as the NBES with the same stack $NB118[s]$ distribution. More precisely, we split the range between $19 < NB118[s] < 24$ into 40 bins. The objects in the comparison samples (CS) were randomly drawn from a selection, where we did by contrast to the NBES not impose a color-significance or color-cut. In order to completely avoid NB excess objects in the comparison sample, we also created stricter versions, where we imposed $J_{corr} - NB118[s] < 0$ (SCS).

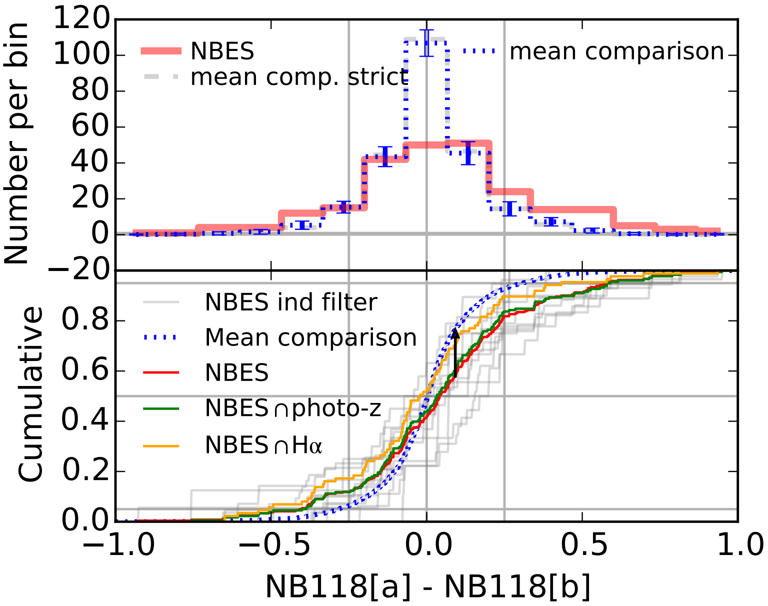

Figure 4.10 Statistical distribution of magnitude differences for objects with observations available in two different NB118 filters. Histograms are shown for the sample of 244 objects with NB excess (NBES), and for 100 comparison samples. The comparison samples have in each of the 12 contributing filter combinations the same number of objects and distribution of stack magnitudes as the NBES, but no NB excess was required. **Upper:** Both the histogram for the NBES and the histograms obtained from the mean of the 100 comparison samples are shown. In the latter case, the standard deviation between the different samples is indicated by error bars. **Lower:** Cumulative distribution for the mean of the comparison samples and for the NBES sample. The maximal differences between the two samples is indicated as arrow. In addition, for the NBES, the cumulative histograms are included for the individual filter combinations. Further, two subsets of the NBES based are plotted.

4.5.4 STATISTICAL ANALYSIS OF THROUGHPUT VARIATIONS

We tested whether we see at all NB excess objects showing throughput differences beyond the statistical fluctuations. In the upper panel of Fig. 4.10, the histogram of magnitude differences, $\Delta mag = NB118[a] - NB118[b]$, is shown as solid red curve for the NBES. All 12 filter combinations are included in the same histogram, where the identifiers a and b generically refer to the filter numbers in the pairs, with $a < b$. Also included in the figure is the mean histogram of the 100 CS and the corresponding standard deviation. The SCS sample is indicated as a dashed light gray line, which is hardly visible as it is basically identical with the CS histogram.

Including predominantly objects without emission in the NB118 filters, the spread in the CS should be caused by noise only. By contrast, the spread in the histogram for the NBES is expected to be caused both by noise and actual throughput variations, and indeed, it clearly differs from the comparison sample. The difference can also be evaluated in the lower panel of Fig. 4.10, where the cumulative histograms are shown. Applying the two-sample KS test to the two histograms, we can formally rule out the null-hypothesis that both samples are originating from the same distribution.[12] The maximum difference

---

[11] The Vega system is used during the processing of the UltraVISTA VIRCAM data

[12] At the 99.99999% level; more precisely, the comparison sample used in the KS test was the combination of the 100 realizations, having effectively 100*244 objects

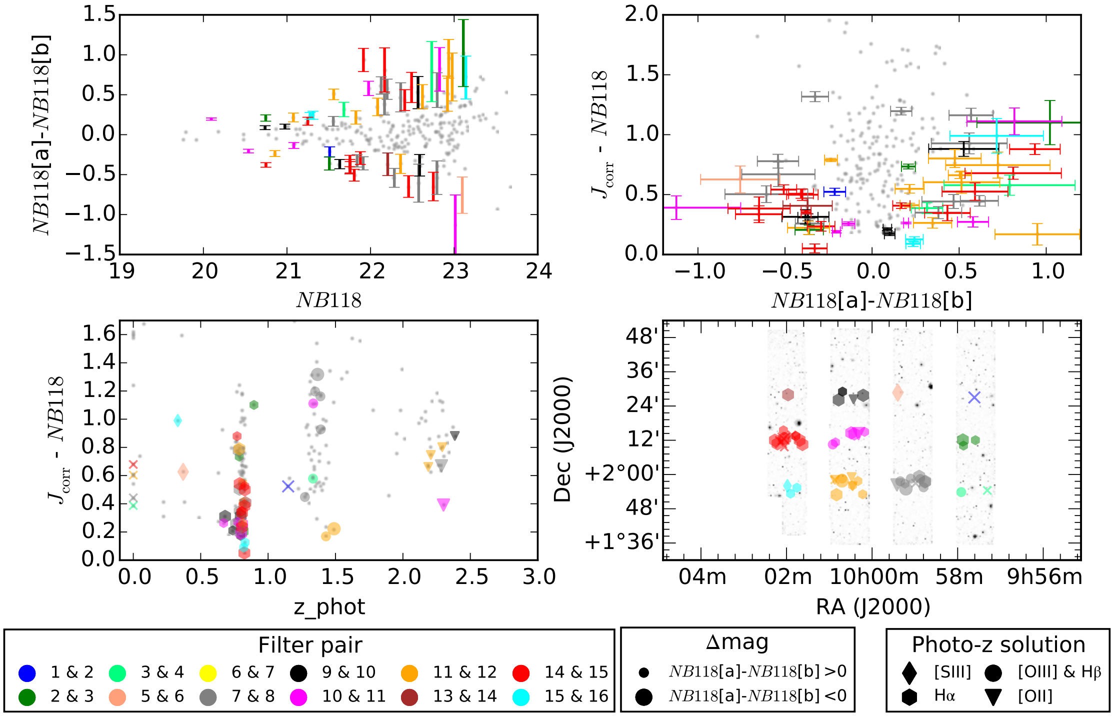

Figure 4.11 Magnitude, redshift, and field distribution for our sample of NB excess objects with observations available in two different NB118 filters (NBES). Those NBES objects with their magnitudes in the two contributing NB118 filters differing by more than 2.5σ are shown in color, with the colors referring to the different filter pairs. All other NBES objects objects are shown in the background in gray. **Upper left:** The difference in magnitude between the two individual contributing filters is plotted against the magnitude in the stack. Magnitudes were measured in 2″ diameter apertures and error bars are 1σ uncertainties. **Upper right**: The $J - NB118_{corr}$ color excess is plotted against the magnitude difference between the individual NB118 filters. $J - NB118_{corr}$ is corrected for the continuum slope by means of the $Y - J$ color (see sec. 4.5.3) **Lower left**: $J - NB118_{corr}$ plotted against the photometric redshift (Ilbert et al., 2013). The three main groups are Hα ($z \sim 0.8$), [O III]+ Hβ ($z \sim 1.4$), and [O II] ($z \sim 2.2$). Different symbols refer to membership in these groups. The X symbol (not in legend) marks objects, where no association with a specific line was possible. **Lower right:** Position of the objects in the field of view. The DR2 NB118 stack is shown in the background. Larger symbols have a $NB118[a] - NB118[b] > 0$ and smaller symbols have $NB118[a] - NB118[b] < 0$.

between the two cumulative curves is marked as an arrow in the figure.

One relevant concern is that objects with unusually large random or systematic errors in one of the two filters could show the required NB excess exactly for that reason, which might lead to a misidentification of such objects as NB excess objects and hence an inclusion in the NBES, biasing this sample to objects with large throughput variations. However, as discussed above and further shown in Fig. 4.11, photometric redshifts of 73% of the NBES objects can be well identified with actual lines, indicating a relatively clean sample. Reassuringly, the average cumulative magnitude difference curve does not change much using only this sub-sample (green curve in Fig. 4.10). For the subsample of Hα emitters the difference to the general population is slightly smaller, being explainable as the most extreme $EW_{\rm obs}$ NB excess objects are predominately [O III] emitters.

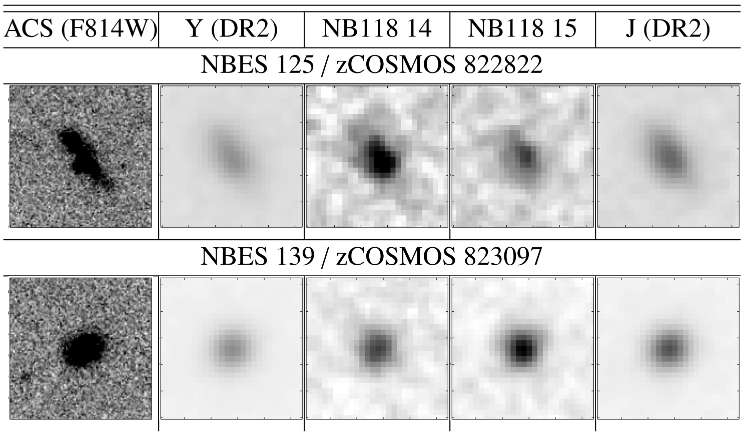

Figure 4.12 4″x4″ cutouts in UltraVISTA DR2 Y and J, NB118 14 and 15, and HST/ACS/F814W for two Hα emitters with significant throughput differences between filters 14 & 15. Both objects have spectroscopic redshifts from zCOSMOS (Lilly et al., 2009) and are included in Table 4.4. For each object, the four UltraVISTA panels are scaled to the same surface-brightness in f_ν.

As a next step, we selected those objects from the main NB-excess sample (NBES), which show a flux difference between the two filters differing from zero at least at the 2.5σ level, have a $\Delta mag > 0.05$, and are fainter than $NB118[s] = 20$. The latter two criteria are meant to avoid objects, where the difference might be caused by small remaining zeropoint errors or by small PSF differences, being especially relevant for merging objects.

The resulting 56 objects, 8 of which are so close to a neighboring object that SExtractor marked them as de-blended[13], are shown in four different plots in Fig. 4.11. While all objects of the NBES are included in the plots as gray dots, objects in the throughput difference sample are color-coded by the relevant filter pairs. Adding to the confidence that those objects with strong TPV are indeed NB excess objects caused by emission lines, a comparison of this subsample to the photometric redshifts of Ilbert et al. (2013) allowed in an even larger fraction than in the full NBES for an identification with one of the four main redshift solutions (86% vs 73%).[14] The 8 remaining objects are classified in the Ilbert et al. (2013) catalog as either masked (2), star (1), XMM detected (1), a photo-z not in the intervals (1), or we could not find a match within a radius of 0.5″ (3).

While the number of objects is too small to make strong statistical conclusions for the individual filters, we find that strong throughput variations are indeed mainly found in those pairs for which they were expected (14 & 15, and also 15 & 16 and 9 & 10). However, there is one major exception. Filter pair 7 & 8 shows surprisingly (cf. Fig. 4.2) a relatively large number of objects with strong differences. With some of them being brighter in filter 7 and others in filter 8, an erroneous ZP can be ruled out as reason for the behavior. A visual inspection of the objects also does not indicate obvious problems. Therefore, we need to conclude that one of the two filters seems to substantially differ from our expectations (cf. also A.1).

Table 4.4 λ_0 and f_0 estimates for H α both from our TPV method and other methods. The latter are based on conversions from zCOSMOS [O II] and Hβ fluxes (cf. sec. 4.5.6), on H α estimates from SED fitting (cf. sec. 4.5.6), and on SFR estimates from the combination of UV + IR (cf. sec. 4.5.6). As an example, cutouts for objects 125 and 139 are shown in Fig. 4.12. Properties of the best-fit SEDs and the EW_{obs} from the TPV are given in the Appendix as part of the supplementing Table A.3.

ID [a]	zCOSMOS [b]	pair[c]	λ_0[d](TPV)	λ_0[d](spec)	λ_0[4,5](photo-z)	$f_{H\alpha}$[f](TPV)	$f_{H\alpha}$[f]([$O\,II$])	$f_{H\alpha}$[f](Hβ)	$f_{H\alpha}$[f](total)	$f_{H\alpha}$[f](SED)
7	810332	15/16	$1202.2^{+0.2}_{-0.2}$	1201.3	1201	$38.5^{+2.0}_{-2.1}$	16.3 ± 4.5	33.7 ± 6.6	$56.0^{+72.4}_{-23.7}$	$25.4^{+16.6}_{-7.6}$
14		15/16	$1185.5^{+2.1}_{-1.4}$		1180	$4.0^{+1.3}_{-1.1}$			$5.1^{+12.8}_{-3.8}$	$5.1^{+14.0}_{-2.5}$
33	810529	15/16	$1201.1^{+0.3}_{-0.3}$	1199.1	1194	$23.6^{+2.1}_{-2.1}$	13.3 ± 4.2		$27.9^{+56.6}_{-12.8}$	$21.3^{+19.6}_{-10.4}$
97		14/15	$1197.5^{+0.4}_{-0.4}$		1199	$13.6^{+1.2}_{-1.3}$			$27.7^{+48.4}_{-22.2}$	$1.6^{+13.5}_{-1.5}$
99	822610	14/15	$1198.9^{+0.4}_{-0.4}$	1197.6	1186	$13.0^{+1.2}_{-1.2}$	9.7 ± 3.2		$9.1^{+15.7}_{-4.1}$	$12.1^{+16.6}_{-5.8}$
100		14/15	$1194.6^{+0.5}_{-0.6}$		1204	$14.0^{+1.0}_{-1.0}$			$14.9^{+16.4}_{-8.1}$	$10.6^{+13.4}_{-3.9}$
102	822560	14/15	$1186.2^{+1.1}_{-0.9}$	1189.9	1191	$9.8^{+1.6}_{-1.2}$	2.1 ± 1.4		$17.5^{+35.5}_{-11.4}$	$8.7^{+24.4}_{-5.0}$
107		14/15	$1186.6^{+1.3}_{-1.1}$		1201	$5.0^{+0.9}_{-0.6}$			$13.4^{+15.4}_{-8.8}$	$3.7^{+6.2}_{-0.9}$
108[7,8]	822732	14/15	$1199.6^{+0.1}_{-0.1}$	1199.4	AGN	$66.7^{+2.7}_{-2.6}$	0.9 ± 0.6	18.3 ± 8.5	$216.6^{+191.8}_{-160.9}$	$18.5^{+65.2}_{-1.1}$
115		14/15	$1198.1^{+0.7}_{-0.9}$		1197	$5.8^{+1.0}_{-1.2}$			$7.8^{+12.0}_{-4.7}$	$7.3^{+6.0}_{-3.6}$
117	823319	14/15	$1198.4^{+0.5}_{-0.6}$	1197.7	1186	$7.4^{+1.1}_{-1.1}$	5.0 ± 1.6	7.0 ± 2.7	$13.2^{+25.5}_{-6.9}$	$6.7^{+7.5}_{-2.1}$
118	822686	14/15	$1193.8^{+0.6}_{-0.6}$	1193.2	1190	$13.4^{+1.0}_{-0.9}$	11.0 ± 3.4		$12.3^{+17.3}_{-5.5}$	$8.1^{+15.8}_{-3.1}$
121[g]	822508	14/15	$1193.1^{+0.7}_{-0.7}$	1194.7	AGN	$29.2^{+1.9}_{-1.8}$	7.1 ± 5.1		$96.2^{+177.0}_{-72.6}$	$15.1^{+65.7}_{-3.6}$
125	822822	14/15	$1197.5^{+0.3}_{-0.3}$	1197.3	1174	$14.7^{+1.1}_{-1.1}$	16.8 ± 5.4	28.8 ± 7.2		$17.1^{+13.7}_{-7.5}$
126		14/15	$1200.6^{+0.5}_{-0.4}$		1197	$12.3^{+1.4}_{-1.5}$			$18.7^{+34.6}_{-12.8}$	$9.1^{+24.6}_{-4.1}$
128		14/15	$1189.2^{+2.9}_{-2.5}$		1188	$2.3^{+0.6}_{-0.3}$				
129	822496	14/15	$1196.8^{+0.7}_{-0.7}$	1198.5	1190	$11.4^{+1.8}_{-1.6}$	4.9 ± 2.4		$22.3^{+36.2}_{-13.0}$	$7.1^{+8.9}_{-5.8}$
130		14/15	$1183.3^{+0.6}_{-0.6}$		1199	$8.5^{+1.3}_{-1.3}$				$6.3^{+7.0}_{-2.3}$
132		14/15	$1184.2^{+0.3}_{-0.3}$		1162	$15.5^{+1.2}_{-1.1}$				$15.2^{+14.4}_{-5.1}$
135		14/15	$1186.1^{+2.2}_{-1.5}$		1201	$3.5^{+1.1}_{-0.7}$				$3.1^{+5.2}_{-1.1}$
139[i]	823097	14/15	$1185.9^{+0.7}_{-0.6}$	1184.5		$10.5^{+1.3}_{-1.1}$	4.5 ± 4.4	18.4 ± 9.3	$78.7^{+99.7}_{-64.1}$	$5.1^{+33.3}_{-1.8}$
142	822504	14/15	$1190.8^{+0.6}_{-0.5}$	1195.0	1186	$19.2^{+0.7}_{-0.5}$	25.8 ± 6.7	22.4 ± 6.0	$10.6^{+13.6}_{-3.9}$	$17.4^{+10.9}_{-7.3}$
151		14/15	$1189.8^{+2.4}_{-2.9}$		1153	$4.7^{+0.9}_{-0.3}$				$5.5^{+5.7}_{-2.6}$
154		14/15	$1193.7^{+1.0}_{-1.5}$		1188	$7.1^{+0.9}_{-1.0}$				$7.7^{+10.8}_{-3.7}$
157		14/15	$1195.9^{+0.8}_{-1.0}$		1182	$6.7^{+1.0}_{-1.0}$				$7.6^{+10.6}_{-2.4}$
165		14/15	$1196.9^{+0.8}_{-1.2}$		1211	$7.5^{+1.1}_{-1.3}$				$5.0^{+8.9}_{-2.5}$
168		14/15	$1182.8^{+0.6}_{-0.5}$		1184	$9.1^{+1.3}_{-1.3}$				$8.2^{+7.7}_{-2.7}$
171	823087	14/15	$1190.3^{+0.4}_{-0.3}$	1191.7		$27.4^{+0.4}_{-0.3}$	27.8 ± 7.6	44.5 ± 10.6	$32.5^{+34.7}_{-13.9}$	$26.0^{+14.4}_{-11.3}$
174		14/15	$1192.8^{+1.6}_{-2.2}$		1186	$5.3^{+0.7}_{-0.6}$				$4.9^{+7.0}_{-1.6}$
176		09/10	$1198.9^{+0.5}_{-0.5}$		1180	$7.3^{+1.1}_{-1.1}$				$3.8^{+6.6}_{-1.4}$
190	839235	09/10	$1199.3^{+0.2}_{-0.2}$	1197.6	1104	$17.0^{+1.2}_{-1.3}$	9.6 ± 4.5	17.8 ± 7.2	$19.6^{+24.7}_{-11.7}$	$10.2^{+15.7}_{-5.2}$
208	838539	09/10	$1183.2^{+0.6}_{-0.4}$	1182.3	1141	$23.8^{+3.9}_{-4.2}$	4.4 ± 2.7		$30.8^{+51.5}_{-16.7}$	$6.6^{+8.0}_{-6.0}$
209	838552	09/10	$1182.9^{+0.5}_{-0.4}$	1181.6	1180	$19.9^{+2.9}_{-3.3}$	7.2 ± 3.2		$36.1^{+54.6}_{-20.2}$	$14.5^{+21.7}_{-9.1}$
230		09/10	$1197.0^{+0.6}_{-0.6}$		1201	$9.6^{+1.3}_{-1.1}$			$25.0^{+34.9}_{-14.8}$	$12.5^{+22.3}_{-6.2}$
240		09/10	$1184.3^{+1.1}_{-0.6}$		1185	$7.9^{+1.3}_{-1.7}$				$4.2^{+6.4}_{-1.8}$

[a] NBES [b] zCOSMOS bright 20k (Lilly et al., 2009) ID [c] contributing NB118 filters
[d] Hα central wavelength [nm] [e] redshifts from Ilbert et al. (2013) [f] [10^{-17} erg s^{-1} cm^{-2}]
[g] *Chandra* point source (Civano et al., 2012) [h] *zCOSMOS* confidence class 13.5 (BL AGN)
[i] [Ne V]λ3426 detected in *zCOSMOS* spectrum

4.5.5 NB118 Hα MEASUREMENTS FOR INDIVIDUAL OBJECTS

Estimation with TPV

We applied our parameter estimation method to all those NB excess objects in our sample, which are located in one of the three filter pairs suited for our method (9 & 10, 14 & 15, 15 & 16) and which we

---

[13] SExtractor FLAGS = 2 or 3

[14] For one of two [SIII]λ9533 candidates, visual inspection of the SED allowed for an unambiguous identification with an extreme *EW* object at $z = 0.8$, showing a z'-filter excess corresponding to a rest-frame [OIII] + Hβ equivalent exceeding 100 nm

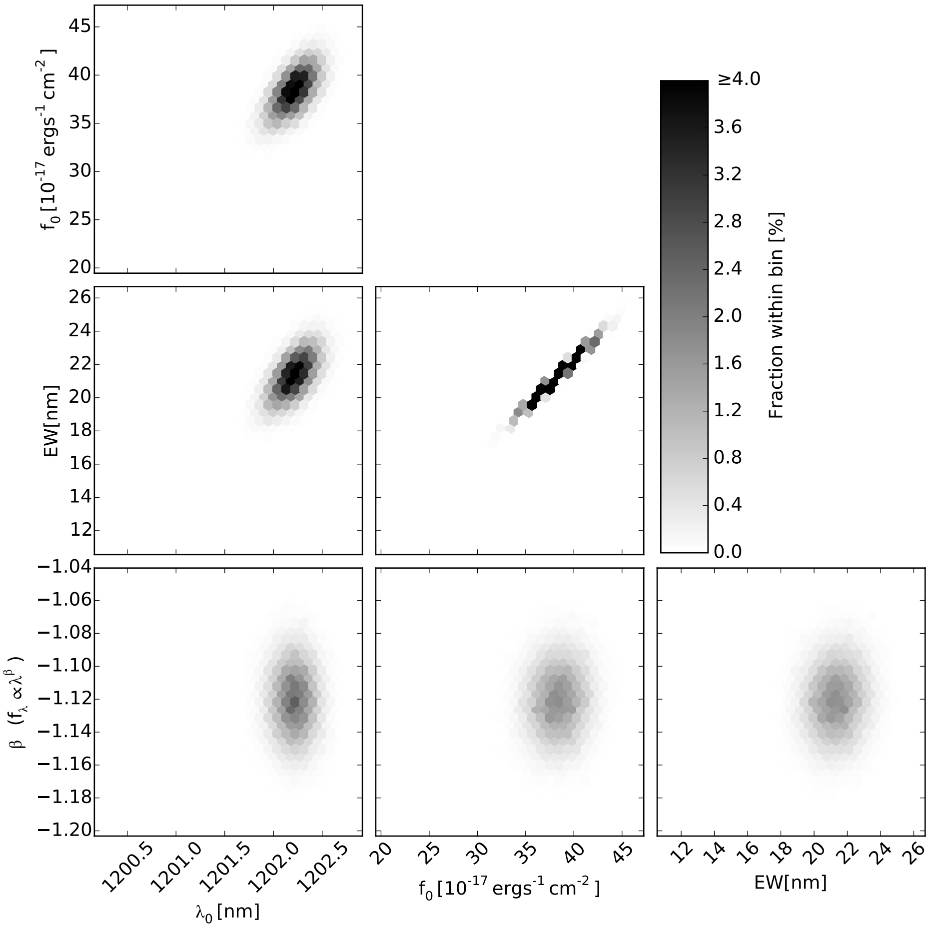

Figure 4.13 Results from the TPV parameter estimation with our MCMC code for the example object with the NBES ID 7 (zCOSMOS ID 810332). Shown are the 2D histograms, indicating the correlations between the four fitted parameters.

classify as H α emitters. For those objects we estimated all Hα flux (f_0), central wavelength (λ_0), EW_{obs}, and continuum slope (β), and the corresponding uncertainties based on the MCMC implementation of our algorithm (cf. sec. 4.3.4). Estimated λ_0 and f_0 for all objects are listed in Table 4.4. An example for the resulting credibility intervals is shown in Fig. 4.13 for the object with NBES ID 7, an object with high H α flux and being located at the boundaries of the passband. The statistical uncertainties are very small, but as discussed above, systematic errors are at least of the same order.

Estimation with generic NB118 method

For comparison, we also estimated fluxes with a conventional NB estimation method using the stack NB118 magnitudes. Here we used as estimator:

$$f_0 = (f_{\lambda;NB118[s]} - f_{\lambda;J_{\mathrm{corr}}}) \times W_{\mathrm{NB118}} \tag{4.17}$$

The effective filter width, W_{NB118}, was determined for the combined effective filters using the approach described by Pascual et al. (2007)[15]. In the W_{NB118} we took account for the [N II] contribution following the approach of Pascual et al. (2007). The f_λ were determined from the AB magnitudes in the common way. The used estimator is the simplest possible form, which assumes that the impact of the emission line to the broadband magnitude can be neglected.

4.5.6 INDEPENDENT Hα FLUX ESTIMATES

In order to asses the quality of our NB118 parameter estimation, we needed to compare to estimates of λ_0 and f_0 from independent methods. While a direct comparison to J spectroscopy would be ideal, we had to rely in the absence of such data on information obtained from available optical spectroscopy and multi-wavelength photometry. This is, we obtained H α flux estimates in three ways:

1. H α fluxes obtained from SED fitting
2. Conversion of the total SFR obtained from UV+IR into H α fluxes
3. Conversions between Hβ and/or [O II] fluxes from zCOSMOS spectra into H α fluxes

Estimation from SED fitting

We performed SED fitting using our own python code *coniecto*, which normalizes through a common χ^2 minimization a set of models with respect to mass, and allows consequently to find the model allowing for the smallest χ^2. Our parameter grid was chosen fine enough to avoid biases due to degeneracies between different parameters. The full range of parameters is stated in Table 4.2.

As input we used the Muzzin et al. (2013) photometric catalog and included in total 29 filters in the fitting, from GALEX FUV to IRAC 4. The photometry in Muzzin et al. (2013) is based on $2''.1$ diameter apertures applied to PSF homogenized images. We compared for each of the objects our $2''$ aperture photometry for Y, J, H to that in the Muzzin et al. (2013) catalog.[16] On average, the difference in the magnitudes is with 0.018 mag very small. We corrected all quantities obtained based on the Muzzin et al. (2013) photometry to match our apertures, which also crudely takes care of small differences in the centroid from our detection and that in Muzzin et al. (2013).

In addition to stellar continua based on BC03 (Bruzual & Charlot, 2003) models using a Salpeter IMF, we also add dust and nebular emission to the models, including lines and continuum. For the dust emission we use the Dale & Helou (2002) models under the assumption of energy conservation, meaning that all radiation absorbed by dust must be reemitted. Emission from dust, including PAH features, is in the IRAC bands at $z = 0.81$ only of minor importance.

Throughout this and the following sections we consistently used a Calzetti et al. (2000) extinction law. The extinction of the stellar continuum, $E_S(B-V)$, was chosen to be a factor 0.7 lower than the nebular extinction, $E_N(B-V)$. E.g. Calzetti et al. (2000) find based on a sample of local starburst galaxies (Calzetti, 1997) a factor 0.44 between the two extinctions. On the other hand, under this assumption Erb et al. (2006) find a systematic discrepancy between H α and UV based SFRs at $z \sim 2$, with equal extinction for both components giving more consistent results. Our value can be understood as a compromise. It also gives reasonable agreement between the different H α estimates obtained for this work. For Ly α, we use either the same $E_N(B-V)$ as for all other lines or somewhat arbitrarily a ten times higher extinction. Finally, we apply IGM absorption to the SED models using the parameterization of Inoue et al. (2014).

For estimating the 68% uncertainties on the parameters, we are here following (Noll et al., 2009). As we are adding 5% of the flux to the formal flux-uncertainties, in order to reduce artificial impacts

---

[15] The relevant equations from Pascual et al. (2007) are especially 7 and 12.

[16] The Y,J,H data in the Muzzin et al. (2013) catalog is based on UltraVISTA DR1 data

of possible ZP uncertainties and template mismatches, the stated uncertainties should however not be overinterpreted. They are typically overestimates.

Estimation from total SFR

For those objects with significant Spitzer/MIPS $24\,\mu$m detection in the Muzzin et al. (2013) catalog, we obtained total SFRs from the sum of UV and IR based SFRs. While Muzzin et al. (2013) provide these values as part of their catalog, we can assume a more precise redshift and it is hence worth to recalculate the values.

We determined total IR luminosities, L_{FIR}, by scaling the Dale & Helou (2002) templates so that synthetic MIPS magnitudes match the measured ones, and consequently integrating the scaled templates over the range from 8–$1000\,\mu$m. Following Wuyts et al. (2008) we used as result the mean of the Dale & Helou (2002) models for α between 1–2.5, where α is the power law index, characterizing the fractional dust mass, dM_d heated by a certain interstellar radiation intensity, U, meaning $dM_d(U) \propto U^{-\alpha} dU$. Upper and lower limit of the stated uncertainties are given by the values obtained for $\alpha = 1$ and $\alpha = 2.5$. It is noteworthy, that in the case of contribution from an AGN, the determined values will not be correct.

The total infrared luminosity can be converted into a SFR by (Kennicutt, 1998):

$$\mathrm{SFR_{IR}}(M_\odot\ \mathrm{yr}^{-1}) = 4.5 \times 10^{-44} L_{FIR}[\ \mathrm{erg\ s^{-1}}] \tag{4.18}$$

For the unobscured UV SFR we determined first the continuum luminosity density at a rest-frame wavelength of $\lambda = 2800$Å from our best fit SED model and converted this luminosity into a SFR by using (Kennicutt, 1998):

$$\mathrm{SFR_{UV}}(M_\odot\ \mathrm{yr}^{-1}) = 1.4 \times 10^{-28} L_\nu[\ \mathrm{erg\ s^{-1}\ Hz^{-1}}] \tag{4.19}$$

Finally, we converted the determined total $\mathrm{SFR_{tot}}$, being the sum of $\mathrm{SFR_{UV}}$ and $\mathrm{SFR_{IR}}$, to Hα fluxes, using the relation from Kennicutt (1998),

$$\mathrm{SFR}(M_\odot\ \mathrm{yr}^{-1}) = 7.9 \times 10^{-42}\ L(\mathrm{H}\alpha)[\mathrm{erg\ s^{-1}}], \tag{4.20}$$

the generic relation between flux and luminosity for our assumed cosmology, and the nebular extinction obtained from the SED fit.

Estimation from zCOSMOS data

In addition, we were using redshifts and line fluxes from the zCOSMOS survey (Lilly et al., 2009). Matching the coordinates of our NBES objects to the zCOSMOS 20k data-set [17] revealed an overlap of 35 objects with redshift information. It is reassuring that for all matched objects the redshifts confirmed the presence of an emission line within the filter, which is for 31 objects Hα + [N II]. The number of those Hα emitters being in the three most useful filter pairs 9&10, 14&15, and 15&16 are 3, 11, and 2, respectively.

The zCOSMOS VLT/VIMOS spectra are covering the wavelength range from 550 to 970nm. This means that they include for an object with Hα in the NB118 filter both [O II]$\lambda\lambda 3727, 3729$, being unresolved in the VIMOS data, and Hβ at observed-frame wavelengths of 675 nm and 880 nm, respectively, assuming $z = 0.81$.

We matched the *zCOSMOS* spectral fluxes to our imaging apertures by multiplying the continuum flux density at the lines' wavelength obtained from the SED fitting with the respective zCOSMOS EW_{obs}.

---

[17] The publicly available zCOSMOS DR2 10k is a subset of this catalog.

In this way, we avoid slit loss and flux calibration issues, with some remaining discrepancy expected from the spatial distribution of H II regions, if objects are more extended than the PSF.

The [O II] fluxes can be converted into SFRs, using the calibration by Kewley et al. (2004):

$$\mathrm{SFR}(M_\odot\ \mathrm{yr}^{-1}) = (6.58 \pm 1.65) \times 10^{-42}\ L([\mathrm{OII}])[\mathrm{erg\ s}^{-1}] \tag{4.21}$$

This equation is for intrinsic, meaning reddening corrected luminosities. Therefore, we de-reddened the measured [O II] fluxes as an intermediate step, again assuming the $E_N(B-V)$ from the best fit SED. The obtained SFR was then converted into a H α flux using again eq. 4.20.

The ratio between [O II] and H α is depending to some degree on metallicity and the ionization parameter (e.g. Moustakas et al., 2006). By contrast, Hβ allows for a more direct conversion, with the additional advantage of a lower difference in reddening between the wavelengths of Hβ and Hα than between [O II] and Hα. Unfortunately, the Hβ S/N is relatively low in the zCOSMOS spectra. For those objects with Hβ detection at least at the 2σ level, we obtained a H α estimate by converting between the reddening corrected values. The intrinsic ratio between H α and Hβ is 2.86 for typical conditions in H II regions, assumed to be n_e = 100 cm^{-2} and T_e = 10000 K (Osterbrock, 1989, p. 84).

4.5.7 COMPARISON OF TPV WITH OTHER ESTIMATES

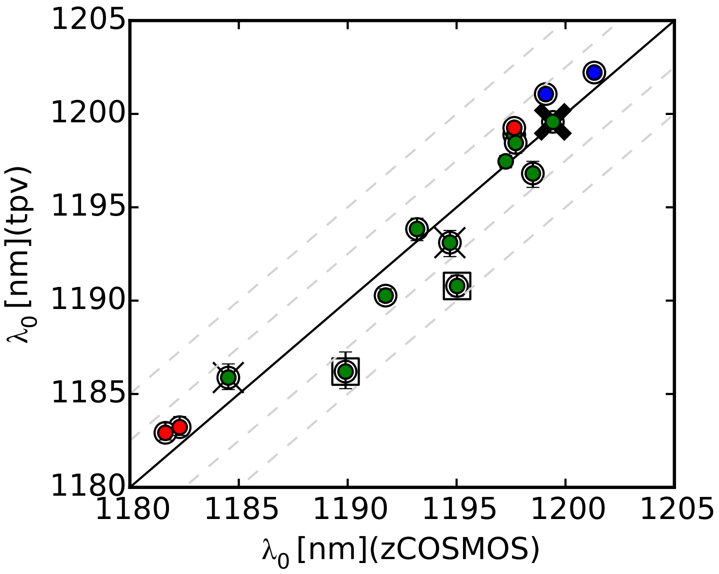

Figure 4.14 Comparison between H α central wavelengths obtained from the *zCOSMOS* redshifts and those obtained from our TPV method. The dashed diagonal lines indicate differences of 2.5 nm and 5 nm from the 1:1 relation, respectively. Used symbols are explained in the legend of Fig. 4.15.

Using the zCOSMOS redshifts and the line flux estimates of sec. 4.5.6, we can now directly compare the TPV estimates with those from completely independent measurements and thereby measure the success of the TPV method. First, we consider the redshifts. Because of the high accuracy of the spectroscopic redshifts, the accuracy of the TPV estimates can be directly assessed with a straight forward comparison. In Fig. 4.14, the TPV estimates of the wavelength λ_0 is plotted against the λ_0 obtained from the spectroscopic *zCOSMOS* survey. It can be seen that the TPV wavelength estimates closely follow spectroscopic estimates, with a mean difference of −0.10 nm and a scatter of 1.9 nm. All except two objects are within 2.5 nm. Excluding these two outliers, the scatter decreases to 1.2 nm. We remark that the observed scatter is larger than the statistical error estimate from our estimation code. This indicates that the errors are dominated by systematic effects. Expected systematic uncertainties result from mismatches between true and estimation continua, discrepancies between true and assumed [N II] ratios, and uncertainties in the available filter curves (cf. appendix A.1).

Next, we consider the H α line flux measurements. In this case, individual independent estimates are not necessarily more accurate than the TPV estimates. For that reason, we combined UV+IR, SED, [O II] and Hβ based estimates by taking the mean of the individual values. In Fig. 4.15 (upper panel), the ratio of the NB118 line flux estimates to the combined estimates are plotted versus wavelength. The top panel show the TPV estimates, while the bottom panel shows the generic discussed in Sec. 4.5.5. The same data is shown in a different way in Fig. 4.16. In this figure the ratios between the three different estimates can be directly assessed for individual objects.

For a several objects the UV+IR and the SED based estimates differ by more than a factor ten. The combined line flux for these objects is therefore uncertain, and these objects are shown faded in the figure. Except in one case, these objects are AGNs. Specifically marked in the figure is one of the objects, which is according to the zCOSMOS flag 13.5 (cf. Lilly et al. 2009) a broad line AGN, and one object which shows [Ne V] λ3426 in its spectrum and is hence identified as hosting a type II AGN (e.g. Mignoli et al., 2013). Matching to the Chandra point source catalog (Civano et al., 2012) revealed one further X-ray detected object. We classify it for the plot as narrow line (NL) AGN. Our independent flux estimates for these objects with certain AGN contribution are only of limited usefulness.

The figure demonstrates that the agreement between the TPV and combined independent line flux estimates is good. The mean of the differences is −0.02 dex with a standard deviation of 0.13 dex. In particular, there is no trend with wavelength over the complete wavelength range of the bandpass. By contrast, the generic single NB filter estimate leads to substantially biased line flux estimates, that can underestimate the flux by as much as a factor of 10 towards the edge of the filter band. Such a bias would for example have significant impact on the investigation of the structure at wavelengths around 1198 nm (see sec. 4.5.8).

Overall, we conclude that our TPV flux estimates are robust and unbiased, and the error on the flux is by as much as a factor of 20 smaller than using generic single NB estimates to derive line fluxes.

4.5.8 Spatial and redshift distribution in example filter pair

The use of the TPV method allows us to directly identify three dimensional structures, like filaments or sheets, the detection of which would otherwise require spectroscopic observations with sufficient resolution.

This is demonstrated in Fig. 4.17, which shows the spatial distribution of Hα emitters observed with the filter pair 14 & 15, combined with the wavelength information obtained from the TPV. The size of one NB118 detector corresponds to a comoving distance of 9.7 Mpc at the redshift of Hα in the NB118 filter, while the depth of the volume covered by the wavelength range from 1180 nm to 1205nm is much larger, namely 103 Mpc comoving[18]. Observations with a single NB118 filter can not resolve the depth of the field.

By contrast, the redshift resolution obtained with the TPV is sufficient to identify several objects that are at similar redshifts as the BL-AGN, revealing substantial clustering associated with the AGN. In addition, there are also several H α emitters within the field but at the other redshift end of the volume,

---

[18] Alternatively, expressing central wavelength differences as redshift velocities, 1 nm corresponds to 252 km s^{-1}.

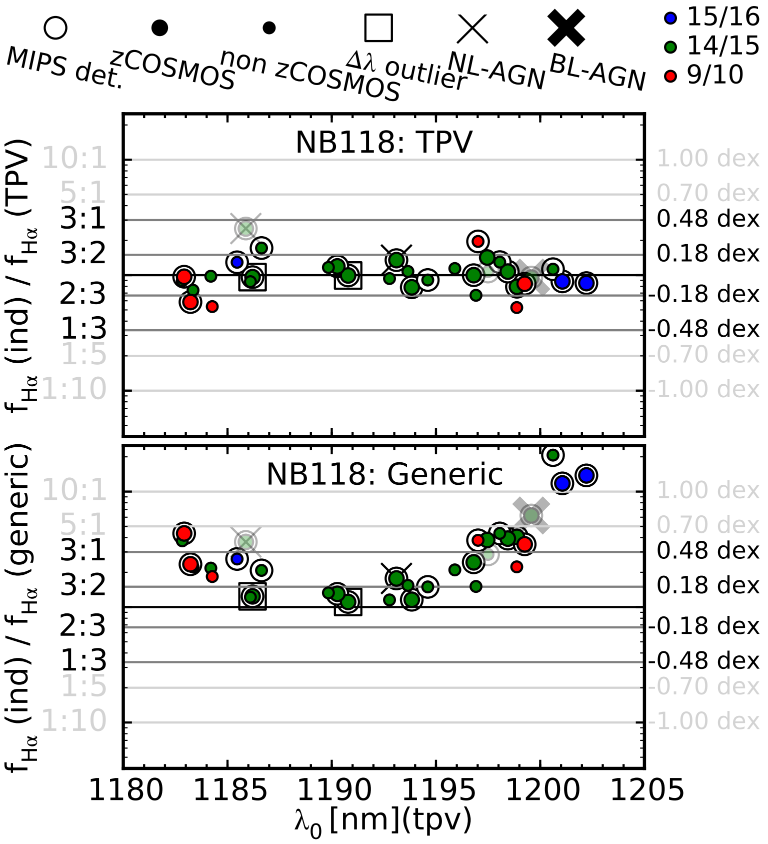

Figure 4.15 **Upper panel:** Ratios between the Hα fluxes estimated from a combination of different methods, which are independent from the NB118 data (ind; cf. sec. 4.5.6 and 4.5.7), and those estimated based on the NB118 data using the TPV technique. Colors refer to the three considered filter pairs, while symbols have meanings as indicated in the legend, with combinations of the different symbols possible. Objects with strongly discrepant individual independent flux estimates are shown faded. **Lower panel:** Similar ratios as in the upper panel, but now using instead of the TPV method a generic NB estimation method.

i.e. they are spatially well separated from the AGN cluster. Finally, there is a string of objects towards the east. This feature includes objects at various redshifts, and is likely a sheet-like structure. While a deeper discussion of these structures is beyond the scope of this paper, this example demonstrates the amount of additional information which can be gained from the TPV.

4.5.9 OPTIMIZING THE OBSERVING PATTERN

As discussed in sec. 4.2.2, the best suited pairs have $\Delta\,mag$–λ_0 curves with averages slopes in $\Delta\,mag$ of 0.10 mag nm^{-1} and are monotonous over the relevant wavelength range. Unfortunately, the standard UltraVISTA observing pattern leads to only three cases where the same position on the sky is observed with such ideal filter combinations, namely the filter combinations 9 & 10, 14 & 15, and 15 & 16. One reason for this is that the filter arrangement within the VISTA camera was chosen to maximize the obtainable depth and hence the filters are as similar as possible within each column (Nilsson, 2007;

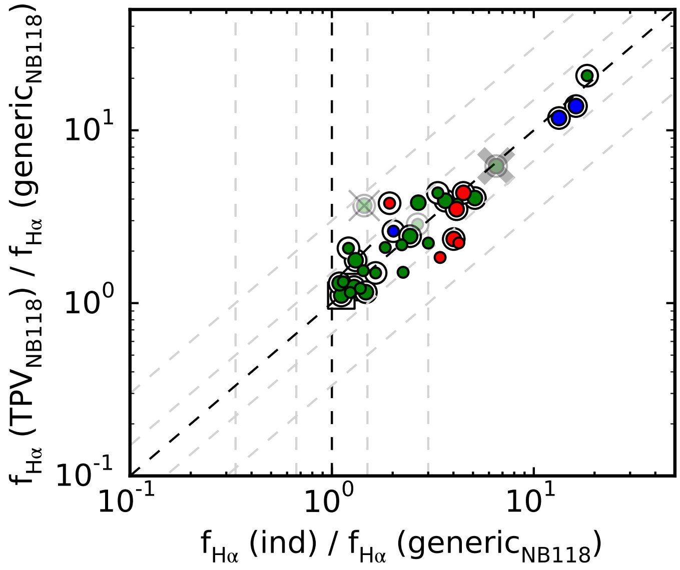

Figure 4.16 Ratio between the TPV and a generic NB118 flux estimate is plotted against the ratio between an independent flux estimate and the generic NB118 flux estimate. For objects on the diagonal the independent estimate and the TPV NB118 estimate are identical. The dashed lines indicate factors of 1.5 and 3 between the estimates. Used symbols are explained in the legend of Fig. 4.15.

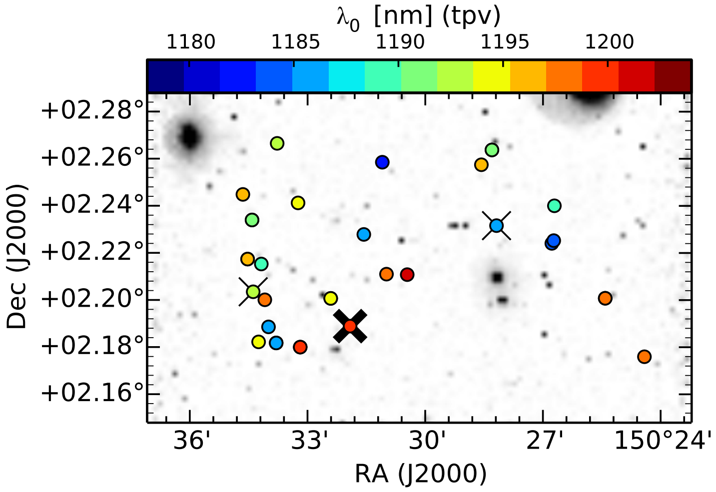

Figure 4.17 Position and Hα wavelength obtained with the TPV method for objects in the part of UltraVISTA that is covered by the NB118 filter pair 14 & 15. Indicated as thick cross is a BL AGN, while two NL AGNs are indicated as thin crosses. The UltraVISTA DR2 NB118 image is shown in the background.

Milvang-Jensen et al., 2013). Therefore, the overlapping filters are in most cases more similar than the overall spread between the 16 NB118 filters suggests (cf. Fig. A.1).

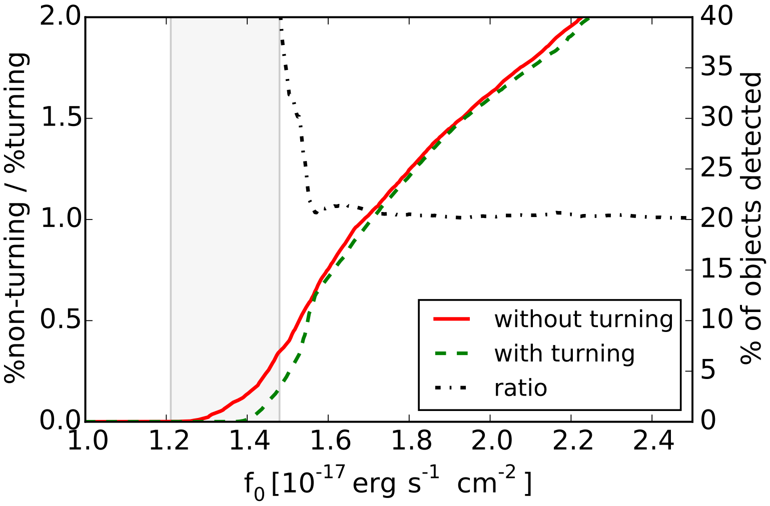

Figure 4.18 Simulated detection completeness as a function of line flux both for the standard UltraVISTA observing pattern (without turning; solid) and a possible modification (with turning; dashed). The dotted-dashed line gives the ratio between the two completeness curves. Fluxes for which 200% more objects are expected in the standard pattern than in the modified pattern are indicated by the shaded area. No objects will be detected left of this area in either of the two observing patterns. The completeness curves were calculated for point sources with a spectrum consisting of a single infinite *EW* emission line. The underlying detection criterion was a color-significance of the NB118 excess in the stack including data from the 16 filters jointly at least at the 5σ level (cf. sec. 4.5.9 for more details).

In order to make use of the full potential of the TPV method, the observing pattern should be modified to increase the number of cases where repeated observations of the same field use dissimilar filters. One easy to implement strategy is to turn the telescope by 180% for half of the observation time. With this strategy, every observed position is covered by at least two filters, whereas in the standard observing pattern, about 75% of all positions are covered with only one filter. Furthermore, in the other patches, where already in the standard observing pattern two filters contribute, there would be data from four filters. This increases the number of combinations, which are different enough to allow for a good parameter estimation. Out of the 44 patches more than half (24) have an average slope of the Δmag–λ_0 curve larger than 0.10 mag nm^{-1}.[19]

While the turning pattern would be an enormous step forward for the method, it comes at a prize. The specific positioning of similar filters is the logical step in order to maximize the reachable depth, being most crucial for one of the main science goals of the VISTA NB118 observations, the search for $z = 8.8$ Lyα emitters. We evaluated the impact of this loss in depth with the simulation described in Appendix A.3.1. This simulation takes account for the difference in filter profiles and background in the individual filters. In short, we randomly assigned positions on the sky and central-wavelengths to 3×10^5 objects, simulated the observations, and determined the fraction of input objects which would be detected as a function of wavelength. Different from the selection criteria in sec. 4.5.3, we required here a 5σ color-significance in the complete stack instead of the two-filter criteria, and considered the complete field. To test effects of the finite number of simulated objects, we also tested the variance between 10 subsets of 3×10^4 objects, and found negligible impact on the results.

---

[19] The average slope was calculated as further described in Appendix A.2. For those patches, where four filters contribute, we calculated an average slope from the three largest slopes for all six possible combinations.

In Fig. 4.18, the fraction of detected objects as function of the flux is shown both for the standard observing pattern and the turning modified one. There is clearly a non-negligible fraction of objects that will be missed at the very faint end when using the turning pattern. Therefore, deciding against or in favor of the turning pattern is a difficult trade-off.

4.6 SUMMARY AND CONCLUSIONS

In this paper, we have proposed the TPV method to derive redshifts and line fluxes from wavelength dependent throughput differences between NB filters with slightly differing, yet overlapping passbands, and corresponding broadband filters. While it is possible to specifically design NB filters for this method, suitable filters and data taken with such filters already exist, e.g. the UltraVISTA survey taken with ESO's VISTA/VIRCAM. For our analysis, we focussed on the Hα line in the narrowband NB118 filters of that survey. About 1/4 of the UltraVISTA fields are covered by at least two different NB118 filters. We used simulations to assess the expected accuracy of our method given the current exposure time of the survey. We found that for the most suitable filter pair, the simulations predict that it is possible to measure wavelengths with random and systematic errors as low as 1 nm for a line with $f_0 = 10{\times}10^{-17}$ erg s^{-1} cm^{-2} independent of EW. The wavelength estimation results were also shown to be not strongly affected by assumptions on the line-width and the required [N II]λ6583/Hα ratio.

The accuracy in redshift compares favorable to photometric redshifts. A wavelength error of 1 nm corresponds to a $\sigma_{\frac{\Delta z}{1+z}} = 0.001$. By comparison, highest quality photometric redshifts in the COSMOS field can at best reach a resolution of about $\sigma_{\frac{\Delta z}{1+z}} = 0.01$ (e.g. Ilbert et al., 2013).

In addition to the simulations, we also applied the method to the actual UltraVISTA DR2 data. A comparison of wavelengths estimated with our method and those obtained from the spectroscopic zCOSMOS 20k catalog (Lilly et al., 2009) shows an excellent agreement. Independent predictions for the Hα line flux, both based on spectroscopic [O II] and Hβ fluxes and photometric data, also confirm that the proposed method works very well and is a significant improvement compared to the results from a generic line flux estimation. This improvement is shown again in Fig. 4.16.

We therefore conclude that the TPV method is a powerful tool to derive relative accurate redshift and flux estimates from NB surveys that employ multiple versions of similar filters. One of the advantages of the method is that it exploits information that is routinely collected with some instruments. The improvement over the standard analysis is as much as an order of magnitude reduction in the errors.

4.7 ACKNOWLEDGMENTS

The Dark Cosmology Centre is funded by the Danish National Research Foundation. BMJ and JPUF acknowledge support from the ERC-StG grant EGGS-278202. Part of this research was funded by an ESO DGDF grant to WF and PM. Based on data products from observations made with ESO Telescopes at the La Silla Paranal Observatory under ESO program ID 179.A-2005 and on data products produced by TERAPIX and the Cambridge Astronomy Survey Unit on behalf of the UltraVISTA consortium. The zCOSMOS observations are based on observations made with ESO Telescopes at the La Silla or Paranal Observatories under program ID 175.A-0839.

5

CONCLUSION AND OUTLOOK

In the following sections I will summarize each of the three projects, which I have presented in this thesis. In addition, I will discuss my plans for the future in the context of the respective projects.

5.1 FINDING, CONFIRMING, AND UNDERSTANDING THE MOST DISTANT GALAXIES

5.1.1 PRESENTED WORK

In chapter 2, I have presented XSHOOTER spectroscopy for a Lyman-α emitter at $z = 6.6$, which is commonly referred to as *Himiko* (cf. Ouchi et al., 2009). Our high quality spectrum confirms previous Ly α measurements for this object. In addition and remarkably, our spectrum allowed to detect the UV continuum redwards of the Ly α line. As expected for this redshift, the continuum is completely absent bluewards of the Ly α line. This confirmed that all detected flux is originating from the source(s) at $z = 6.6$.

Based on SED fitting, we demonstrated that the stellar population of Himiko is despite substantial observational efforts still not well constrained. A very young population dominating the photometry would be consistent with all available data.

Our main goal was to search for rest-frame UV emission lines, like C IV, C III], He II. The presence and strength of these lines allows to decide, whether an AGN is the powering source for the strong and extended Ly α emission. We do not detect any of these lines significantly and the obtained upper-limits allow to disfavor strong AGN contribution.

5.1.2 ONGOING/PLANNED WORK

Rest-frame UV spectrography of high redshift galaxies The search for AGN activity in highest redshift galaxies is of major importance for our understanding of galaxy evolution; but it is not the only driver behind emission line searches in the rest-UV spectra.

As rest-frame optical spectroscopy will not be possible for the highest redshift objects until the advent of the JWST, and as the Ly α line is likely heavily suppressed due to a damping wing of the IGM for the majority of high redshift galaxies at $z > 7$, the detection of rest-frame UV lines can be considered as the best possibility for spectroscopic confirmations of galaxies at highest redshifts. Further, for those objects with Ly α in emission, the detection of a non-resonant line would allow to find the systemic redshift of the galaxy more precisely, which would consequently allow for a better interpretation of the resonant Ly α.

Given sufficiently deep observations, rest-frame UV lines can also be detected in the absence of an AGN but with an origin from the H II regions surrounding very young and relatively metal poor stellar populations. C III] is expected to be the strongest among the rest-frame UV lines in such populations (Erb et al., 2010; Christensen et al., 2012; Stark et al., 2014b, e.g.). A detection of strong He II in the absence of any metal lines can indicate ongoing star-formation out of gas with primordial element composition (Pop III). Finding such a population is one of the major challenges in the study of high redshift galaxies.

We have obtained XSHOOTER spectra for two other high redshift Ly α emitters (PI: Hans Ulrik Nørgaard-Nielsen, 089.A-0679(A)). Due to adverse weather and seeing conditions, the data is not of the expected quality and the analysis is still ongoing. First successful detections of C III] lines, which can likely be explained through ionization by a stellar population, have been made at similar redshifts as the objects observed by us (Stark et al., 2014a), demonstrating that such searches are not in vain. One of my goals in the future will be to further optimize the reduction of XSHOOTER and NIR spectra in general for the purpose of finding faint spectral features. Several projects, which I am involved in, would benefit from such improvements.

High redshift GRBs An exciting possibility to find the highest redshifts galaxies is through long-duration gamma ray bursts (GRB), which are the highly energetic explosions ending the lives of certain massive stars. Their optical afterglow spectra can be bright enough to be detected spectroscopically at highest redshifts, and a detection of a Lyman-break caused by the neutral hydrogen in the IGM allows for a save redshift determination (see Tanvir 2013 for an overview of highest redshift GRB studies)). I am involved in an ongoing project on GRB 120923A, which is likely at redshift $z \sim 8$ (Tanvir et al., in preparation).

Passively evolving galaxies at $z \sim 2$: It is certainly not only of interest to find and understand the highest redshift galaxies themselves, but also how and into what they evolve with time. With the wide availability of NIR imaging, a population of distant red galaxies (DRG) with quenched stellar populations has been found at $z \gtrsim 2$ (e.g. McCarthy et al., 2004). This puts their last major episode of star-formation at $z > 3$ or a time when the universe was less than 15% of its present age. The DRGs have a remarkably compact morphology (e.g. Daddi et al., 2005; Trujillo et al., 2006b; Toft et al., 2007; Newman et al., 2012; Krogager et al., 2014). The corresponding high stellar densities are probably produced during a dissipative process which channels gas into the core. This process could be either triggered by disk instabilities (e.g. Dekel & Burkert, 2014; Barro et al., 2014) or gas rich major mergers (Wuyts et al., 2010). Followed by quenching from the induced starburst itself or triggered AGN activity, the transformation would be completed. High redshift submillimeter galaxies have been recently identified as likely candidates for objects in this transition phase (e.g. Toft et al., 2014; Ikarashi et al., 2014).

The most advanced NIR spectrographs, like VLT/XSHOOTER and KMOS, Keck/MOSFIRE, or Subaru/MOIRCS allow to measure the rest-frame optical spectra of DRGs, including the relevant absorption lines (Toft et al., 2012; Onodera et al., 2014; Tanaka et al., 2013; Belli et al., 2014; van de Sande et al., 2014; Mendel et al., 2015). Measurements of absorption lines are of fundamental importance for several reasons. For example, they allow to break the degeneracy between age, metallicity, and dust, which is inherent to SED fitting without such information. No less important is the kinematical information obtained from the absorption lines. I am involved in studies of DRGs with XSHOOTER led by S. Toft.

There is strong evidence that the DRGs are pressure supported and will be the cores of nowadays ellipticals. However, we are currently working on the spectrum of a gravitationally lensed DRG, in which we find signature of rotation (Toft et al., in preparation). If found to be common, this exciting result might require an adjustment of the current paradigm.

5.2 HYDROGEN AROUND STAR-FORMING GALAXIES PROBED THROUGH EXTENDED Ly α EMISSION

5.2.1 PRESENTED WORK

In chapter 3, I have presented a stacking analysis of a sample of Ly α emitters at redshift $z = 2.3$. The goal was to investigate for presence or absence of an extended Ly α halo on large spatial scales. Two previous studies have shown ambiguous results at this redshift. Momose et al. (2014) have found such a halo, while Feldmeier et al. (2013) did not. In our sample, we have found a halo, similar to that in Momose et al. (2014).

5.2.2 PLANNED WORK

The most important goal for the future will be to understand how the presence and strength of the halos correlates with different physical properties of the galaxies. While it has already been demonstrated that the strength of the halos correlates with the density of the environment, the UV brightness (Matsuda et al., 2012), and the Ly α EW_0 measured for the central galaxy (Steidel et al., 2011), there is a wealth of possible correlations left to explore. E.g., where Ly α spectra with sufficient spectral resolution are available, a possible dependence of the halos on the Ly α line shape might give interesting insights into the interplay between ISM kinematics and Ly α halos. Certainly, it is also of major importance to understand the exact mechanism responsible for the extended emission. At this point there exist still several possibilities (cf. e.g. sec. 3.6.2 of this thesis or Lake et al. (2015) as an example from the literature).

Unfortunately, our sample is not large enough for more detailed studies. Currently, the only samples which will allow for such studies are the large Subaru/Suprime-Cam samples (e.g. Matsuda et al., 2012; Momose et al., 2014). Therefore, a continuation of the NB based work might only be possible through a collaboration with these groups. However, with the availability of advanced integral field spectrographs, like VLT/MUSE (Bacon et al., 2010), exciting new data is becoming available. Individual observations of Lyman-α blobs will allow for ground-breaking insights into the circumgalactic medium for objects at the peak of the cosmic density fields. In addition, the various MUSE observations will also accumulate over time huge samples of typical field LAEs. One of my plans for the future is to work on a robust analysis and stacking technique for emission on large scales based on then archival MUSE data.

Another important aspect, which needs to be fully understood is the relationship between these halos and damped Lyman-α absorbers (DLAs). This might allow to understand the puzzling scale difference between the impact parameters of DLAs (up to about 30 kpc) and the associated galaxy counterparts' extent in stellar light (effective radii < 1 kpc; e.g. Fynbo et al. 2013; Krogager et al. 2013).

5.3 EXPLOITATION OF THE VISTA NB118 DATA

5.3.1 PRESENTED WORK

Finally, I have presented in chapter 4 a project based on the UltraVISTA NB118 narrowband data. We have developed a NB observation technique, which allows to obtain remarkably good redshift resolution: an order of magnitude higher than that expected from the passband width of the filters. The trick behind our method is to observe the same objects through two NB filters with slightly different passbands. Such filters are available in VIRCAM/VISTA, as its 16 detectors are covered by individual copies of the NB118 filters. These copies are due to production variations not completely identical.

Predictions for the accuracy of the redshift estimation, which we have derived from simulations, were confirmed in the actual application to UltraVISTA DR2 data. We could conclude this through a comparison to spectroscopic redshifts from the zCOSMOS survey (Lilly et al., 2009). Concurrent with increasing the redshift resolution, the method allows for very accurate line flux measurements for individual objects. This is with generic NB measurement methods not possible for non-tophat NB filters, as the VISTA NB118 filters are.

5.3.2 ONGOING/PLANNED WORK

The presented throughput variations method gives a unique possibility to study the large scale structure: the sample in a deep line-flux limited NB survey, like UltraVISTA, will include objects with significantly fainter continuum flux density than those included in current wide-field spectroscopic surveys (see e.g. Kochiashvili et al. 2015 for a discussion). However, the current usefulness of the method for the UltraVISTA data is limited, because of the pointing strategy used in the ongoing survey (cf. sec. 4.5.9). As modifying the current strategy might not be feasible, I will consider applying for observation time specifically for the purpose of the discussed method. In addition, the method should be understood as general concept and other suitable data exist at other telescopes. I am planning to reach out to groups with such data available.

The spatial information which can be obtained from the throughput variation method is only one aspect of the science possible with the NB118 data. Among others, there are three NB118 projects, which I am particularly interested in.

First, I am leading a case study for follow-up spectroscopy of those NB118 excess objects, where the NB excess is caused by [O II] at $z = 2.2$. Some brief insights into this initiated project are given in the following section 5.4.

Secondly, I am am planning to find out whether weak (or strong) extended emission can also be found in other lines than Ly α around typical high redshift star-forming galaxies. The main focus will be on [O III] at $z = 1.4$ and [O II] at $z = 2.2$. A systematic search for such halos in typical field galaxies is in its infancy. Recently, Yuma et al. (2013) have published the first study for extended emission in [O II] at $z = 1.2$. They could identify several objects with individually detected extended emission, while a stack of all [O II] emitters in their sample did not show such emission. The presence of extended emission in these metal lines can be connected to outflows, as confirmed for their sample through ISM absorption line spectroscopy (see also Harikane et al. 2014). With the UltraVISTA data we can perform such a study at higher redshifts, close to the peak of cosmic star-formation activity. As strong outflows are likely correlated with the quenching of star-formation, it will be very interesting to investigate for a correlation of extended metal line emission with the position of the galaxies on the main-sequence of star-formation (e.g. Noeske et al., 2007; Daddi et al., 2007).

Thirdly, I am also interested in contributing to an optimal search for presence or absence of Ly α emitters at $z = 8.8$, which is the main science goal of the UltraVISTA NB118 survey.

5.4 DETAILED STUDY OF STAR-FORMING GALAXIES AT $z = 2.2$

Narrowband selection of emission-line galaxies can provide very useful samples for follow-up spectroscopy. The combination of a NB excess combined with a photo-z from broadband data allows for a robust and relatively precise redshift estimation. This even holds for redshifts above $z > 1.5$, where broadband photo-z's alone become less accurate, as the 4000 Å break moves into the NIR. Precise knowledge of the redshift is important for the follow-up at these redshifts. Otherwise not all important rest-frame optical emission lines might be observable within the windows of high atmospheric transmission in the NIR.

From VISTA/VIRCAM NB118 observations we can select a huge sample of emission line galaxies

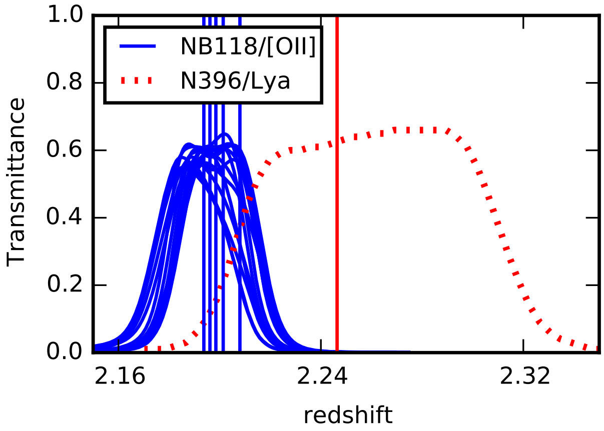

Figure 5.1 Filter transmittance as a function of redshift for [O II] in the 16 copies of the VISTA/NB118 filters (cf. sec. A.1) and for Ly α in the N396 filter (cf. chapter 3). The vertical lines show the redshifts of six galaxies for which we have obtained XSHOOTER spectra.

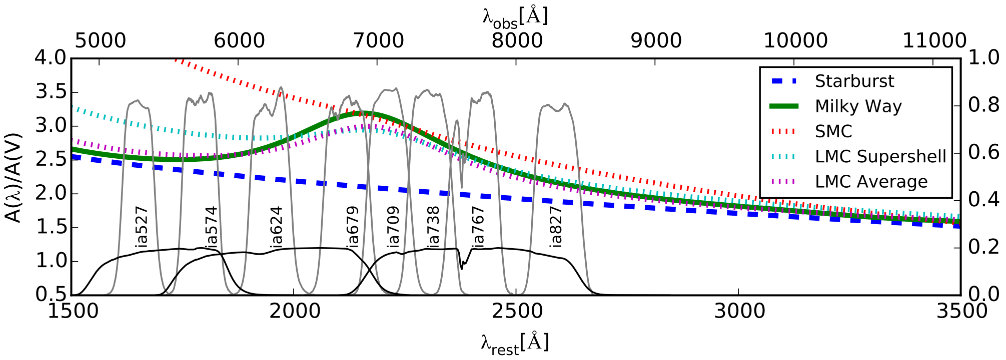

Figure 5.2 Five different dust extinction curves at redshift $z = 2.2$. Filter curves for eight Subaru mediumband filters ('iaxxx'), and the three broadband filters r^+, V_J, i^+. They differ both in the slope and the presence of the 2175Å dust bump. The eight shown Subaru mediumband filters ('iaxxx'), for which data is available in the COSMOS field, will allow to probe the 2175Å bump with good resolution. For the relevant references and further details about the extinction curves compare Fig. 1.4 of the introduction.

at a redshift $z = 2.2$ through their [O II] λ3727 emission. This is an ideal redshift for a follow-up study with VLT/XSHOOTER. We will complement the [O II] sample with the N396 sample of Ly α emitters (Nilsson et al., 2009) as used in chapter 3 of this thesis. These objects are selected from a redshift range adjunct to the NB118 [O II] sample, as can be seen in Fig. 5.1. As the N396 field is a subset of the field for which NB118 data is available, the objects are also close in space. This provides the important possibility to compare samples selected based on these two different lines around the same cosmic time in a similar part of space.

Our study aims at understanding these $z = 2.2$–2.3 star-forming galaxies in detail. This includes following measurements:

- Constraining the fundamental relations between mass, metallicity, SFR, environment, etc.

- Comparing dynamical masses with stellar masses.
- Finding signatures of out- or inflows from low and high ionization interstellar absorption lines, from the profile of the resonant Ly α line, and from the profiles of the non-resonant emission lines.
- Performing detailed SED fitting for the objects including all available multi-wavelength data in the COSMOS field to infer as many physical properties as possible.
- Characterizing the AGN contributions through different methods, including line ratios between rest-frame optical lines, presence and strength of rest-frame UV emission lines, X-ray data, far-infrared SED.
- Characterizing the dust extinction curve for the [O II] and Ly α emitters. As we are selecting a sample at a well defined redshift, we can effectively probe the 2175Å bump through the COSMOS medium band data (cf. Fig. 5.2). For those objects, for which we manage to secure spectra, we can directly measure the nebular extinction through the Balmer decrement from the Hβ to H α ratio. This can be compared to stellar extinction obtained from SED fitting.
- Understanding the differences in the physical properties between the Ly α and [O II] selected samples. Further, we will compare to broadband selected studies. This will be the main goal of this study.

Some of the measurements require spectroscopic follow-up. As a case study we have obtained VLT/XSHOOTER spectra for five VISTA NB118 selected [O II] emitters and one LAE from the sample of Nilsson et al. (2009). While the sample size does not allow to derive statistical conclusions, we use it to test the feasibility of our science goals and to demonstrate the high quality of the XSHOOTER spectra. In this section I give a few impressions, which are not meant as a final analysis.

Selection of a large sample of [O II] emitters from the VISTA NB118 data

We selected the objects for this case study based on all data taken through the VISTA / VIRCAM NB118 filters in the COSMOS field. This includes the GTO (Milvang-Jensen et al., 2013) and UltraVISTA observations (McCracken et al., 2012)[1], which have a typical per pixel exposure time of 13.3 hr and 22.8 hr, respectively. Both the NB118 GTO and DR2 data cover four spatially distinct columns. This is due to the detector layout of VIRCAM and the employed observation strategy (cf. also sec. 4.5.1). The field coverage of the two datasets is complementary, and they cover combined almost the total field for which COSMOS HST/ACS observations are available (Koekemoer et al., 2007) and an additional area towards the west (cf. Fig. 5.3). In addition to the NB118 data, we used in our preliminary analysis the UltraVISTA DR2 Y, J, H, and Ks data and the multi-band photometric catalog of Muzzin et al. (2013).

Our selection of NB excess objects is shown in Fig. 5.4. We refer to section 4.5.3 of this thesis for details about the selection. In contrast to the analysis presented there, we used here not the data from the individual filters. In other words, the requirements of a significant positive color excess (eq. 4.9) and a minimum color excess (eq. 4.8) were applied to the combined stack of all data instead.[2]

In the upper row of Fig. 5.4 we show the selected NB excess samples for different requirements on the significance of the NB excess (3,4,5σ). In the lower panels we plot those NB excess objects from the 3σ sample which have photometric redshifts within the three specific redshift ranges of $0.6 < z < 0.95$, $1.25 < z < 1.55$, $0.95 < z < 1.55$. The lowest redshift bin mainly includes Hα+[N II]$\lambda\lambda$ 6548, 6583 or

---

[1] Here, we used the DR2: `www.eso.org/sci/observing/phase3/data_releases/uvista_dr2.pdf`

[2] Eq. 4.10 is not relevant here. For the analysis presented in this section we did not use the constant J_{corr} for $Y - J > 0.45$. This choice is further discussed towards the end of this section.

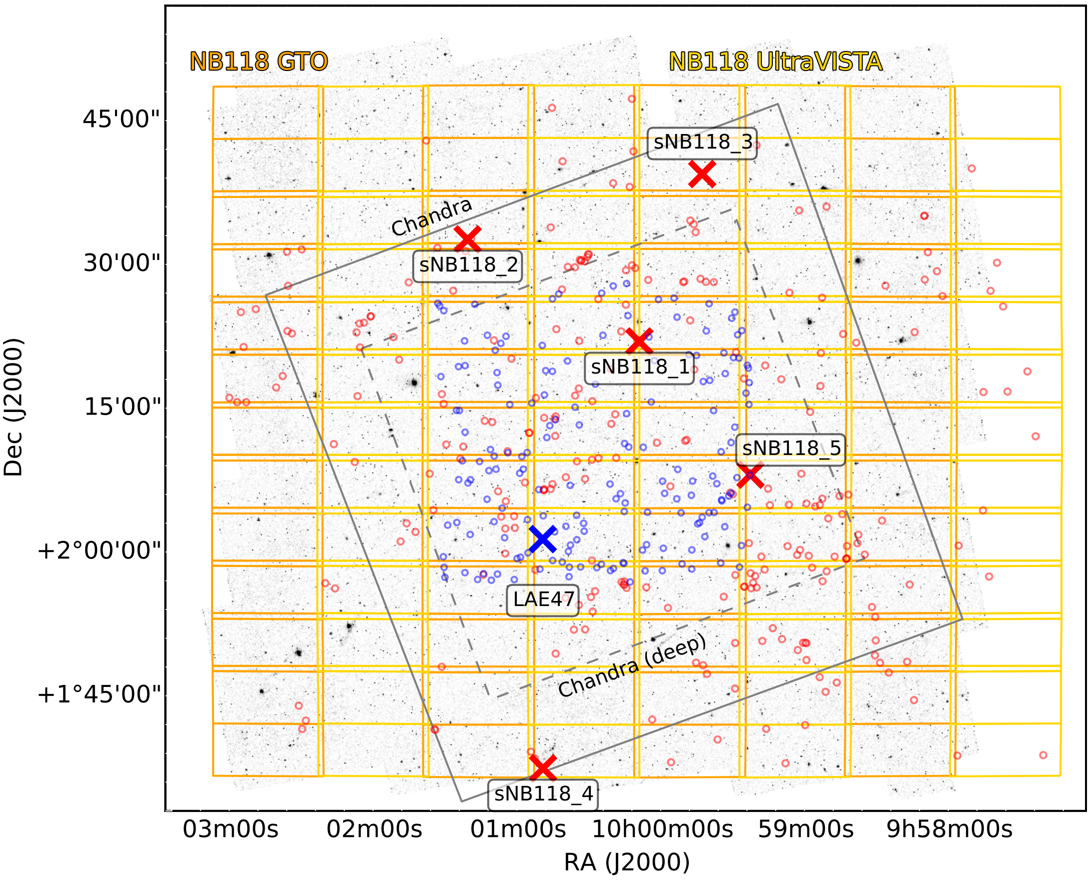

Figure 5.3 The field coverage of the NB118 GTO and NB118 UltraVISTA observations is shown in orange and yellow, respectively. Red circles are objects in our sample of NB118 selected [O II] emitters. Blue circles indicate LAEs from the sample of Nilsson et al. (2009). The turned rectangles are the coverage of the Chandra COSMOS survey (Elvis et al., 2009), with the dashed line indicating the deep coverage. The six objects, for which we have XSHOOTER follow-up spectroscopy, are specifically marked by crosses. In the background the ACS F814W image is shown.

for some cases [S II]$\lambda\lambda$ 6716, 6731, the middle bin [O III]$\lambda\lambda$ 4959, 5007 or Hβ, and the highest redshift bin [O II]$\lambda\lambda$ 3727, 3729. These three different redshift solutions can also be clearly separated using the BzK color-color diagram (Daddi et al. 2004, cf also sec. 1.3.8) instead of the full photometric redshifts, as shown in Figure 5.5. As no error-bars are included in this plot, individual outliers should not be over-interpreted at this point.

The robust selection and measurement of [O II] in the NB118 filters is somewhat complicated, as the NB118 filters have a wavelength at the blue end of the J passband. A linear combination of Y and J, like (cf. also eq. 4.15)

$$J_{\mathrm{corr}} = J + 0.25(Y - J) \tag{5.1}$$

allows for a good estimate of the continuum for objects at redshifts corresponding to H α or [O III]+Hβ in the NB118 filters; but it is not a good estimator for objects around $z = 2.2$, which is the redshift of [O II] in the NB118 filters. This is a consequence of the Balmer/4000 Å break and the associated strong

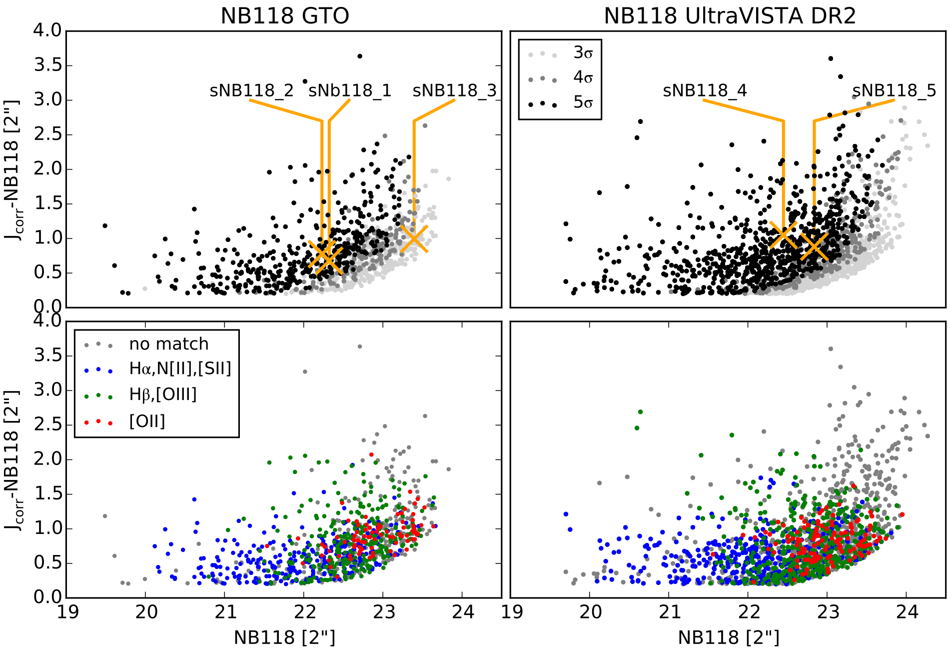

Figure 5.4 The NB excess measured as the magnitude difference between J_{corr} and $NB118$ is plotted against $NB118$ for all objects which we select as NB excess objects. The left panels show results for the NB118 GTO data, while the right column is for the UltraVISTA NB118 data. In the upper row we plot results for three different constraints on the significance of the flux excess relative to estimated continuum (cf. eq. 4.9). In the lower row objects within three photometric redshift bins are indicated (cf. sec. 5.4). J_{corr} is the J magnitude which we corrected through eq. 5.1 to the wavelength of the NB118 filter. All magnitudes are $2''$ aperture magnitudes.

absorption lines, as already discussed by Milvang-Jensen et al. (2013) (cf. their Fig. 7).

The wrong continuum estimation can lead to false positives, which means the selection of objects without line emission. This is illustrated in the left panel of Fig. 5.6. NB excesses with $J_{corr} - NB118$ as high as 0.4 mag are possible for stellar populations without star-formation at redshifts slightly below $z = 2.2$ when using the estimator in eq. 5.1. We concluded this based on simulations with synthetic stellar populations using BC03 (Bruzual & Charlot, 2003) models.

These possible interlopers have very red $Y - J$ colors. Therefore, one way to mitigate the described problematic is to use at high $Y-J$ a higher threshold on $J_{\mathrm{corr}}-NB118$.[3] However, as a consequence of such a conservative choice very dusty and hence red line emitters would be missed. In addition, for galaxies which indeed have [O II] in the NB118 filters J_{corr} can, depending on the SFH, actually overestimate the continuum. An increase in the color threshold would even worsen the situation. This is illustrated in the right panel of Fig. 5.6.

It is noteworthy that once it can be decided that an object is an [O II] emitter, we can accurately estimate the continuum flux at the position of [O II] by the use of the linear combination:

$$Y_{\mathrm{eff}} = Y - 1.27(z' - Y) \tag{5.2}$$

Such a more precise estimation will be necessary when applying the throughput variation method, as

---

[3] Similar, the J_{corr} can be defined in a different way at high $Y - J$ than in eq. 5.1. This could be for example $J_{\mathrm{corr}} = J + \mathrm{a}$ as used in Milvang-Jensen et al. (2013) and in chapter 4 of this thesis, where 'a' is a constant.

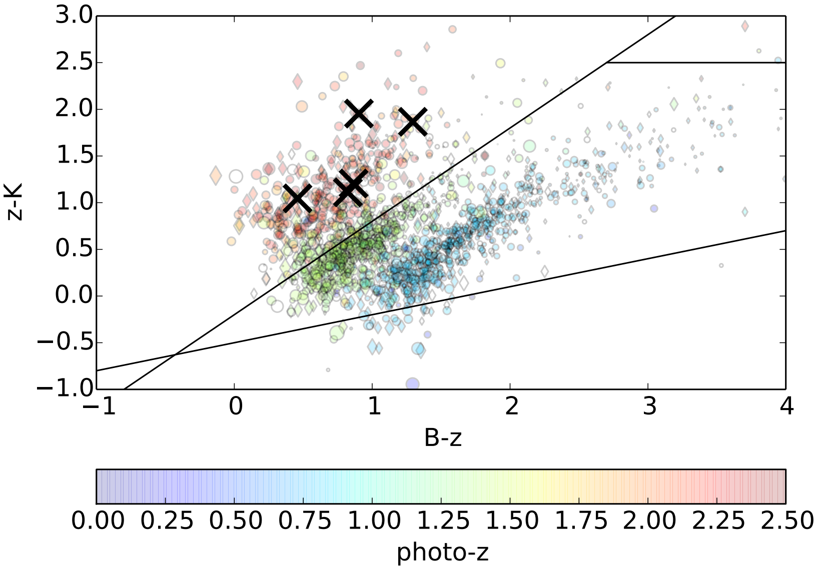

Figure 5.5 Color-color diagram showing $B_J - z^+$ vs $z^+ - Ks$, as pioneered by Daddi et al. (2004). The used B_J, z^+, Ks magnitudes are based on the PSF homogenized catalog of Muzzin et al. (2013), to which we matched our NB sample. Colors indicate the photometric redshift from the catalog of Ilbert et al. (2013). Sizes indicate the NB excess, $J_{\mathrm{corr}} - NB118$. Diamonds and circles are used for objects with a origin from the GTO and UltraVISTA DR2 data, respectively.

discussed in chapter 4, to the [O II] emitters. One of the goals of this project will be to further improve on the [O II] selection, possibly by performing careful SED fitting including the NB data.

Spectroscopy

We selected five [O II] emitters from the NB118 data for spectroscopic follow-up. Two of the objects are from the UltraVISTA DR2 and three from the GTO sample. The photo-z's from the Ilbert et al. (2013) catalog are favoring in all five cases [O II] as the line causing the NB excess. We picked these specific objects so that we span a range in mass and in strength of the NB excess. However, all objects have a NB excess strong enough, so that no contamination from objects as shown in the left panel of Fig. 5.6 is possible. Therefore, we expected a 100% success rate. The selected objects are marked in figures 5.3, 5.4, 5.5. PSF homogenized cutouts[4] are shown in Fig. 5.7 for all five objects in 10 bands.

We obtained VLT/XSHOOTER spectra for these five objects. In addition, we include for our analysis one previously observed LAE from the sample of Nilsson et al. (2009).[5] Date of observation, used exposure times, and the respective ESO program IDs are listed in table 5.1.

We reduced the spectra using a modified version of the XSHOOTER pipeline (Modigliani et al., 2010, version 2.3.0)[6]. The UVB and VIS reductions were done in stare mode and the NIR reduction in nodding mode. We reduced the individual frames, or pairs in the case of NIR, separately with the pipeline, and

---

[4] The PSF homogenization is preliminary.

[5] Dynamical mass and H α based SFR have been already published based on this spectroscopic observation (Rhoads et al., 2014). No information beyond this is published.

[6] The modification is described in sec. 2.2.2 of this thesis

False selection of objects without line emission in NB118	Inaccurate continuum estimation for objects with [O II] in NB118
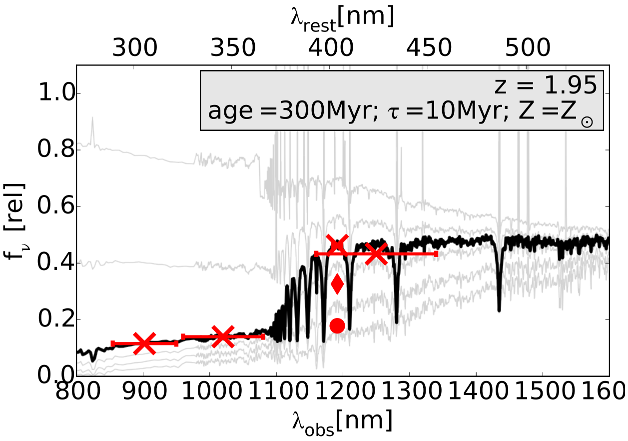	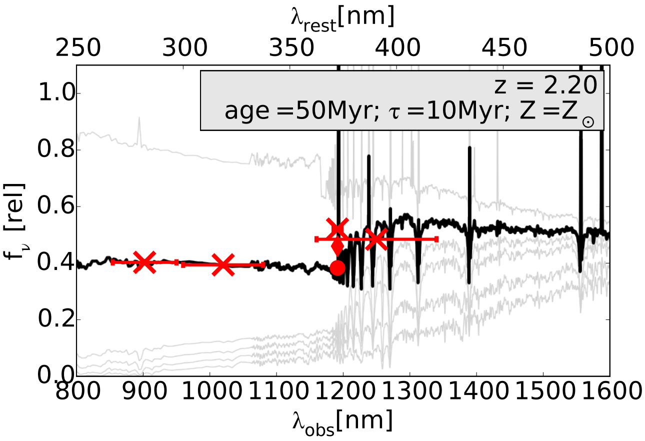

Figure 5.6 Problematic of continuum estimation at the wavelength of the NB118 filter through broadband filters. The two plots show synthetic stellar populations using the high resolution BC03 (Bruzual & Charlot, 2003) models based on BaSeL3.1 (Westera et al., 2002) for ages of 300 and 50 Myr at redshifts of $z = 1.95$ and $z = 2.2$, respectively. In the background, populations are shown at these redshifts for ages of 10, 50, 300, 500 Myr, 1 Gyr, 2.9 Gyr. We added nebular emission following Ono et al. (2010). Further, a $\tau = 10$ Myr star-formation history, solar metallicity, and a Salpeter (Salpeter, 1955) IMF were assumed. Crosses indicate for the highlighted SEDs filter-averaged flux densities in z^+, Y, NB118, and J, where the horizontal bars indicate the respective effective filter widths. The diamond is the continuum estimate from a linear combination of Y and J ($J_{\rm corr}$, eq. 5.1), and the circle is that for a linear combination between z^+ and Y ($Y_{\rm corr}$; eq. 5.2). The flux density corresponding to $J_{\rm corr}$ is for the 100 Myr population significantly below the actual continuum magnitude at $z = 1.95$, a redshift which would be difficult to separate from $z = 2.2$ through photo-z's. Hence, if a low cut on the color-excess was used in the selection of line emitters, this could lead to the selection of false positives. The 50 Myr SED has still detectable emission lines. Indeed, one would measure an elevated flux density in the NB filter at $z = 2.2$. However, the flux density corresponding to $J_{\rm corr}$ does significantly overestimate the continuum at the wavelength of the [O II] line and the object would not be selected as a NB excess object. A much better continuum estimate (circle) can be obtained at $z = 2.2$ with $Y_{\rm corr}$; but this estimator would be even worse with respect to the selection of false positives.

Table 5.1 Dates of observation, exposure times in the three arms of XSHOOTER, and ESO program ids are listed for each of the observed objects.

OBJECT	DATE	exposure time [s] (UVB/VIS/NIR)	ESO Program ID
LAE 47	Mar 20 2010	2x1800/2x1800/6x600	084.A-0303(C) (PI: Fynbo)
sNB118_1	Apr 22 2012	4x1169/4x1124/8x900	089.B-0710(A) (PI: Zabl)
sNB118_2	Apr 22 2012	2x1769/2x1724/4x900	089.B-0710(A) (PI: Zabl)
sNB118_3	Apr 22 2012	4x1770/4x1725/8x900	089.B-0710(A) (PI: Zabl)
sNB118_4	Mar 16 2013	2x1769/2x1724/4x900	090.A-0147(A)(PI: Fynbo)
sNB118_5	Mar 16 2013	2x1769/2x1724/4x900	090.A-0147(A) (PI: Fynbo)

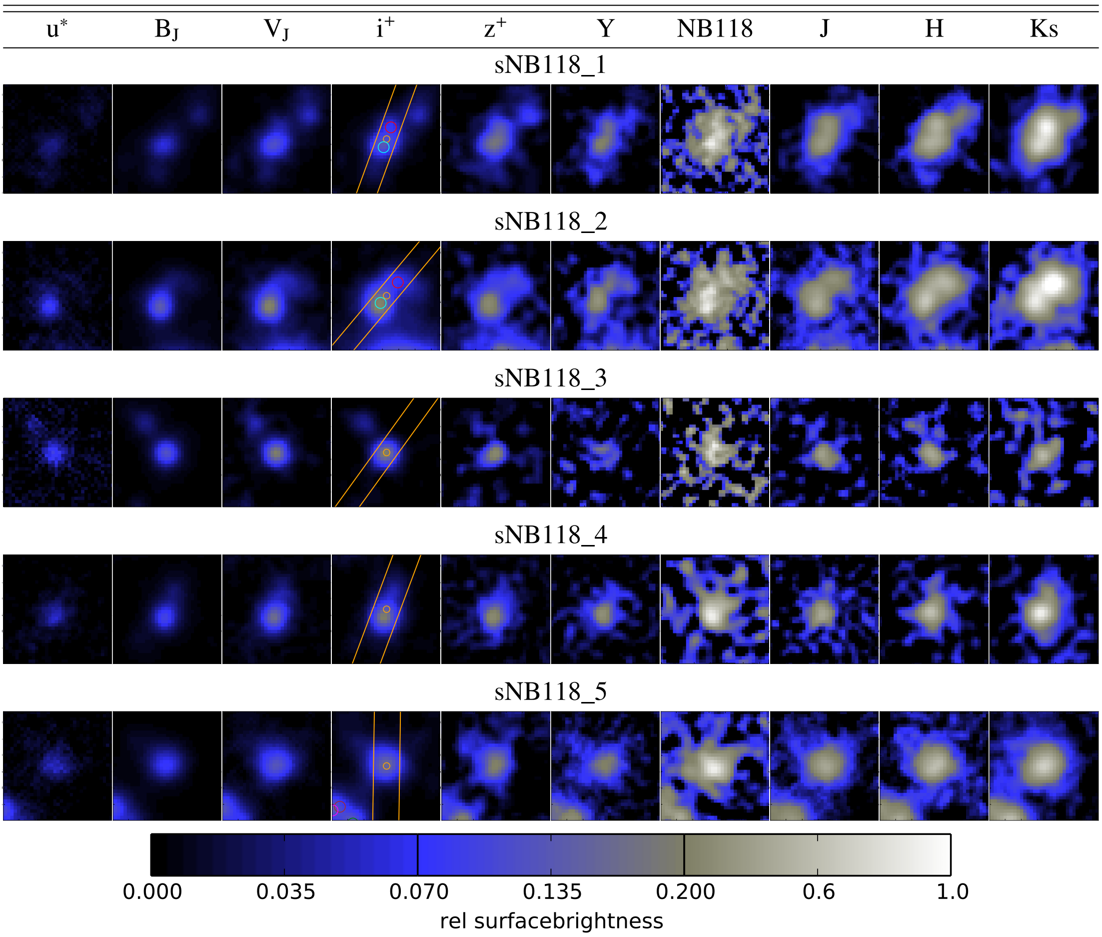

Figure 5.7 $5'' \times 5''$ cutouts in 10 filters. We PSF homogenized the images with convolution kernels created based on close-by stars using the algorithm by Alard & Lupton (1998). Kernels were created for each of the objects separately. A three parted color-scale is used, which allows to show the complete dynamic range of the spectral energy distributions. This color-scale is linear in each of the three parts. Slit widths in the NIR arm and position angles, as used during the observations, are overplotted on the i^+ cutouts. For sNB118_1 and sNB118_2 we indicate in addition to the slit center (orange circle) two individually identifiable sub-components. We refer to the position with cyan circle with 'a' and to that with a red circle with 'b'.

subsequently combined them based on optimal weighting with our own python scripts. NIR spectra for all six objects are shown in Fig. 5.8. The seeing during the observations of *sNB*118_1 and *sNB*118_2 was excellent. Therefore, we could for both objects extract the traces of two close-by components separately. These pairs of likely merging objects are also identifiable in the cutouts shown in Fig. 5.7.

We determined redshift, line fluxes and line widhts for the strong rest-frame optical emission-lines jointly. This allows to get robust estimates of line fluxes, even if part of a line is covered by a sky line. While we assumed for all lines the same redshift, we allowed for two different widths of the Gaussian profiles: one for the Balmer and one for the forbidden lines, respectively.[7] For both the ratios of [N II] λ6583 to [N II] λ6548 and [O III] λ5007 to [O III] λ4959, we assumed fixed ratios of 3:1 (e.g. Osterbrock & Fer-

---

[7] At the current stage we did not correct for the stellar continuum, but plan to do so for our final analysis.

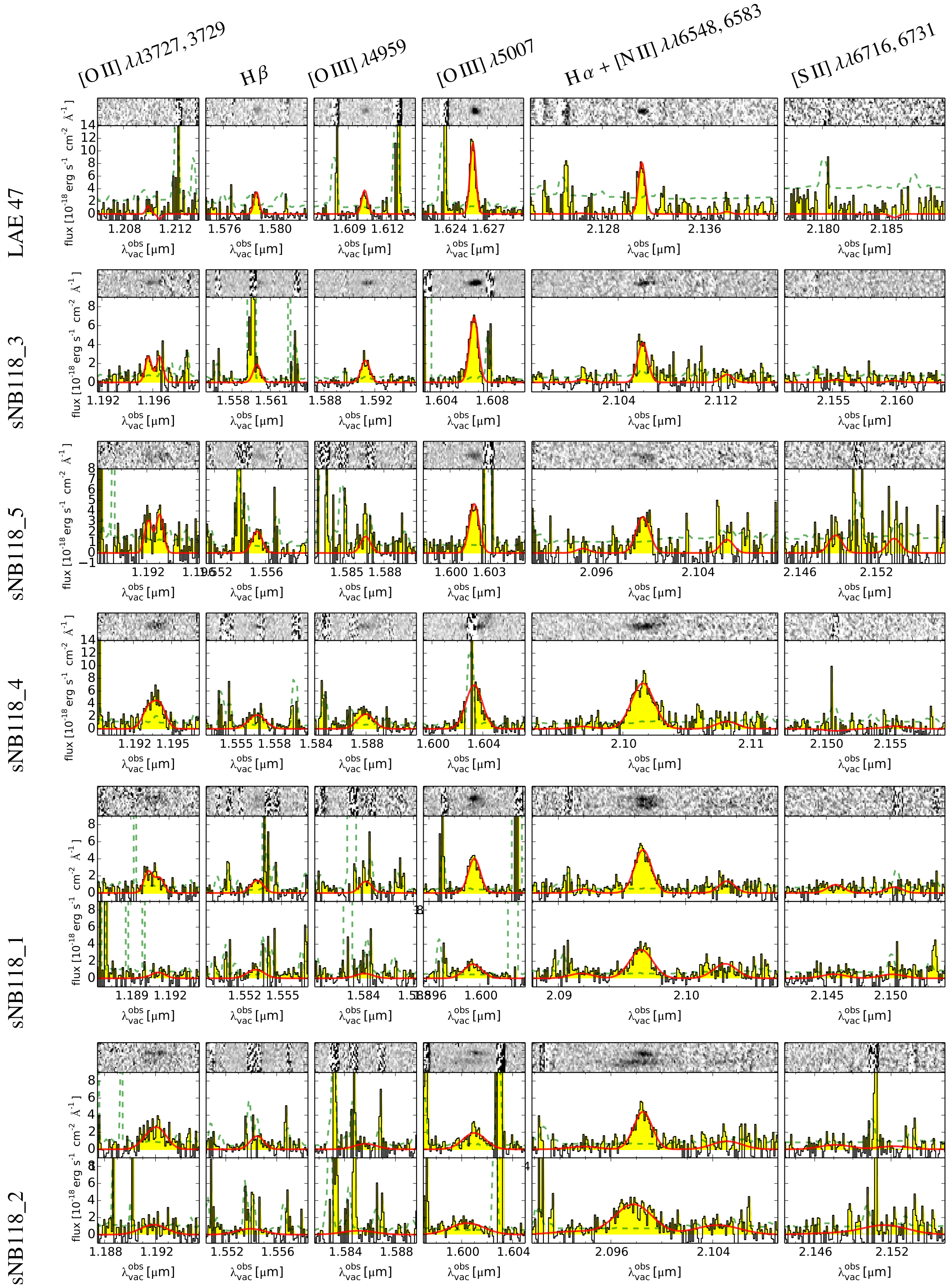

Figure 5.8 NIR 2D and 1D spectra around relevant rest-frame optical emission lines for the six objects described in this section. In the 1D spectrum, the black curve is the extracted trace, the green dashed curve is the error spectrum. The shaded yellow area indicates all flux above zero. The red curve is the best fit model, as obtained from a joint fit to the lines. The integrated line-fluxes of the best-fit Gaussian are listed in Table 5.2. For sNB118_1 and sNB118_2, we have extracted and fit to an upper and lower trace separately.

Table 5.2 Redshifts and line fluxes as measured from the XSHOOTER NIR spectrum by simultaneously fitting to the strong rest-frame optical emission lines. For sNB118_1 and sNB118_2 we fit the two components separately. The 'a' components correspond to the upper traces in Fig. 5.8.

ID	z	$[OII]\lambda3726^{a}$	$[OII]\lambda3729^{a}$	$H\beta^{a}$	$[OIII]\lambda5007^{a,b}$	$H\alpha^{a}$	$[NII]\lambda6583^{a,c}$
sNB118_1a	2.1936	$0.1^{+0.3}_{-0.4}$	$0.9^{+0.3}_{-0.3}$	$1.7^{+0.2}_{-0.2}$	$2.9^{+0.2}_{-0.2}$	$7.6^{+0.3}_{-0.3}$	$3.9^{+0.4}_{-0.3}$
sNB118_1b	2.1939	$2.2^{+0.2}_{-0.2}$	$1.5^{+0.2}_{-0.2}$	$1.8^{+0.1}_{-0.1}$	$4.8^{+0.1}_{-0.1}$	$8.5^{+0.2}_{-0.2}$	$2.2^{+0.2}_{-0.2}$
sNB118_2a	2.1956	$0.3^{+0.8}_{-0.8}$	$2.7^{+0.8}_{-0.8}$	$1.9^{+0.3}_{-0.4}$	$4.5^{+0.3}_{-0.3}$	$13.0^{+0.6}_{-0.4}$	$4.9^{+0.6}_{-0.6}$
sNB118_2b	2.1967	$2.1^{+0.4}_{-0.4}$	$3.3^{+0.4}_{-0.4}$	$2.1^{+0.3}_{-0.3}$	$4.3^{+0.2}_{-0.3}$	$8.0^{+0.3}_{-0.3}$	$2.8^{+0.4}_{-0.4}$
sNB118_3	2.2080	$1.8^{+0.2}_{-0.2}$	$1.8^{+0.2}_{-0.2}$	$1.4^{+0.1}_{-0.1}$	$5.9^{+0.1}_{-0.1}$	$4.2^{+0.3}_{-0.3}$	$1.0^{+0.2}_{-0.2}$
sNB118_4	2.2014	$3.7^{+0.4}_{-0.4}$	$4.5^{+0.4}_{-0.4}$	$3.6^{+0.3}_{-0.3}$	$11.2^{+0.3}_{-0.4}$	$16.1^{+0.6}_{-0.6}$	$2.4^{+0.4}_{-0.4}$
sNB118_5	2.1985	$2.2^{+0.3}_{-0.3}$	$2.6^{+0.3}_{-0.3}$	$2.1^{+0.2}_{-0.2}$	$4.5^{+0.3}_{-0.3}$	$4.7^{+0.4}_{-0.4}$	$1.6^{+0.5}_{-0.5}$
LAE47	2.2464	$0.6^{+0.4}_{-0.5}$	$-0.3^{+0.4}_{-0.4}$	$1.8^{+0.3}_{-0.3}$	$6.4^{+0.3}_{-0.3}$	$5.5^{+0.9}_{-1.1}$	$0.3^{+0.5}_{-0.5}$

[a] line flux $[10^{-17}\,\mathrm{erg\,s^{-1}\,cm^{-2}}]$ [b] [O III] λ4959 had in the fit a fixed flux of 1/3 of [O III] λ5007

[c] [N II] λ6548 had in the fit a fixed flux of 1/3 of [N II] λ6583

land, 2006, p.56). Best-fit redshifts, corrected to a heliocentric standard, and line fluxes are listed in Table 5.2. The stated uncertainties were determined with our MCMC line fitting code.

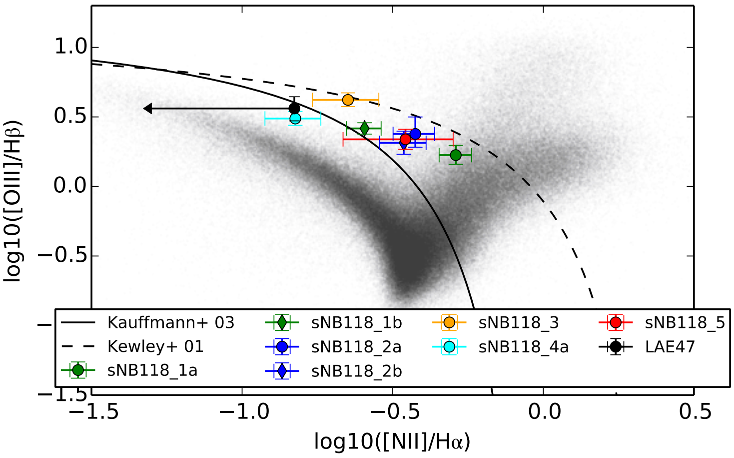

Figure 5.9 BPT diagream. Plotted are the logarithmic line flux ratios of [O III] λ5007/Hβ against those of [N II] λ6583/Hα. Plotted in grey are emission-line galaxies from the SDSS survey (here DR8: Aihara et al. 2011). The solid black line is the empirical separator between ionization by stellar-population or AGN of Kauffmann et al. (2003), while the dashed lines is the line indicating the maximum ionization from theoretical star-burst models (Kewley et al., 2001). Objects towards the right of the lines are considered to have AGN contribution. For sNB118_1 and sNB118_2 we pplot points for the upper and lower component separately.

In Fig. 5.9, we plot our objects in a BPT diagram (Baldwin et al., 1981). Such a diagram can serve to identify AGN activity (e.g. Kewley et al., 2001; Kauffmann et al., 2003). As found by several recent studies (Hainline et al., 2009; Yabe et al., 2012; Steidel et al., 2014; Shapley et al., 2015, e.g.), high redshift star-forming galaxies are offset w.r.t to the distribution of SDSS galaxies in the local universe.

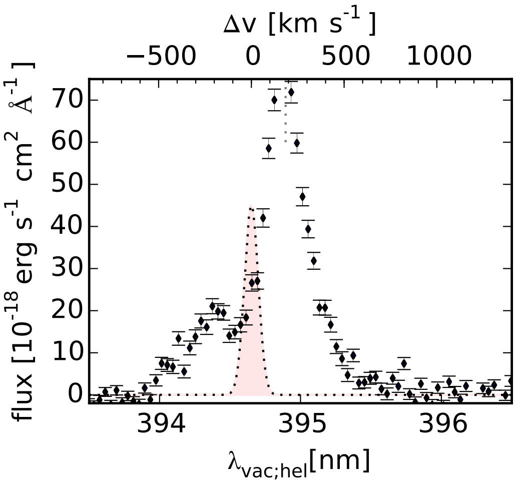

Figure 5.10 H α (red) and Ly α (yellow) are shown on the same plot. The upper x-axis give the velocity offset from the systemic redshift of the lines. The lower x-axis is the observed-frame wavelength for the Ly α line.

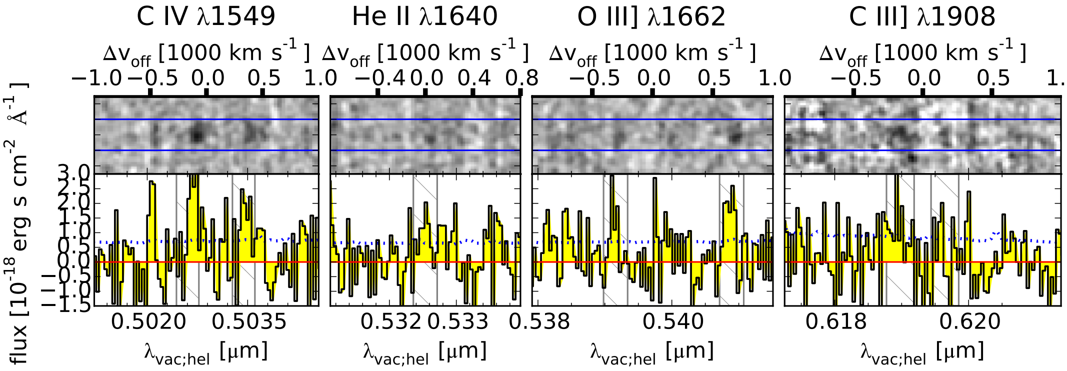

Figure 5.11 Rest-frame UV 2D and 1D spectrum for LAE47 at the wavelength of specific high-ionization lines. The solid black line is the extracted trace, while the dotted line is the error-spectrum C IV, C III], and O III] are doublets. The expected wavelengths for the respective components are indicated as hatched areas. The redshift as obtained from the fit to the rest-frame optical lines was assumed.

LAE47 shows as expected a strong Ly α line (Fig. 5.10). It is double peaked with a stronger red and a weaker, yet present, blue component. The presence of the blue peak indicates a relatively low outflow velocity of the ISM (Verhamme et al. 2006; see also discussion in Christensen et al. (2012)). The line ratio between the Ly α and H α line is 7.1.[8] Comparison to the theoretical value of 8.1 (cf. Table. 1.1) indicates a very high Ly α escape fraction. In addition to Ly α, several emission lines in the rest-frame UV, which require relatively high ionization energies, are marginally detected (Fig. 5.11). We are currently investigating, if these fluxes can be explained with a very young stellar population, or if only an AGN can produce a sufficiently hard ionization spectrum.

For sNB118_2a, we plot in Fig. 5.12 the UVB spectrum. We clearly detect both high and low ionization metal absorption lines in addition to Ly α in absorption. For none of the five [O II] emitters do

---

[8] This is a preliminary analysis; no relative slit-loss corrections have been applied yet.

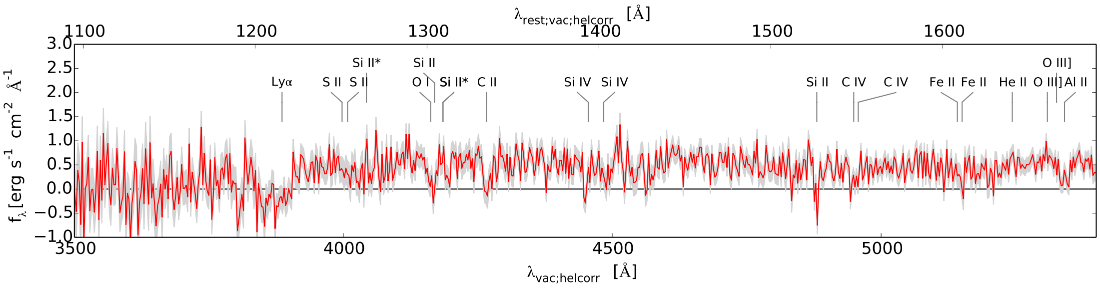

Figure 5.12 Rest-frame UV spectrum for sNB118_2. Indicated are several identifiable lines.

we find strong Ly α emission.

5.4.1 Conclusion of this outlook

We can conclude that our NB118 [O II] selection works robustly. The follow-up spectra are of excellent quality. However, to derive signifcant conclusion we will need to try to increase the sample size.

A

Appendix for paper NB118

A.1 The NB118 filter curves

Throughout this paper our results were based on the set of VISTA NB118 filters. In Fig. A.1 we show all 16 filter curves used in this study. So far, we neglected the uncertainties in the measured filter curves. Unfortunately, there are several sources of potentially significant errors in the available filter curves. We therefore summarize in this appendix the origin of the assumed filter curves and our current understanding of their accuracy.

The VIRCAM filter curves are based on laboratory scans carried out at room temperature in the normal incidence collimated beam. These measurements have been supplied by the filter manufacturer, NDC [1].

However, as the NB118 filters are multilayer dielectric interference filters, the transmittance curves depend both on the temperature and the angle of incidence of the beam. Qualitatively, both a cooling and

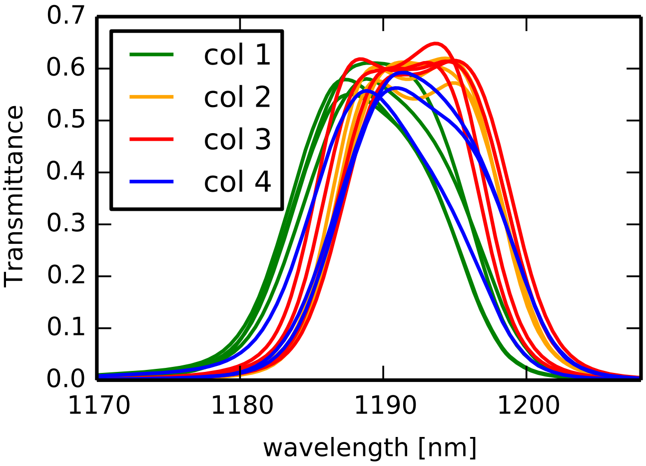

Figure A.1 The passbands of 16 NB118 filters after convergent beam transformation, with QE and mirror reflectivities applied, and artificially shifted by 3.5nm towards the red, as motivated by the results in Milvang-Jensen et al. (2013). Filters in the four different columns of the observing pattern are marked in four different colors. Columns numbers are counted from right to left in Fig. 4.9.

---

[1] NDC Infrared Engineering; http://www.ndcinfrared.com

the change of the collimated beam to a larger incidence angles lead to a shift of the passband towards shorter wavelengths (Morelli, 1991). This is relevant, as in VIRCAM the filters are located in a fast convergent beam (e.g. Atad-Ettedgui & Worswick, 2003) at cryogenic temperatures. The convergent beam can be understood as formed by rays coming from different incidence angles, each of which sees a filter curve corresponding to the incidence angle.

One way to approximate the actual filter curves within the cryogenic convergent beam is to do an entirely theoretical conversion from the collimated beam measurement. Assuming a temperature dependence of 0.0186 nm K^{-1} (NDC), the difference of 205 K between room temperature and filter temperature in VIRCAM ($\sim$ 90 K; private communication ESO), equals a blueward shift of 4.26 nm. We made the assumption that the shape of the transmittance-curve is preserved under the temperature shift. The justification of this assumption was confirmed by a re-measurement of a witness sample done by NDC in 2013.

The transformation between collimated and convergent beam was based on the assumption that it is possible to approximate the filter curve in a collimated beam with non-normal incidence angle θ from that for normal incidence by:

$$T_\theta(\lambda) \approx T_0\left(\frac{1}{\cos(\frac{\theta}{n_{eff}})}\lambda\right) \tag{A.1}$$

As the range of relevant incidence angles in the VISTA beam extents up to $\sim$ 20 deg, eq. A.1 must be a good approximation for a large range of angles. According to Morelli (1991) a conservation of the general filter curve shape is a good approximation up to angles of 30 deg. In the literature exist a few examples, where measurements of similar NIR filters have been published for different incidence angles. For some of them the results seem approximately consistent with eq. A.1 (e.g. Ghinassi et al., 2002), while there is for others a stronger discrepancy (e.g Vanzi et al., 1998). Again based on a witness-sample, NDC provided us with measurements of the material for incidence angles up to 12 deg. The shape was indeed approximately conserved.

VISTA's beam can be characterized by the radiant intensity as a function of the angle of incidence, $\epsilon(\phi, \theta)$. Here, ϕ and θ are the two dimensional polar-coordinates characterizing the latter. Neglecting all effects of wave optics, $\epsilon(\phi, \theta)$ can be described to first order by an annulus with constant value. The annulus's inner radius ρ_{in} and outer radius ρ_{out} have values of 3.85 deg and 8.75 deg, respectively (Nilsson et al., 2007). This annulus is shifted corresponding to the object's position in the field of view in the ϕ,θ plane. The angle of incidence of the annulus's center is related to the object's position on the sky by $1.208^\circ \times \frac{\vec{d}_{\mathrm{per}}}{100}$ (Findlay, 2012). The position $\vec{d}_{\mathrm{per}}$ is stated here in percentages of detectors.

With this input, the effective filter curve for the complete beam can be calculated by (e.g. Lissberger, 1970):

$$T(\lambda) = \frac{\int_\Omega \epsilon(\phi, \theta) T_\theta(\lambda) d\Omega}{\int_\Omega \epsilon(\phi, \theta) d\Omega} \tag{A.2}$$

Consequently, we can finally estimate the shape of the filter curves in VIRCAM's convergent beam by combining equations A.1 and A.2.

$$T(\lambda) = \frac{\int_{annulus} T_0\left(\frac{1}{\cos\frac{\sqrt{(\theta_x+\theta_x^c)^2+(\theta_y+\theta_y^c)^2}}{n_{eff}}}\lambda\right) d\theta_x d\theta_y}{\int_{annulus} d\theta_x d\theta_y} \tag{A.3}$$

We tested our script doing the actual convergent beam conversion based on a 1% top-hat filter and comparing the results to those presented in Bland-Hawthorn et al. (2001).

Filter curves for the different steps in the conversion were shown in Fig. 4 of Milvang-Jensen et al. (2013). Milvang-Jensen et al. (2013) found an unexpected shift of the filter curves towards the red by about 3.5 nm. While we are still investigating possible physical reasons for the shift, we assume in this work the predicted convergent beam curves shifted by 3.5 nm towards the red to account for this finding. The fact that the presented TPV method works well for the actual data under this assumption, further indicates that these filter curves are a reasonable assumption.

A.2 Quantitative assessment of throughput variation for all possible NB118 pairs

The suitability of a filter combination for the TPV can be assessed through Δmag-λ_0 curves, as discussed in sec. 4.2.2. We characterized the Δmag-λ_0 curves for all 120 possible VIRCAM NB118 combinations by following three quantities:

- Difference between maximum and minimum Δmag
- Percentage of the wavelength range, where the Δmag values are unique
- Average absolute slope ($|\mathrm{d}\Delta mag/\mathrm{d}\lambda_0|$) and its standard deviation

For the calculation of these values a relevant wavelength interval needs to be chosen. We assumed the wavelength range, where the transmittance of the combined effective filter is not below 2/30 of its maximum value. This threshold is a reasonable number, as it approximately corresponds to the ratio between the FWHMs of the NB118 filters and J. Consequently, an emission line causes a stronger excess in the NB118 filters than in J within the included range.

The resulting values for all 120 combinations are listed in Table A.1. For the example filter-combination 14 & 15, as shown in Fig. 4.1, the range in Δmag values is 3.12 with a uniqueness of 100%. The average absolute slope is 0.14 mag nm^{-1}. The assumed wavelength interval, as defined above, is indicated in the left panel of Fig. 4.1.

Assuming e.g. 5σ detections in each of the two filters, corresponding to an error of $\delta\Delta\mathrm{mag} \sim 0.3$ for the magnitude difference, this would allow on average for a very good wavelength resolution of about 2 nm.

A.3 Expected number of Hα emitters in regions of filter overlap

A.3.1 Simulation

We estimated the number of Hα emitters expected to be found in the field covered by two differing filters as a function of line flux both for the DR2 and the finalized UltraVISTA. For this purpose we created 300000 simulated objects with a continuum flat in f_ν, a fixed [N II] ratio of either $w_{6583} = 0$ or $w_{6583} = 0.3$, a random Hα central wavelength between 1167–1209 nm, and assigned to each of these objects the same fixed input line luminosity, $\mathcal{L}_0[in]$. The Hα EW_0 were drawn from a log-normal distribution with a $\langle\log_{10}(\mathrm{EW}_0/\mathrm{nm})\rangle = 0.35$ and $\sigma[\log_{10}(\mathrm{EW}/\mathrm{nm})] = 0.4$. These values were taken from the best fit distribution obtained by Ly et al. (2011) based on NEWFIRM narrowband observations at a similar wavelength as the UltraVISTA NB118 filters.

After assigning to these 300000 objects random positions within a $1.4x1.4$ deg^2 field, we determined for each of the jitter positions in each of the three pawprints in the UltraVISTA NB118 observing pattern, whether an object is observed and if yes, in which filter. For computational reasons, we only did 28 random jitters drawn from a 2”x 2” box.

	1	2	3	4	5	6	7	8	9	10	11	12	13	14	15	16
1		0.07±0.05	0.06±0.06	0.04±0.03	0.15±0.09	0.12±0.09	0.13±0.10	0.13±0.07	0.16±0.09	0.08±0.07	0.09±0.08	0.14±0.08	0.13±0.06	0.14±0.08	0.03±0.01	0.16±0.10
2	77./ 1.39		0.01±0.00	0.05±0.03	0.21±0.12	0.18±0.11	0.19±0.13	0.20±0.10	0.21±0.12	0.12±0.08	0.14±0.09	0.20±0.11	0.19±0.09	0.19±0.11	0.07±0.05	0.22±0.13
3	71./ 1.30	40./ 0.20		0.05±0.03	0.21±0.12	0.18±0.12	0.19±0.13	0.19±0.10	0.21±0.12	0.11±0.08	0.14±0.08	0.20±0.11	0.19±0.09	0.19±0.11	0.07±0.05	0.22±0.13
4	17./ 0.57	95./ 1.05	72./ 0.92		0.18±0.11	0.15±0.11	0.17±0.12	0.16±0.09	0.19±0.11	0.09±0.08	0.11±0.09	0.17±0.10	0.15±0.09	0.16±0.10	0.06±0.04	0.19±0.12
5	90./ 3.36	83./ 4.71	86./ 4.64	82./ 3.86		0.04±0.03	0.04±0.03	0.03±0.02	0.03±0.02	0.12±0.08	0.09±0.06	0.01±0.01	0.06±0.04	0.04±0.03	0.16±0.07	0.08±0.06
6	82./ 2.52	76./ 3.88	80./ 3.81	63./ 3.05	48./ 0.69		0.02±0.01	0.04±0.02	0.05±0.04	0.09±0.06	0.06±0.04	0.03±0.03	0.08±0.05	0.07±0.04	0.12±0.08	0.10±0.08
7	79./ 2.74	73./ 4.10	77./ 4.04	59./ 3.27	29./ 0.43	28./ 0.26		0.04±0.02	0.05±0.04	0.11±0.08	0.08±0.05	0.03±0.02	0.08±0.05	0.07±0.04	0.13±0.09	0.10±0.07
8	82./ 2.79	78./ 4.16	81./ 4.08	77./ 3.32	68./ 0.56	2./ 0.34	0./ 0.25		0.04±0.03	0.10±0.08	0.07±0.06	0.02±0.01	0.05±0.04	0.04±0.04	0.13±0.06	0.08±0.08
9	86./ 3.44	75./ 4.76	79./ 4.72	77./ 3.95	37./ 0.42	50./ 0.98	48./ 0.80	81./ 0.85		0.13±0.10	0.10±0.08	0.03±0.02	0.05±0.04	0.04±0.02	0.16±0.07	0.06±0.05
10	27./ 1.30	83./ 2.38	92./ 2.28	43./ 1.56	81./ 2.37	55./ 1.68	51./ 1.93	55./ 1.85	65./ 2.60		0.04±0.02	0.11±0.08	0.10±0.09	0.11±0.10	0.08±0.05	0.15±0.12
11	53./ 1.74	78./ 2.97	87./ 2.89	71./ 2.16	68./ 1.69	45./ 1.00	43./ 1.25	42./ 1.18	58./ 1.93	78./ 0.68		0.08±0.06	0.09±0.08	0.09±0.08	0.09±0.06	0.13±0.11
12	87./ 3.09	81./ 4.45	84./ 4.38	79./ 3.61	37./ 0.20	30./ 0.50	20./ 0.35	46./ 0.36	79./ 0.53	69./ 2.14	65./ 1.48		0.05±0.03	0.04±0.02	0.15±0.06	0.08±0.06
13	99./ 2.96	93./ 4.29	95./ 4.20	90./ 3.35	22./ 0.81	5./ 0.58	3./ 0.61	1./ 0.46	42./ 0.87	44./ 1.88	24./ 1.31	18./ 0.61		0.02±0.02	0.14±0.05	0.06±0.04
14	93./ 3.04	83./ 4.38	86./ 4.31	83./ 3.53	16./ 0.59	17./ 0.64	13./ 0.55	16./ 0.54	52./ 0.62	53./ 2.05	35./ 1.42	9./ 0.39	28./ 0.31		0.14±0.06	0.05±0.04
15	6./ 0.25	57./ 1.37	48./ 1.29	8./ 0.56	100./ 3.41	91./ 2.55	88./ 2.77	93./ 2.82	92./ 3.49	41./ 1.25	66./ 1.69	100./ 3.14	99./ 3.00	100./ 3.12		0.17±0.09
16	91./ 3.70	84./ 4.99	86./ 4.95	84./ 4.17	12./ 0.79	15./ 1.24	14./ 1.08	19./ 1.01	3./ 0.55	50./ 2.76	39./ 2.10	12./ 0.80	44./ 1.01	32./ 0.71	98./ 3.77	

Table A.1 Stated are the quantities as introduced in sec. A.2 to characterize the suitability of a given filter pair for the TPV. The table includes these values for all possible 120 NB118 filter-combinations. Both the part of the well-defined wavelength range, where the Δmag values are unique (in percentage), and the span between maximum and minimum Δmag are stated. In the upper right triangle, the average absolute slope ($|\mathrm{d}\Delta mag/\mathrm{d}\lambda_0|$ [mag/nm]) and its standard deviation are listed. The grey-shaded combinations are those NB118 combinations, for which observations will become available within the default UltraVISTA survey.

In each of the individual simulated pointings we determined for each object falling within the boundaries corresponding to a filter the synthetic f_ν (eq. 4.2) and the corresponding error on the f_ν, which we separated into $\delta_o f$ and $\delta_b f$ for object and background, respectively.[2] The calculations were based on the same ZPs, gains, and detector-depended sky-counts, and observation times for the DR2 and final UltraVISTA, as described in sec. 4.4.3. Finally, we combined for each of the individual pawprints the signal from the different jitter positions by weighting with $\frac{1}{\delta_b^2 f}$ and propagated the errors on the noise. This simulated observing and stacking strategy resembles that for the actual UltraVISTA observations.

A.3.2 METHOD

As the measured source flux density scales for fixed EW_{obs} linearly with line luminosity both for the NB and the BB filter, we can based on $f_{\nu;NB118/J}$, $\delta_o f_{NB118/J}$, $\delta_b f_{NB118/J}$ obtained for the input line luminosity, $\mathcal{L}_{0;\mathrm{in}}$, directly determine for a chosen color-significance κ the required $\mathcal{L}_{0,\mathrm{req}}$ to fulfill the inequality 4.9. This is to solve a quadratic equation $a_{quad}\ \alpha_{col}^2 + b_{quad}\ \alpha_{col} + c_{quad} = 0$ in the common way, where a_{quad}, b_{quad}, and c_{quad} are given as:[3]

$$a_{quad} = \quad (f_{NB118} - f_J)^2 \tag{A.4}$$

$$b_{quad} = \quad -1\ \kappa^2(\delta_o^2 f_{NB118} + \delta_o^2 f_J) \tag{A.5}$$

$$c_{quad} = \quad -1\ \kappa^2(\delta_b^2 f_{NB118} + \delta_b^2 f_J) \tag{A.6}$$

$$\tag{A.7}$$

α_{col} is the ratio between $\mathcal{L}_{0,\mathrm{req}}$ and $\mathcal{L}_{0;\mathrm{in}}$. Similarly, we can determine the factor α_{detsig}, required to fulfill eq. 4.10. Having determined the factors α_{col} and α_{detsig} for each of the two contributing filters, we find the minimum factor α, which fulfills the color-significance combined with the color-cut in one of the two filters and the detection significance in the other filter. If any of the criteria is not fulfilled at any flux, we set α to ∞. We also applied the same region mask as used for the actual data (cf. eq. 4.11).

Based on the α's obtained for each simulated object, we directly determined the fraction of input objects being detected as a function of line luminosity. Eventually, multiplying this luminosity completeness function with luminosity functions from the literature and the volume covered by the random box allowed for an estimate of the number of objects expected to be detected as a function of line luminosity, taking fully account for the filter curve shapes and the differing background in the individual filters.

We used the Schechter (1976) parameterizations of the three LFs stated by Ly et al. (2011), including their own and the two $z = 0.84$ LFs of Villar et al. (2008) and Sobral et al. (2009). The LFs stated in Ly et al. (2011) are reddening and completeness corrected. As we need for the purpose of our simulation non-reddening corrected LFs, we convert their Schechter LFs to reddened LFs, by inverting the same SFR depended correction as used in Ly et al. (2011), which is based on Hopkins et al. (2001).[4] Assuming the underlying direct proportionality between SFR and Hα luminosity (Kennicutt, 1998), the relation between intrinsic, $L_{\mathrm{H}\alpha;\mathrm{int}}$, and observed H$\alpha$ luminosity, $L_{\mathrm{H},\alpha;\mathrm{int}}$, can be written as (Ly et al., 2011):

$$L_{\mathrm{H}\alpha;\mathrm{obs}} = L_{\mathrm{H}\alpha;\mathrm{int}} \times \left(\frac{0.797\log(SFR_{int}[H\alpha]) + 3.786}{2.86}\right)^{-2.360} \tag{A.8}$$

---

[2] As the considered observations are background-limited, we could in principle ignore σ_o. We kept it for generality of our simulator.

[3] For the strongly background limited UltraVISTA observations, the inclusion of the source noise is in principle not necessary and is only included for generality.

[4] There are small differences in the two versions, as mentioned in Ly et al. (2007)

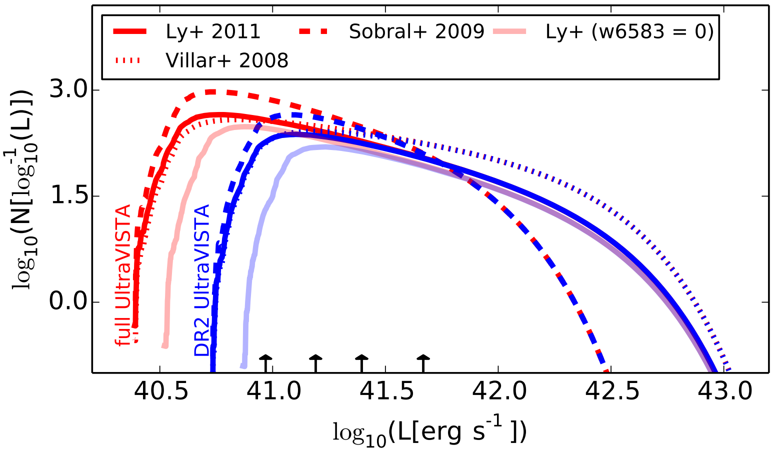

Figure A.2 The expected number of Hα emitters in the part of the UltraVISTA NB118 field with data from two different NB118 filters is shown per unit logarithmic interval as a function of line luminosity. Predicted curves are included both for the UltraVISTA DR2 (blue) and the final UltraVISTA data (red) based on three different $z = 0.8$ Hα LFs from the literature. Results are in all three cases available for the assumption of $w_{6583} = 0.3$ and in the case of the Ly et al. (2011) LF also for $w_{6583} = 0$. Small arrows indicate luminosities corresponding to line fluxes of 3.0, 5.0, 10.0, and 20.0×10^{-17} erg s^{-1} cm^{-2}. The integrated numbers for objects brighter than the respective marked fluxes are stated in Table A.2.

A.3.3 RESULTS

The number of galaxies expected to be selected per unit logarithmic interval by the criteria stated in eq. 4.7–4.11 are shown in Fig. A.2 for the three different LFs. For the Ly et al. (2011) LF, the result is shown in addition to assuming $w_{6583} = 0.3$ also for the assumption of $w_{6583} = 0$. For orientation, luminosities corresponding to fluxes of approximately 3.0, 5.0, 10.0, and 20.0×10^{-17} erg s^{-1} cm^{-2} are marked with small arrows.[5]

Integrated numbers within the 12 patches with contribution of two differing filters are stated down to the detection limit and to the four reference fluxes in Table A.2. Already in the DR2, we would expect to have between 100 and 200 Hα emitters in the patches of overlapping filters. The total UltraVISTA field is expected to have about three times the numbers stated in Table A.2 and the number in the final UltraVISTA data will almost double the number compared to the DR2.

A.4 EXPECTED LINE S/N IN NB AND BB FILTERS

Fig. A.3 shows the inverse of the S/N that an emission line point source with infinite EW would reach for a given line flux in J and NB118, respectively, both for the UltraVISTA DR2 and the expected full UltraVISTA. The calculation was based on eq. 4.6 and the simulation inputs described in sec. 4.4.1. Assuming that the continuum flux density could be estimated without uncertainty, these would be the S/N values for the line alone, independent of the EW.

NB118 results are shown for the peak of filter 15, which has a typical sky-brightness, and are plotted both for the typical per-pixel integration time and half its value. The latter would be applicable when sharing the available time equally between two contributing filters.

---

[5] Approximately, as the actual ratio between line flux and line luminosity depends on the luminosity distance, which slightly varies over the considered wavelength range

Table A.2 Integrated numbers of H α emitters expected in the UltraVISTA survey above different flux thresholds. Values outside the brackets are for $w_{6583} = 0.3$ and inside brackets for $w_{6583} = 0$. For more details see caption of Fig. A.2.

		flux $[10^{-17}\text{erg s}^{-1}\text{ cm}^{-2}]$			
LF	all	> 3.0	> 5.0	> 10.0	> 20.0
		UltraVISTA DR2			
LY11	184 (113)	169 (113)	119 (90)	77 (60)	39 (30)
SO09	250 (165)	237 (164)	184 (140)	132 (102)	76 (59)
VI08	275 (156)	246 (155)	150 (113)	79 (61)	25 (19)
		Full UltraVISTA			
LY11	373 (235)	198 (154)	126 (98)	79 (62)	39 (30)
SO09	413 (280)	268 (209)	192 (150)	135 (106)	76 (60)
VI08	666 (400)	299 (233)	161 (126)	81 (64)	25 (19)

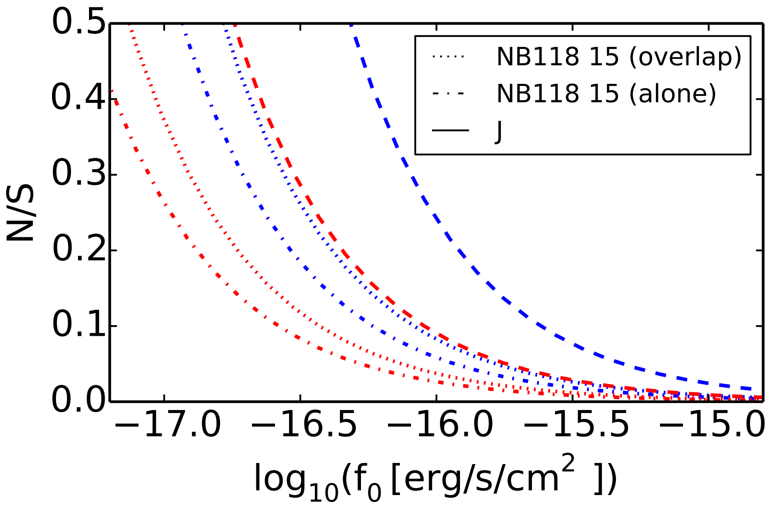

Figure A.3 Inverse of the signal-to-noise as a function of line flux for an infinite *EW* line in J and at peak transmittance of NB118 filter 15. Curves are shown both for exposure times as in the UltraVISTA DR2 (blue) and for the final UltraVISTA survey (red). Moreover, for the NB118 filter results are included for the typical per pixel integration time and for half this value, with the latter being relevant for the regions of overlapping filters (cf. sec. 4.5.1).

Even so the UltraVISTA BB data is extremely deep, the line S/N in the NB118 is a factor 4.1 or 3.4 higher than that in J, for the DR2 and the expected final survey data respectively. On the other hand, at low transmittances of the NB filters, the line S/N in BB filter becomes equivalent or even higher than that in the NB filter.

A.5 FULL SED FITTING RESULTS

The full results from the SED fitting for the sample of NB excess objects with observations available in either of the NB118 pairs 9&10, 14&15, or 15&16, as described in sec. 4.5.6, are listed in Table A.3.

Table A.3 This table extends Table 4.4. Here mainly the properties of the best fit SEDs are listed. In addition, EW_{obs} from the TPV is included.

			SED Fitting								TPV
ID[a]	RA (J2000)	DEC (J2000)	Mass[b]	E_{B-V}	Age [c]	τ [d]	SFR[e]	$\overline{SFR}$ [f]	Z [g]	$f_{\mathrm{esc;ion}}$ [h]	EW_{obs} [i]
7	+10:00:49.874	+01:52:56.21	$10.2^{+0.1}_{-0.2}$	$0.14^{+0.08}_{-0.08}$	$9.1^{+0.3}_{-0.4}$	$9.7^{+0.8}_{-1.0}$	$12.7^{+8.1}_{-5.6}$	$12.8^{+9.2}_{-5.6}$	$1.00^{+1.50}_{-0.80}$	$0.7^{+0.3}_{-0.0}$	$21.4^{+0.0}_{-1.2}$
14	+10:00:21.308	+01:52:59.77	$10.2^{+0.1}_{-0.2}$	$0.14^{+0.24}_{-0.08}$	$9.2^{+0.4}_{-0.5}$	$8.7^{+1.4}_{-0.6}$	$1.8^{+9.0}_{-0.9}$	$1.9^{+9.8}_{-1.0}$	$1.00^{+1.50}_{-0.80}$	$1.0^{+0.0}_{-0.3}$	$3.9^{+0.0}_{-1.1}$
33	+10:00:11.714	+01:53:08.67	$10.3^{+0.1}_{-0.1}$	$0.20^{+0.10}_{-0.08}$	$9.2^{+0.4}_{-0.5}$	$9.1^{+1.0}_{-0.8}$	$8.8^{+11.1}_{-4.7}$	$9.1^{+12.0}_{-4.5}$	$0.20^{+0.80}_{-0.00}$	$0.7^{+0.3}_{-0.0}$	$11.6^{+0.0}_{-1.1}$
97	+9:57:19.341	+01:53:11.92	$10.3^{+0.1}_{-0.1}$	$0.24^{+0.28}_{-0.16}$	$9.2^{+0.4}_{-0.4}$	$8.5^{+0.8}_{-0.6}$	$0.5^{+10.0}_{-0.5}$	$0.6^{+11.1}_{-0.6}$	$0.40^{+0.60}_{-0.20}$	$1.0^{+0.0}_{-0.3}$	$14.9^{+0.0}_{-1.4}$
99	+9:57:49.750	+01:53:19.01	$9.9^{+0.2}_{-0.1}$	$0.30^{+0.08}_{-0.12}$	$8.5^{+0.7}_{-0.2}$	$8.1^{+1.8}_{-0.2}$	$6.7^{+10.5}_{-3.8}$	$10.2^{+10.5}_{-6.1}$	$0.40^{+0.60}_{-0.20}$	$0.7^{+0.3}_{-0.0}$	$12.8^{+0.0}_{-1.2}$
100	+10:01:54.356	+01:53:18.36	$10.0^{+0.1}_{-0.2}$	$0.20^{+0.12}_{-0.08}$	$9.0^{+0.4}_{-0.5}$	$8.9^{+1.2}_{-0.6}$	$6.0^{+7.9}_{-3.0}$	$6.4^{+8.7}_{-3.1}$	$1.00^{+1.50}_{-0.80}$	$0.7^{+0.3}_{-0.0}$	$14.5^{+0.0}_{-1.1}$
102	+10:00:14.473	+01:53:20.04	$10.6^{+0.1}_{-0.1}$	$0.24^{+0.18}_{-0.12}$	$9.2^{+0.4}_{-0.4}$	$8.7^{+1.0}_{-0.6}$	$4.2^{+15.9}_{-2.5}$	$4.7^{+17.2}_{-2.8}$	$0.40^{+0.60}_{-0.20}$	$0.7^{+0.3}_{-0.0}$	$4.5^{+0.0}_{-0.5}$
107	+10:00:18.584	+01:53:27.83	$8.9^{+0.2}_{-0.3}$	$0.02^{+0.16}_{-0.02}$	$8.6^{+0.4}_{-0.6}$	$8.3^{+1.8}_{-0.4}$	$0.7^{+2.6}_{-0.2}$	$0.9^{+2.8}_{-0.1}$	$0.20^{+0.20}_{-0.00}$	$1.0^{+0.0}_{-0.3}$	$19.0^{+0.0}_{-2.4}$
108	+9:59:18.753	+01:53:29.68	$10.3^{+0.0}_{-0.7}$	$0.00^{+0.26}_{-0.00}$	$9.4^{+0.2}_{-1.7}$	$10.5^{+0.2}_{-1.4}$	$9.5^{+58.3}_{-0.7}$	$9.5^{+62.9}_{-0.7}$	$2.50^{+0.00}_{-0.00}$	$0.7^{+0.3}_{-0.0}$	$28.1^{+0.0}_{-1.2}$
115	+10:01:56.308	+01:53:34.01	$9.5^{+0.2}_{-0.3}$	$0.20^{+0.14}_{-0.10}$	$9.0^{+0.4}_{-0.5}$	$8.9^{+1.2}_{-0.6}$	$2.1^{+4.0}_{-1.1}$	$2.2^{+4.3}_{-1.2}$	$0.20^{+0.80}_{-0.00}$	$1.0^{+0.0}_{-0.3}$	$14.7^{+0.0}_{-3.2}$
117	+9:59:15.255	+01:53:38.74	$9.5^{+0.1}_{-0.2}$	$0.08^{+0.12}_{-0.04}$	$8.8^{+0.4}_{-0.4}$	$8.5^{+1.6}_{-0.4}$	$2.1^{+3.6}_{-0.7}$	$2.4^{+3.9}_{-0.8}$	$1.00^{+1.50}_{-0.80}$	$1.0^{+0.0}_{-0.3}$	$13.7^{+0.0}_{-2.1}$
118	+9:57:54.913	+01:53:50.97	$9.8^{+0.2}_{-0.1}$	$0.22^{+0.08}_{-0.10}$	$8.4^{+0.8}_{-0.1}$	$7.9^{+2.0}_{-0.0}$	$4.7^{+7.8}_{-2.3}$	$9.3^{+8.3}_{-5.3}$	$1.00^{+0.00}_{-0.80}$	$0.7^{+0.3}_{-0.0}$	$12.0^{+0.0}_{-0.8}$
121	+10:01:57.962	+01:53:57.58	$10.9^{+0.2}_{-0.1}$	$0.12^{+0.26}_{-0.02}$	$9.1^{+0.5}_{-0.3}$	$8.5^{+1.2}_{-0.4}$	$6.9^{+38.5}_{-1.2}$	$8.0^{+40.8}_{-1.5}$	$2.50^{+0.00}_{-2.30}$	$1.0^{+0.0}_{-0.3}$	$5.1^{+0.0}_{-0.3}$
125	+9:57:52.656	+01:54:08.07	$9.8^{+0.1}_{-0.2}$	$0.18^{+0.10}_{-0.08}$	$9.0^{+0.3}_{-0.6}$	$9.5^{+0.8}_{-1.0}$	$6.5^{+7.5}_{-3.2}$	$6.6^{+8.3}_{-3.2}$	$1.00^{+1.50}_{-0.80}$	$1.0^{+0.0}_{-0.3}$	$18.3^{+0.0}_{-1.4}$
126	+9:58:55.991	+01:54:01.18	$10.4^{+0.2}_{-0.1}$	$0.36^{+0.20}_{-0.10}$	$8.8^{+0.5}_{-0.3}$	$8.3^{+1.6}_{-0.4}$	$7.0^{+22.1}_{-4.1}$	$9.0^{+23.0}_{-5.1}$	$2.50^{+0.00}_{-2.30}$	$1.0^{+0.0}_{-0.3}$	$8.9^{+0.0}_{-1.1}$
128	+9:57:31.875	+01:54:13.10									$15.3^{+0.0}_{-2.2}$
129	+10:00:30.626	+01:54:13.88	$10.6^{+0.1}_{-0.2}$	$0.26^{+0.14}_{-0.14}$	$9.3^{+0.3}_{-0.4}$	$8.7^{+0.4}_{-0.6}$	$2.2^{+4.8}_{-1.9}$	$2.5^{+5.8}_{-2.1}$	$0.20^{+0.80}_{-0.00}$	$1.0^{+0.0}_{-0.3}$	$5.7^{+0.0}_{-0.8}$
130	+9:57:19.395	+01:54:15.11	$9.3^{+0.1}_{-0.3}$	$0.08^{+0.14}_{-0.06}$	$9.0^{+0.3}_{-0.6}$	$8.9^{+1.4}_{-0.6}$	$1.4^{+3.5}_{-0.4}$	$1.5^{+3.8}_{-0.4}$	$0.20^{+0.20}_{-0.00}$	$1.0^{+0.0}_{-0.3}$	$19.5^{+0.0}_{-3.1}$
132	+10:00:19.447	+01:54:22.95	$9.2^{+0.1}_{-0.3}$	$0.06^{+0.10}_{-0.04}$	$8.5^{+0.3}_{-0.6}$	$8.9^{+1.4}_{-0.6}$	$4.5^{+5.9}_{-1.3}$	$4.8^{+6.4}_{-1.4}$	$1.00^{+1.50}_{-0.80}$	$1.0^{+0.0}_{-0.3}$	$30.0^{+0.0}_{-2.3}$
135	+9:57:18.325	+01:54:26.02	$8.7^{+0.4}_{-0.4}$	$0.16^{+0.12}_{-0.10}$	$8.2^{+0.7}_{-0.6}$	$7.9^{+2.0}_{-0.0}$	$1.3^{+2.9}_{-0.6}$	$2.5^{+3.0}_{-1.5}$	$0.40^{+2.10}_{-0.20}$	$0.7^{+0.3}_{-0.0}$	$20.6^{+0.0}_{-4.1}$
139	+10:00:34.144	+01:54:28.81	$10.3^{+0.2}_{-0.1}$	$0.18^{+0.30}_{-0.08}$	$8.9^{+0.5}_{-0.4}$	$8.3^{+1.6}_{-0.4}$	$2.6^{+25.5}_{-1.0}$	$3.4^{+26.7}_{-1.6}$	$2.50^{+0.00}_{-2.30}$	$1.0^{+0.0}_{-0.3}$	$6.5^{+0.0}_{-0.7}$
142	+9:57:31.089	+01:54:32.10	$9.5^{+0.2}_{-0.1}$	$0.18^{+0.06}_{-0.10}$	$8.4^{+0.6}_{-0.2}$	$8.1^{+2.0}_{-0.2}$	$5.2^{+5.7}_{-2.4}$	$7.9^{+5.8}_{-4.4}$	$0.40^{+0.60}_{-0.20}$	$1.0^{+0.0}_{-0.3}$	$24.1^{+0.0}_{-0.8}$
151	+9:57:19.313	+01:54:33.35	$9.2^{+0.2}_{-0.2}$	$0.20^{+0.12}_{-0.12}$	$8.6^{+0.6}_{-0.4}$	$8.3^{+1.8}_{-0.4}$	$1.7^{+3.4}_{-0.9}$	$2.3^{+3.7}_{-1.2}$	$0.40^{+0.60}_{-0.20}$	$1.0^{+0.0}_{-0.3}$	$13.9^{+0.0}_{-0.9}$
154	+10:00:34.614	+01:54:42.17	$9.6^{+0.2}_{-0.2}$	$0.22^{+0.10}_{-0.12}$	$8.4^{+0.7}_{-0.2}$	$7.9^{+2.0}_{-0.0}$	$2.5^{+5.9}_{-1.3}$	$4.9^{+6.1}_{-2.8}$	$0.40^{+0.60}_{-0.20}$	$1.0^{+0.0}_{-0.3}$	$10.8^{+0.0}_{-1.5}$
157	+9:57:31.836	+01:54:41.87	$9.6^{+0.2}_{-0.2}$	$0.08^{+0.12}_{-0.06}$	$8.7^{+0.5}_{-0.3}$	$8.3^{+1.8}_{-0.4}$	$2.3^{+4.8}_{-0.7}$	$3.0^{+5.1}_{-1.0}$	$1.00^{+0.00}_{-0.80}$	$1.0^{+0.0}_{-0.3}$	$8.9^{+0.0}_{-1.4}$
165	+9:59:03.212	+01:54:42.21	$10.0^{+0.1}_{-0.3}$	$0.16^{+0.18}_{-0.08}$	$9.6^{+0.2}_{-0.9}$	$9.5^{+0.8}_{-1.0}$	$1.9^{+5.5}_{-1.0}$	$1.9^{+5.9}_{-1.0}$	$0.20^{+0.80}_{-0.00}$	$0.7^{+0.3}_{-0.0}$	$11.1^{+0.0}_{-1.9}$
168	+9:59:22.555	+01:54:53.08	$9.3^{+0.2}_{-0.1}$	$0.16^{+0.06}_{-0.10}$	$8.4^{+0.6}_{-0.2}$	$8.1^{+2.0}_{-0.2}$	$3.4^{+3.4}_{-1.5}$	$5.1^{+3.5}_{-2.8}$	$0.40^{+0.60}_{-0.20}$	$0.7^{+0.3}_{-0.0}$	$16.2^{+0.0}_{-2.4}$
171	+9:57:29.089	+01:54:53.91	$9.7^{+0.1}_{-0.2}$	$0.14^{+0.08}_{-0.08}$	$8.9^{+0.3}_{-0.5}$	$9.5^{+0.8}_{-1.0}$	$7.3^{+7.4}_{-3.2}$	$7.4^{+8.4}_{-3.1}$	$0.40^{+0.60}_{-0.20}$	$1.0^{+0.0}_{-0.3}$	$28.5^{+0.0}_{-0.4}$
174	+9:59:12.510	+01:54:58.38	$9.3^{+0.2}_{-0.1}$	$0.14^{+0.10}_{-0.08}$	$8.5^{+0.6}_{-0.2}$	$8.1^{+2.0}_{-0.2}$	$1.8^{+3.2}_{-0.6}$	$2.7^{+3.3}_{-1.2}$	$0.20^{+0.80}_{-0.00}$	$0.7^{+0.3}_{-0.0}$	$10.9^{+0.0}_{-1.2}$
176	+10:00:40.584	+01:55:20.38	$9.6^{+0.1}_{-0.3}$	$0.00^{+0.22}_{-0.00}$	$9.4^{+0.2}_{-0.7}$	$9.1^{+1.2}_{-0.8}$	$0.7^{+3.3}_{-0.3}$	$0.7^{+3.5}_{-0.2}$	$0.20^{+0.80}_{-0.00}$	$1.0^{+0.0}_{-0.3}$	$15.1^{+0.0}_{-2.4}$
190	+10:00:29.560	+01:55:21.13	$10.2^{+0.1}_{-0.2}$	$0.18^{+0.16}_{-0.08}$	$9.3^{+0.3}_{-0.6}$	$9.1^{+1.2}_{-0.8}$	$4.0^{+9.4}_{-2.3}$	$4.2^{+10.0}_{-2.3}$	$0.20^{+0.80}_{-0.00}$	$0.7^{+0.3}_{-0.0}$	$14.4^{+0.0}_{-1.1}$
208	+10:01:45.444	+01:55:22.99	$11.0^{+0.1}_{-0.1}$	$0.40^{+0.12}_{-0.14}$	$9.2^{+0.2}_{-0.3}$	$8.5^{+0.4}_{-0.6}$	$2.7^{+5.9}_{-2.6}$	$3.1^{+8.0}_{-3.1}$	$0.20^{+0.80}_{-0.00}$	$1.0^{+0.0}_{-0.3}$	$7.6^{+0.0}_{-1.4}$
209	+9:58:47.838	+01:55:31.80	$10.5^{+0.1}_{-0.1}$	$0.18^{+0.14}_{-0.10}$	$9.2^{+0.2}_{-0.5}$	$8.7^{+0.8}_{-0.6}$	$3.9^{+11.6}_{-2.2}$	$4.3^{+12.3}_{-2.4}$	$0.20^{+0.20}_{-0.00}$	$1.0^{+0.0}_{-0.3}$	$7.7^{+0.0}_{-1.3}$
230	+10:00:27.355	+01:55:55.11	$10.5^{+0.1}_{-0.2}$	$0.18^{+0.16}_{-0.10}$	$9.4^{+0.2}_{-0.6}$	$9.1^{+1.0}_{-0.8}$	$4.9^{+13.2}_{-2.7}$	$5.1^{+13.9}_{-2.8}$	$0.20^{+0.80}_{-0.00}$	$0.7^{+0.3}_{-0.0}$	$5.1^{+0.0}_{-0.6}$
240	+9:59:26.106	+01:55:57.41	$9.2^{+0.2}_{-0.6}$	$0.10^{+0.18}_{-0.06}$	$9.3^{+0.3}_{-1.2}$	$10.7^{+0.0}_{-1.8}$	$1.1^{+3.9}_{-0.4}$	$1.1^{+4.2}_{-0.4}$	$0.40^{+2.10}_{-0.20}$	$1.0^{+0.0}_{-0.3}$	$35.6^{+0.0}_{-8.2}$

[a] NBES [b] $\log_{10}(M[\mathrm{M}_\odot]$; mass in stars at time of observation [c] $\log_{10}(Age[\mathrm{yr}])$ [d] $\log_{10}(\tau[\mathrm{yr}])$ [e] $[\mathrm{M}_\odot\ \mathrm{yr}^{-1}]$; instantaneous SFR at time of observation [f] $[\mathrm{M}_\odot\ \mathrm{yr}^{-1}]$; SFR averaged over 100 Myr before time of observation [g] metallicity in $[\mathrm{Z}_\odot]$ [h] fraction of ionizing radiation escaping the galaxy [i] [nm]

Additionally, the table includes the EW_{obs} estimated through the TPV.

B

APPENDIX: USEFUL RELATIONS

B.1 COLOR CORRECTED CONTINUUM MAGNITUDES

When selecting or measuring emission lines through a flux excess in a narrowband filter, estimates of the continuum flux density need to be obtained. In many cases, the continuum around the narrowband (NB) filter can be well approximated by a power law. Then, a linear combination between the magnitudes of two close by filters allow for an accurate estimate of the continuum magnitude at the wavelength of the NB filter independent of the slope of the power law. In the following, I demonstrate how the optimal linear combination can be determined.

I assume a power law SED, $f_\lambda \propto \lambda^\beta$, and three filters A, B, NB. These have effective wavelengths λ_A, λ_B, λ_{NB}. Then, the synthetic magnitudes on the AB system are to first order given by:

$$A = -2.5(-\beta - 2)\log_{10}(\lambda_A) + c_1 \tag{B.1}$$

$$B = -2.5(-\beta - 2)\log_{10}(\lambda_B) + c_1 \tag{B.2}$$

$$NB_{\mathrm{cont}} = -2.5(-\beta - 2)\log_{10}(\lambda_{NB}) + c_1 \tag{B.3}$$

Here c_1 is a constant, which absorbs both the normalization of the continuum and the ZP of the AB system.

Assuming that the magnitudes in the filters A and B are the inputs and the continuum magnitude at the position of the NB filter is the quantity of interest, this results in a well defined equation system: there are three equations for the three unknowns β, c_1, and NB_{cont}.

B.1 - B.2 gives:

$$A - B = -2.5(-\beta - 2)(\log_{10}(\lambda_A) - \log_{10}(\lambda_B)) \tag{B.4}$$

$$\Rightarrow \tag{B.5}$$

$$-2.5(-\beta - 2) = \frac{A - B}{\log_{10}(\lambda_A) - \log_{10}(\lambda_B)} \equiv \alpha \tag{B.6}$$

$$\tag{B.7}$$

Putting α into B.1:

$$c_1 = A - \alpha \log_{10}(\lambda_A) \tag{B.8}$$

Finally, this allows to calculate NB_{cont} by using α and c_1 in eq. B.3:

$$NB_{\mathrm{cont}} = \alpha \log_{10}(\lambda_{NB}) + A - \alpha \log_{10}(\lambda_A) \tag{B.9}$$

$$= A + \frac{\log_{10}(\lambda_{NB}) - \log_{10}(\lambda_A)}{\log_{10}(\lambda_A) - \log_{10}(\lambda_B)} \cdot (A - B) \tag{B.10}$$

$\frac{\log_{10}(\lambda_{NB})-\log_{10}(\lambda_A)}{\log_{10}(\lambda_A)-\log_{10}(\lambda_B)}$ is a constant.

B.2 Relation between FWHM and half light radius for a Gaussian

SExtractor allows to determine the observed half light radius for the detected objects. Then, it can be of interest to compare these values to the FWHM of a point source, e.g. determined with IRAF/imexam. But what half light radius does a point source with certain FWHM have? The point spread function (PSF) can to first order be approximated through a two-dimensional Gaussian.

The flux distribution for a (normalized) 2D Gaussian in polar coordinates does not depend on the angle θ and is given by:

$$f(r) = \frac{1}{2\pi\sigma^2} \mathrm{e}^{-\frac{1}{2}\frac{r^2}{\sigma^2}} \tag{B.11}$$

The half light radius, $R_{1/2}$, is found by requiring:

$$\frac{1}{2} = 2\pi \int_0^{R_{1/2}} f(r)\, r\, \mathrm{d}r \tag{B.12}$$

$$= 2\pi \int_0^{R_{1/2}} \frac{1}{2\pi\sigma^2} \mathrm{e}^{-\frac{1}{2}\frac{r^2}{\sigma^2}}\, r\, \mathrm{d}r = \mathrm{e}^{-\frac{1}{2}\frac{r^2}{\sigma^2}} \Big|_{R_{1/2}}^{0} \tag{B.13}$$

This results in:

$$1 - \frac{1}{2} = \frac{1}{2} = \mathrm{e}^{-\frac{1}{2}\frac{R_{1/2}^2}{\sigma^2}} \tag{B.14}$$

$$\frac{1}{2} = \mathrm{e}^{-\frac{1}{2}\frac{R_{1/2}^2}{\sigma^2}} \tag{B.15}$$

This means that for the Gaussian the $FWHM$ is identical to $2R_{1/2}$. Therefore, $R_{1/2}$ is given by:

$$R_{1/2} = \sqrt{2\log_e(2)}\sigma \approx 1.177\,\sigma \tag{B.16}$$

Consequently, the FWHM is:

$$FWHM = 2\,R_{1/2} \approx 2.355\,\sigma \tag{B.17}$$

BIBLIOGRAPHY

Acquaviva, V., Gawiser, E., & Guaita, L. 2011, The Astrophysical Journal, 737, 47

Adams, T. F. 1972, The Astrophysical Journal, 174, 439

Ahn, C. P., Alexandroff, R., Allende Prieto, C., et al. 2012, The Astrophysical Journal Supplement Series, 203, 21

Aihara, H., Allende Prieto, C., An, D., et al. 2011, The Astrophysical Journal Supplement Series, 193, 29

Alard, C., & Lupton, R. H. 1998, Astrophysical Journal, 503, 325

Allen, M. G., Groves, B. A., Dopita, M. A., Sutherland, R. S., & Kewley, L. J. 2008, The Astrophysical Journal Supplement Series, 178, 20

Aller, L. H. 1984, Dordrecht, 112

Alpher, R. A., Bethe, H., & Gamow, G. 1948, Physical Review, 73, 803

Arabsalmani, M., Møller, P., Fynbo, J. P. U., et al. 2015, Monthly Notices of the Royal Astronomical Society, 446, 990

Ashby, M. L. N., Willner, S. P., Fazio, G. G., et al. 2013, The Astrophysical Journal, 769, 80

Atad-Ettedgui, E., & Worswick, S. P. 2003, Specialized Optical Developments in Astronomy. Edited by Atad-Ettedgui, 4842, 95

Bacon, R., Accardo, M., Adjali, L., et al. 2010, in Society of Photo-Optical Instrumentation Engineers (SPIE) Conference Series, Vol. 7735, 8

Baek, S., & Ferrara, A. 2013, Monthly Notices of the Royal Astronomical Society: Letters, L77

Baker, J. G., & Menzel, D. H. 1938, The Astrophysical Journal, 88, 52

Baldwin, J. A., Phillips, M. M., & Terlevich, R. 1981, Publications of the Astronomical Society of the Pacific, 93, 5

Barro, G., Faber, S. M., Perez-Gonzalez, P. G., et al. 2014, The Astrophysical Journal, 791, 52

Bastian, N., Covey, K. R., & Meyer, M. R. 2010, Annual Review of Astronomy and Astrophysics, 48, 339

Belli, S., Newman, A. B., Ellis, R. S., & Konidaris, N. P. 2014, The Astrophysical Journal Letters, 788, L29

Benitez, N., Dupke, R., Moles, M., et al. 2014, eprint arXiv:1403.5237

Bertin, E. 2006, in Astronomical Data Analysis Software and Systems XV, 112

Bertin, E., & Arnouts, S. 1996, Astronomy and Astrophysics Supplement, 117, 393

Bertin, E., Mellier, Y., Radovich, M., et al. 2002, in Astronomical Data Analysis Software and Systems XI, 228

Bessell, M. S. 2005, Annual Review of Astronomy and Astrophysics, 43, 293

Best, P., Smail, I., Sobral, D., et al. 2010, eprint arXiv:1003.5183

Bezanson, R., van Dokkum, P. G., Tal, T., et al. 2009, The Astrophysical Journal, 697, 1290

Black, J. H., & Dalgarno, A. 1976, The Astrophysical Journal, 203, 132

Blanc, G. A., Adams, J. J., Gebhardt, K., et al. 2011, Astrophysical Journal, 736, 31

Bland-Hawthorn, J., van Breugel, W., Gillingham, P. R., Baldry, I. K., & Jones, D. H. 2001, The Astrophysical Journal, 563, 611

Blumenthal, G. R., Faber, S. M., Primack, J. R., & Rees, M. J. 1984, Nature, 311, 517

Bolton, A. S., Schlegel, D. J., Aubourg, E., et al. 2012, The Astronomical Journal, 144, 144

Bond, H. E. 1981, The Astrophysical Journal, 248, 606

Bond, N. A., Feldmeier, J. J., Matković, A., et al. 2010, The Astrophysical Journal Letters, 716, L200

Bouwens, R. J., Illingworth, G. D., Oesch, P. A., et al. 2010, The Astrophysical Journal Letters, 708, L69

Bouwens, R. J., Bradley, L., Zitrin, A., et al. 2014, The Astrophysical Journal, 795, 126

Bowler, R. A. A., Dunlop, J. S., McLure, R. J., et al. 2012, Monthly Notices of the Royal Astronomical Society, 426, 2772

Breit, G., & Teller, E. 1940, The Astrophysical Journal, 91, 215

Brocklehurst, M. 1971, Monthly Notices of the Royal Astronomical Society, 153, 471

Bromm, V. 2013, Reports on Progress in Physics, 76, 112901

Bruzual, G., & Charlot, S. 2003, Monthly Notices of the Royal Astronomical Society, 344, 1000

Bunker, A., Smith, J., Spinrad, H., Stern, D., & Warren, S. 2003, Astrophysics and Space Science, 284, 357

Bunker, A. J., Warren, S. J., Hewett, P. C., & Clements, D. L. 1995, Monthly Notices of the Royal Astronomical Society, 273, 513

Burbidge, E. M., Burbidge, G. R., Fowler, W. A., & Hoyle, F. 1957, Reviews of Modern Physics, 29, 547

Buser, R. 1986, Highlights of Astronomy, 7, 799

Cai, Z., Fan, X., Jiang, L., et al. 2011, The Astrophysical Journal, 736, L28

Calzetti, D. 1997, The Astronomical Journal, 113, 162

Calzetti, D., Armus, L., Bohlin, R. C., et al. 2000, The Astrophysical Journal, 533, 682

Capak, P., Aussel, H., Ajiki, M., et al. 2007, The Astrophysical Journal Supplement Series, 172, 99

Cardelli, J. A., Clayton, G. C., & Mathis, J. S. 1989, The Astrophysical Journal, 345, 245

Caruana, J., Bunker, A. J., Wilkins, S. M., et al. 2012, Monthly Notices of the Royal Astronomical Society, 427, 3055

—. 2014, Monthly Notices of the Royal Astronomical Society, 443, 2831

Cen, R., & Ostriker, J. P. 1999, The Astrophysical Journal, 514, 1

Cen, R., & Zheng, Z. 2013, The Astrophysical Journal, 775, 112

Chabrier, G. 2003, Publications of the Astronomical Society of the Pacific, 115, 763

Charlot, S., & Fall, S. M. 2000, The Astrophysical Journal, 539, 718

Chonis, T. S., Blanc, G. A., Hill, G. J., et al. 2013, The Astrophysical Journal, 775, 99

Christensen, L., Møller, P., Fynbo, J. P. U., & Zafar, T. 2014, Monthly Notices of the Royal Astronomical Society, 445, 225

Christensen, L., Laursen, P., Richard, J., et al. 2012, Monthly Notices of the Royal Astronomical Society, 427, 1973

Chromey, F. R. 2010, To Measure the Sky (Cambridge, UK: Cambridge University Press)

Civano, F., Elvis, M., Brusa, M., et al. 2012, The Astrophysical Journal Supplement Series, 201, 30

Clark, P. C., Glover, S. C. O., Klessen, R. S., & Bromm, V. 2011, The Astrophysical Journal, 727, 110

Clément, B., Cuby, J.-G., Courbin, F., et al. 2012, Astronomy & Astrophysics, 538, A66

Coc, A., Uzan, J.-P., & Vangioni, E. 2014, Journal of Cosmology and Astro-Particle Physics, 10, 050

Coe, D., Zitrin, A., Carrasco, M., et al. 2013, The Astrophysical Journal, 762, 32

Cole, S., Aragon-Salamanca, A., Frenk, C. S., Navarro, J. F., & Zepf, S. E. 1994, Monthly Notices of the Royal Astronomical Society, 271, 781

Conselice, C. J. 2014, Annual Review of Astronomy and Astrophysics, 52, 291

Cooke, J., Ryan-Weber, E. V., Garel, T., & Díaz, C. G. 2014, Monthly Notices of the Royal Astronomical Society, 441, 837

Cox, D. P., & Tucker, W. H. 1969, The Astrophysical Journal, 157, 1157

Daddi, E., Cimatti, A., Renzini, A., et al. 2004, The Astrophysical Journal, 617, 746

Daddi, E., Renzini, A., Pirzkal, N., et al. 2005, The Astrophysical Journal, 626, 680

Daddi, E., Dickinson, M., Morrison, G., et al. 2007, The Astrophysical Journal, 670, 156

Dale, D. A., & Helou, G. 2002, The Astrophysical Journal, 576, 159

Dale, D. A., Barlow, R. J., Cohen, S. A., et al. 2010, Astrophysical Journal, 712, L189

Dalton, G. B., Caldwell, M., Ward, A. K., et al. 2006, in Society of Photo-Optical Instrumentation Engineers (SPIE) Conference Series, Vol. 6269

Davis, M., Efstathiou, G., Frenk, C. S., & White, S. D. M. 1985, The Astrophysical Journal, 292, 371

Davis, S. W., Woo, J.-H., & Blaes, O. M. 2007, The Astrophysical Journal, 668, 682

Dayal, P., Ferrara, A., & Dunlop, J. S. 2013, Monthly Notices of the Royal Astronomical Society, 430, 2891

Dekel, A., & Burkert, A. 2014, Monthly Notices of the Royal Astronomical Society, 438, 1870

Dekel, a., Birnboim, Y., Engel, G., et al. 2009, Nature, 457, 451

Delvecchio, I., Gruppioni, C., Pozzi, F., et al. 2014, Monthly Notices of the Royal Astronomical Society, 439, 2736

Dey, A., Bian, C., Soifer, B. T., et al. 2005, The Astrophysical Journal, 629, 654

Dijkstra, M. 2008, The Astrophysical Journal, 690, 82

Dijkstra, M. 2014, Publications of the Astronomical Society of Australia, 31, 40

Dijkstra, M., Haiman, Z., & Spaans, M. 2006, The Astrophysical Journal, 649, 14

Dijkstra, M., Lidz, A., & Wyithe, J. S. B. 2007, Monthly Notices of the Royal Astronomical Society, 377, 1175

Dijkstra, M., & Loeb, A. 2009, Monthly Notices of the Royal Astronomical Society, 400, 1109

Dijkstra, M., Wyithe, S., Haiman, Z., Mesinger, A., & Pentericci, L. 2014, Monthly Notices of the Royal Astronomical Society, 440, 3309

Djorgovski, S., Spinrad, H., McCarthy, P., & Strauss, M. A. 1985, Astrophysical Journal, 299, L1

Domínguez, A., Siana, B., Brooks, A. M., et al. 2014, eprint arXiv:1408.5788

Dopita, M. A., & Sutherland, R. S. 1996, The Astrophysical Journal Supplement Series, 102, 161

Draine, B. 2003, Annual Review of Astronomy and Astrophysics, 41, 241

Dunlop, J., Akiyama, M., Alexander, D., et al. 2007, Spitzer Proposal, 40021

Dunlop, J. S., McLure, R. J., Robertson, B. E., et al. 2012, Monthly Notices of the Royal Astronomical Society, 420, 901

Eggen, O. J., Lynden-Bell, D., & Sandage, A. R. 1962, The Astrophysical Journal, 136, 748

Elvis, M., Wilkes, B. J., McDowell, J. C., et al. 1994, The Astrophysical Journal Supplement Series, 95, 1

Elvis, M., Civano, F., Vignali, C., et al. 2009, The Astrophysical Journal Supplement Series, 184, 158

Emerson, J., McPherson, A., & Sutherland, W. 2006, The Messenger, 126, 41

Erb, D. K., Pettini, M., Shapley, A. E., et al. 2010, The Astrophysical Journal, 719, 1168

Erb, D. K., Steidel, C. C., Shapley, A. E., et al. 2006, The Astrophysical Journal, 647, 128

Fan, X., Strauss, M. A., Becker, R. H., et al. 2006, The Astronomical Journal, 132, 117

Fardal, M. A., Katz, N., Gardner, J. P., et al. 2001, The Astrophysical Journal, 562, 605

Faucher-Giguère, C.-A., Kereš, D., Dijkstra, M., Hernquist, L., & Zaldarriaga, M. 2010, The Astrophysical Journal, 725, 633

Feldmeier, J. J., Hagen, A., Ciardullo, R., et al. 2013, The Astrophysical Journal, 776, 75

Ferland, G. J. 1980, Astronomical Society of the Pacific, 92, 596

Ferland, G. J., Korista, K. T., Verner, D. A., et al. 1998, The Publications of the Astronomical Society of the Pacific, 110, 761

Field, G. B., Somerville, W. B., & Dressler, K. 1966, Annual Review of Astronomy and Astrophysics, 4, 207

Findlay, J. 2012, PhD thesis, Queen Mary, University of London

Finkelstein, S. L., Rhoads, J. E., Malhotra, S., & Grogin, N. 2009, The Astrophysical Journal, 691, 465

Finkelstein, S. L., Papovich, C., Dickinson, M., et al. 2013, Nature, 502, 524

Finlator, K., & Davé, R. 2008, Monthly Notices of the Royal Astronomical Society, 385, 2181

Foot, C. J. 2005, Atomic physics (Oxford, New York: Oxford University Press)

Fosbury, R. A. E., Villar-Martín, M., Humphrey, A., et al. 2003, The Astrophysical Journal, 596, 797

Francis, P. J., Williger, G. M., Collins, N. R., et al. 2001, The Astrophysical Journal, 554, 1001

Friedmann, A. 1922, Zeitschrift fur Physik, 10, 377

Fujita, S. S., Ajiki, M., Shioya, Y., et al. 2003, Astrophysical Journal, 586, L115

Furlanetto, S. R., Oh, S. P., & Briggs, F. H. 2006, Physics Reports, 433, 181

Fynbo, J. P. U., Ledoux, C., Møller, P., Thomsen, B., & Burud, I. 2003, Astronomy & Astrophysics, 407, 147

Fynbo, J. P. U., Prochaska, J. X., Sommer-Larsen, J., Dessauges-Zavadsky, M., & Møller, P. 2008, The Astrophysical Journal, 683, 321

Fynbo, J. P. U., Ledoux, C., Noterdaeme, P., et al. 2011, Monthly Notices of the Royal Astronomical Society, 413, 2481

Fynbo, J. P. U., Geier, S. J., Christensen, L., et al. 2013, Monthly Notices of the Royal Astronomical Society, 436, 361

Fynbo, J. U., Møller, P., & Thomsen, B. 2001, Astronomy & Astrophysics, 374, 443

Fynbo, J. U., Møller, P., & Warren, S. J. 1999, Monthly Notices of the Royal Astronomical Society, 305, 849

Fynbo, J. U., Thomsen, B., & Møller, P. 2000, Astronomy & Astrophysics, 353, 457

Gallazzi, A., Bell, E. F., Zibetti, S., Brinchmann, J., & Kelson, D. D. 2014, The Astrophysical Journal, 788, 72

Gallazzi, A., Charlot, S., Brinchmann, J., White, S. D. M., & Tremonti, C. A. 2005, Monthly Notices of the Royal Astronomical Society, 362, 41

Gandhi, P., Fabian, A. C., & Crawford, C. S. 2006, Monthly Notices of the Royal Astronomical Society, 369, 1566

Geach, J. E., Bower, R. G., Alexander, D. M., et al. 2014, The Astrophysical Journal, 793, 22

Ghinassi, F., Licandro, J., Oliva, E., et al. 2002, Astronomy & Astrophysics, 386, 1157

Giavalisco, M. 2002, Annual Review of Astronomy and Astrophysics, 40, 579

Gordon, K. D., Clayton, G. C., Misselt, K. A., Landolt, A. U., & Wolff, M. J. 2003, The Astrophysical Journal, 594, 279

Gott, J. R., I., & Thuan, T. X. 1976, The Astrophysical Journal, 204, 649

Grogin, N. A., Kocevski, D. D., Faber, S. M., et al. 2011, The Astrophysical Journal Supplement, 197, 35

Grove, L. F., Fynbo, J. P. U., Ledoux, C., et al. 2009, Astronomy & Astrophysics, 497, 689

Guaita, L., Francke, H., Gawiser, E., et al. 2013, Astronomy & Astrophysics, 551, 93

Gunn, J. E., & Peterson, B. A. 1965, The Astrophysical Journal, 142, 1633

Haardt, F., & Madau, P. 2012, The Astrophysical Journal, 746, 125

Haiman, Z., & Rees, M. J. 2001, The Astrophysical Journal, 556, 87

Haiman, Z., Spaans, M., & Quataert, E. 2000, The Astrophysical Journal Letters, 537, L5

Hainline, K. N., Shapley, A. E., Greene, J. E., & Steidel, C. C. 2011, The Astrophysical Journal, 733, 31

Hainline, K. N., Shapley, A. E., Kornei, K. A., et al. 2009, The Astrophysical Journal, 701, 52

Harikane, Y., Ouchi, M., Yuma, S., et al. 2014, The Astrophysical Journal, 794, 129

Harrington, J. P. 1973, Monthly Notices of the Royal Astronomical Society, 162, 43

Hashimoto, T., Ouchi, M., Shimasaku, K., et al. 2013, Astrophysical Journal, 765, 70

Hayes, M., Scarlata, C., & Siana, B. 2011a, Nature, 476, 304

Hayes, M., Schaerer, D., Östlin, G., et al. 2011b, The Astrophysical Journal, 730, 8

Hayes, M., Östlin, G., Schaerer, D., et al. 2010, Nature, 464, 562

—. 2013, The Astrophysical Journal Letters, 765, L27

Henry, A., Scarlata, C., Domínguez, A., et al. 2013, The Astrophysical Journal Letters, 776, L27

Hewett, B. C., Warren, S. J., Leggett, S. K., & Hodgkin, S. T. 2006, Monthly Notices of the Royal Astronomical Society, 367, 454

Hogg, D. W. 1999, eprint arXiv:astro-ph/9905116

Holmberg, E. 1958, Meddelanden fran Lunds Astronomiska Observatorium Serie II, 136, 1

Hopkins, A. M., Irwin, M. J., & Connolly, A. J. 2001, The Astrophysical Journal, 558, L31

Horne, K. 1986, Astronomical Society of the Pacific, 98, 609

Horrobin, M., Goldoni, P., Royer, F., et al. 2008, The 2007 ESO Instrument Calibration Workshop, 221

Howell, S. B. 2000, Handbook of CCD Astronomy (Cambridge, U.K. ; New York: Cambridge University Press)

Hubble, E. P. 1926, The Astrophysical Journal, 64, 321

—. 1936, Realm of the Nebulae (New Haven: Yale University Press)

Hummer, D. G. 1994, Monthly Notices of the Royal Astronomical Society, 268, 109

Humphrey, A., Villar-Martin, M., Vernet, J., et al. 2008, Monthly Notices of the Royal Astronomical Society, 383, 11

Ikarashi, S., Ivison, R. J., Caputi, K. I., et al. 2014, eprint arXiv:1411.5038

Ilbert, O., McCracken, H. J., Le Fèvre, O., et al. 2013, Astronomy & Astrophysics, 556, 55

Inoue, A. K., Shimizu, I., Iwata, I., & Tanaka, M. 2014, eprint arXiv:1402.0677

Ivanov, V. D., & Szeifert, T. 2009, VIRCAM/VISTA User Manual, 1st edn., EUROPEAN SOUTHERN OBSERVATORY

Iwamuro, F., Motohara, K., Maihara, T., et al. 2003, The Astrophysical Journal, 598, 178

Jiang, L., Egami, E., Mechtley, M., et al. 2013a, The Astrophysical Journal, 772, 99

Jiang, L., Egami, E., Fan, X., et al. 2013b, Astrophysical Journal, 773, 153

Kant, I. 1755, Allgemeine Naturgeschichte und Theorie des Himmels

Kashikawa, N., Shimasaku, K., Malkan, M. A., et al. 2006, The Astrophysical Journal, 648, 7

Kashikawa, N., Nagao, T., Toshikawa, J., et al. 2012, The Astrophysical Journal, 761, 85

Kauffmann, G., Heckman, T. M., Tremonti, C., et al. 2003, Monthly Notices of the Royal Astronomical Society, 346, 1055

Kausch, W., Noll, S., Smette, A., et al. 2015, Astronomy & Astrophysics, 576, A78

Kennicutt, R. C. 1998, Annual Review of Astronomy and Astrophysics, 36, 189

Kewley, L. J., & Dopita, M. A. 2002, The Astrophysical Journal Supplement Series, 142, 35

Kewley, L. J., Dopita, M. A., Sutherland, R. S., Heisler, C. A., & Trevena, J. 2001, The Astrophysical Journal, 556, 121

Kewley, L. J., Geller, M. J., & Jansen, R. A. 2004, The Astronomical Journal, 127, 2002

Kippenhahn, R., Weigert, A., & Weiss, A. 2012, Stellar Structure and Evolution (Berlin; Heidelberg: Springer-Verlag)

Kochiashvili, I., Møller, P., Milvang-Jensen, B., et al. 2015, eprint arXiv:1504.03005

Koekemoer, A. M., Aussel, H., Calzetti, D., et al. 2007, The Astrophysical Journal Supplement Series, 172, 196

Koekemoer, A. M., Faber, S. M., Ferguson, H. C., et al. 2011, The Astrophysical Journal Supplement, 197, 36

Konno, A., Ouchi, M., Ono, Y., et al. 2014, The Astrophysical Journal, 797, 16

Kramida, A., Yu. Ralchenko, Reader, J., & and NIST ASD Team. 2014, NIST Atomic Spectra Database (ver. 5.2), [Online]. Available: `http://physics.nist.gov/asd` [2015, January 3]. National Institute of Standards and Technology, Gaithersburg, MD.

Krogager, J. K., Zirm, A. W., Toft, S., Man, A., & Brammer, G. 2014, The Astrophysical Journal, 797, 17

Krogager, J.-K., Fynbo, J. P. U., Ledoux, C., et al. 2013, Monthly Notices of the Royal Astronomical Society, 433, 3091

Kroupa, P. 2001, Monthly Notices of the Royal Astronomical Society, 322, 231

Krueger, H., Fritze-v Alvensleben, U., & Loose, H. H. 1995, Astronomy & Astrophysics, 303, 41

Krug, H. B., Veilleux, S., Tilvi, V., et al. 2012, The Astrophysical Journal, 745, 122

Kuhlen, M., & Faucher-Giguère, C.-A. 2012, Monthly Notices of the Royal Astronomical Society, 423, 862

Kurk, J., Röttgering, H., Pentericci, L., & Miley, G. 2000, Clustering at High Redshift, 200, 424

Lake, E., Zheng, Z., Cen, R., et al. 2015, eprint arXiv:1502.01349

Lamareille, F., Brinchmann, J., Contini, T., et al. 2009, Astronomy & Astrophysics, 495, 53

Larson, R. B. 1975, Monthly Notices of the Royal Astronomical Society, 173, 671

Laursen, P., Duval, F., & Östlin, G. 2013, The Astrophysical Journal, 766, 124

Laursen, P., Razoumov, A. O., & Sommer-Larsen, J. 2009a, The Astrophysical Journal, 696, 853

Laursen, P., & Sommer-Larsen, J. 2007, The Astrophysical Journal Letters, 657, L69

Laursen, P., Sommer-Larsen, J., & Andersen, A. C. 2009b, The Astrophysical Journal, 704, 1640

Laursen, P., Sommer-Larsen, J., & Razoumov, A. O. 2011, The Astrophysical Journal, 728, 52

Lawrence, A., Warren, S. J., Almaini, O., et al. 2007, Monthly Notices of the Royal Astronomical Society, 379, 1599

Le Borgne, J. F., Bruzual, G., Pello, R., et al. 2003, Astronomy & Astrophysics, 402, 433

Lehner, N., Howk, J. C., Tripp, T. M., et al. 2013, The Astrophysical Journal, 770, 138

Leitherer, C., Schaerer, D., Goldader, J. D., et al. 1999, The Astrophysical Journal Supplement Series, 123, 3

Lilly, S. J., Le Brun, V., Maier, C., et al. 2009, The Astrophysical Journal Supplement, 184, 218

Lissberger, P. H. 1970, Reports on Progress in Physics, 33, 197

Ly, C., Lee, J. C., Dale, D. A., et al. 2011, The Astrophysical Journal, 726, 109

Ly, C., Malkan, M. A., Kashikawa, N., et al. 2012, Astrophysical Journal, 757, 63

—. 2007, The Astrophysical Journal, 657, 738

Madau, P., & Dickinson, M. 2014, Annual Review of Astronomy and Astrophysics, 52, 415

Maiolino, R., Nagao, T., Grazian, A., et al. 2008, Astronomy & Astrophysics, 488, 463

Malhotra, S., & Rhoads, J. E. 2002, The Astrophysical Journal Letters, 565, L71

Malhotra, S., Rhoads, J. E., Finkelstein, S. L., et al. 2012, The Astrophysical Journal Letters, 750, L36

Mannucci, F., Cresci, G., Maiolino, R., Marconi, A., & Gnerucci, A. 2010, Monthly Notices of the Royal Astronomical Society, 408, 2115

Maraston, C. 1998, Monthly Notices of the Royal Astronomical Society, 300, 872

—. 2005, Monthly Notices of the Royal Astronomical Society, 362, 799

Maraston, C., Daddi, E., Renzini, A., et al. 2006, The Astrophysical Journal, 652, 85

Matsuda, Y., Yamada, T., Hayashino, T., Yamauchi, R., & Nakamura, Y. 2006, The Astrophysical Journal, 640, L123

Matsuda, Y., Yamada, T., Hayashino, T., et al. 2004, The Astronomical Journal, 128, 569

—. 2012, Monthly Notices of the Royal Astronomical Society, 425, 878

Matsuoka, Y. 2012, The Astrophysical Journal, 750, 54

Matteucci, F. 2012, Chemical Evolution of Galaxies (Berlin; Heidelberg: Springer-Verlag)

McCarthy, P. J. 1993, Annual Review of Astronomy and Astrophysics, 31, 639

McCarthy, P. J., Le Borgne, D., Crampton, D., et al. 2004, The Astrophysical Journal, 614, L9

McCracken, H. J., Milvang-Jensen, B., Dunlop, J., et al. 2012, Astronomy & Astrophysics, 544, 156

McKee, C. F., & Ostriker, J. P. 1977, The Astrophysical Journal, 218, 148

McLinden, E. M., Malhotra, S., Rhoads, J. E., et al. 2013, Astrophysical Journal, 767, 48

McLinden, E. M., Finkelstein, S. L., Rhoads, J. E., et al. 2011, The Astrophysical Journal, 730, 136

Mendel, J. T., Saglia, R. P., Bender, R., et al. 2015, eprint arXiv:1503.08831

Metropolis, N., Rosenbluth, A. W., Rosenbluth, M. N., Teller, A. H., & Teller, E. 1953, Journal of Chemical Physics, 21, 1087

Meurer, G. R., Heckman, T. M., & Calzetti, D. 1999, The Astrophysical Journal, 521, 64

Mignoli, M., Vignali, C., Gilli, R., et al. 2013, Astronomy & Astrophysics, 556, 29

Mihos, J. C., & Hernquist, L. 1996, The Astrophysical Journal, 464, 641

Miller, L., Peacock, J. A., & Mead, A. R. G. 1990, Monthly Notices of the Royal Astronomical Society, 244, 207

Milvang-Jensen, B., Freudling, W., Zabl, J., et al. 2013, Astronomy & Astrophysics, 560, A94

Modigliani, A., Goldoni, P., Royer, F., et al. 2010, in Society of Photo-Optical Instrumentation Engineers (SPIE) Conference Series, Vol. 7737

Møller, P., Fynbo, J. P. U., Ledoux, C., & Nilsson, K. K. 2013, Monthly Notices of the Royal Astronomical Society, 430, 2680

Møller, P., & Warren, S. J. 1993, Astronomy & Astrophysics, 270, 43

—. 1998, Monthly Notices of the Royal Astronomical Society, 299, 661

Momose, R., Ouchi, M., Nakajima, K., et al. 2014, Monthly Notices of the Royal Astronomical Society, 442, 110

Morelli, D. W. 1991, Interference filter handbook. A guide for specifying optimum filter performance, Santa Rosa, Ca.: Optical Coating Laboratory Inc. (OCLI)

Mori, M., & Umemura, M. 2007, Astrophysics and Space Science, 311, 111

Mori, M., Umemura, M., & Ferrara, A. 2004, The Astrophysical Journal, 613, L97

Mosleh, M., Williams, R. J., Franx, M., et al. 2012, The Astrophysical Journal Letters, 756, L12

Moustakas, J., Kennicutt, Jr, R. C., & Tremonti, C. A. 2006, The Astrophysical Journal, 642, 775

Muzzin, A., Marchesini, D., Stefanon, M., et al. 2013, The Astrophysical Journal Supplement Series, 206, 8

Nagao, T., Motohara, K., Maiolino, R., et al. 2005, The Astrophysical Journal, 631, L5

Nakajima, K., Ouchi, M., Shimasaku, K., et al. 2012, The Astrophysical Journal, 745, 12

Nelder, J. A., & Mead, R. 1965, The Computer Journal, 7, 308

Neufeld, D. A. 1990, The Astrophysical Journal, 350, 216

—. 1991, The Astrophysical Journal Letters, 370, L85

Newman, A. B., Ellis, R. S., Bundy, K., & Treu, T. 2012, The Astrophysical Journal, 746, 162

Nilsson, K. K. 2007, PhD thesis, Dark Cosmology Centre, Niels Bohr Institute Faculty of Science, University of Copenhagen

Nilsson, K. K., Fynbo, J. P. U., Møller, P., Sommer-Larsen, J., & Ledoux, C. 2006, Astronomy & Astrophysics, 452, L23

Nilsson, K. K., Östlin, G., Møller, P., et al. 2011, Astronomy & Astrophysics, 529, 9

Nilsson, K. K., Tapken, C., Møller, P., et al. 2009, Astronomy & Astrophysics, 498, 13

Nilsson, K. K., Møller, P., Möller, O., et al. 2007, Astronomy & Astrophysics, 471, 71

Noeske, K. G., Weiner, B. J., Faber, S. M., et al. 2007, The Astrophysical Journal, 660, L43

Noll, S., Burgarella, D., Giovannoli, E., et al. 2009, Astronomy & Astrophysics, 507, 1793

Nomoto, K., Kobayashi, C., & Tominaga, N. 2013, Annual Review of Astronomy and Astrophysics, 51, 457

Nussbaumer, H., & Schmutz, W. 1984, Astronomy & Astrophysics, 138, 495

Oesch, P. A., Bouwens, R. J., Illingworth, G. D., et al. 2014, The Astrophysical Journal, 786, 108

Oke, J. B. 1974, The Astrophysical Journal Supplement Series, 27, 21

Ono, Y., Ouchi, M., Shimasaku, K., et al. 2010, The Astrophysical Journal, 724, 1524

Onodera, M., Carollo, C. M., Renzini, A., et al. 2014, eprint arXiv:1411.5023, 1411.5023

Osterbrock, D. E. 1962, The Astrophysical Journal, 135, 195

Osterbrock, D. E. 1989, Astrophysics of gaseous nebulae and active galactic nuclei (Mill Valley, CA: University Science Books)

Osterbrock, D. E., & Ferland, G. J. 2006, Astrophysics of gaseous nebulae and active galactic nuclei (Sausalito, CA: University Science Books)

Östlin, G., Hayes, M., Kunth, D., et al. 2009, The Astronomical Journal, 138, 923

Ouchi, M., Shimasaku, K., Furusawa, H., et al. 2003, The Astrophysical Journal, 582, 60

Ouchi, M., Shimasaku, K., Akiyama, M., et al. 2008, The Astrophysical Journal Supplement Series, 176, 301

Ouchi, M., Ono, Y., Egami, E., et al. 2009, The Astrophysical Journal, 696, 1164

Ouchi, M., Shimasaku, K., Furusawa, H., et al. 2010, The Astrophysical Journal, 723, 869

Ouchi, M., Ellis, R., Ono, Y., et al. 2013, The Astrophysical Journal, 778, 102

Pagel, B. E. J., Edmunds, M. G., Blackwell, D. E., Chun, M. S., & Smith, G. 1979, Monthly Notices of the Royal Astronomical Society, 189, 95

Pallottini, A., Ferrara, A., Gallerani, S., Salvadori, S., & D'Odorico, V. 2014, Monthly Notices of the Royal Astronomical Society, 440, 2498

Partridge, R. B., & Peebles, P. J. E. 1967, The Astrophysical Journal, 147, 868

Pascual, S., Gallego, J., & Zamorano, J. 2007, Publications of the Astronomical Society of the Pacific, 119, 30

Pei, Y. C., & Fall, S. M. 1995, The Astrophysical Journal, 454, 69

Pengelly, R. M. 1964, Monthly Notices of the Royal Astronomical Society, 127, 145

Pentericci, L., Grazian, A., Fontana, A., et al. 2009, Astronomy & Astrophysics, 494, 553

Pentericci, L., Vanzella, E., Fontana, A., et al. 2014, The Astrophysical Journal, 793, 113

Percival, W. J., Reid, B. A., Eisenstein, D. J., et al. 2010, MNRAS, 401, 2148

Perlmutter, S., Aldering, G., Goldhaber, G., et al. 1999, The Astrophysical Journal, 517, 565

Planck Collaboration, Ade, P. A. R., Aghanim, N., et al. 2014, Astronomy & Astrophysics, 571, A16

Poggianti, B. M. 2004, Clusters of Galaxies: Probes of Cosmological Structure and Galaxy Evolution, 245

Prescott, M. K. M., Dey, A., & Jannuzi, B. T. 2009, The Astrophysical Journal, 702, 554

Prescott, M. K. M., Dey, A., & Jannuzi, B. T. 2012, The Astrophysical Journal, 748, 125

Prescott, M. K. M., Momcheva, I., Brammer, G. B., Fynbo, J. P. U., & Møller, P. 2015, The Astrophysical Journal, 802, 32

Rafelski, M., Wolfe, A. M., Prochaska, J. X., Neeleman, M., & Mendez, A. J. 2012, The Astrophysical Journal, 755, 89

Raiter, A., Schaerer, D., & Fosbury, R. A. E. 2010, Astronomy & Astrophysics, 523, 64

Rauch, M., Haehnelt, M., Bunker, A., et al. 2008, The Astrophysical Journal, 681, 856

Razoumov, A. O., & Sommer-Larsen, J. 2010, The Astrophysical Journal, 710, 1239

Rees, M. J., & Ostriker, J. P. 1977, Monthly Notices of the Royal Astronomical Society, 179, 541

Rhoads, J. E., Malhotra, S., Dey, A., et al. 2000, The Astrophysical Journal Letters, 545, L85

Rhoads, J. E., Malhotra, S., Richardson, M. L. A., et al. 2014, The Astrophysical Journal, 780, 20

Rieke, G. 2007, Annual Review of Astronomy and Astrophysics, 45, 77

Riess, A. G., Filippenko, A. V., Challis, P., et al. 1998, The Astronomical Journal, 116, 1009

Roberts, G. O., & Rosenthal, J. S. 2001, Statistical Science, 16, 351

Rosenthal, J. S. 2014, in Statistics in Action: A Canadian Outlook (CRC Press), 93–106

Rousselot, P., Lidman, C., Cuby, J.-G., Moreels, G., & Monnet, G. 2000, Astronomy & Astrophysics, 354, 1134

Rubin, K. H. R., Hennawi, J. F., Prochaska, J. X., et al. 2014, eprint arXiv:1411.6016

Saito, T., Shimasaku, K., Okamura, S., et al. 2006, The Astrophysical Journal, 648, 54

Salpeter, E. E. 1955, Astrophysical Journal, 121, 161

Savaglio, S., Glazebrook, K., Le Borgne, D., et al. 2005, The Astrophysical Journal, 635, 260

Scannapieco, E., Schneider, R., & Ferrara, A. 2003, The Astrophysical Journal, 589, 35

Scarlata, C., Colbert, J., Teplitz, H. I., et al. 2009, The Astrophysical Journal, 706, 1241

Schaerer, D. 2002, Astronomy & Astrophysics, 382, 28

Schaerer, D., Boone, F., Zamojski, M., et al. 2015, Astronomy & Astrophysics, 574, A19

Schaerer, D., & de Barros, S. 2009, Astronomy & Astrophysics, 502, 423

—. 2010, Astronomy & Astrophysics, 515, 73

Schechter, P. 1976, Astrophysical Journal, 203, 297

Schenker, M. A., Ellis, R. S., Konidaris, N. P., & Stark, D. P. 2014, The Astrophysical Journal, 795, 20

Schlegel, D. J., Finkbeiner, D. P., & Davis, M. 1998, The Astrophysical Journal, 500, 525

Scoville, N., Aussel, H., Brusa, M., et al. 2007, The Astrophysical Journal Supplement Series, 172, 1

Shankar, F., Weinberg, D. H., & Miralda-Escudé, J. 2009, The Astrophysical Journal, 690, 20

Shapley, A. E., Steidel, C. C., Pettini, M., & Adelberger, K. L. 2003, The Astrophysical Journal, 588, 65

Shapley, A. E., Reddy, N. A., Kriek, M., et al. 2015, The Astrophysical Journal, 801, 88

Shibuya, T., Kashikawa, N., Ota, K., et al. 2012, The Astrophysical Journal, 752, 114

Simpson, C., Martínez-Sansigre, A., Rawlings, S., et al. 2006, Monthly Notices of the Royal Astronomical Society, 372, 741

Smette, A., Sana, H., Noll, S., et al. 2015, ArXiv e-prints, 1501, 7239

Smith, D. J. B., & Jarvis, M. J. 2007, Monthly Notices of the Royal Astronomical Society: Letters, 378, L49

Sobral, D., Best, P. N., Geach, J. E., et al. 2010, Monthly Notices of the Royal Astronomical Society, 404, 1551

Sobral, D., Best, P. N., Matsuda, Y., et al. 2012, MNRAS, 420, 1926

Sobral, D., Best, P. N., Smail, I., et al. 2011, Monthly Notices of the Royal Astronomical Society, 411, 675

Sobral, D., Best, P. N., Geach, J. E., et al. 2009, Monthly Notices of the Royal Astronomical Society, 398, 75

Sommer-Larsen, J., & Fynbo, J. P. U. 2008, Monthly Notices of the Royal Astronomical Society, 385, 3

Song, M., Finkelstein, S. L., Gebhardt, K., et al. 2014, Astrophysical Journal, 791, 3

Songaila, A. 2004, The Astronomical Journal, 127, 2598

Spitzer, L. J., & Greenstein, J. L. 1951, The Astrophysical Journal, 114, 407

Springel, V., & Hernquist, L. 2005, The Astrophysical Journal Letters, 622, L9

Stark, D. P., Ellis, R. S., Chiu, K., Ouchi, M., & Bunker, A. 2010, Monthly Notices of the Royal Astronomical Society, 408, 1628

Stark, D. P., Richard, J., Charlot, S., et al. 2014a, eprint arXiv:1408.3649

Stark, D. P., Richard, J., Siana, B., et al. 2014b, Monthly Notices of the Royal Astronomical Society, 445, 3200

Steidel, C. C., Adelberger, K. L., Giavalisco, M., Dickinson, M., & Pettini, M. 1999, The Astrophysical Journal, 519, 1

Steidel, C. C., Adelberger, K. L., Shapley, A. E., et al. 2000, The Astrophysical Journal, 532, 170

Steidel, C. C., Adelberger, K. L., Shapley, A. E., et al. 2003, The Astrophysical Journal, 592, 728

Steidel, C. C., Bogosavljević, M., Shapley, A. E., et al. 2011, The Astrophysical Journal, 736, 160

Steidel, C. C., Erb, D. K., Shapley, A. E., et al. 2010, The Astrophysical Journal, 717, 289

Steidel, C. C., Shapley, A. E., Pettini, M., et al. 2004, The Astrophysical Journal, 604, 534

Steidel, C. C., Rudie, G. C., Strom, A. L., et al. 2014, The Astrophysical Journal, 795, 165

Storey, P. J., & Hummer, D. G. 1995, Monthly Notices of the Royal Astronomical Society, 272, 41

Susa, H., Hasegawa, K., & Tominaga, N. 2014, The Astrophysical Journal, 792, 32

Sutherland, R. S., & Dopita, M. A. 1993, The Astrophysical Journal Supplement Series, 88, 253

Takahashi, M. I., Shioya, Y., Taniguchi, Y., et al. 2007, The Astrophysical Journal Supplement Series, 172, 456

Tanaka, M., Toft, S., Marchesini, D., et al. 2013, The Astrophysical Journal, 772, 113

Taniguchi, Y., & Shioya, Y. 2000, The Astrophysical Journal, 532, L13

Taniguchi, Y., Scoville, N., Murayama, T., et al. 2007, The Astrophysical Journal Supplement Series, 172, 9

Tanvir, N. R. 2013, eprint arXiv:1307.6156

Toft, S., Gallazzi, A., Zirm, A., et al. 2012, The Astrophysical Journal, 754, 3

Toft, S., van Dokkum, P., Franx, M., et al. 2007, The Astrophysical Journal, 671, 285

Toft, S., Smolcic, V., Magnelli, B., et al. 2014, The Astrophysical Journal, 782, 68

Toomre, A. 1977, in Evolution of Galaxies and Stellar Populations, ed. B. M. Tinsley & R. B. G. Larson, D. Campbell, 401

Tremonti, C. A., Heckman, T. M., Kauffmann, G., et al. 2004, The Astrophysical Journal, 613, 898

Treu, T., Schmidt, K. B., Trenti, M., Bradley, L. D., & Stiavelli, M. 2013, The Astrophysical Journal Letters, 775, L29

Trujillo, I., Förster Schreiber, N. M., Rudnick, G., et al. 2006a, The Astrophysical Journal, 650, 18

Trujillo, I., Förster Schreiber, N. M., Rudnick, G., et al. 2006b, The Astrophysical Journal, 650, 18

Tumlinson, J., & Shull, J. M. 2000, The Astrophysical Journal Letters, 528, L65

Tumlinson, J., Venkatesan, A., & Shull, J. M. 2004, The Astrophysical Journal, 612, 602

Ueda, J., Iono, D., Yun, M. S., et al. 2014, The Astrophysical Journal Supplement Series, 214, 1

van de Sande, J., Kriek, M., Franx, M., Bezanson, R., & van Dokkum, P. G. 2014, The Astrophysical Journal Letters, 793, L31 van Dokkum, P. G., Labbé, I., Marchesini, D., et al. 2009, Publications of the Astronomical Society of the Pacific, 121, 2

van Ojik, R., Roettgering, H. J. A., Miley, G. K., & Hunstead, R. W. 1997, Astronomy & Astrophysics, 317, 358

Vanden Berk, D. E., Richards, G. T., Bauer, A., et al. 2001, The Astronomical Journal, 122, 549

Vanzella, E., Grazian, A., Hayes, M., et al. 2010, Astronomy & Astrophysics, 513, 20

Vanzi, L., Gennari, S., Ciofini, M., & Testi, L. 1998, Experimental Astronomy, 8, 177

Vazdekis, A., Sánchez-Blázquez, P., Falcón-Barroso, J., et al. 2010, Monthly Notices of the Royal Astronomical Society

Vázquez, G. A., & Leitherer, C. 2005, The Astrophysical Journal, 621, 695

Verhamme, A., Schaerer, D., & Maselli, A. 2006, Astronomy & Astrophysics, 460, 397

Vernet, J., Dekker, H., D'Odorico, S., et al. 2011, Astronomy & Astrophysics, 536, 105

Villar, V., Gallego, J., Pérez-González, P. G., et al. 2008, The Astrophysical Journal, 677, 169

Villar-Martín, M. 2007, New Astronomy Reviews, 51, 194

Villar-Martín, M., Cerviño, M., & González Delgado, R. M. 2004, Monthly Notices of the Royal Astronomical Society, 355, 1132

Villar-Martín, M., Sánchez, S. F., Humphrey, A., et al. 2007, Monthly Notices of the Royal Astronomical Society, 378, 416

Villar-Martín, M., Tadhunter, C., Pérez, E., et al. 2010, Monthly Notices of the Royal Astronomical Society, 407, L6

Vogelsberger, M., Genel, S., Springel, V., et al. 2014, Nature, 509, 177

Wagg, J., & Kanekar, N. 2012, The Astrophysical Journal Letters, 751, L24

Wagoner, R. V., Fowler, W. A., & Hoyle, F. 1967, The Astrophysical Journal, 148, 3

Walcher, J., Groves, B., Budavári, T., & Dale, D. 2010, Astrophysics and Space Science, 331, 1

Wardlow, J. L., Malhotra, S., Zheng, Z., et al. 2014, The Astrophysical Journal, 787, 9

Weidinger, M., Møller, P., & Fynbo, J. P. U. 2004, Nature, 430, 999

Westera, P., Lejeune, T., Buser, R., Cuisinier, F., & Bruzual, G. 2002, Astronomy & Astrophysics, 381, 524

White, S. D. M., & Frenk, C. S. 1991, The Astrophysical Journal, 379, 52

White, S. D. M., & Rees, M. J. 1978, Monthly Notices of the Royal Astronomical Society, 183, 341

Wiersma, R. P. C., Schaye, J., & Smith, B. D. 2009, Monthly Notices of the Royal Astronomical Society, 393, 99

Wright, T. I. o. D. 1750, An Original Theory Or New Hypothesis of the Universo, Founded Upon the Laws of Nature, and Solving by Mathematical Principles the General Phaenomena of the Visible Creation and Particularly the Via Lactea. - London (London: Chapelle)

Wuyts, S., Cox, T. J., Hayward, C. C., et al. 2010, Astrophysical Journal, 722, 1666

Wuyts, S., Labbe, I., Schreiber, N. M. F., et al. 2008, Astrophysical Journal, 682, 985

Yabe, K., Ohta, K., Iwamuro, F., et al. 2012, Publications of the Astronomical Society of Japan, 64, 60

Yajima, H., Li, Y., & Zhu, Q. 2013a, The Astrophysical Journal, 773, 151

—. 2013b, The Astrophysical Journal, 773, 151

Yajima, H., Li, Y., Zhu, Q., & Abel, T. 2012, eprint arXiv:1211.0014

Yang, Y., Zabludoff, A., Tremonti, C., Eisenstein, D., & Davé, R. 2009, The Astrophysical Journal, 693, 1579

Yang, Y., Zabludoff, A. I., Dave, R., et al. 2006, The Astrophysical Journal, 640, 539

Yuma, S., Ouchi, M., Drake, A. B., et al. 2013, The Astrophysical Journal, 779, 53

Zackrisson, E., Bergvall, N., Olofsson, K., & Siebert, A. 2001, Astronomy & Astrophysics, 375, 814

Zackrisson, E., Rydberg, C.-E., Schaerer, D., Östlin, G., & Tuli, M. 2011, The Astrophysical Journal, 740, 13

Zackrisson, E., Zitrin, A., Trenti, M., et al. 2012, Monthly Notices of the Royal Astronomical Society, 427, 2212

Zahid, H. J., Kewley, L. J., & Bresolin, F. 2011, The Astrophysical Journal, 730, 137

Zheng, Z., Cen, R., Weinberg, D., Trac, H., & Miralda-Escudé, J. 2011, The Astrophysical Journal, 739, 62

Zheng, Z.-Y., Malhotra, S., Wang, J.-X., et al. 2012, The Astrophysical Journal, 746, 28

Zibetti, S., Gallazzi, A., Charlot, S., Pierini, D., & Pasquali, A. 2012, Monthly Notices of the Royal Astronomical Society, sts126

Zitrin, A., Zheng, W., Broadhurst, T., et al. 2014, The Astrophysical Journal Letters, 793, L12

Zwaan, M. A., van der Hulst, J. M., Briggs, F. H., Verheijen, M. A. W., & Ryan-Weber, E. V. 2005, Monthly Notices of the Royal Astronomical Society, 364, 1467